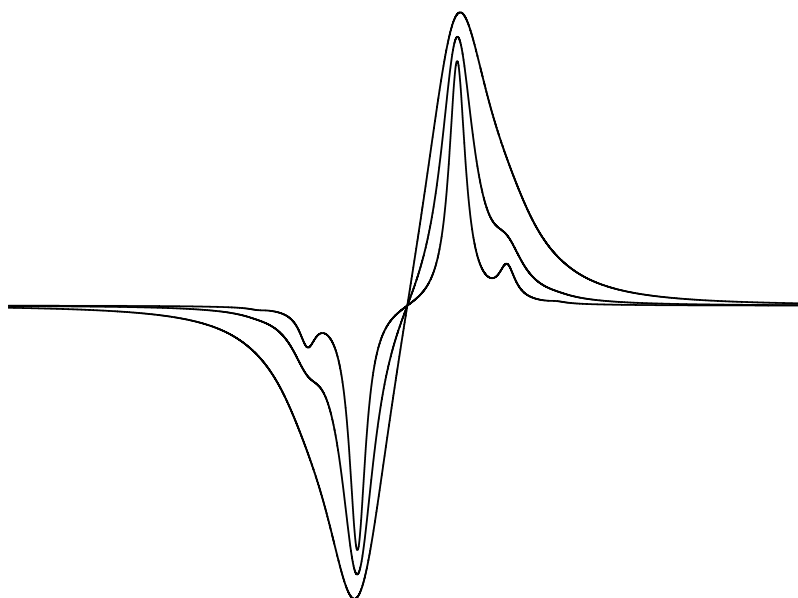


SINGLE-TONE MID-INFRARED FREQUENCY  
MODULATION SPECTROSCOPY  
FOR GAS-PHASE REACTION KINETICS



DISSERTATION

in Fulfillment of the Requirements  
for the Degree **Dr. rer. nat.**  
of the Faculty of Mathematics and Natural Sciences  
at Kiel University

submitted by

Michael Stuhr

Kiel, 2024



Michael Stuhr

Single-Tone Mid-Infrared Frequency Modulation Spectroscopy for Gas-Phase Reaction Kinetics

1st Referee: Prof. Dr. Gernot Friedrichs

2nd Referee: Prof. Dr. Melanie Schnell

Date of oral examination: April 16, 2024

Signature of faculty dean:





## Abstract

Quantitative and sensitive detection of chemical species plays a key role in the study of gas-phase reactions that occur in combustion processes, earth’s atmosphere, and many other environments. In this context, frequency modulation spectroscopy (FMS) is particularly attractive, since it enables robust in-situ species detection with high sensitivity on short timescales. The mid-infrared (MIR) spectral region spans over high-intensity fundamental rovibrational transitions of many species of interest, but MIR applications of FMS have remained rare as of yet.

In the present work, a new single-tone mid-infrared frequency modulation (ST-MIR-FM) spectrometer has been developed and characterized in detail. For the first time, ST-MIR-FM spectroscopic detection was realized by the use of an external electro-optic modulator and, in the case of the most recent version of the spectrometer, by all-digital demodulation. The ST-MIR-FM detection system reaches minimum detectable fractional absorption levels of  $A_{\min} = 2.9 \times 10^{-4}$  at a time resolution of  $t = 1 \mu\text{s}$ . Although ST-MIR-FMS does not yet reach the shot-noise limit, a notable sensitivity improvement compared to conventional dual-beam laser absorption spectroscopy with  $A_{\min} \approx 2 \times 10^{-3}$  was achieved. The present work presents ST-MIR-FM detection of  $\text{CH}_4$ ,  $\text{HCl}$ , and  $\text{OH}$  radicals in low-pressure flow cells and of  $\text{HCN}$  behind shock waves. As a first test, FM spectra of  $\text{CH}_4$  were recorded and found to be in excellent agreement with spectral simulations. Concentration-time profiles of  $\text{HCl}$  and  $\text{OH}$  radicals in a low-pressure photolysis reactor served to demonstrate time-resolved ST-MIR-FM detection on  $\mu\text{s}$  timescales.

In a measurement campaign at the Swiss Light Source (SLS), the UV photolysis of oxalyl chloride,  $(\text{ClCO})_2$ , was investigated to determine the quantum yield of the recently discovered direct  $\text{Cl}_2$  formation channel using time-of-flight mass spectrometry. Complementary  $(\text{ClCO})_2$  photolysis experiments were performed at Kiel University, where  $\text{HCl}$  was detected by ST-MIR-FMS in  $(\text{ClCO})_2/\text{C}_2\text{H}_6/\text{Ar}$  gas mixtures. Kinetic profiles of  $\text{HCl}$  served to trace the unimolecular decomposition of the  $\text{ClCO}$  radical, which was necessary for analyzing the  $\text{Cl}_2$  data recorded at the SLS. The determined room-temperature rate constant confirmed earlier indirectly measured results for  $\text{ClCO} + \text{M}$  in argon buffer gas. With  $\text{ClCO}$  decomposition accounted for, analysis of the kinetic  $\text{Cl}_2$  profiles provided wavelength-dependent photolysis quantum yields for direct  $\text{Cl}_2$  formation of up to 10%. This clearly indicates that the previously accepted picture of  $(\text{ClCO})_2$  photofragmentation has to be revised.

In the past, FMS has been successfully used for species detection in shock tube experiments. Due to the derivative nature of FM signal generation, it is much less effected by shock-induced mechanical noise than conventional laser absorption methods. With ST-MIR-FMS,  $\text{HCN}$  could be sensitively detected by targeting its rovibrational P(26) transition line in the fundamental C-H stretch vibration band. In order to ensure quantitative detection, FM spectra of  $\text{HCN}$  were reconstructed from individual shock tube experiments around the absorption line. Lineshape analysis of the high-temperature FM spectra provided the pressure-broadening parameters of the P(26) transition. For typical post-shock conditions of  $T = 1700 \text{ K}$  and  $p = 1.2 \text{ bar}$ , an  $\text{HCN}$  detection limit of 22 ppm at a time resolution of  $t = 1 \mu\text{s}$  was achieved. This is low enough to perform direct rate constant measurements of elementary reactions involving  $\text{HCN}$ , which thus far has been a major challenge.

Using the newly established ST-MIR-FM system for quantitative  $\text{HCN}$  detection, two combustion-related reactions were investigated with shock tube experiments. Firstly, the total rate constant of  $\text{HCN}$  oxidation by  $\text{O}$  atoms was measured in the temperature range  $1400 \text{ K} < T < 2000 \text{ K}$ . The resulting Arrhenius parameters complete the available rate constants for  $\text{HCN} + \text{O}$ , which have previously been derived by detecting other involved species. Secondly, the channel branching of the prompt-NO switch reaction  $\text{NCN} + \text{H}$  was investigated behind incident shock waves. By employing simultaneous detection of  $\text{NCN}$  and  $\text{HCN}$  via UV laser absorption and ST-MIR-FMS, respectively, the branching fraction of the  $\text{HCN}$ -forming channel has been determined, yielding  $0.22 < \phi < 0.63$  within  $1200 \text{ K} < T < 2000 \text{ K}$ . These experiments represent the first direct branching fraction measurements of the prompt-NO switch reaction  $\text{NCN} + \text{H}$ . The determined branching fractions clearly show that the  $\text{HCN}$ -forming channel is already active at typical flame temperatures, which is in stark contrast to the most recent theoretical predictions.

## Kurzzusammenfassung

Der quantitative und empfindliche Nachweis von chemischen Spezies spielt eine zentrale Rolle bei der Untersuchung von Gasphasenreaktionen, die in Verbrennungsprozessen, in der Erdatmosphäre und in vielen anderen Umgebungen stattfinden. In diesem Zusammenhang ist die Frequenzmodulationsspektroskopie (FMS) besonders interessant, da sie die robuste In-situ-Detektion von Spezies mit hoher Empfindlichkeit auf kurzen Zeitskalen ermöglicht. Der Spektralbereich des mittleren Infrarots (MIR) erstreckt sich über intensive rovibronische Übergänge vieler interessanter Spezies, dennoch sind MIR-Anwendungen von FMS bisher sehr selten.

In dieser Arbeit wurde ein neues Single-Tone-Mid-Infrared-Frequenzmodulationsspektrometer (ST-MIR-FMS) aufgebaut und ausgiebig charakterisiert. Erstmals wurde ST-MIR-FM-spektroskopische Detektion mit Hilfe von externer elektrooptischer Modulation und, im Fall der neuesten Version des Spektrometers, mit volldigitaler Demodulation realisiert. Das Nachweissystem erreicht eine minimal detektierbare Absorption von  $A_{\min} = 2.9 \times 10^{-4}$  bei einer Zeitauflösung von  $t = 1 \mu\text{s}$ . Obwohl ST-MIR-FMS bisher noch nicht das Schrotrauschlimit erreicht, wurde bereits eine deutliche Empfindlichkeitsverbesserung im Vergleich zu konventioneller Zweistrahl-Laserabsorptionsspektroskopie mit  $A_{\min} \approx 2 \times 10^{-3}$  erreicht. Die vorliegende Arbeit beschreibt die ST-MIR-FM-Detektion von  $\text{CH}_4$ ,  $\text{HCl}$  und  $\text{OH}$ -Radikalen in einer Niederdruck-Flusszelle und von  $\text{HCN}$  hinter Stoßwellen. Als erster Test wurden FM-Spektren von  $\text{CH}_4$  gemessen und mit spektralen Simulationen verglichen, wobei eine ausgezeichnete Übereinstimmung festgestellt wurde. Zur Demonstration von zeitaufgelöster ST-MIR-FM-Detektion auf der  $\mu\text{s}$ -Zeitskala wurden Konzentrations-Zeit-Profile von  $\text{HCl}$  und  $\text{OH}$ -Radikalen in einem Niederdruck-Photolysereaktor aufgenommen.

In einer Messkampagne an der Swiss Light Source (SLS) wurde die UV-Photolyse von Oxalylchlorid,  $(\text{ClCO})_2$ , untersucht, indem die Quantenausbeute des kürzlich entdeckten direkten  $\text{Cl}_2$ -Bildungskanal durch Flugzeit-Massenspektrometrie bestimmt wurde. Komplementäre  $(\text{ClCO})_2$ -Photolyseexperimente wurden an der CAU Kiel durchgeführt, in denen  $\text{HCl}$  durch ST-MIR-FMS in  $(\text{ClCO})_2/\text{C}_2\text{H}_6/\text{Ar}$ -Gasmischungen nach UV-Photolyse detektiert wurde. Kinetische  $\text{HCl}$ -Profile dienten hierbei zur Verfolgung des unimolekularen Verfalls des  $\text{ClCO}$ -Radikals, der zur Auswertung der  $\text{Cl}_2$ -Daten von der SLS benötigt wurde. Die bestimmte Gesamtgeschwindigkeitskonstante bei Zimmertemperatur bestätigt frühere, indirekt gemessene Ergebnisse für  $\text{ClCO} + \text{M}$  in Argon-Badgas. Dadurch konnten die kinetischen  $\text{Cl}_2$ -Profile analysiert werden, woraus wellenlängenabhängige Photolysequantenausbeuten der direkten  $\text{Cl}_2$ -Bildung von bis zu 10% ermittelt wurden. Diese Ergebnisse weisen deutlich darauf hin, dass die bisherige Sicht auf die  $(\text{ClCO})_2$ -Photofragmentation revidiert werden muss.

FMS wurde in früheren Arbeiten erfolgreich für die Detektion von Spezies in Stoßwellenexperimenten eingesetzt. Durch ihre differentielle Signalerzeugung wird FMS von stoßwelleninduzierten mechanischen Störungen deutlich weniger beeinträchtigt als konventionelle Laserabsorptionsmethoden. Mit Hilfe von ST-MIR-FMS konnte  $\text{HCN}$  auf der rovibronischen P(26)-Linie im fundamentalen Band der C-H-Streckschwingung empfindlich nachgewiesen werden. Um quantitative Detektion zu gewährleisten, wurden FM-Spektren von  $\text{HCN}$  aus einzelnen Stoßwellenexperimenten in der Nähe der Absorptionslinie rekonstruiert. Die Linienprofil-Analyse der Hochtemperatur-FM-Spektren ergab die Druckverbreiterungsparameter der P(26)-Linie. Für typische Stoßwellenbedingungen von  $T = 1700 \text{ K}$  und  $p = 1.2 \text{ bar}$  wurde ein  $\text{HCN}$ -Nachweislimit von 22 ppm bei einer Zeitauflösung von  $t = 1 \mu\text{s}$  erreicht. Dies ermöglicht die direkte Messung von Geschwindigkeitskonstanten elementarer  $\text{HCN}$ -Reaktionen, was bisher eine große Herausforderung darstellte.

Mit dem neuen ST-MIR-FM-System für quantitative  $\text{HCN}$ -Detektion wurden zwei verbrennungsrelevante Reaktionen in einer Reihe von Stoßwellenexperimenten untersucht. Zunächst wurde die Gesamtgeschwindigkeitskonstante der  $\text{HCN}$ -Oxidation durch O-Atome im Temperaturbereich  $1400 \text{ K} < T < 2000 \text{ K}$  gemessen. Die erhaltenen Arrhenius-Parameter vervollständigen die bekannten Werte für die Gesamtgeschwindigkeitskonstante von  $\text{HCN} + \text{O}$ , welche in früheren Arbeiten durch Detektion anderer beteiligter Spezies erhalten wurden. Darüber hinaus wurde die Kanalverzweigung der Prompt-NO-Switch-Reaktion  $\text{NCN} + \text{H}$  hinter einfallenden Stoßwellen untersucht. Durch simultane Detektion von  $\text{NCN}$  und  $\text{HCN}$  durch UV-Laserabsorption bzw. ST-MIR-FMS wurde das Kanalverzweigungsverhältnis  $\phi$  des  $\text{HCN}$ -bildenden Kanals von  $\text{NCN} + \text{H}$  bestimmt, wobei  $0.22 < \phi < 0.63$  im Bereich  $1200 \text{ K} < T < 2000 \text{ K}$  ermittelt wurde. Diese Ergebnisse stellen die erste direkte Kanalverzweigungsmessung der Prompt-NO-Switch-Reaktion  $\text{NCN} + \text{H}$  dar, wodurch ein wertvoller Einblick in die  $\text{NO}_x$ -Bildung gewährt wird. Die bestimmten Kanalverzweigungsverhältnisse weisen deutlich darauf hin, dass der  $\text{HCN}$ -bildende Kanal bereits bei typischen Flammentemperaturen aktiv ist, was im starken Gegensatz zu den neuesten theoretischen Vorhersagen steht.

---

# Contents

---

<b>1</b>	<b>Introduction</b>	<b>1</b>
1.1	Laser-Based Detection Techniques for Gas-Phase Kinetics . . . . .	1
1.2	Frequency Modulation in Laser Spectroscopy . . . . .	2
1.3	Objectives and Structure of This Work . . . . .	5
	References . . . . .	7
<b>2</b>	<b>Theoretical Background</b>	<b>11</b>
2.1	Frequency Modulation Spectroscopy . . . . .	11
2.1.1	The Electro-Optic Effect . . . . .	11
2.1.2	Electro-Optic Phase Modulators . . . . .	15
2.1.3	Principle of Frequency Modulation Spectroscopy . . . . .	17
2.1.4	The FM Factor . . . . .	21
2.2	Noise in FM Spectroscopy . . . . .	27
2.2.1	RAM Noise . . . . .	30
2.3	Allan Sensitivity Analysis . . . . .	31
	References . . . . .	33
<b>3</b>	<b>Experimental</b>	<b>37</b>
3.1	Single-Tone Mid-Infrared FM Spectrometer . . . . .	37
3.2	Gain factor $G$ and Modulation Index $M$ . . . . .	42
3.3	Shock Tube Apparatus . . . . .	43
3.4	Calculation Methods . . . . .	45
	References . . . . .	47
<b>4</b>	<b>Publication I: Single-Tone MIR-FM Spectroscopy</b>	<b>49</b>
4.1	Introduction . . . . .	50
4.2	Theoretical Background . . . . .	52
4.3	Experimental . . . . .	54
4.4	Results . . . . .	55
4.5	Conclusion . . . . .	62
	References . . . . .	63

<b>5</b>	<b>Publication II: UV Photolysis of Oxalyl Chloride</b>	<b>67</b>
5.1	Introduction . . . . .	68
5.2	Experimental . . . . .	71
5.3	Results . . . . .	74
5.4	Discussion . . . . .	82
5.5	Summary . . . . .	88
	References . . . . .	88
<b>6</b>	<b>Publication III: MIR-FM Detection of HCN behind Shock Waves</b>	<b>93</b>
6.1	Introduction . . . . .	94
6.2	Experimental . . . . .	96
6.3	Results and Discussion . . . . .	96
6.4	Conclusions . . . . .	104
	References . . . . .	104
<b>7</b>	<b>Publication IV: The Reaction <math>\text{HCN} + \text{O}</math> behind Shock Waves</b>	<b>107</b>
7.1	Introduction . . . . .	108
7.2	Experimental . . . . .	110
7.3	Results and Discussion . . . . .	115
7.4	Summary . . . . .	125
	References . . . . .	126
<b>8</b>	<b>Publication V: Branching Fraction Measurement of the Reaction <math>\text{NCN} + \text{H}</math></b>	<b>131</b>
8.1	Introduction . . . . .	132
8.2	Experimental . . . . .	134
8.3	Results and Discussion . . . . .	136
8.4	Conclusions . . . . .	143
	References . . . . .	143
<b>9</b>	<b>Summary and Outlook</b>	<b>145</b>
	<b>Appendix</b>	<b>151</b>
<b>A</b>	<b>Supplementary Material for Publication II</b>	<b>151</b>
<b>B</b>	<b>Supplementary Material for Publication V</b>	<b>159</b>
	<b>Scientific Contributions</b>	<b>171</b>
	<b>Curriculum Vitae</b>	<b>173</b>
	<b>Acknowledgments</b>	<b>175</b>

---

## List of Figures

---

1.1	Simplified scheme of frequency modulation spectroscopy . . . . .	3
2.1	Index ellipsoids of different crystal types . . . . .	12
2.2	Example tensors of linear electro-optic coefficients . . . . .	13
2.3	Longitudinal and transverse EOMs . . . . .	16
2.4	Bessel functions $J_n(M)$ and frequency-modulated electric field $E_m(t)$ . . . . .	19
2.5	Exemplary FM profiles for $\theta = 0^\circ$ and $\theta = 90^\circ$ . . . . .	24
2.6	$x_m$ - $M$ heatmap for $\Delta f_{\max}$ and exemplary $\Delta f(M)$ functions . . . . .	25
2.7	Polar $\Delta f_{\max}(\theta)$ plot and exemplary FM profiles for different $\theta$ values . . . . .	26
2.8	Signal-to-noise ratio $\text{SNR}(I)$ and noise spectral density $S(f)$ . . . . .	29
2.9	ADEV-OADEV comparison and Allan deviation for different noise types . . . . .	32
3.1	Detailed schematic of the single-tone MIR-FM setup . . . . .	38
3.2	Interferometer transmission spectrum and $\text{C}_2\text{H}_2$ spectra . . . . .	42
3.3	Schematic of shock wave propagation and shock tube apparatus . . . . .	44
4.1	Schematic of the MIR-FM setup . . . . .	54
4.2	FM spectra of $\text{CH}_4$ and scanning etalon transmission spectrum . . . . .	57
4.3	Kinetic profiles of $\text{HCl}$ and $\text{OH}$ . . . . .	58
4.4	FM signal noise and Allan plot regarding $I_{\text{FM}}$ . . . . .	60
4.5	Allan plot regarding $A_{\min}$ and log-log extrapolation . . . . .	61
5.1	Kinetic $\text{HCl}$ profile and sensitivity plot for 355 nm . . . . .	75
5.2	Kinetic $\text{HCl}$ profile for 266 nm and pseudo-first order plot for $\text{ClCO} + \text{M}$ . . . . .	77
5.3	Example time-of-flight mass spectrum for $(\text{ClCO})_2$ photolysis . . . . .	78
5.4	Kinetic $\text{Cl}_2$ profiles for 213 nm, 266 nm, and 355 nm . . . . .	79
5.5	Kinetic $\text{Cl}_2$ profile for 266 nm and sensitivity plot . . . . .	81
5.6	Quantum yield plot for $(\text{ClCO})_2$ photolysis . . . . .	82
5.7	Rate constant ratio $r$ for $(\text{ClCO})_2$ photolysis . . . . .	83
5.8	Potential energy diagram for $(\text{ClCO})_2$ photofragmentation . . . . .	85
6.1	Temperature-dependent linestrengths $S$ for $\text{HCN}$ lines . . . . .	97
6.2	Typical $\text{HCN}$ traces measured behind shock waves . . . . .	99
6.3	log-log plot for the temperature dependence of $2\gamma_{\text{Ar}}$ . . . . .	101

6.4	Allan plot regarding $A_{\min}$ for HCN detection behind shock waves . . . . .	102
6.5	Kinetic HCN profile during $\text{HCN} + \text{O}$ . . . . .	103
7.1	Schematic of the single-tone MIR-FM setup . . . . .	111
7.2	FM parameters for HCN detection behind shock waves . . . . .	117
7.3	Allan plot for HCN detection limit and log-log extrapolation . . . . .	118
7.4	Example kinetic HCN profile behind the reflected shock wave . . . . .	121
7.5	Experimental and simulated HCN profiles and sensitivity plots . . . . .	122
7.6	Arrhenius plot for $\text{HCN} + \text{O}$ . . . . .	123
8.1	Example kinetic $^3\text{NCN}$ and HCN profiles and sensitivity plots . . . . .	137
8.2	Arrhenius plot and branching fraction plot for $^3\text{NCN} + \text{H}$ . . . . .	140
A.1	Exemplary $\text{ClCO}^+$ mass signal . . . . .	153
A.2	Rate constant ratio $r$ as function of density . . . . .	153
A.3	Photoelectron images for $\text{Cl}_2$ . . . . .	154
A.4	Images of optimized G4 structures for the transitions states TS1–5. . . . .	156
B.1	Additional example profiles of HCN and $^3\text{NCN}$ . . . . .	166
B.2	Arrhenius plot for reaction $\text{BrCN} + \text{H}$ . . . . .	167
B.3	Comparison of manual and global fit results for $\phi_{1b}$ . . . . .	169
B.4	Arrhenius plot and branching fraction plot for $^3\text{NCN} + \text{H}$ in color . . . . .	169

# CHAPTER 1

---

## Introduction

---

The detection of atomic and molecular species plays a central role in studying chemical reactions. Gas-phase reactions are the driving forces in combustion and atmospheric processes, many industrial operations, plasma chemistry, and other natural and artificial systems. Such systems are highly dynamic and characterized by the interactions and reaction networks between many chemical species. The underlying elementary reactions take place on different timescales, involved species are generated at different concentration levels, and all observables may vary with conditions such as temperature, pressure, and composition. Physicochemical models of reactive gas-phase systems rely on accurate kinetic mechanisms and suitable detection methods are needed to measure concentrations-time profiles of involved atoms and molecules. Species-specific detection may be pursued in the field or in dedicated laboratory setups, including shock tubes, flame burners, plasma reactors, and flash photolysis cells, among many others.

Reaction kinetic studies that target individual reactions can be very demanding in terms of detection sensitivity and time resolution, depending on the species of interest and the particular application. Additionally, harsh experimental conditions, as they occur behind shock waves or in particle-forming environments, can strongly interfere with recorded signals and compromise the kinetic analysis. Such requirements constitute a major challenge for many detection methods, which vary widely in detection sensitivity, species specificity, time resolution, technical robustness, and versatility of application.

### 1.1 Laser-Based Detection Techniques for Gas-Phase Kinetics

Within the general framework outlined above, species detection by optical means stands out, since it is principally capable of non-intrusive species-specific measurements in real-time. Due to high optical power, high spectral resolution, and high beam collimation, laser-based techniques are particularly attractive for sensitive and quantitative detection of individual trace gas species. For example, reaction kinetic studies using shock tubes require species-specific detection on short timescales, often in the  $\mu\text{s}$  range, and at low concentrations, sometimes even down to the sub-ppm level, and thus benefit greatly from laser-based detection methods [1, 2]. In the context of combustion research, the most important laser-based detection techniques include, but are not limited to, laser absorption spectroscopy (LAS), laser-induced fluorescence (LIF), coherent anti-Stokes Raman scattering (CARS), degenerate four-wave mixing (DFWM), and

polarization spectroscopy (PS). These methods provide unique diagnostic capabilities and operate under different practical limitations. Their fundamental principles and areas of combustion-related application are discussed in a number of reviews [3–8].

Laser absorption spectroscopy is one of the most widespread and broadly applicable approaches for quantitative species detection and offers a number of potential advantages over its competitors. Firstly, LAS is a linear spectroscopic method with a straightforward relationship between measured absorption signal and underlying species concentration (Beer-Lambert law). Compared to non-linear and emission-based techniques, this greatly simplifies quantitative measurements of species concentrations. Since absorption signals are well-defined by the linestrength and lineshape of the probed absorption feature, species detection with LAS is largely insensitive to changes in experimental parameters other than temperature and pressure. Secondly, absorption measurements tend to be experimentally simple with comparatively few instrumental requirements. Thirdly, despite operating in line-of-sight configuration, LAS uses highly directional laser beams and thus allows for tomographic measurements with high spatial resolution [9], which can provide valuable insight into anisotropic gas-phase systems such as plasma discharges and flames.

However, laser-based absorption measurements are also subject to certain limitations. Some experimental circumstances can cause strong interference with measured absorption signals and lead to unreliable concentration data. This is particularly relevant for quantitative species detection behind shock waves, which induce mechanical vibrations and beam steering, or in particle-forming environments, where broadband absorption may play a significant role. The most common obstacle to high-sensitivity detection with laser absorption-based methods is laser intensity noise, also referred to as laser excess noise. Typically, laser excess noise decreases towards higher detection frequencies ( $1/f$  noise) and can therefore be reduced by modulation strategies operating at sufficiently high frequencies.

## 1.2 Frequency Modulation in Laser Spectroscopy

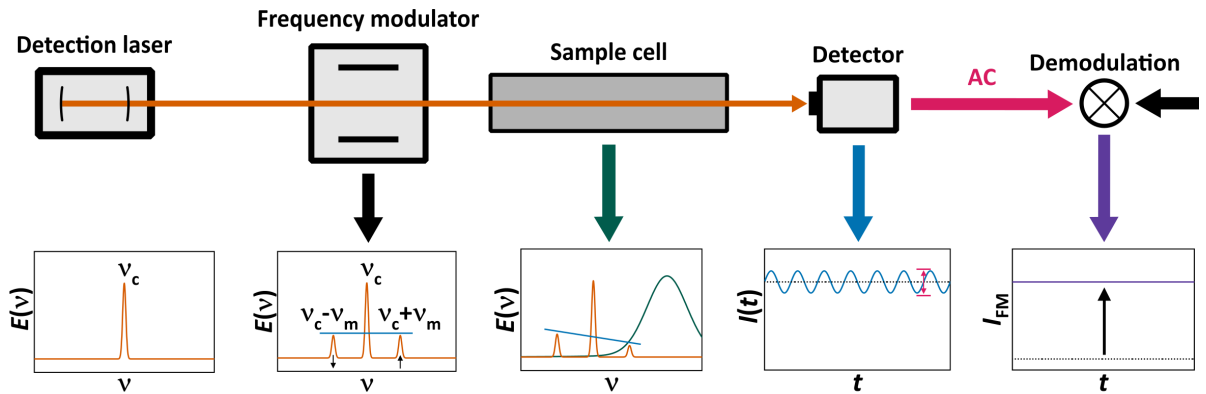
Frequency modulation (FM) appears in many technological fields, such as radio [10], radar [11], audio synthesis [12], and spectroscopy. The common thread in these very different areas of application is the use of a modulation signal, most commonly a sinusoidal wave, to introduce periodic frequency variations around a carrier frequency. Generally speaking, frequency modulation allows for information to be encoded in the carrier wave by changing its instantaneous frequency in a controlled manner. In the context of laser spectroscopy, FM serves to improve the sensitivity of absorption measurements via an upshift in detection frequency, thereby suppressing  $1/f$  noise. Frequency modulation spectroscopy (FMS) was pioneered by researchers around Gary C. Bjorklund in the early 1980s [13, 14]. Since then, many other important contributions regarding fundamental aspects of FMS have been made, including the influential theoretical works of Silver [15] and Supplee et al. [16].

Figure 1.1 illustrates the basic principle behind FMS; a detailed theoretical description is given later in Sections 2.1.3 and 2.1.4. While conventional LAS relies on quantifying the intensity



depletion imposed by absorption, FMS is a differential method that utilizes the absorption imbalance between different frequency components in frequency-modulated laser light.

To this end, the narrow-bandwidth output beam of a detection laser is subjected to sinusoidal frequency modulation, which transfers some intensity from the carrier wave  $\nu_c$  into frequency sidebands, which are separated from the carrier by integer multiples of the modulation frequency  $\nu_m$ . In the simplest case, this results in a triplet of frequency components: the carrier wave at  $\nu_c$  and two sidebands at  $\nu_c \pm \nu_m$ . For pure frequency modulation, the electric field of the detection beam  $E$  has a time-dependent instantaneous frequency  $\nu(t)$ , but its intensity envelope  $I$  remains constant. When the frequency-modulated light passes through an absorbing sample, the two sidebands may experience unequal attenuation, depending on the selected detection laser frequency. Unequal sideband attenuation causes the total detection laser intensity to exhibit amplitude modulation, which contains the absorption information. To highlight this aspect, FMS is often referred to as an optical heterodyne detection technique. In general, heterodynes, also referred to as beat frequencies, are signal components that oscillate at distinct frequencies different from the carrier frequency. In this case, they emerge from different absorption levels acting on the two sidebands, causing signal beating at  $\nu_m$ , which manifests itself as amplitude modulation. The time-dependent intensity envelope  $I(t)$  of the amplitude-modulated laser beam is then measured by a fast photodetector and the AC intensity component is demodulated with respect to  $\nu_m$  (phase-sensitive detection) [17]. After demodulation, one receives the FM signal with intensity  $I_{\text{FM}}$ , which is proportional to the attenuation imposed by the spectral line of interest, and the underlying absorption signal is fully recovered. Conventional LAS, on the other hand, is a homodyne technique, where the incident and transmitted laser fields contain the same single frequency, i.e., the carrier [18], and the absorption signal is derived from the reduction of the total intensity  $I$ . Thus, any fluctuations in  $I$  directly compromise the detection performance of LAS. Since FM signals arise from differential sideband absorption, FMS is largely immune to instrumental changes in the detection laser intensity, including laser excess noise. This significantly improves detection sensitivity and robustness. Ideally, the measured FM signal  $I_{\text{FM}}$  is only non-



**Figure 1.1:** Simplified scheme of the principle behind frequency modulation spectroscopy.  $E$ : electric field,  $\nu$ : frequency,  $\nu_c$ : carrier frequency,  $\nu_m$ : modulation frequency,  $I(t)$ : time-dependent signal intensity,  $I_{\text{FM}}$ : FM signal intensity, AC: alternating current.

zero when the sidebands experience different absorption levels, thereby enabling background-free detection.

At this point, it is instructive to introduce some basic conceptual distinctions with regards to FMS as a spectroscopic technique. There are single-tone (ST) and two-tone (TT) variants of FMS, the latter of which employs modulation at two distinct frequencies rather than one. In TT-FMS, demodulation is performed with respect to the difference of the two modulation frequencies, which reduces the bandwidth requirement of potential photodetectors. Throughout this work, the general term "frequency modulation spectroscopy" refers to single-tone FMS, unless specified otherwise. A technique closely related to FMS is wavelength modulation spectroscopy (WMS), which also relies on modulation of the detection laser frequency, albeit at a much lower modulation frequency. The distinction between WMS and FMS is somewhat arbitrary, but a common approach restricts WMS and FMS to modulation frequencies much smaller and larger than the spectral linewidth of the probed absorption feature, respectively [15, 16]. An alternative definition constrains WMS to modulation frequencies below  $\sim 10$  MHz and FMS to modulation with frequencies above  $\sim 100$  MHz. Regardless of the preferred terminology, WMS and FMS both rely on probing absorption lines of chemical species with frequency-modulated laser fields. Moreover, there are two distinct approaches to create frequency-modulated light for spectroscopic measurements. Frequency modulation is either introduced at the laser source (direct modulation) or by using a dedicated modulator (indirect/external modulation). Both methods are commonly used, but direct modulation often has a detrimental effect on FM detection performance, as will become clear in Section 2.2.1.

Applications of species detection with FMS can be broadly grouped into spectral and fixed-frequency measurements. FM spectra can be used to determine the position of weak absorption lines or to study time-dependent lineshape effects [19]. There is a large number of species for which FM spectra have been recorded, including closed-shell species such as  $\text{CH}_4$  [20],  $\text{N}_2\text{O}$  [21], and  $\text{ND}_4$  [22] as well as radicals like  $\text{SiH}_2$  [23],  $\text{HCO}$  [24],  $\text{CN}$  [19], and  $\text{CH}_2$  [25, 26]. Arguably more important, however, is the use of FMS at fixed selected detection laser frequencies, since the method excels at time-resolved concentration measurements in reaction kinetic studies. As a highly sensitive and robust technique, FMS is capable of operating under difficult experimental conditions that would be untenable for conventional LAS.

Furthermore, there is a number of advanced FM-based applications that employ a second sensitivity-enhancing strategy in addition to frequency modulation. Examples for this approach include FM-enhanced variants of polarization spectroscopy [27], Faraday rotation spectroscopy [28, 29] and Stark modulation spectroscopy [30]. These techniques either aim to improve the performance of an FM-based detection scheme or to counter the shortcomings of the other spectroscopic technique by complementing it with frequency modulation.

FM detection has been most successful in the visible range, where quantitative and sensitive detection of transient species down to the shot-noise limit was achieved [31, 32]. Combustion research in particular has benefitted from the favorable detection capabilities of visible-range FM spectroscopy. The research groups of Wagner and Hanson have been at the forefront of FM-based

detection behind shock waves, targeting electronic transitions of transient species such as  $\text{NH}_2$  [31, 33, 34],  $\text{CH}_2$  [35], and  $\text{HCO}$  [32]. To a lesser extent, FM-based detection has also been successfully employed in the near-infrared (NIR) region [36–38]. More recently, an effort has been made to establish FMS in other spectral ranges. For example, the OH radical was detected in the ultraviolet (UV) range by the Hanson group [39] and the first use of FMS in the vacuum-UV (VUV) was realized by Hollenstein et al. [40].

As demonstrated by the wide variety of reported applications, FMS represents a powerful diagnostics tool in the field of gas-phase reaction kinetics. However, FMS has only enjoyed limited success in the mid-infrared (MIR) region, since MIR-FMS suffers from three main drawbacks compared to applications in the visible range. Firstly, MIR-spectroscopic techniques are subject to much higher thermal and background noise, which greatly hampers detection sensitivity. Secondly, electro-optic modulators for creating frequency-modulated detection light are much less efficient in the MIR compared to the visible range, making sensitive MIR-FM detection more challenging. Thirdly, MIR photodetectors struggle to match the strict bandwidth requirements for recording high-frequency beat signals. This issue can be addressed by using two-tone FMS, thereby avoiding the need for high-bandwidth MIR photodetectors. However, depending on the particular detection parameters, this may also limit the sensitivity gain achieved by employing modulation at high frequency [15, 41]. As an example, the Taatjes group used TT-MIR-FM detection of HCl [42, 43] to study the reaction kinetics of Cl atoms in a low-pressure reactor. Prior to the studies conducted for the present thesis, single-tone MIR-FM detection has not been realized for reaction kinetic studies.

It is worth highlighting that single-tone FM spectroscopy in the mid-infrared region opens up new or alternative detection avenues for many chemical species. Most notably, the MIR range spans over the fundamental transitions of C-H, O-H, and N-H stretch vibrations, giving access to species such as HCN,  $\text{CH}_4$ ,  $\text{CH}_3$ ,  $\text{HO}_2$ , and  $\text{NH}_3$ . Compared to spectroscopic applications in the NIR region, which target overtone and combination bands, MIR detection offers much higher absorption cross sections, and therefore lower detection limits. In the context of combustion research, the fundamental C-H stretch vibration bands at around  $3\text{ }\mu\text{m}$  are particularly interesting for detecting hydrocarbons.

## 1.3 Objectives and Structure of This Work

The overarching aim of the experiments described in the present thesis was to establish single-tone MIR-FM spectroscopy as a reliable, quantitative, and sensitive detection technique for reaction kinetic studies. To this end, three main research goals were pursued:

1. Setup of the first ST-MIR-FM spectrometer with external modulation and verification of quantitative species detection.
2. Characterization of the detection system with regards to sensitivity and other key performance indicators.

3. Practical implementation of ST-MIR-FMS for highly sensitive species detection in pulsed laser photolysis and shock tube experiments.

The abovementioned topics were investigated in five research articles, which are embedded in this thesis (Publications I–V). Publication I reports the first version of the ST-MIR-FM detection system and the current iteration is described in Publication IV. With regards to reaction kinetic applications of the spectrometer, Publications I and II focus on ST-MIR-FM detection for experiments in low-pressure flow reactors, whereas Publications III–V are concerned with quantitative high-temperature detection of HCN in shock-heated reactive gas mixtures. The contents of the individual studies can be briefly summarized as follows:

- **Publication I** (Chapter 4): This work reports the first implementation of ST-MIR-FMS with external modulation. FM spectra of  $\text{CH}_4$  were recorded to confirm the capacity of the FM spectrometer for quantitative species detection. Concentration-time profiles of HCl and OH radicals were measured and analyzed to demonstrate the diagnostic potential of the new spectrometer for reaction kinetic studies. The detection sensitivity of the spectrometer was assessed by means of an Allan analysis.
- **Publication II** (Chapter 5): The UV photolysis of  $(\text{ClCO})_2$  was investigated with time-of-flight mass spectrometric measurements in the photoelectron photoion coincidence spectroscopy (PEPICO) setup at the VUV beamline of the Swiss Light Source (SLS), focusing on the previously neglected direct  $\text{Cl}_2$  formation channel. In complementary UV photolysis experiments at Kiel University, ST-MIR-FM spectroscopy was employed to record concentration-time profiles of HCl, which was formed by the reaction  $\text{Cl} + \text{C}_2\text{H}_6$ , in order to trace the thermal decomposition of the ClCO radical into Cl and CO.
- **Publication III** (Chapter 6): High-temperature detection of HCN by means of ST-MIR-FMS was realized by targeting the rovibrational P(26) line in the fundamental C-H stretch band. Several sets of shock tube experiments with different temperatures and pressures behind the incident and reflective waves were conducted in order to derive the argon-broadening parameters of the probed absorption line. These measurements represent the first MIR-FM species detection behind shock waves and highlight the importance of pressure broadening in quantitative absorption-based detection.
- **Publication IV** (Chapter 7): An improved version of the spectrometer was established, thoroughly characterized in terms of its detection sensitivity, and utilized for HCN detection behind shock waves during the reaction  $\text{HCN} + \text{O}$ . Temperature-dependent rate constants for this reaction were determined in the previously understudied temperature region  $1400 \text{ K} < T < 2000 \text{ K}$ .
- **Publication V** (Chapter 8): For the first time, the temperature-dependent branching fractions of the prompt-NO switch reaction  $\text{NCN} + \text{H}$  were directly measured. This was achieved by recording kinetic profiles of the reactant NCN and the product HCN behind

shock waves within  $1200\text{ K} < T < 2000\text{ K}$  via simultaneous detection with UV-LAS and ST-MIR-FMS, respectively.

Each of the five studies represents either a significant diagnostic development and/or a practical application of MIR-FMS for topical research in gas-phase reaction kinetics. The following Chapter 2 gives a thorough description of the theoretical background, starting with the electro-optic effect for frequency modulation of laser light and basic FM theory. Afterwards, more advanced aspects of quantitative FM detection and detection sensitivity are discussed. Chapter 3 provides the instrumental details of the ST-MIR-FM spectrometer as well as an overview of the Kiel shock tube facility and the methods used for data analysis. The thesis concludes with a summary of key results and a brief outlook on future applications and further potential improvements of the ST-MIR-FM detection system in Chapter 9.

## References

- [1] R. K. Hanson, Applications of quantitative laser sensors to kinetics, propulsion and practical energy systems, *Proc. Combust. Inst.* **2011**, *33*, 1–40, DOI [10.1016/j.proci.2010.09.007](https://doi.org/10.1016/j.proci.2010.09.007).
- [2] C. S. Goldenstein, R. Spearrin, J. B. Jeffries, R. K. Hanson, Infrared laser-absorption sensing for combustion gases, *Prog. Energy Combust. Sci.* **2017**, *60*, 132–176, DOI [10.1016/j.pecs.2016.12.002](https://doi.org/10.1016/j.pecs.2016.12.002).
- [3] K. Kohse-Höinghaus, Laser techniques for the quantitative detection of reactive intermediates in combustion systems, *Prog. Energy Combust. Sci.* **1994**, *20*, 203–279, DOI [10.1016/0360-1285\(94\)90015-9](https://doi.org/10.1016/0360-1285(94)90015-9).
- [4] J. W. Daily, Laser induced fluorescence spectroscopy in flames, *Prog. Energy Combust. Sci.* **1997**, *23*, 133–199, DOI [10.1016/S0360-1285\(97\)00008-7](https://doi.org/10.1016/S0360-1285(97)00008-7).
- [5] J. Kiefer, P. Ewart, Laser diagnostics and minor species detection in combustion using resonant four-wave mixing, *Prog. Energy Combust. Sci.* **2011**, *37*, 525–564, DOI [10.1016/j.pecs.2010.11.001](https://doi.org/10.1016/j.pecs.2010.11.001).
- [6] M. Bolshov, Y. Kuritsyn, Y. Romanovskii, Tunable diode laser spectroscopy as a technique for combustion diagnostics, *Spectrochim. Acta B* **2015**, *106*, 45–66, DOI [10.1016/j.sab.2015.01.010](https://doi.org/10.1016/j.sab.2015.01.010).
- [7] A. Ehn, J. Zhu, X. Li, J. Kiefer, Advanced Laser-Based Techniques for Gas-Phase Diagnostics in Combustion and Aerospace Engineering, *Appl. Spectrosc.* **2017**, *71*, 341–366, DOI [10.1177/0003702817690161](https://doi.org/10.1177/0003702817690161).
- [8] M. Aldén, Spatially and temporally resolved laser/optical diagnostics of combustion processes: From fundamentals to practical applications, *Proc. Combust. Inst.* **2023**, *39*, 1185–1228, DOI [10.1016/j.proci.2022.06.020](https://doi.org/10.1016/j.proci.2022.06.020).
- [9] C. Liu, L. Xu, Laser absorption spectroscopy for combustion diagnosis in reactive flows: A review, *Appl. Spectrosc. Rev.* **2019**, *54*, 1–44, DOI [10.1080/05704928.2018.1448854](https://doi.org/10.1080/05704928.2018.1448854).
- [10] E. Armstrong, A Method of Reducing Disturbances in Radio Signaling by a System of Frequency Modulation, *Proc. Inst. Radio Eng.* **1936**, *24*, 689–740, DOI [10.1109/JRPROC.1936.227383](https://doi.org/10.1109/JRPROC.1936.227383).
- [11] D. G. Luck, *Frequency Modulated Radar*, McGraw-Hill, **1949**.
- [12] J. M. Chowning, The Synthesis of Complex Audio Spectra by Means of Frequency Modulation, *Comput. Music J.* **1977**, *1*, 46–54.
- [13] G. C. Bjorklund, Frequency-modulation spectroscopy: a new method for measuring weak absorptions and dispersions, *Opt. Lett.* **1980**, *5*, 15–17, DOI [10.1364/OL.5.000015](https://doi.org/10.1364/OL.5.000015).
- [14] G. C. Bjorklund, M. D. Levenson, W. Lenth, C. Ortiz, Frequency modulation (FM) spectroscopy, *Appl. Phys. B* **1983**, *32*, 145–152, DOI [10.1007/bf00688820](https://doi.org/10.1007/bf00688820).

- [15] J. A. Silver, Frequency-modulation spectroscopy for trace species detection: theory and comparison among experimental methods, *Appl. Opt.* **1992**, *31*, 707–717, DOI [10.1364/ao.31.000707](#).
- [16] J. M. Supplee, E. A. Whittaker, W. Lenth, Theoretical description of frequency modulation and wavelength modulation spectroscopy, *Appl. Opt.* **1994**, *33*, 6294–6302, DOI [10.1364/AO.33.006294](#).
- [17] D. P. Blair, P. H. Sydenham, Phase sensitive detection as a means to recover signals buried in noise, *J. Phys. E* **1975**, *8*, 621–627, DOI [10.1088/0022-3735/8/8/001](#).
- [18] J. L. Hall, L. Hollberg, M. Long-sheng, T. Baer, H. G. Robinson, Progress Toward Phase-Stable Optical Frequency Standards, *J. Phys. Colloques* **1981**, *42*, 59–71, DOI [10.1051/jphyscol:1981808](#).
- [19] S. W. North, X. S. Zheng, R. Fei, G. E. Hall, Line shape analysis of Doppler broadened frequency-modulated line spectra, *J. Chem. Phys.* **1996**, *104*, 2129–2135, DOI [10.1063/1.470969](#).
- [20] I. D. Lindsay, P. Groß, C. J. Lee, B. Adhimoolam, K.-J. Boller, Mid-infrared wavelength- and frequency-modulation spectroscopy with a pump-modulated singly-resonant optical parametric oscillator, *Opt. Express* **2006**, *14*, 12341–12346, DOI [10.1364/OE.14.012341](#).
- [21] S. Borri, S. Bartalini, P. D. Natale, M. Inguscio, C. Gmachl, F. Capasso, D. Sivco, A. Cho, Frequency modulation spectroscopy by means of quantum-cascade lasers, *Appl. Phys. B* **2006**, *85*, 223–229, DOI [10.1007/s00340-006-2343-6](#).
- [22] E. A. Whittaker, B. J. Sullivan, G. C. Bjorklund, H. R. Wendt, H. E. Hunziker, ND<sub>4</sub> Schüler band absorption observed by laser FM spectroscopy in a photochemical reaction, *J. Chem. Phys.* **1984**, *80*, 961–962, DOI [10.1063/1.446757](#).
- [23] J. M. Jasinski, E. A. Whittaker, G. C. Bjorklund, R. W. Dreyfus, R. D. Estes, R. E. Walkup, Detection of SiH<sub>2</sub> in silane and disilane glow discharges by frequency modulation absorption spectroscopy, *Appl. Phys. Lett.* **1984**, *44*, 1155–1157, DOI [10.1063/1.94675](#).
- [24] E. A. Whittaker, H. R. Wendt, H. E. Hunziker, G. C. Bjorklund, Laser FM spectroscopy with photochemical modulation, *Appl. Phys. B* **1984**, *35*, 105–111, DOI [10.1007/BF00697429](#).
- [25] A. J. Marr, T. J. Sears, B.-C. Chang, Near-infrared spectroscopy of CH<sub>2</sub> by frequency modulated diode laser absorption, *J. Chem. Phys.* **1998**, *109*, 3431–3442, DOI [10.1063/1.476938](#).
- [26] G. E. Hall, S. W. North, Transient Laser Frequency Modulation Spectroscopy, *Annu. Rev. Phys. Chem.* **2000**, *51*, 243–274, DOI [10.1146/annurev.physchem.51.1.243](#).
- [27] M. Romagnoli, M. D. Levenson, G. C. Bjorklund, Frequency-modulation–polarization spectroscopy, *Opt. Lett.* **1983**, *8*, 635–637, DOI [10.1364/OL.8.000635](#).
- [28] M. C. McCarthy, J. C. Bloch, R. W. Field, Frequency-modulation enhanced magnetic rotation spectroscopy: A sensitive and selective absorption scheme for paramagnetic molecules, *J. Chem. Phys.* **1994**, *100*, 6331–6346, DOI [10.1063/1.467095](#).
- [29] J. M. Smith, J. C. Bloch, R. W. Field, J. I. Steinfeld, Trace detection of NO<sub>2</sub> by frequency-modulation-enhanced magnetic rotation spectroscopy, *J. Opt. Soc. Am. B* **1995**, *12*, 964–969, DOI [10.1364/JOSAB.12.000964](#).
- [30] P. Werle, S. Lechner, Stark-modulation-enhanced FM-spectroscopy, *Spectrochim. Acta A* **1999**, *55*, 1941–1955, DOI [10.1016/S1386-1425\(99\)00067-0](#).
- [31] J. Deppe, G. Friedrichs, A. Ibrahim, H.-J. Römmling, H. G. Wagner, The thermal decomposition of NH<sub>2</sub> and NH radicals, *Ber. Bunsenges. Phys. Chem.* **1998**, *102*, 1474–1485, DOI [10.1002/bbpc.199800016](#).
- [32] G. Friedrichs, J. T. Herbon, D. F. Davidson, R. K. Hanson, Quantitative detection of HCO behind shock waves: The thermal decomposition of HCO, *Phys. Chem. Chem. Phys.* **2002**, *4*, 5778–5788, DOI [10.1039/b205692e](#).
- [33] M. Votsmeier, S. Song, D. F. Davidson, R. K. Hanson, Shock tube study of monomethylamine thermal decomposition and NH<sub>2</sub> high temperature absorption coefficient, *Int. J. Chem. Kinet.* **1999**, *31*, 323–330, DOI [10.1002/\(SICI\)1097-4601\(1999\)31:5<323::AID-KIN1>3.0.CO;2-X](#).



- [34] M. Votsmeier, S. Song, D. Davidson, R. Hanson, Sensitive detection of  $\text{NH}_2$  in shock tube experiments using frequency modulation spectroscopy, *Int. J. Chem. Kinet.* **1999**, *31*, 445–453, DOI [10.1002/\(SICI\)1097-4601\(1999\)31:6<445::AID-KIN6>3.0.CO;2-4](https://doi.org/10.1002/(SICI)1097-4601(1999)31:6<445::AID-KIN6>3.0.CO;2-4).
- [35] G. Friedrichs, H. G. Wagner, Quantitative FM spectroscopy at high temperatures: The detection of  $^1\text{CH}_2$  behind shock waves, *Z. Phys. Chem.* **2000**, *214*, 1723–1746, DOI [10.1524/zpch.2000.214.12.1723](https://doi.org/10.1524/zpch.2000.214.12.1723).
- [36] E. P. Clifford, J. T. Farrell, J. D. DeSain, C. A. Taatjes, Infrared frequency-modulation probing of product formation in alkyl +  $\text{O}_2$  reactions: I. The reaction of  $\text{C}_2\text{H}_5$  with  $\text{O}_2$  between 295 and 698 K, *J. Phys. Chem. A* **2000**, *104*, 11549–11560, DOI [10.1021/jp0024874](https://doi.org/10.1021/jp0024874).
- [37] N. Kanno, K. Tonokura, A. Tezaki, M. Koshi, Water Dependence of the  $\text{HO}_2$  Self Reaction: Kinetics of the  $\text{HO}_2\text{-H}_2\text{O}$  Complex, *J. Phys. Chem. A* **2005**, *109*, 3153–3158, DOI [10.1021/jp044592+](https://doi.org/10.1021/jp044592+).
- [38] K. Suzuki, K. Tsuchiya, M. Koshi, A. Tezaki, Analysis of  $\text{HO}_2$  and OH Formation Mechanisms Using FM and UV Spectroscopy in Dimethyl Ether Oxidation, *J. Phys. Chem. A* **2007**, *111*, 3776–3788, DOI [10.1021/jp067646j](https://doi.org/10.1021/jp067646j).
- [39] S. Wang, R. K. Hanson, Ultra-sensitive spectroscopy of OH radical in high-temperature transient reactions, *Opt. Lett.* **2018**, *43*, 3518–3521, DOI [10.1364/ol.43.003518](https://doi.org/10.1364/ol.43.003518).
- [40] U. Hollenstein, H. Schmutz, J. A. Agner, M. Sommovilla, F. Merkt, Vacuum-ultraviolet frequency-modulation spectroscopy, *J. Chem. Phys.* **2017**, *146*, 014201/1–9, DOI [10.1063/1.4973011](https://doi.org/10.1063/1.4973011).
- [41] G. R. Janik, C. B. Carlisle, T. F. Gallagher, Two-tone frequency-modulation spectroscopy, *J. Opt. Soc. Am. B* **1986**, *3*, 1070–1074, DOI [10.1364/JOSAB.3.001070](https://doi.org/10.1364/JOSAB.3.001070).
- [42] J. T. Farrell, C. A. Taatjes, Infrared frequency-modulation probing of  $\text{Cl} + \text{C}_3\text{H}_4$  (allene, propyne) reactions: kinetics of HCl production from 292 to 850 K, *J. Phys. Chem. A* **1998**, *102*, 4846–4856, DOI [10.1021/jp981265r](https://doi.org/10.1021/jp981265r).
- [43] C. A. Taatjes, Infrared frequency-modulation measurements of absolute rate coefficients for  $\text{Cl} + \text{HD} \rightarrow \text{HCl(DCl)} + \text{D(H)}$  between 295 and 700 K, *Chem. Phys. Lett.* **1999**, *306*, 33–40, DOI [10.1016/s0009-2614\(99\)00420-0](https://doi.org/10.1016/s0009-2614(99)00420-0).





# CHAPTER 2

---

## Theoretical Background

---

In this chapter, a theoretical basis for optical frequency modulation and single-tone frequency modulation spectroscopy (ST-FMS) is presented. Afterwards, FM spectroscopy is compared to conventional absorption spectroscopy and some advanced aspects of FM detection are discussed. Finally, the chapter concludes with an outline of common noise components in FM spectroscopy and detection sensitivity analysis based on Allan deviation.

### 2.1 Frequency Modulation Spectroscopy

Frequency modulation of laser light is realized most efficiently by using electro-optic modulators (EOMs), which change the refractive index of an optical material by means of an externally applied electric field. An introduction to the electro-optic effect and the implications for frequency modulation spectroscopy is given in the following sections. For a more comprehensive description of the electro-optic effect and the underlying theory of optics, the reader is referred to the respective literature [1–5].

#### 2.1.1 The Electro-Optic Effect

Optical anisotropy in crystals is responsible for a wide variety of interesting phenomena, such as birefringence, optical rotation, as well as acousto-optic and electro-optic effects. These phenomena are directly related to the properties of the optical medium and the incident light as well as the interactions between them. The propagation characteristics of electromagnetic (EM) waves in crystals can be described using the index ellipsoid (optical indicatrix). In Cartesian coordinates, the index ellipsoid is given by

$$\frac{x^2}{n_x^2} + \frac{y^2}{n_y^2} + \frac{z^2}{n_z^2} = 1 \quad (2.1)$$

where  $(x, y, z)$  denote the principal coordinates and  $(n_x, n_y, n_z)$  are the respective indices of refraction along the three principal axes. Any crystal can be optically isotropic, uniaxial, or biaxial, depending on the relationship of refractive indices along the principal axes (see Fig. 2.1).

Isotropic crystals have equal indices of refraction for all three axes and their index ellipsoid is a sphere (see Fig. 2.1a). Uniaxial crystals have two different values for  $(n_x, n_y, n_z)$  and their propagation properties are represented by a spheroid (ellipsoid of revolution), with  $n_x = n_y = n_o$  and  $n_z = n_e$ .  $n_o$  and  $n_e$  denote the refractive indices of the ordinary (polarization in  $x$  or  $y$

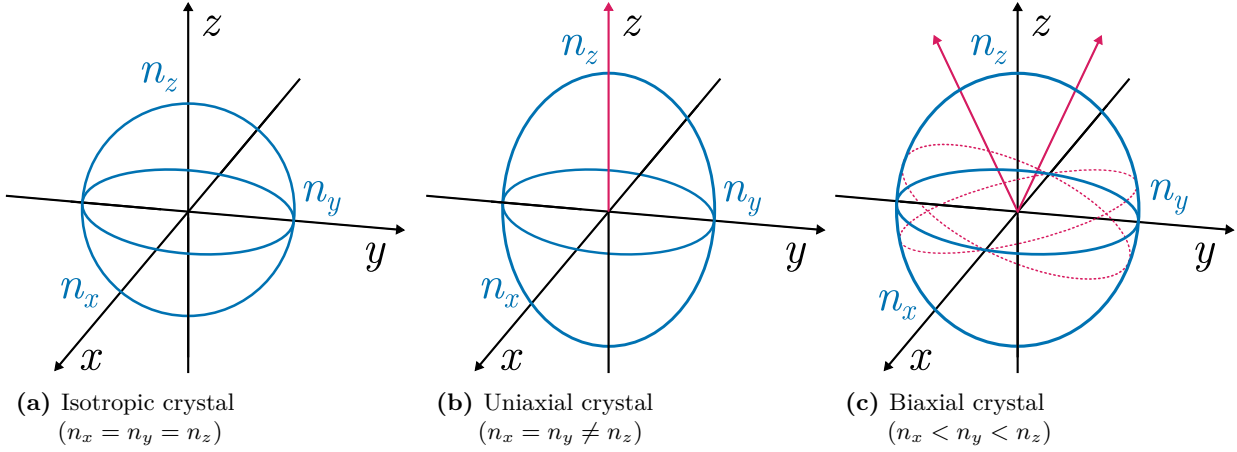


**Figure 2.1:** Schematic of index ellipsoids of isotropic (a), uniaxial (b), and biaxial (c) crystals in principal coordinates  $(x, y, z)$ . Note that the index ellipsoid shown in (b) is optically positive.

direction) and extraordinary beam (polarization in  $z$  direction), respectively, with  $z$  as the optic axis of the crystal (magenta arrow in Fig. 2.1b). The optic axis indicates the direction in the crystal along which a ray of transmitted light experiences no birefringence. Depending on the values for  $n_o$  and  $n_e$ , uniaxial crystals are either referred to as optically positive ( $n_o < n_e$ ) or negative ( $n_o > n_e$ ). Crystals with three different refractive indices are biaxial with two optic axes (magenta arrows in Fig. 2.1c) and their optical indicatrix is a general ellipsoid. Light entering a uniaxial or biaxial crystal will exhibit different phase velocities for different polarization components, depending on the propagation direction, and the crystal is therefore anisotropic with respect to its optical properties.

Optical anisotropy can either be intrinsic, such as in birefringent materials like calcite ( $\text{CaCO}_3$ ), lithium niobate ( $\text{LiNbO}_3$ ), and lithium tantalate ( $\text{LiTaO}_3$ ), or induced by external influences, or a combination of the two. Changes to the refractive index of a material due to an applied electric field  $E$  are described by the electro-optic effect. The induced change is either proportional to  $E$  (Pockels effect), mediated by the linear electro-optic coefficients  $r_{ij}$ , or proportional to  $E^2$  (Kerr effect), mediated by the quadratic electro-optic coefficients  $s_{ij}$ . For the sake of brevity, the focus will be kept on the linear contribution to the electro-optic effect. In materials with non-zero linear electro-optic coefficients  $r_{ij}$ , the overall electro-optic effect is typically dominated by the Pockels effect, since the quadratic coefficients  $s_{ij}$  are typically smaller by several orders of magnitude. Cubic and even higher order terms are usually irrelevant for practical applications.

It is convenient to describe the electro-optic effect in terms of the optical impermeability  $\eta = 1/n^2$ , which is used for many effects related to optical anisotropy. When an electric field is applied to a crystal and only the Pockels effect is considered, a linear impermeability change  $\Delta\eta_i$  emerges:

$$\Delta\eta_i = \Delta(1/n^2)_i = \sum_{j=1}^3 r_{ij} E_j \quad (2.2)$$

with  $i = 1, 2, \dots, 6$  and  $j = 1, 2, 3$  ( $x, y, z$ ).  $E_j$  are the electric field components along the three axes,  $(E_x, E_y, E_z)$ , and  $r_{ij}$  is a  $6 \times 3$  tensor containing the linear electro-optic coefficients. Under most conditions,  $\Delta\eta_i$  is very small, typically less than  $10^{-5}$ , and the changes in  $\eta$  are therefore often referred to as perturbations [4].

Symmetry considerations require that a medium must be asymmetric with respect to inversion to exhibit linear electro-optic properties, while the quadratic component of the electro-optic effect can occur in all media. Figure 2.2 shows three  $r_{ij}$  tensors for common crystal classes of electro-optic materials as examples. In centrosymmetric materials, all elements of the  $r_{ij}$  tensor are zero.

Under an electric field  $E$ , the electro-optically perturbed index ellipsoid of a crystal can be represented by [1]

$$\eta_1 x^2 + \eta_2 y^2 + \eta_3 z^2 + 2\eta_4 yz + 2\eta_5 xz + 2\eta_6 xy = 1 \quad (2.3)$$

with the contracted impermeability indices  $i = 1, 2, \dots, 6$  [6]. The new equation for the perturbed ellipsoid contains cross terms with  $yz$ ,  $xz$ , and  $xy$ , which account for distortions of the index ellipsoid in non-principal directions. Without an external electric field present ( $E = 0$ ), the ellipsoid represented by Eq. 2.3 reduces to the unperturbed ellipsoid from Eq. 2.1, since  $\eta_i(E = 0) = 1/n_i^2$  for  $i = 1, 2, 3$ , corresponding to  $(x, y, z)$ , and  $\eta_i(E = 0) = 0$  for  $i = 4, 5, 6$ .

In the presence of an external electric field  $E$ , the index ellipsoid of any electro-optically active material changes in size, shape and/or orientation. Generally speaking, the principal axes of the perturbed index ellipsoid no longer coincide with  $(x, y, z)$  and a new principal coordinate system for  $E \neq 0$  needs to be found. The transformation into this new coordinate system is accomplished by diagonalization of the  $\eta(E)$  matrix, i.e., by finding its eigenvalues and eigenvectors, for example by using the Jacobi method [4]. In the end, this procedure results in an electro-optically perturbed ellipsoid with refractive indices  $(n'_x, n'_y, n'_z)$  with respect to the new principal coordinates  $(x', y', z')$ .

A complete description of the propagation behavior of light in an electro-optic crystal has to take into account (1) the polarization angle of the light, (2) the direction of the applied electric field relative to the crystal axes, (3) the electro-optic characteristics of the crystal, and (4) possible intrinsic birefringence of the crystal [2, 3]. In a generalized and application-oriented view, given proper alignment of the crystal axes and the applied electric field, an electro-optic material shows

$$r_{ij} = \begin{pmatrix} 0 & 0 & 0 \\ 0 & 0 & 0 \\ 0 & 0 & 0 \\ r_{41} & 0 & 0 \\ 0 & r_{41} & 0 \\ 0 & 0 & r_{63} \end{pmatrix} \quad r_{ij} = \begin{pmatrix} 0 & 0 & 0 \\ 0 & 0 & 0 \\ 0 & 0 & 0 \\ r_{41} & 0 & 0 \\ 0 & r_{41} & 0 \\ 0 & 0 & r_{41} \end{pmatrix} \quad r_{ij} = \begin{pmatrix} 0 & -r_{22} & r_{13} \\ 0 & r_{22} & r_{13} \\ 0 & 0 & r_{33} \\ 0 & r_{51} & 0 \\ r_{51} & 0 & 0 \\ -r_{22} & 0 & 0 \end{pmatrix}$$

**Figure 2.2:** Linear electro-optic coefficients  $r_{ij}$  for tetragonal ( $\bar{4}2m$  ( $2 \parallel x_1$ ); e.g., KDP), cubic ( $\bar{4}3m, 23$ ; e.g., GaAs and CdTe), and trigonal ( $3m$  ( $m \perp x_1$ ); e.g., LiNbO<sub>3</sub> and LiTaO<sub>3</sub>) crystals in tensor form [3, 4]. The crystal classes are specified in Hermann–Mauguin notation.

a change in its refractive index according to

$$n(E) = n + \Delta n(E) = n - \frac{1}{2} n^3 r E - \frac{1}{2} n^3 s E^2 - \dots \quad (2.4)$$

Here,  $n$  is the index of refraction for the appropriate direction and  $\Delta n(E)$  is the electro-optically induced birefringence.  $r$  and  $s$  are the effective linear and quadratic electro-optic coefficients for this alignment, respectively. Equation 2.4 can be rewritten in terms of the optical impermeability  $\eta$ , using  $\Delta\eta(E) = (dn/dn) \Delta n(E)$ , yielding

$$\eta(E) = \eta + \Delta\eta(E) = \eta + r E + s E^2 + \dots \quad (2.5)$$

Thus, the coefficients  $r$  and  $s$  simply represent the linear and quadratic contributions to the impermeability change  $\Delta\eta(E)$  induced by the external electric field  $E$ .

For the purpose of illustration, the linear electro-optic effect in trigonal crystals with 3m symmetry, such as LiNbO<sub>3</sub> and LiTaO<sub>3</sub>, shall serve as an illustrative example [6, 7]. Such crystals are uniaxial, and thus naturally birefringent, with  $n_x = n_y = n_o$  and  $n_z = n_e$ . Suppose the applied electric field  $E$  only acts in the  $z$  direction, i.e., along the optic axis of the crystal, with  $E = (0, 0, E_z)$ . Using Eq. 2.2, the  $r_{ij}$  tensor in Fig. 2.2c, matrix multiplication, and Eq. 2.3, we obtain a perturbed index ellipsoid in terms of the impermeability  $\eta = 1/n^2$  according to

$$(\eta_o + r_{13} E) x^2 + (\eta_o + r_{13} E) y^2 + (\eta_e + r_{33} E) z^2 = 1 \quad (2.6)$$

This is equivalent to the original expression for the index ellipsoid (see Eq. 2.1), but with additional terms accounting for refractive index changes caused by the electric field. The ordinary and extraordinary impermeabilities under the electric field  $E$  are therefore given by

$$\eta_o(E) = \eta_o + r_{13} E \quad (2.7)$$

and

$$\eta_e(E) = \eta_e + r_{33} E, \quad (2.8)$$

respectively. Using the definition of  $\eta$  and  $\Delta n(E) = (dn/d\eta) \Delta\eta(E)$ , we arrive at expressions for  $n_o$  and  $n_e$  as function of the electric field:

$$n_o(E) = n_o - \frac{1}{2} n_o^3 r_{13} E \quad (2.9)$$

$$n_e(E) = n_e - \frac{1}{2} n_e^3 r_{33} E \quad (2.10)$$

Equation. 2.6 for the exemplary perturbed index ellipsoid shows  $E$ -dependent changes for each

individual axis, but does not contain any cross terms with products of  $x$ ,  $y$ , and  $z$ . Thus, the index ellipsoid is modified along all three axes with unchanged directionality, i.e., the crystal remains uniaxial and maintains the original principal axes  $(x, y, z)$ . Due to the direction of the electric field relative to the crystal axes chosen for this particular example, the results are very similar to the generalized expression for  $n(E)$  in Eq. 2.4. Depending on the values of  $(E_x, E_y, E_z)$ , more complicated results with directional changes to the index ellipsoid can emerge. For example, if we consider the case  $E = (E_x, 0, 0)$ ,  $\eta_1$ ,  $\eta_2$ , and  $\eta_3$  remain constant, but the cross terms  $\eta_5 xz$  and  $\eta_6 xy$  become nonzero. As a consequence, with an electric field acting along the  $x$  axis, LiNbO<sub>3</sub> and LiTaO<sub>3</sub> crystals become biaxial.

Since the refractive index of a medium is directly related to the phase velocity of an electromagnetic wave passing through it, electro-optically active crystals can be used for phase modulation of light. With proper configuration of the crystal and appropriate beam polarization, purely phase-modulated beams can be realized without effecting the amplitude or polarization of the light. Typically, phase modulation is achieved by applying sinusoidal electric fields to electro-optic crystals positioned between two capacitor plates. The phase  $\varphi$  of an electromagnetic wave with wavelength  $\lambda$  traveling through a crystal with refractive index  $n$  and length  $l$  is given by

$$\varphi = \frac{2\pi}{\lambda} l n \quad (2.11)$$

Accounting only for the Pockels effect and using the generalized approach from Eq. 2.4, the time-dependent phase shift  $\Delta\varphi_m$  induced by the electric field relative to the natural phase  $\varphi_0$  is

$$\Delta\varphi_m = \varphi_0 - \varphi(E) = \frac{2\pi}{\lambda} \Delta n(E) l = \frac{\pi}{\lambda} n^3 r E l = \frac{\pi}{\lambda} n^3 r \frac{V}{d} l \quad (2.12)$$

where  $d$  is the distance between the capacitor plates,  $l$  is the length of the crystal, and  $E = E_m \sin(\omega_m t)$  is the applied electric field with amplitude  $E_m = V_m/d$ . The modulation depth, i.e., the extent to which the phase  $\varphi$  responds to the applied modulation voltage, is typically described by the (phase) modulation index  $M$ :

$$M = \frac{\pi}{\lambda} n^3 r V_m \frac{l}{d} = \frac{\pi V_m}{V_\pi} \quad (2.13)$$

Here,  $V_\pi$  is the half-wave voltage, which is the necessary voltage for a phase shift of  $\Delta\varphi_m = \pi$ .  $V_\pi$  is a key characteristic of an EOM, since it represents a direct measure of modulation efficiency. The modulation index  $M$  plays a central role in the quantitative analysis of measured FM signals and will be discussed in more detail in Sections 2.1.3 and 2.1.4.

### 2.1.2 Electro-Optic Phase Modulators

A wide variety of dedicated devices based on the electro-optic effect has been developed, including phase modulators, amplitude/intensity modulators, spatial light modulators, and beam scanners [7]. Electro-optic phase modulators can be built in longitudinal and transverse configuration (see Fig. 2.3), with the direction of the applied electric field  $E$  either parallel or perpendicular to the

direction of light propagation, respectively.

Longitudinal EOMs, with equal capacitor plate distance and crystal length ( $d = l$ ), cause an electro-optically induced phase shift of

$$\Delta\varphi_m = \frac{\pi}{\lambda} n^3 r E l = \frac{\pi}{\lambda} n^3 r V \quad (2.14)$$

and therefore do not benefit from an increased crystal length  $l$ . In contrast, the phase shift for transverse EOMs is

$$\Delta\varphi_m = \frac{\pi}{\lambda} n^3 r E l = \frac{\pi}{\lambda} n^3 r V \frac{l}{d} \quad (2.15)$$

and thus proportional to  $l$ . An additional advantage of transverse EOMs is that they do not require transparent or otherwise modified capacitor plates to accommodate the incident light.

Electro-optic phase modulators can also be separated into two distinct categories on the basis of their allowed frequency ranges. Broadband EOMs contain a simple capacitive circuit that accepts a wide range of operating frequencies. However, the half-wave voltages  $V_\pi$  of broadband modulators are typically on the order of 100 V, sometimes even above 1 kV.

In so-called resonant EOMs, the electro-optic crystals are integrated into impedance-matched series RLC circuits [8]. RLC circuits in resonance can produce very high voltages across the crystal, which greatly increases the modulation depth of the EOM. In resonant EOMs, the inductance  $L$  and capacitance  $C$  of the circuit are tuned to a specific angular resonance frequency  $\omega_m = (LC)^{-1/2}$  with a preferably low resistance  $R$ . By purposefully choosing  $L$  and  $C$ , high quality factors  $Q = 1/(\omega_m RC)$  on the order of 100 can be achieved at the expense of a constrained usable modulation frequency range with very narrow bandwidth  $\Delta\omega_{BW} = R/L$ . The higher achievable modulation depths are particularly beneficial for applications in the MIR, since the electro-optic phase shift  $\Delta\varphi_m$  is inversely proportional to the wavelength  $\lambda$ . A disadvantage of resonant EOMs is their tendency towards thermal drift, which is caused by the high power in the circuit and the

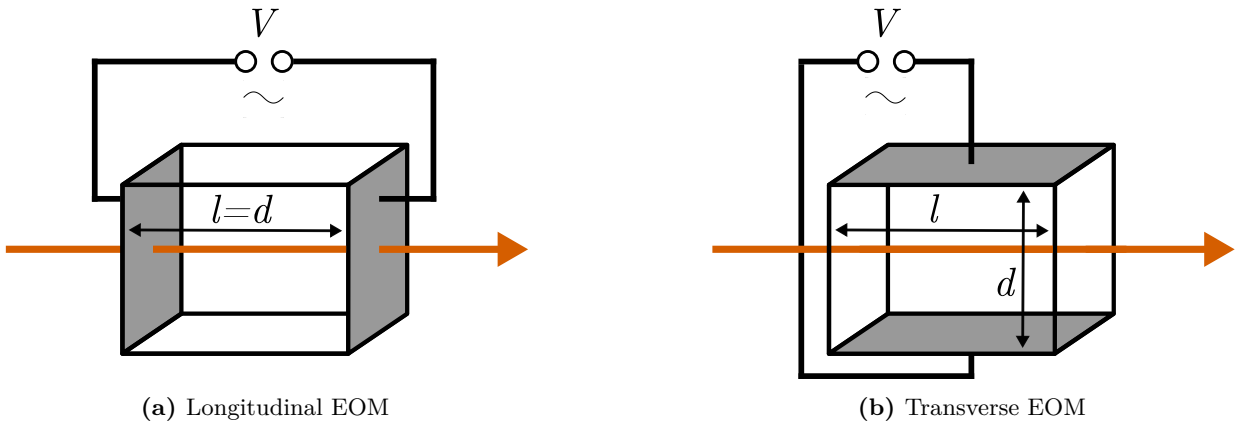


**Figure 2.3:** Schematic of longitudinal (a) and transverse (b) electro-optic phase modulators. The capacitor plates are shown in grey. For transverse EOMs, the phase shift  $\Delta\varphi_m$  caused by the applied electric field is proportional to the length  $l$  of the crystal along the axis of incidence.

narrow bandwidth. As a result, resonant EOMs often require repeated adjustment of the resonance frequency in free-running operation, typically by tuning a screw pressing on the resonant cavity. The issue of thermal drift can be eliminated by thermal stabilization of the modulator.

### 2.1.3 Principle of Frequency Modulation Spectroscopy

The basic theory of frequency modulation spectroscopy (FMS) was originally described by Gary C. Bjorklund in the early 1980s [9, 10]. Since then, various theoretical and practical aspects of this method have been studied, including FM lineshapes [10–12], detection sensitivity [13–15], and FM theory in the context of direct laser frequency modulation [14, 16]. With regards to terminology and definitions, the present work and the associated Publications I, III, and IV [17–19] mostly follow Ref. 15. Although this text only considers single-tone FM spectroscopy, many of the basic concepts outlined here can also be applied to two-tone FM spectroscopy (TT-FMS) as well. For detailed descriptions of the theory behind TT-FM spectroscopy, the interested reader is referred to the respective literature [16, 20, 21].

Consider an EOM under modulation with voltage  $V(t) = V_m \sin(\omega_m t)$  and angular modulation frequency  $\omega_m$ . When a narrow-bandwidth laser beam travels through the device, it experiences phase modulation according to

$$\Delta\varphi_m = M \sin(\omega_m t) \quad (2.16)$$

with the wavelength-dependent modulation index  $M$  as defined in Eq. 2.13. The corresponding phase of the electric field as function of time is given by

$$\varphi(t) = \varphi_c - \Delta\varphi_m \quad (2.17)$$

with  $\varphi_c$  as the phase of the carrier wave, i.e., the electric field phase of the unmodulated laser beam. The instantaneous frequency  $\omega(t)$  of the laser light is the time derivative of its phase  $\varphi(t)$  according to

$$\omega(t) = \frac{d\varphi(t)}{dt} = \omega_c - M \omega_m \cos(\omega_m t) \quad (2.18)$$

where  $\omega_c$  is the carrier frequency of the laser. It becomes obvious from Eqs. 2.17 and 2.18 that phase and frequency modulation are closely related. Phase modulation of narrow-bandwidth light with phase amplitude  $M$  directly results in frequency modulation with frequency amplitude  $M \omega_m$ .

In exponential notation, the electric field of an unmodulated laser beam with the carrier frequency  $\omega_c$  is given by

$$E(t) = E_0 \exp(i\omega_c t) \quad (2.19)$$

With the help of Eq. 2.16, the frequency-modulated electric field after passing through the EOM

can be expressed as

$$E_m(t) = E_0 \exp(i\omega_c t + i\Delta\varphi_m) = E_0 \exp(i\omega_c t + iM \sin(\omega_m t)) \quad (2.20)$$

By using the Jacobi–Anger expansion [22]

$$\exp(iM \sin(\omega_m t)) = \sum_{n=-\infty}^{+\infty} J_n(M) \exp(in\omega_m t) \quad (2.21)$$

the frequency-modulated electric field can be rewritten in terms of an infinite sum of  $n$ th-order Bessel functions  $J_n(M)$ :

$$\begin{aligned} E_m(t) &= E_0 \exp(i\omega_c t) \sum_{n=-\infty}^{+\infty} J_n(M) \exp(in\omega_m t) \\ &= E_0 \sum_{n=-\infty}^{+\infty} J_n(M) \exp(i(\omega_c + n\omega_m)t) \end{aligned} \quad (2.22)$$

Each term in Eq. 2.22 represents a distinct component in the frequency spectrum of  $E_m(t)$  with electric field amplitude  $E_0 J_n$  and angular frequency  $\omega_c + n\omega_m$ , where  $n = 0$  represents the carrier wave.

Figure 2.4a shows the first five Bessel functions with  $n \geq 0$  as function of the modulation index  $M$ . For each modulation index  $M$ , there is a specific set of Bessel function values  $J_n$  that fully describes the frequency-modulated electric field. Without modulation ( $M = 0$ ),  $J_0 = 1$  and  $J_{n \neq 0} = 0$ , which means that all intensity of the beam is retained by the carrier. With increasing  $M$ , the carrier contribution to the total electric field  $E_m(t)$  decreases and higher order sidebands become relevant. At  $M = 2.4$ , the Bessel function of the carrier  $J_0(M)$  becomes zero and the carrier frequency  $\omega_c$  vanishes from the spectrum of  $E_m(t)$ . Towards higher modulation depths, the average contribution of each individual sideband to  $E_m(t)$  diminishes. As long as the light is purely phase-modulated, it holds that  $J_n(M) = (-1)^n J_{-n}(M)$ , such that opposite-phase components in  $E_m(t)$  cancel each other out, and the amplitude of  $E_m(t)$  remains constant. Figure 2.4b shows the electric field spectra of frequency-modulated light corresponding to  $M = 0.2$  and  $M = 1.0$ , with  $n$ th order sidebands shifted from the carrier frequency by  $n\omega_m$ .

If the frequency-modulated light passes through an absorbing medium, its electric field  $E_m(t)$  can experience amplitude attenuation (absorption) and phase shift (dispersion). This can be accounted for by multiplication of  $E_m(t)$  with the complex transmission function

$$T(\omega_n) = \exp(-\delta_n - i\phi_n) \quad (2.23)$$

where  $\delta_n$  and  $\phi_n$  denote the attenuation and dispersion coefficients with regards to the electric field, respectively, and  $\omega_n = \omega_c + n\omega_m$ . The complex nature of  $T(\omega_n)$  can be rationalized by considering that absorption and dispersion are connected via a Kramers-Kronig relation, which



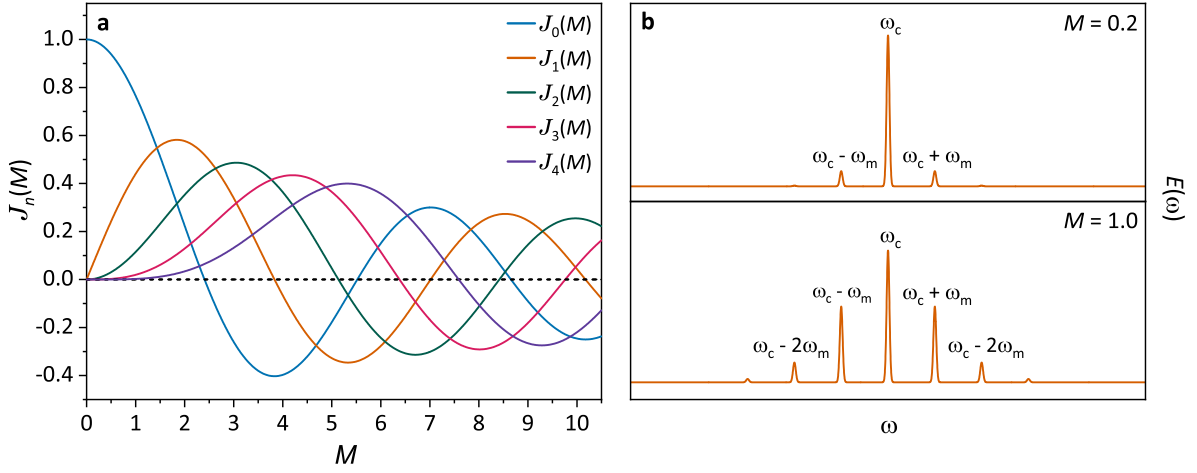


**Figure 2.4:** (a) Bessel functions  $J_n$  of the  $n$ th-order as function of the modulation index  $M$  for  $0 \leq n \leq 4$ . Higher order sidebands only play a role at very high modulation indices, which are rarely achieved in FM spectroscopy. (b) Frequency spectrum of  $E_m(\omega)$  for  $M = 0.2$  and  $M = 1.0$  with  $n$ th-order sidebands at  $\omega_n = \omega_c + n\omega_m$ .

links the absorption coefficient of a spectral line to the imaginary part of the complex refractive index [23]. For an individual frequency component  $\omega_n$ , the real part of the transmission function  $\exp(-\delta_n)$  causes attenuation of the amplitude  $E_0 J_n(M)$ , whereas the imaginary part  $\exp(-i\phi_n)$  induces a shift in the absolute phase  $(\omega_c + n\omega_m)t$ .

The transmitted electric field  $E_T(t)$  can be written as

$$E_T(t) = E_m(t) \times T(\omega_n) = E_0 \exp(i\omega_c t) \sum_{n=-\infty}^{+\infty} T(\omega_n) J_n(M) \exp(in\omega_m t) \quad (2.24)$$

For a given detection laser frequency  $\nu$ , different frequency components of  $E_T(t)$  experience different levels of attenuation and phase shift. Depending on the features of the probed absorption line and the modulation depth, this causes  $E_T(t)$  to vary with time. Therefore, in addition to frequency modulation, the transmitted light now also exhibits amplitude modulation, which contains the absorption information. The transmitted intensity envelope  $I_T(t)$ , which can be measured by a photodetector, is proportional to the square modulus of the frequency and amplitude-modulated electric field,  $I_T(t) \propto |E_T(t)|^2$ .  $I_T(t)$  has a large constant DC component and a small AC component, the latter of which can be demodulated by a lock-in amplifier to recover the absorption caused by the sample (see also Fig. 1.1 in the Introduction for illustration).

In order to derive a manageable expression for  $|E_T(t)|^2$ , two approximations will be made. Firstly, differences in attenuation and phase shift of adjacent sidebands are assumed to be small such that  $|\delta_n - \delta_{n+1}| \ll 1$  and  $|\phi_n - \phi_{n+1}| \ll 1$ . In other words, we require either that frequency changes on the order of  $\omega_m$  only cause small changes in the absorption and dispersion levels induced by the spectral line [24] or that the absolute magnitude of absorption or dispersion is small. Secondly, only components of  $|E_T(t)|^2$  oscillating at the modulation frequency  $\omega_m$  will be considered. Therefore, the resulting equations only hold for demodulation with respect to  $\omega_m$ ,

which is also referred to as  $1f$  demodulation. Under  $1f$  demodulation, which is the most common approach in single-tone FM spectroscopy, AC signal components at the harmonic frequencies  $2\omega_m$ ,  $3\omega_m$ , etc. are rejected by the demodulation scheme. This is in contrast to wavelength modulation spectroscopy, where  $2f$  demodulation on the second harmonic of  $\omega_m$  and normalization to the  $1f$  signal is often used to further reduce noise from intensity fluctuations [25, 26].

Under the assumptions mentioned above, the square modulus of  $E_T(t)$  can be expressed as [16, 24]

$$\begin{aligned}
 |E_T(t)|^2 = & \overbrace{E_0^2 \exp(-2\delta_0)}^{\text{DC}} + E_0^2 \exp(-2\delta_0) \times \\
 & \overbrace{\left[ \cos(\omega_m t) \times 2 \sum_{n=0}^{\infty} J_n(M) J_{n+1}(M) (\delta_{-n-1} - \delta_{n+1} + \delta_{-n} - \delta_n) \right]}^{A_{\text{AC}}} + \\
 & \overbrace{\sin(\omega_m t) \times 2 \sum_{n=0}^{\infty} J_n(M) J_{n+1}(M) (\phi_{-n-1} - \phi_{-n} + \phi_{n+1} - \phi_n)}^{D_{\text{AC}}}
 \end{aligned} \tag{2.25}$$

$A_{\text{AC}}$  and  $D_{\text{AC}}$  are the in-phase and quadrature components of  $|E_T(t)|^2$ , both of which oscillate at  $\omega_m$ . In single-tone FM spectroscopy,  $A_{\text{AC}}$  and  $D_{\text{AC}}$  are equivalent to the absorption and dispersion contributions to the induced amplitude modulation at  $\omega_m$ , respectively.

At this point, it is convenient to define the FM factor  $\Delta f$  such that

$$\Delta f = \frac{1}{\delta_c} \times [A_{\text{AC}} \cos(\theta) + D_{\text{AC}} \sin(\theta)] \tag{2.26}$$

with  $\delta_c$  as the electric field attenuation coefficient at the center of the spectral line and  $\theta$  as the demodulation phase angle with respect to  $\omega_m$ , i.e. the phase difference between the measured AC signal and the  $1f$  demodulation signal.  $\Delta f$  contains all contributions to the demodulated FM signal intensity and defines the lineshape of FM profiles. A thorough discussion of  $\Delta f$  and its practical implications for FM spectroscopy is given in the next Section 2.1.4.

The demodulated AC signal component of  $I_T(t)$  is the FM signal  $I_{\text{FM}}$ , which is proportional to  $E_0^2 \exp(-2\delta_0)$ . For small overall attenuation,  $E_0^2 \exp(-2\delta_0) \approx E_0^2 \propto I_0$ , the resulting FM signal of an absorption measurement is given by

$$I_{\text{FM}} = I_0 \Delta f \delta_c G = \frac{1}{2} I_0 \Delta f \alpha_c \ell G = \frac{1}{2} I_0 \Delta f A G \tag{2.27}$$

where  $\ell$  is the absorption path length and  $\alpha_c = 2\delta_c/\ell$  is the absorption coefficient at line center, corresponding to a fractional absorption of  $A = \alpha_c \ell = \sigma_c N \ell$ .  $\sigma_c$  and  $N$  are the absorption cross section at line center and number density of the absorbing species, respectively. The electronic gain factor  $G$  of the FM scheme accounts for amplification and attenuation of the FM signal exerted by the detection-demodulation system.

As can be seen from the FM working equation 2.27, for an FM spectroscopic measurement of a spectral line, the FM-equivalent absorption can be directly derived from the demodulated AC signal of the measured intensity  $I_T(t)$ , i.e., the FM signal  $I_{\text{FM}}$ . The in-phase ( $\theta = 0^\circ, 180^\circ$ ) and quadrature ( $\theta = 90^\circ, 270^\circ$ ) components of  $I_{\text{FM}}$  emerge from absorption and dispersion induced by the probed absorption line, respectively. As will become clearer in the next section, the FM factor  $\Delta f$  represents the central link between a measured FM signal  $I_{\text{FM}}$  and the underlying absorption caused by the probed spectral line.

#### 2.1.4 The FM Factor

The FM factor  $\Delta f$  is one of the primary performance indicators of FM-based detection systems. Most importantly,  $\Delta f$  quantifies the detection efficiency of FM spectroscopy compared to conventional absorption methods and defines the magnitude of measured FM signals for a particular absorption experiment.

Consider a conventional absorption setup measuring the remaining light intensity  $I$  after passing through the sample at incident light intensity  $I_0$ . If the intensity depletion  $\Delta I = I_0 - I$  is small, the absorbance according to the Beer-Lambert law,  $A = \ln(I_0/I)$ , can be replaced by fractional absorption such that

$$A = \frac{\Delta I/G'}{I_0} = \sigma N \ell \quad (2.28)$$

since  $\exp(-A) \approx 1 - A$  for  $A \ll 1$ . The gain factor  $G'$  accounts for amplification of  $\Delta I$  relative to  $I_0$ , which is common in difference amplification schemes. Correspondingly, the FM-equivalent absorption can be expressed as

$$A = \frac{2}{\Delta f} \frac{I_{\text{FM}}/G}{I_0} \quad (2.29)$$

using the FM working equation 2.27. By combining Eqs. 2.28 and 2.29, we obtain

$$\frac{I_{\text{FM}}/G}{\Delta I/G'} = \frac{\Delta f}{2} \quad (2.30)$$

This expression shows that the gain-corrected ratio of the FM signal  $I_{\text{FM}}$  to the conventional absorption signal  $\Delta I$  is fully described by  $\Delta f$ , which takes into account modulation depth, the interaction of different sidebands with the sample, signal demodulation, and lineshape effects. As an absorption-based detection technique, FMS relies on the transfer of absorption information to amplitude modulation and the subsequent quantification of this amplitude by demodulation. Thus, the FM factor  $\Delta f$  can be interpreted as the conversion efficiency of this procedure for given values of  $M$ ,  $\omega_m$ , and  $\theta$  as function of the detection laser frequency  $\nu$ . Note that the factor of 2 in Eq. 2.30 arises from the fact that  $\Delta f$  was initially introduced with respect to electric field attenuation  $\delta$  [12, 15] rather than intensity attenuation, i.e., fractional absorption  $A = \alpha \ell = 2\delta$ . For the sake of consistency, the original FM factor of electric field attenuation  $\Delta f$  was used in this

work rather than working with an equivalent FM factor of absorption  $\Delta F = \Delta f/2$ .

Under in-phase demodulation ( $\theta = 0^\circ, 180^\circ$ ), a single-tone FM detection system measures pure absorption with an FM factor of

$$\Delta f_A = \frac{A_{AC}}{\delta_c} = \frac{2}{\delta_c} \times \sum_{n=0}^{\infty} J_n(M) J_{n+1}(M) (\delta_{-n-1} - \delta_{n+1} + \delta_{-n} - \delta_n) \quad (2.31)$$

whereas under quadrature demodulation ( $\theta = 90^\circ, 270^\circ$ ), it measures pure dispersion with

$$\Delta f_D = \frac{D_{AC}}{\delta_c} = \frac{2}{\delta_c} \times \sum_{n=0}^{\infty} J_n(M) J_{n+1}(M) (\phi_{-n-1} - \phi_{-n} + \phi_{n+1} - \phi_n) \quad (2.32)$$

For an arbitrary demodulation phase angle  $\theta$ , however, the FM signal  $I_{FM}$  emerges from both absorption and dispersion, and  $\Delta f = \Delta f_A \cos(\theta) + \Delta f_D \sin(\theta)$ .

By assuming low modulation depth, the expressions for  $\Delta f$  in Eqs. 2.31 and 2.32 can be greatly simplified. For  $M \ll 1$ , only the zeroth-order and first-order Bessel functions make significant contributions to the frequency-modulated electric field  $E_m(t)$ , since  $J_0 \approx 1$ ,  $J_{\pm 1} \approx M/2$ , and  $J_{|n|>1} \approx 0$ . It follows that at low values of  $M$ , the expression for the FM factor under in-phase demodulation reduces to

$$\Delta f = M \left( \frac{\delta_{-1} - \delta_{+1}}{\delta_c} \right) \quad (2.33)$$

while the FM factor under quadrature demodulation becomes

$$\Delta f = M \left( \frac{\phi_{-1} - 2\phi_0 + \phi_{+1}}{\delta_c} \right) \quad (2.34)$$

The limiting case for pure absorption hints at the derivative nature of FMS, with an FM signal  $I_{FM}$  that is directly proportional to the electric field attenuation imbalance between the positive and negative first-order sidebands  $\delta_{-1} - \delta_{+1}$ .

It should be emphasized that combining Eq. 2.33 and the FM working equation 2.27 is a common approach to evaluate FM signals, where one assumes  $M$  to be small, explicitly or implicitly. This approach, however, should be viewed with caution. In fact, for all experiments described in this work, the assumption of low modulation depth does not hold. Even at a relatively moderate modulation index of  $M = 0.48$  used in the experiments described in Publication I (Chapter 4), the approximation  $J_1 \approx M/2$  already deviates from the actual value by about 3%, which causes an error in  $\Delta f$  of  $\sim 5\%$  for pure absorption.

FM factors can be positive or negative, depending on the demodulation phase angle  $\theta$  and the in-phase and quadrature components of the induced amplitude modulation  $A_{AC}$  and  $D_{AC}$  (see Eq. 2.26). Since  $A_{AC}$  and  $D_{AC}$  take into account attenuation and dispersion acting on the different frequency sidebands, they are functions of the detection laser frequency  $\nu$  relative to the position of the absorption line  $\nu_a$ . For example, under in-phase demodulation with  $\theta = 0^\circ$ ,  $\Delta f$  can only be

negative if  $A_{AC} < 0$ . This requires that positive-order sidebands experience higher attenuation than negative-order sidebands and  $(\delta_{-n-1} - \delta_{n+1} + \delta_{-n} - \delta_n) < 0$ , which is only the case if the detection laser frequency is down-shifted compared to the line position such that  $\nu < \nu_a$ .

The interaction of frequency-modulated light with an absorption feature is highly dependent on the spectral separation of individual frequency components in  $E_m(t)$  and the width of the absorption line of interest. In ST-FM spectroscopy, the spectral distance is equal to the (regular) modulation frequency  $\nu_m = \omega_m/2\pi$ . Since the absolute values of these quantities vary from case to case, it is useful to analyze FM profiles with regards to linewidth-normalized modulation frequencies by introducing the parameter  $x_m$  according to

$$x_m = \frac{\nu_m}{\Delta\nu} \quad (2.35)$$

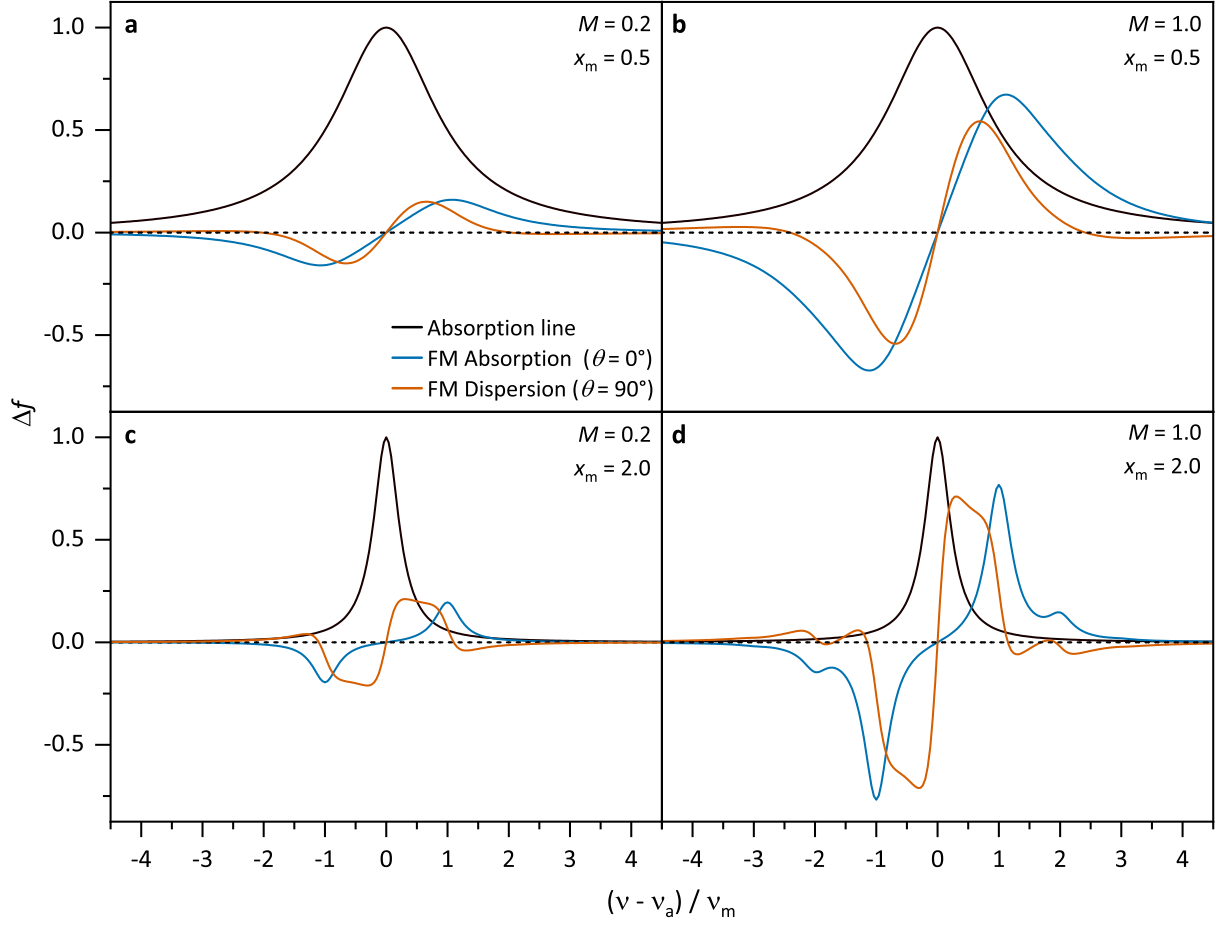
where  $\Delta\nu$  is the full width at half maximum (FWHM) of the spectral line.

Figure 2.5 shows simulations of FM profiles in terms of  $\Delta f$  as function of  $\nu$  for different combinations of  $M$  and  $x_m$  at  $\theta = 0^\circ$  (blue curves) and  $\theta = 90^\circ$  (orange curves). It is often useful to visualize FM profiles in terms of  $\Delta f(\nu)$ , because the FM factor contains all detection frequency-dependent information and is inherently normalized to the underlying absorption profile according to Eq. 2.26. All simulation shown in Fig. 2.5 are based on purely Lorentzian absorption profiles (black curves), each with peak values at the line center frequency  $\nu_a$  of  $\Delta f = 1$  by definition.

At low values for  $M$  and  $x_m$  (see Fig. 2.5a),  $\Delta f(\nu)$  is much smaller than unity, indicating low FM detection efficiency and thus small FM signal intensities. Firstly, at low modulation depth, the frequency sidebands contain only a small fraction of the total electric field  $E_m(t)$ , which is instead mostly retained by the carrier. All contributions to the AC component of  $|E_T(t)|^2$  as defined in Eq. 2.25 with  $n \neq 0$  are therefore negligible. Secondly, the low ratio  $x_m$  of the modulation frequency to the spectral linewidth results in small differences of absorption/dispersion between adjacent frequency components, i.e., small values for  $\delta_0 - \delta_{+1}$ ,  $\delta_{+1} - \delta_{+2}$ , etc. Consequently, there is only weak signal beating at  $\omega_m$  and  $\Delta f$  remains small.

Towards higher values for  $x_m$  (see Fig. 2.5c and 2.5d), the FM spectrum starts to separate into individual peaks. As the distance between adjacent sidebands increases, the attenuation/dispersion contrast improves and higher peak values of  $\Delta f$  are reached. In this context, the two limiting cases  $x_m \ll 1$  and  $x_m \gg 1$  for pure absorption are instructive. For  $x_m \ll 1$ , the distance between adjacent frequency sidebands and the corresponding attenuation/dispersion differences are very small such that the induced amplitude modulation essentially follows the slope of the absorption profile. The resulting FM spectrum of absorption closely resembles the first derivative of the probed spectral line. Conversely, for  $x_m \gg 1$ , the absorption line is probed by each sideband individually and at each detection frequency  $\nu = \nu_c \pm n \nu_m$  only  $\delta_n$  is nonzero. This results in an FM absorption profile with isolated spectral features that simply reproduce the spectral line.

When the modulation depth is increased (see Fig. 2.5b and 2.5d), the maximum FM factors initially become larger due to higher Bessel function values  $J_n(M)$ . In the case of high modulation frequencies ( $x_m > 1$ ), additional signal peaks start to appear in the FM spectrum (see Fig. 2.5d),



**Figure 2.5:** Simulated FM profiles of pure absorption ( $\theta = 0^\circ$ , blue curves) and pure dispersion ( $\theta = 90^\circ$ , orange curves) for different combinations of  $M$  and  $x_m$  as function of the detection laser frequency  $\nu$ . The underlying Lorentzian absorption lines with peak positions at  $\nu_a$  are shown as well (black curves).

because the beating between adjacent higher order sidebands becomes more significant. However, since the individual  $n$ th-order contributions to  $A_{AC}$  and  $D_{AC}$  are proportional to  $J_n J_{n+1}$ , the FM detection efficiency does not necessarily improve with increasing modulation depth.

The  $x_m$ – $M$  heatmap in Fig. 2.6a illustrates changes of  $\Delta f$  in more detail. It shows the maximum value for  $\Delta f$  of each FM profile,  $\Delta f_{\max}$ , as function of  $x_m$  and  $M$  for in-phase demodulation with  $\theta = 0^\circ$ . Again, the FM factor simulations were based on Lorentzian profiles.

Figure 2.6b shows exemplary  $\Delta f_{\max}(M)$  cross sections of the heatmap for selected values of  $x_m$  (colored curves). The two dashed lines display  $\Delta f_{\max}(M)$  values for the limiting case of low modulation depth ( $M \ll 1$ ). As can be seen from both graphs in Fig. 2.6, the  $\Delta f_{\max}$  value of FM profiles generally increases with both  $x_m$  and  $M$ , but not strictly so, since more complicated behavior emerges at higher modulation depths. Most notably, if the linewidth-normalized modulation frequency  $x_m$  is above roughly 0.5, local maxima and minima emerge in the  $\Delta f_{\max}(M)$  cross sections at modulation indices of  $M = 1.4, 2.7, 3.9, \dots$  and  $M = 2.2, 3.4, \dots$ , respectively. This is connected to the  $M$ -dependence of the Bessel functions and the position

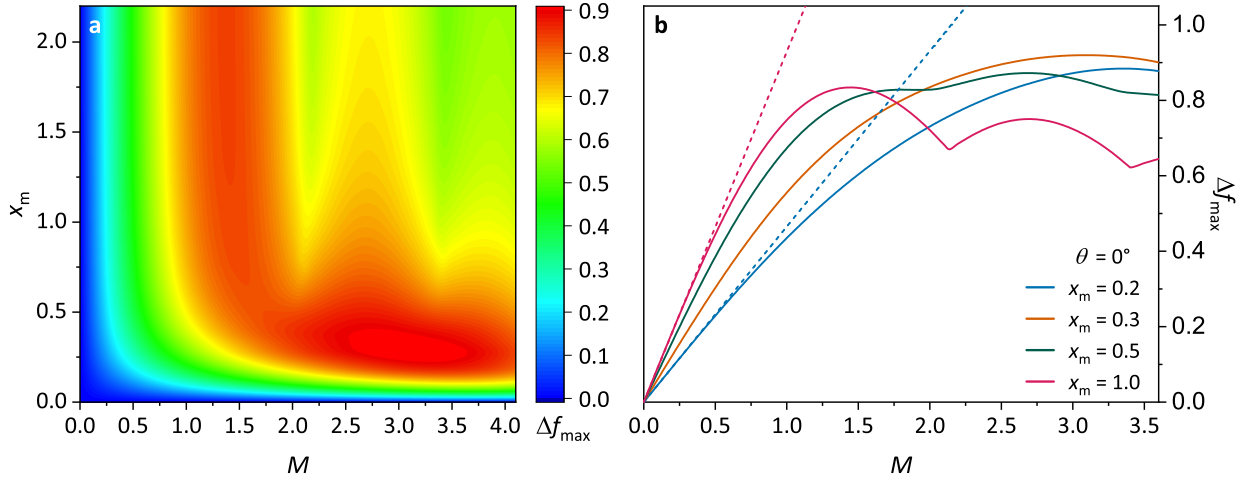


**Figure 2.6:** (a)  $x_m$ – $M$  heatmap for  $\Delta f_{\max}$  at  $\theta = 0^\circ$ . The highest value  $\Delta f_{\max} = 0.92$  is found at  $x_m = 0.28$  and  $M = 3.2$ . (b) Selected  $\Delta f_{\max}(M)$  cross sections for  $0.2 \leq x_m \leq 1.0$ . The dashed lines indicate the limiting case  $M \ll 1$ . For all the calculations presented here, a purely Lorentzian absorption feature has been assumed.

of individual frequency sidebands relative to the carrier. For detection on the first sideband at  $\nu = \nu_a \pm \nu_m$ , the FM signal arises from terms in  $\Delta f$  with  $J_0 J_1$  and  $J_1 J_2$  (see Eq. 2.25). Likewise, for detection on the second sideband at  $\nu = \nu_a \pm 2\nu_m$ , terms with  $J_1 J_2$  and  $J_2 J_3$  determine  $\Delta f$ , and so forth. Whenever a local  $\Delta f_{\max}(M)$  minimum is reached and the value starts to increase again, detection on the next frequency sideband becomes preferable, as the next pair of Bessel functions takes over.

Two regions in Fig. 2.6a with considerable  $\Delta f_{\max}$  values deserve special attention. Firstly, the high- $\Delta f_{\max}$  band at around  $M = 1.4$  stands out. At this modulation depth, the sum of  $A_{AC}$  terms with  $J_0 J_1$  and  $J_1 J_2$  reaches its maximum, resulting in high FM factors above 0.8. Thus, for sufficiently high modulation frequencies, raising  $M$  above 1.4 does not actually improve the performance of the FM detection system. Secondly, there is a ridge with  $\Delta f_{\max}$  values close to unity at high modulation indices of  $M \approx 3$  and low values of  $x_m \approx 0.3$ . This is caused by a favorable overlap of FM signal contributions to  $\Delta f$  from adjacent sidebands with  $n = 1, 2, 3$ , which all experience some degree of attenuation/dispersion at the same detection laser frequency. Therefore, efficient FM detection can be realized even with low modulation frequencies, as long as high modulation indices are achievable. Due to technical limitations, however, it is usually not practically feasible to adjust the modulation index or the modulation frequency to any desired value in order to maximize  $\Delta f$ .

The demodulation phase angle  $\theta$  determines to what extent absorption and dispersion contribute to the measured FM signal, thereby strongly influencing the FM spectral lineshape. Two polar plots for  $\Delta f_{\max}$  at  $M = 1.0$  in Fig. 2.7a illustrate the  $\theta$ -dependence of FM spectra, with the dashed lines indicating the optimal demodulation phase angles  $\theta_{\text{opt}}$  to achieve the highest possible value for  $\Delta f_{\max}$ . Additionally, exemplary FM profiles at selected values for  $\theta$  are shown in Figs. 2.7b and 2.7c.



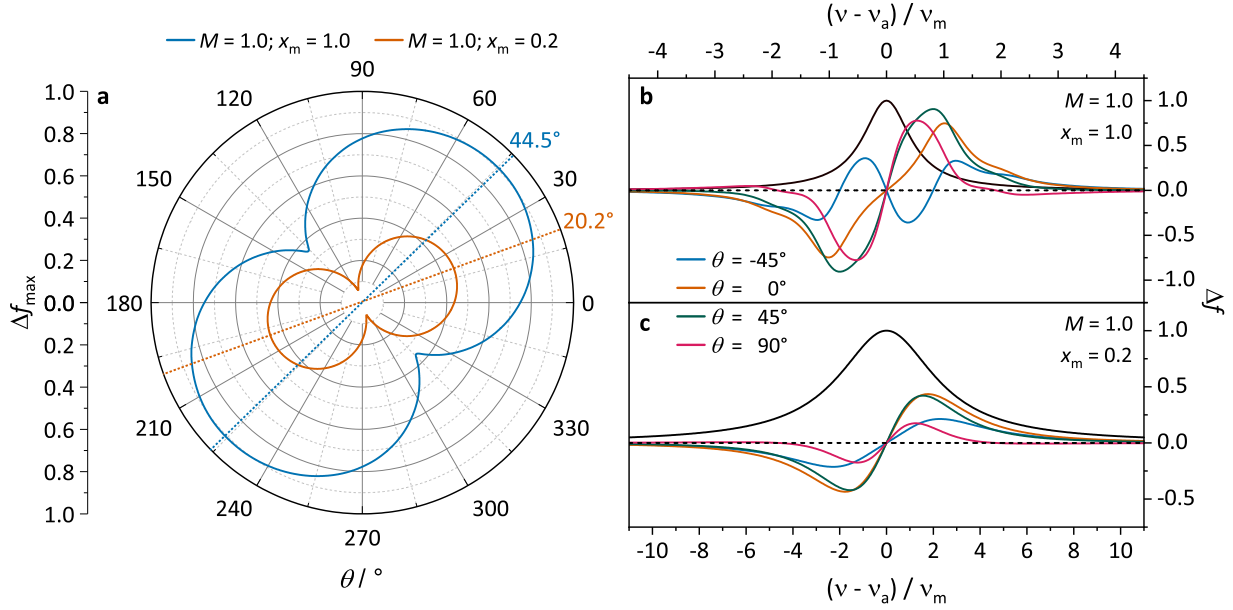


**Figure 2.7:** (a) Polar plot of  $\Delta f_{\max}(\theta)$  at  $M = 1.0$  for  $x_m = 1.0$  (blue curve) and  $x_m = 0.2$  (orange curve). The dashed lines indicate the optimal demodulation phase angle  $\theta_{\text{opt}}$ . Selected FM profiles corresponding to the data shown in (a) in terms of  $\Delta f(\nu)$  for  $x_m = 1.0$  (b) and  $x_m = 0.2$  (c) with  $-45^\circ \leq \theta \leq 90^\circ$ . Note that the required detection laser frequency for  $\Delta f_{\max}$  changes considerably with  $\theta$  for  $x_m = 1.0$ .

At a given demodulation phase angle, the FM factor contains a certain composition of absorption and/or dispersion components according to Eq. 2.26. Importantly, as shown in Fig. 2.7a, the highest  $\Delta f_{\max}$  value does not correspond to pure absorption ( $\theta = 0^\circ, 180^\circ$ ) or pure dispersion ( $\theta = 90^\circ, 270^\circ$ ). The example with higher spectral sideband separation ( $x_m = 1.0$ , blue curve) benefits from demodulation with roughly equal influence from absorption and dispersion at  $\theta_{\text{opt}} = 44.5^\circ$ , whereas the example with strongly overlapping sideband contributions ( $x_m = 0.2$ , orange curve) has a smaller, albeit distinctly nonzero, optimal angle of  $\theta_{\text{opt}} = 20.2^\circ$ . In fact, for many combinations of  $x_m$  and  $M$  values,  $\theta_{\text{opt}}$  is greatly affected by constructive overlap of absorption and dispersion signals. However, for the limiting cases  $x_m \ll 1$  and  $x_m \gg 1$ , the optimal demodulation phase angle  $\theta_{\text{opt}}$  actually approaches  $0^\circ$ .

As can be seen from the FM profiles in Figs. 2.7b and 2.7c, the optimal detection laser frequency, i.e., the point in the FM profile where  $\Delta f$  reaches its peak, also depends on  $\theta$ . In the high- $x_m$  example, the optimal detection laser frequency changes strongly with  $\theta$ , but  $\Delta f_{\max}$  never comes close to zero. Conversely, the low- $x_m$  example shows larger relative changes in  $\Delta f_{\max}$ , yet the optimal detection frequency remains at roughly  $\nu \approx \nu_a + 2\nu_m$  for all shown phase angles except  $90^\circ$  (magenta curve in Fig. 2.7c). Generally speaking, FM spectra with separated sideband contributions ( $x_m > 1$ ) vary more strongly in shape as function of  $\theta$  compared to low-contrast FM profiles ( $x_m < 1$ ), since FM signal contributions from closely spaced sidebands are more likely to compensate each other.

In conclusion, the demodulation phase angle  $\theta$  has a profound impact on the shape of FM



spectra, and thereby the optimal wavelength offset relative to the line center. Nevertheless, under typical conditions with  $\theta$  set to pure absorption, FM detection at  $\nu = \nu_c \pm \nu_m$  is a reasonable approach that results in near-optimal values for  $\Delta f$ . This is especially important for experiments where the spectral lineshape of the absorption feature is not known beforehand.

Due to the complicated relationship between the measured FM signal  $I_{\text{FM}}$  and the modulation parameters discussed in this chapter, many previously reported applications of FM spectroscopy rely on concentration standards to measure absolute species concentrations. However, provided that the interaction between detection beam and absorbing sample as well as signal demodulation are treated properly, FM spectroscopy reliably delivers quantitative results [12, 27, 28]. For a given lineshape and detection wavelength, the FM factor  $\Delta f$  can be directly calculated from  $M$ ,  $\theta$ , and  $\omega_m$ , thereby accounting for all FM detection effects, apart from the electronic signal amplification/attenuation gain factor  $G$ , which needs to be determined independently. Thus, quantitative FM detection can be realized without the need for calibration procedures or reference measurements, even at moderate or high modulation depths.

## 2.2 Noise in FM Spectroscopy

The performance of any detection system can be quantified by the signal-to-noise ratio (SNR), which relates the magnitude of a measured signal to the signal fluctuations under a certain set of experimental conditions. In the context of laser absorption spectroscopy, experimental conditions are largely defined by the key quantities of temperature, pressure, sample composition, detection laser wavelength, and detection bandwidth. For FM spectroscopy,  $\Delta f$  must also be considered, since it determines the intensity of measured FM signals, as highlighted in the previous section. In this section, signal noise as the fundamental sensitivity-limiting factor of absorption-based detection systems will be addressed. To this end, different types of noise will be briefly introduced and their implications for FM detection will be outlined.

Noise is any contribution to a measured signal that does not contain useful information. In this text, the notion of noise includes signal disturbances at specific frequencies in addition to broadband signal fluctuations, the latter of which are often referred to as noise in a more narrow sense. Different contributions to signal noise can be classified by their origin, which relates the noise component to a specific physical process, or by their frequency dependency, which describes the behavior of noise with respect to time. The most important noise types in laser spectroscopy are white noise and pink noise ( $1/f$  noise, flicker noise), which are independent of and inversely proportional to the detection frequency  $f$ , respectively.

For an absorption-based detection method, the SNR as function of light intensity  $I$  as seen by the photodetector can be represented by [13]

$$\text{SNR} = \frac{\kappa I}{\sqrt{N_0^2 + (N_{1/2}\sqrt{I})^2 + (N_1 I)^2}} \quad (2.36)$$

Here,  $\kappa$  represents a generalized quantity that connects the detected signal intensity to the light

intensity of the detection beam  $I$  such that they are proportional. In conventional absorption spectroscopy,  $\kappa$  is equivalent to the fractional absorption  $A$  (see Eq. 2.28), while in FM spectroscopy  $\kappa$  also depends on the FM factor  $\Delta f$  (see Eq. 2.29).  $N_i$  denotes coefficients for noise components affecting the measurement that are either independent ( $i = 0$ ), square-root dependent ( $i = 1/2$ ) or linearly dependent ( $i = 1$ ) on the light intensity  $I$ . In this way, the SNR can be examined in different intensity regimes, which can be helpful for identifying the sensitivity-limiting noise components, as can be seen in Publications I and IV (Chapters 4 and 7).

$I$ -independent signal fluctuations described by  $N_0$  are mainly caused by thermal and dark current noise, both of which are white noise components. Under some circumstances, (parasitic) electronic noise components oscillating at specific frequencies may also appear.  $N_{1/2}$  accounts for shot noise, which was first described by Walter Schottky [29, 30]. Shot noise, also referred to as Poisson noise, stems from the discrete nature of photons in the detection beam and charge carriers in the photoactive material of the detector [6, 31]. Any detection beam contains many unsynchronized photons and their individual interactions with the photodetector obey Poisson statistics. In this view, the measured intensity of a detection beam represents the superposition of many Poisson-distributed detection events and is thereby inherently subject to fluctuation. For large numbers of detected photons  $N_{\text{ph}} \propto I$ , the Poisson distribution approaches a Gaussian distribution with a standard deviation proportional to  $\sqrt{N_{\text{ph}}}$ , which quantifies the signal uncertainty due to shot noise. Classical absorption-based spectroscopic methods, including FMS, are fundamentally sensitivity-limited by shot noise. Some specialized techniques use non-classical light, e.g., correlated or single photons, to achieve sub-shot noise sensitivity [32–35], but so far their application has been mostly limited to fundamental studies. Finally, noise components that are covered by the coefficient  $N_1$  in Eq. 2.36 are directly proportional to the incident light intensity  $I$ . The main causes of  $N_1$ -type noise are laser output power fluctuations (laser excess noise) and residual amplitude modulation noise, both of which will be addressed below.

Equation 2.36 suggests that an increase in  $I$  is always preferable, as illustrated in Fig. 2.8a, provided that the photodetector response remains linear and no optical saturation effects occur. For intermediate light intensities, where  $I$ -independent noise covered by  $N_0$  has become negligible, the achievable detection sensitivity depends on the ratio between the noise terms  $N_{1/2}$  and  $N_1$ . In the limit of high light intensity, the SNR reaches a saturation value defined by  $N_1$ -type noise. At any given value for  $I$ , there is a certain noise level acting on measured signals that can be converted into units of (fractional) absorption  $A$ . The minimal detectable (fractional) absorption  $A_{\text{min}}$  of a detection system is commonly defined as the  $A$  value that would be measured at  $\text{SNR} = 1$ , i.e., the noise-equivalent absorption.

Conventional absorption techniques are often sensitivity-limited by laser excess noise, which roughly scales with  $f^{-1}$  ( $1/f$  noise). Since measured absorption signals directly depend on  $I$ , detection systems with strong intensity noise correspond to a high- $N_1$  case with respect to Eq. 2.36, where the SNR does not significantly improve with increasing intensity. Even dual-beam variants of absorption spectroscopy are not capable of fully cancelling laser intensity fluctuations, usually due to interference effects in optical elements [36] and spurious electrical signals [37].

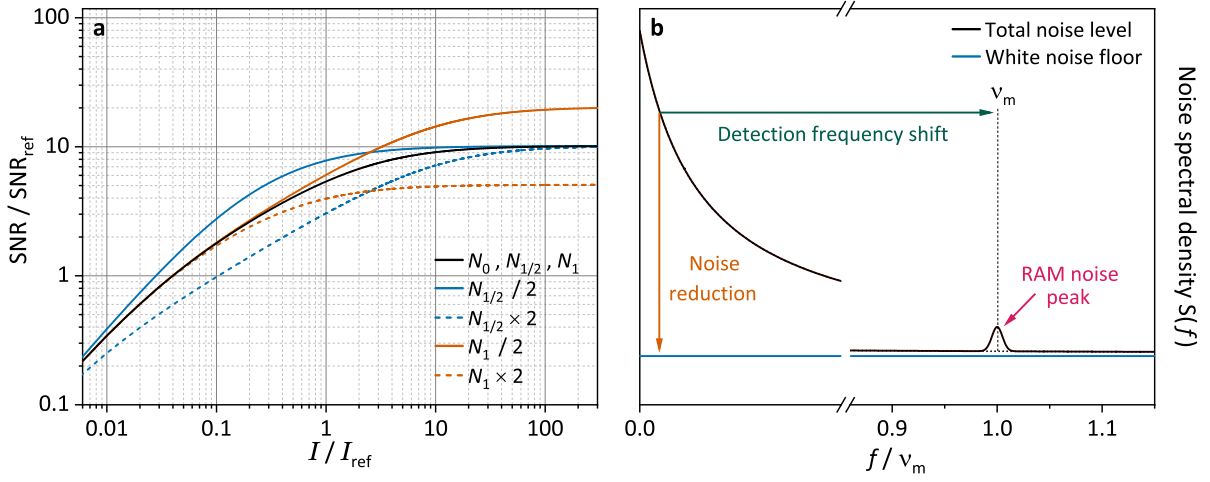


**Figure 2.8:** (a) Double-logarithmic plot of the signal-to-noise ratio (SNR) as function of light intensity  $I$  with arbitrarily selected input values for Eq. 2.36 (black curve). Alternative plots for different  $N_{1/2}$  (blue curves) and  $N_1$  (orange curves) values are shown for comparison.  $\text{SNR}_{\text{ref}}$  and  $I_{\text{ref}}$  are arbitrarily chosen reference values for SNR and  $I$ , respectively. (b) Visualization of the noise spectral density  $S$  as function of the detection frequency  $f$ . Without RAM noise and for sufficiently high modulation frequencies  $\nu_m$ , the total noise level is close to the white noise floor.

The suppression of  $1/f$  noise is one of the key advantages of FM spectroscopy compared to conventional absorption-based detection methods. When frequency-modulated light interacts with the absorbing sample, amplitude modulation is induced and later recovered by demodulation. Thus, the absorption information is converted into an AC signal with high frequency, which is equivalent to an upshift in detection frequency. Ideally,  $\nu_m$  is chosen such that  $1/f$  noise becomes negligible. This principle is illustrated by Fig. 2.8b, which shows the noise spectral density  $S$  affecting the measured signal as function of the detection frequency  $f$ . The total noise in Fig. 2.8b (black curve) is dominated by  $1/f$  noise at low detection frequencies. As  $f$  increases, the noise spectral density  $S$  approaches the frequency-independent white noise floor (blue line) and the detection system becomes sensitivity-limited by thermal, dark current, or shot noise.

Under favorable conditions, i.e., suppressed  $1/f$  noise, low thermal/dark current noise, and sufficiently high light intensity on the detector, FM spectroscopy can achieve shot-noise limited detection [38, 39]. The shot-noise limited minimal detectable absorption for FMS is given by [10, 15]

$$A_{\text{SN}} = \frac{4}{\Delta f_{\text{max}}} \left[ \frac{P_0}{h\nu} \frac{\eta_{\text{det}}}{\Delta f_{\text{det}}} \right]^{-1/2} \quad (2.37)$$

where  $\Delta f_{\text{max}}$  is the maximum FM factor in a specific FM profile,  $P_0$  is the optical power of the detection beam,  $h$  is Planck's constant,  $\nu$  is the detection laser frequency, and  $\eta_{\text{det}}$  is the quantum efficiency of the photodetector. The selected detection bandwidth  $\Delta f_{\text{det}}$  defines the time resolution of the measurement. Well-established FM detection schemes in the visible spectral range routinely achieve minimum detectable absorption levels on the order of  $A_{\text{min}} = 3 \times 10^{-5}$  at a time resolution of around  $1 \mu\text{s}$ , which is only slightly above the respective shot-noise limit [12, 15, 40].

### 2.2.1 RAM Noise

A main obstacle in reaching the shot-noise limit for many FM applications is the so-called residual amplitude modulation (RAM). Broadly speaking, RAM refers to any contribution to the demodulated FM signal that does not stem from absorption or dispersion induced by the spectral feature of interest. Since spurious amplitude modulation must oscillate at  $\nu_m$  to pass the demodulation circuitry, RAM noise can be viewed as a distinct component of additional intensity noise that only occurs at the modulation frequency (see magenta indicator and black peak in Fig. 2.8b). Although RAM is present in all FM detection systems to some degree, it is a more significant factor in applications that rely on direct frequency modulation of the laser source, which typically leads to simultaneous amplitude modulation. For example, applying a sinusoidal modulation signal to the driver current of a laser diode will also modulate the output intensity at the same frequency. As a consequence, many theoretical descriptions of FM theory explicitly factor in RAM by introducing an amplitude modulation (AM) index in addition to the phase/frequency modulation (FM) index [14, 16].

For FM applications using modulation with external EOMs, RAM is typically much weaker and related to the operation of the EOM or its integration into the optical detection system. The most common sources of EOM-related RAM are (1) polarization mismatch between detection light and EOM, (2) optical interference in the modulator crystal, and (3) optical interference in passive reflective elements, all three of which break the pure phase modulation of the detection laser field.

When the polarization of the incident beam is misaligned with the designated EOM input angle, the two perpendicular polarization components experience different phase shifts such that the light's polarization state is modulated [8]. Any polarization-sensitive optical element in the beam path, including the polarizers typically added for setting the demodulation phase angle  $\theta$  (see Fig. 3.1 in the Experimental section, Chapter 3), converts the polarization modulation to amplitude modulation [38, 41]. The polarization mismatch can also drift over time, since intrinsic crystal birefringence is temperature-dependent [42]. Furthermore, if the EOM is well-aligned with respect to the propagation axis of the light, the endfaces of the electro-optic crystal effectively function as low-reflectivity mirrors, causing the modulator to act as an accidental Fabry-Pérot resonator with low, albeit nonzero, finesse. This results in strongly wavelength-dependent RAM background undulations, which are typically referred to RAM fringes, since the resonator transmission differs for individual frequency components of the frequency-modulated light. The etaloning in the crystal can be minimized by tilting the modulator by few degrees relative to the beam axis. Still, interference can still occur in other optical elements, such as optical windows, even without reflections in the modulator crystal itself. An early physical model for RAM from interference effects was described by Whittaker et al. [43], who emphasized the distinction between multi-pass and single-pass RAM generation. They demonstrated that EOM-induced multi-pass RAM is mostly in-phase with the modulation signal and strongly dependent on the detection laser frequency. Non-EOM single-pass RAM, however, was found to be a weaker quadrature contribution.

Generally, excessive RAM noise can be prevented by careful alignment and operation of the EOM

as well as by avoiding etalon effects along the beam path. Next to these operational approaches, RAM noise can also be addressed by dedicated reduction schemes. Reported applications make use of, for example, harmonic modulation with two phase-shifted waves at  $\nu_m$  and  $2\nu_m$  [44], active servo control with additional DC voltage applied to the EOM [38, 41], or active temperature control of the modulator crystal [42]. Moreover, double modulation schemes, like the ones already mentioned in the Introduction (Chapter 1) [45–48], may provide RAM noise cancellation as well.

While all RAM components oscillate at the modulation frequency  $\nu_m$ , changes in their amplitude often occur at lower frequencies. For example, mechanical vibrations, which slightly change the relative alignment of optical elements in the beam path, usually lie in the kHz range. Unfortunately, this can cause significant sensitivity loss due to RAM noise in the respective frequency range, as will be briefly alluded to in Publications I, III, and IV (Chapters 4, 6, and 7).

## 2.3 Allan Sensitivity Analysis

Although Allan analysis was initially developed for studying the frequency stability of oscillators [49], it has become a common method of quantifying detection limits for spectroscopic methods [50]. Conventional standard deviation is a ubiquitous measure for temporal stability of physical quantities and describes the average difference of data points relative to a global mean. However, if the global mean is not stationary, standard deviation will increase with the number of measured samples. In contrast, Allan deviation represents the average difference of adjacent averaged intervals of data points as function of the interval size. Consequently, Allan deviation is capable of handling noise components that would lead to non-converging behavior for conventional standard deviation [51].

In the context of frequency stability analysis, one usually distinguishes between "phase data" and "frequency data". When tracing the time-behavior of an oscillator, the phase  $x$  is subject to random fluctuations, and so is its time derivative  $y = dx/dt$ , which is the (instantaneous) oscillator frequency. For spectroscopic sensitivity analysis, however, no such distinction is necessary, since the time derivative of the measured signal is usually not relevant. Therefore, only "frequency data" ( $y$ ) will be considered here.

Suppose pure noise of an arbitrary quantity  $y$ , e.g., FM signal intensity  $I_{\text{FM}}$  or fractional absorption  $A$ , is measured with a sampling frequency  $f_s$  without dead time, resulting in data points spaced by the time distance  $\tau_0 = 1/f_s$ . Adjacent data points can be merged into  $K$  intervals with interval times of  $\tau = k \tau_0$ , where  $k$  is the adjacent-averaging factor. The Allan variance for  $y$  at a chosen value of  $\tau$  is defined as [51, 52]

$$\sigma_A^2(\tau) = \frac{1}{2(K-1)} \sum_{i=1}^{K-1} (\bar{y}_{i+1} - \bar{y}_i)^2 \quad (2.38)$$

with  $\bar{y}$  as the interval average of  $y$  and  $K-1$  as the number of possible differences between adjacent intervals. Towards longer interval times  $\tau$ , the number of intervals  $K$  decreases and fewer interval differences  $\bar{y}_{i+1} - \bar{y}_i$  are available for calculating  $\sigma_A^2$ . This leads to lower statistical confidence levels for the respective  $\sigma_A^2$  values, which causes high uncertainty in the Allan analysis for large

intervals. More reliable results can be achieved by the use of overlapping Allan variance, which is given by [51]

$$\sigma_O^2(\tau) = \frac{1}{2k^2(K-2k+1)} \sum_{j=1}^{K-2k+1} \left[ \sum_{i=j}^{j+k-1} (\bar{y}_{i+k} - \bar{y}_i) \right]^2 \quad (2.39)$$

with  $\bar{y}$ ,  $k$ , and  $K$  as defined above. Overlapping Allan variance analysis includes all possible interval differences at a given interval time  $\tau$ , which leaves a larger effective noise data set. Figure 2.9a illustrates the difference between non-overlapping (orange arrows) and overlapping (green arrows) sampling for Allan analysis.

Allan deviation (ADEV) and overlapping Allan deviation (ODEV) are the square roots of the variances defined in Eq. 2.38 and 2.39, respectively. At a given averaging time  $\tau$ , which is the time resolution of measurement at adjacent-averaging factor  $k$ , the (overlapping) Allan deviation  $\sigma$  describes the effective noise level of the measured quantity  $y$ . With respect to measured FM signal intensities,  $\sigma$  is the noise-equivalent signal at time resolution  $\tau$  with SNR = 1. In units of absorption,  $\sigma$  represents the minimum detectable absorption  $A_{\min}$ .

Depending on the particular noise types present in the detection system, (overlapping) Allan deviation values  $\sigma$  change with  $\tau$  in different ways. For statistical noise, (overlapping) Allan variance  $\sigma^2$  scales with  $\tau^\mu$  and the corresponding deviation  $\sigma$  is thus proportional to  $\tau^{\mu/2}$ . In frequency space, the noise spectral density  $S$  of any statistical noise component changes according to a power law such that  $S \propto f^a$ , where  $a$  is the characteristic exponent for the particular noise type. It can be shown that the Allan variance slope  $\mu$  and the exponent  $a$  are connected via  $\mu = -a - 1$  [52, 53]. This is illustrated by the double-logarithmic  $\sigma$ – $\tau$  plot in Fig. 2.9b for the

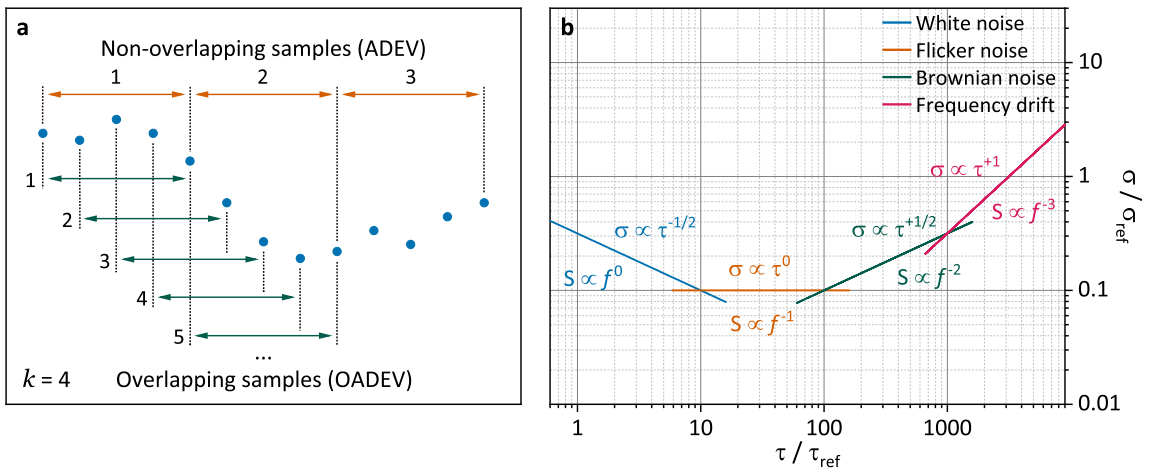


**Figure 2.9:** (a) Comparison between ADEV (orange arrows) and OADEV (green arrows) for adjacent-averaging factor  $k = 4$ . This diagram is based on Fig. 7 from Ref. 51. (b) Double-logarithmic Allan plot showing the (overlapping) Allan deviation ( $\sigma_A$  or  $\sigma_O$ ) as function of the interval time  $\tau$  for different noise types ( $0 \geq a \geq -3$ ).  $\tau_{\text{ref}}$  and  $\sigma_{\text{ref}}$  are arbitrarily chosen reference values for  $\sigma$  (ADEV or OADEV) and  $\tau$ , respectively.



most common noise types with  $0 \geq a \geq -3$ .

White noise components ( $a = 0$ , blue line) have a constant noise spectral density, while more divergent noise types ( $a < 0$ ) exhibit increasing values for  $S$  at lower detection frequencies  $f$ , i.e., longer interval times  $\tau$ . As already mentioned above, laser excess noise is pink noise and exhibits  $1/f$  behavior ( $a = -1$ , orange line). Hence, the corresponding (overlapping) Allan deviation remains constant for all  $\tau$ . Brownian noise ( $a = -2$ , green line) and frequency drift ( $a = -3$ , magenta line), which become dominant on long time scales, set a limit for sensitivity improvement by signal averaging procedures. It should be noted that the term "frequency drift" originates from stability analysis of atomic clocks and is unrelated to drifts in the detection laser frequency.

The  $\sigma$ - $\tau$  behavior for both ADEV and OADEV of any measured quantity arises from the superposition of all noise components acting on the detection system. For most absorption-based detection techniques,  $\sigma$  typically decreases with  $\tau^{-1/2}$  when averaging data measured at high sampling frequencies. As the number of data points used for averaging increases, low-frequency noise components start to come into play until a  $\sigma$  minimum is reached. Allan analysis of measured signal noise provides the minimal detectable signal intensity, and thereby  $A_{\min}$ , as function of the time resolution  $\tau$ . Moreover, it is helpful for identifying the optimal  $\tau$  value that corresponds to maximum sensitivity. In the case of FM spectroscopy, the sensitivity for specific experimental conditions and  $\tau$  values largely depends on the main modulation parameters ( $\nu_m, M, \theta$ ), the light power of the detection beam, the RAM magnitude, and the properties of the photodetector.

## References

- [1] A. Yariv, P. Yeh in *Optical Waves in Crystals: Propagation and Control of Laser Radiation*, John Wiley & Sons, **1983**, Chapter 4 - Electromagnetic Propagation in Anisotropic Media, 69 ff.
- [2] A. Yariv, P. Yeh in *Optical Waves in Crystals: Propagation and Control of Laser Radiation*, John Wiley & Sons, **1983**, Chapter 7 - Electro-Optics, 220 ff.
- [3] A. Yariv in *Quantum Electronics*, 3rd Edition, John Wiley & Sons, **1989**, Chapter 14 - The Modulation of Optical Radiation, 298 ff.
- [4] M. Bass in *Handbook of Optics. Vol. 2, Devices, Measurements, and Properties*. 2nd Edition, McGraw-Hill, **1995**, Chapter 13 - Electro-Optic Modulators.
- [5] A. K. Bain in *Crystal Optics: Properties and Applications*, John Wiley & Sons, **2019**, Chapter 1 - Crystal Optics, 1 ff.
- [6] A. Yariv, P. Yeh in *Photonics: Optical Electronics in Modern Communications*, Oxford University Press, **2007**, Chapter 10 - Noise in Optical Detection and Generation, 364 ff.
- [7] B. E. A. Saleh, M. C. Teich in *Fundamentals of Photonics*, John Wiley & Sons, Ltd, **1991**, Chapter 18 - Electro-Optics, 696 ff. DOI [10.1002/0471213748.ch18](https://doi.org/10.1002/0471213748.ch18).
- [8] A. Yariv, P. Yeh in *Optical Waves in Crystals: Propagation and Control of Laser Radiation*, John Wiley & Sons, **1983**, Chapter 8 - Electro-optic Devices, 276 ff.
- [9] G. C. Bjorklund, Frequency-modulation spectroscopy: a new method for measuring weak absorptions and dispersions, *Opt. Lett.* **1980**, 5, 15–17, DOI [10.1364/OL.5.000015](https://doi.org/10.1364/OL.5.000015).
- [10] G. C. Bjorklund, M. D. Levenson, W. Lenth, C. Ortiz, Frequency modulation (FM) spectroscopy, *Appl. Phys. B* **1983**, 32, 145–152, DOI [10.1007/bf00688820](https://doi.org/10.1007/bf00688820).
- [11] S. W. North, X. S. Zheng, R. Fei, G. E. Hall, Line shape analysis of Doppler broadened frequency-modulated line spectra, *J. Chem. Phys.* **1996**, 104, 2129–2135, DOI [10.1063/1.470969](https://doi.org/10.1063/1.470969).

- [12] G. Friedrichs, H. G. Wagner, Quantitative FM spectroscopy at high temperatures: The detection of  $^1\text{CH}_2$  behind shock waves, *Z. Phys. Chem.* **2000**, *214*, 1723–1746, DOI [10.1524/zpch.2000.214.12.1723](#).
- [13] M. Gehrtz, G. C. Bjorklund, E. A. Whittaker, Quantum-limited laser frequency-modulation spectroscopy, *J. Opt. Soc. Am. B* **1985**, *2*, 1510–1526, DOI [10.1364/JOSAB.2.001510](#).
- [14] J. A. Silver, Frequency-modulation spectroscopy for trace species detection: theory and comparison among experimental methods, *Appl. Opt.* **1992**, *31*, 707–717, DOI [10.1364/ao.31.000707](#).
- [15] G. Friedrichs, Sensitive Absorption Methods for Quantitative Gas Phase Kinetic Measurements. Part 1: Frequency Modulation Spectroscopy, *Z. Phys. Chem.* **2008**, *222*, 1–30, DOI [10.1524/zpch.2008.222.1.1](#).
- [16] D. E. Cooper, R. E. Warren, Frequency modulation spectroscopy with lead-salt diode lasers: a comparison of single-tone and two-tone techniques, *Appl. Opt.* **1987**, *26*, 3726–3732, DOI [10.1364/AO.26.003726](#).
- [17] M. Stuhr, N. Faßheber, G. Friedrichs, Single-tone mid-infrared frequency modulation spectroscopy for sensitive detection of transient species, *Opt. Express* **2019**, *27*, 26499–26512, DOI [10.1364/oe.27.026499](#).
- [18] M. Stuhr, S. Hesse, G. Friedrichs, Quantitative and Sensitive Mid-Infrared Frequency Modulation Detection of HCN behind Shock Waves, *Fuels* **2021**, *2*, 437–447, DOI [10.3390/fuels2040025](#).
- [19] M. Stuhr, G. Friedrichs, Mid-infrared Frequency Modulation Detection of HCN and Its Reaction with O Atoms behind Shock Waves, *J. Phys. Chem. A* **2022**, *126*, 9485–9496, DOI [10.1021/acs.jpca.2c06817](#).
- [20] G. R. Janik, C. B. Carlisle, T. F. Gallagher, Two-tone frequency-modulation spectroscopy, *J. Opt. Soc. Am. B* **1986**, *3*, 1070–1074, DOI [10.1364/JOSAB.3.001070](#).
- [21] V. Avetisov, P. Kauranen, Two-tone frequency-modulation spectroscopy for quantitative measurements of gaseous species: theoretical, numerical, and experimental investigation of line shapes, *Appl. Opt.* **1996**, *35*, 4705–4723, DOI [10.1364/AO.35.004705](#).
- [22] M. Abramowitz, I. A. Stegun, *Handbook of Mathematical Functions with Formulas, Graphs, and Mathematical Tables*, 10th Printing, Dover, New York, **1972**, 355 ff.
- [23] D. C. Hutchings, M. Sheik-Bahae, D. J. Hagan, E. W. V. Stryland, Kramers-Kronig relations in nonlinear optics, *Opt. Quantum Electron.* **1992**, *24*, 1–30, DOI [10.1007/bf01234275](#).
- [24] J. M. Supplee, E. A. Whittaker, W. Lenth, Theoretical description of frequency modulation and wavelength modulation spectroscopy, *Appl. Opt.* **1994**, *33*, 6294–6302, DOI [10.1364/AO.33.006294](#).
- [25] D. T. Cassidy, J. Reid, Atmospheric pressure monitoring of trace gases using tunable diode lasers, *Appl. Opt.* **1982**, *21*, 1185–1190, DOI [10.1364/ao.21.001185](#).
- [26] H. Li, G. B. Rieker, X. Liu, J. B. Jeffries, R. K. Hanson, Extension of wavelength-modulation spectroscopy to large modulation depth for diode laser absorption measurements in high-pressure gases, *Appl. Opt.* **2006**, *45*, 1052–1061, DOI [10.1364/ao.45.001052](#).
- [27] G. Friedrichs, J. T. Herbon, D. F. Davidson, R. K. Hanson, Quantitative detection of HCO behind shock waves: The thermal decomposition of HCO, *Phys. Chem. Chem. Phys.* **2002**, *4*, 5778–5788, DOI [10.1039/b205692e](#).
- [28] N. Faßheber, M. C. Schmidt, G. Friedrichs, Quantitative HNO detection behind shock waves, *Proc. Combust. Inst.* **2017**, *36*, 607–615, DOI [10.1016/j.proci.2016.05.035](#).
- [29] W. Schottky, Über spontane Stromschwankungen in verschiedenen Elektrizitätsleitern (On spontaneous current fluctuations in various electrical conductors), *Ann. Phys.* **1918**, *362*, 541–567, DOI [10.1002/andp.19183622304](#).
- [30] W. Schottky, On spontaneous current fluctuations in various electrical conductors, *J. Micro/ Nanolithogr. MEMS MOEMS* **2018**, *17*, 041001/1–11, DOI [10.1117/1.JMM.17.4.041001](#).



- [31] R. Hui in *Introduction to Fiber-Optic Communications*, Academic Press, **2020**, 137 ff. DOI [10.1016/B978-0-12-805345-4.00004-4](https://doi.org/10.1016/B978-0-12-805345-4.00004-4).
- [32] A. Heidmann, R. J. Horowicz, S. Reynaud, E. Giacobino, C. Fabre, G. Camy, Observation of Quantum Noise Reduction on Twin Laser Beams, *Phys. Rev. Lett.* **1987**, *59*, 2555–2557, DOI [10.1103/PhysRevLett.59.2555](https://doi.org/10.1103/PhysRevLett.59.2555).
- [33] R. Whittaker, C. Erven, A. Neville, M. Berry, J. L. O’Brien, H. Cable, J. C. F. Matthews, Absorption spectroscopy at the ultimate quantum limit from single-photon states, *New J. Phys.* **2017**, *19*, 023013/1–9, DOI [10.1088/1367-2630/aa5512](https://doi.org/10.1088/1367-2630/aa5512).
- [34] E. Knyazev, F. Y. Khalili, M. V. Chekhova, Overcoming inefficient detection in sub-shot-noise absorption measurement and imaging, *Opt. Express* **2019**, *27*, 7868–7885, DOI [10.1364/OE.27.007868](https://doi.org/10.1364/OE.27.007868).
- [35] K. Matsuzaki, T. Tahara, Superresolution concentration measurement realized by sub-shot-noise absorption spectroscopy, *Nat. Commun.* **2022**, *13*, 1–8, DOI [10.1038/s41467-022-28617-w](https://doi.org/10.1038/s41467-022-28617-w).
- [36] V. Liger, Optical fringes reduction in ultrasensitive diode laser absorption spectroscopy, *Spectrochim. Acta A* **1999**, *55*, 2021–2026, DOI [10.1016/S1386-1425\(99\)00074-8](https://doi.org/10.1016/S1386-1425(99)00074-8).
- [37] V. Liger, A. Zybin, Y. Kuritsyn, K. Niemax, Diode-laser atomic-absorption spectrometry by the double-beam-double-modulation technique, *Spectrochim. Acta B* **1997**, *52*, 1125–1138, DOI [10.1016/S0584-8547\(97\)00029-3](https://doi.org/10.1016/S0584-8547(97)00029-3).
- [38] N. Wong, J. L. Hall, Servo control of amplitude modulation in frequency-modulation spectroscopy: demonstration of shot-noise-limited detection, *J. Opt. Soc. Am. B* **1985**, *2*, 1527–1533, DOI [10.1364/JOSAB.2.001527](https://doi.org/10.1364/JOSAB.2.001527).
- [39] P. Werle, F. Slemr, M. Gehrtz, C. Bräuchle, Quantum-limited FM-spectroscopy with a lead-salt diode laser, *Appl. Phys. B* **1989**, *49*, 99–108, DOI [10.1007/bf00332268](https://doi.org/10.1007/bf00332268).
- [40] G. Friedrichs, H. G. Wagner, Direct Measurements of the Reaction  $\text{NH}_2 + \text{H}_2 \rightarrow \text{NH}_3 + \text{H}$  at Temperatures from 1360 to 2130 K, *Z. Phys. Chem.* **2000**, *214*, 1151–1160, DOI [10.1524/zpch.2000.214.8.1151](https://doi.org/10.1524/zpch.2000.214.8.1151).
- [41] W. Zhang et al., Reduction of residual amplitude modulation to  $1 \times 10^{-6}$  for frequency modulation and laser stabilization, *Opt. Lett.* **2014**, *39*, 1980–1983, DOI [10.1364/ol.39.001980](https://doi.org/10.1364/ol.39.001980).
- [42] L. Li, F. Liu, C. Wang, L. Chen, Measurement and control of residual amplitude modulation in optical phase modulation, *Rev. Sci. Instrum.* **2012**, *83*, 043111/1–10, DOI [10.1063/1.4704084](https://doi.org/10.1063/1.4704084).
- [43] E. A. Whittaker, M. Gehrtz, G. C. Bjorklund, Residual amplitude modulation in laser electro-optic phase modulation, *J. Opt. Soc. Am. B* **1985**, *2*, 1320–1326, DOI [10.1364/josab.2.001320](https://doi.org/10.1364/josab.2.001320).
- [44] E. A. Whittaker, C. M. Shum, H. Grebel, H. Lotem, Reduction of residual amplitude modulation in frequency-modulation spectroscopy by using harmonic frequency modulation, *J. Opt. Soc. Am. B* **1988**, *5*, 1253–1256, DOI [10.1364/JOSAB.5.001253](https://doi.org/10.1364/JOSAB.5.001253).
- [45] M. Romagnoli, M. D. Levenson, G. C. Bjorklund, Frequency-modulation–polarization spectroscopy, *Opt. Lett.* **1983**, *8*, 635–637, DOI [10.1364/OL.8.000635](https://doi.org/10.1364/OL.8.000635).
- [46] M. C. McCarthy, J. C. Bloch, R. W. Field, Frequency-modulation enhanced magnetic rotation spectroscopy: A sensitive and selective absorption scheme for paramagnetic molecules, *J. Chem. Phys.* **1994**, *100*, 6331–6346, DOI [10.1063/1.467095](https://doi.org/10.1063/1.467095).
- [47] J. M. Smith, J. C. Bloch, R. W. Field, J. I. Steinfeld, Trace detection of  $\text{NO}_2$  by frequency-modulation-enhanced magnetic rotation spectroscopy, *J. Opt. Soc. Am. B* **1995**, *12*, 964–969, DOI [10.1364/JOSAB.12.000964](https://doi.org/10.1364/JOSAB.12.000964).
- [48] P. Werle, S. Lechner, Stark-modulation-enhanced FM-spectroscopy, *Spectrochim. Acta A* **1999**, *55*, 1941–1955, DOI [10.1016/S1386-1425\(99\)00067-0](https://doi.org/10.1016/S1386-1425(99)00067-0).
- [49] D. W. Allan, Statistics of atomic frequency standards, *Proc. IEEE* **1966**, *54*, 221–230, DOI [10.1109/PROC.1966.4634](https://doi.org/10.1109/PROC.1966.4634).

- 
- [50] P. Werle, R. Mücke, F. Slemr, The limits of signal averaging in atmospheric trace-gas monitoring by tunable diode-laser absorption spectroscopy (TDLAS), *App. Phys. B* **1993**, 57, 131–139, DOI [10.1007/bf00425997](https://doi.org/10.1007/bf00425997).
  - [51] W. J. Riley, *Handbook of Frequency Stability Analysis*, US Department of Commerce, National Institute of Standards and Technology (NIST), **2008**.
  - [52] J. A. Barnes, A. R. Chi, L. S. Cutler, D. J. Healey, D. B. Leeson, T. E. McGunigal, J. A. Mullen, W. L. Smith, R. L. Sydnor, R. F. Vessot, et al., Characterization of frequency stability, *IEEE Trans. Instrum. Meas.* **1971**, 105–120, DOI [10.1109/TIM.1971.5570702](https://doi.org/10.1109/TIM.1971.5570702).
  - [53] D. Allan, M. Weiss, J. Jespersen in Proceedings of the 45th Annual Symposium on Frequency Control 1991, **1991**, pp. 667–678, DOI [10.1109/FREQ.1991.145966](https://doi.org/10.1109/FREQ.1991.145966).

# CHAPTER 3

---

## Experimental

---

As part of this dissertation, a single-tone mid-infrared frequency modulation (ST-MIR-FM) spectrometer with external modulation has been established for the first time. The spectrometer was supplemented by an MIR scanning confocal interferometer that has been designed and implemented to characterize the spectrum of frequency-modulated MIR detection laser light and to measure the modulation depth. This chapter opens with a description of the latest version of the new ST-MIR-FM spectrometer. It is followed by a short introduction into the shock tube method and a brief overview of the Kiel shock tube apparatus, which was used for the experiments on HCN detection behind shock waves described in Publications III–V (Chapters 6, 7, and 8). Finally, the methods for calculating species concentration-time profiles as well as sensitivity coefficients for kinetic experiments, FM factors for quantitative species detection, and Allan deviation values for assessing the detection sensitivity are introduced.

### 3.1 Single-Tone Mid-Infrared FM Spectrometer

The earliest iteration of the ST-MIR-FM spectrometer was already set up prior to this dissertation as part of the author’s M.Sc. thesis and the first instrumental updates to it were briefly discussed in Publication I (Chapter 4). Figure 3.1 shows a schematic of the most recent iteration of the MIR-FM spectrometer, which was characterized in detail as reported in Publication IV (Chapter 7). Its key elements are a thermally stabilized resonant electro-optic modulator, a specifically designed high-bandwidth MIR detector, and an ultrafast digital lock-in amplifier, which are described in the following sections. In contrast to earlier versions of the setup, where demodulation was performed by means of analog electronic components, the current iteration of the spectrometer allows fully digital signal processing.

#### Optical Parametric Oscillator Laser System

The MIR beam for FM detection was generated by a continuous-wave optical parametric oscillator (cw-OPO, Argos 2400-SF-10, Lockheed Martin Aculight, modules B and C). A combination of an Yb-doped fiber seed laser (Koheras AdjustiK Y10 PM, NKT Photonics, 1064 nm, 15 mW) with a distributed feedback (DFB) diode laser and an Yb-doped fiber amplifier (YAR-10K-1064-LP-SF, IPG Photonics, 10 W) provided the pump radiation for the OPO resonator. The pump beam was directly coupled into the bow-tie OPO cavity via a polarization-maintaining collimator and two integrated mirrors. A thermally stabilized periodically poled LiNbO<sub>3</sub> (PPLN) crystal doped with

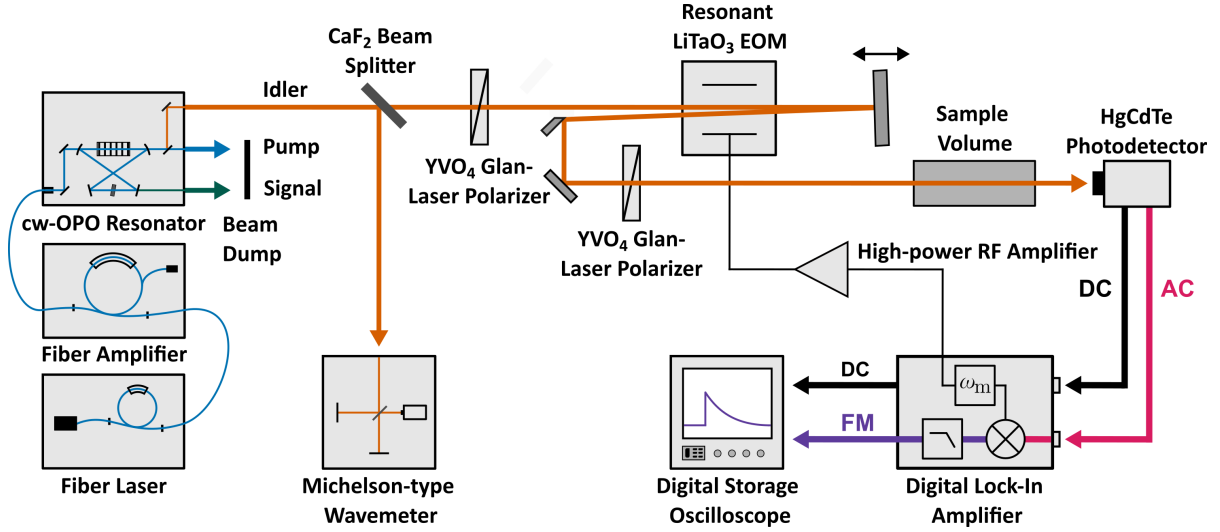


**Figure 3.1:** Schematic of the single-tone MIR-FM setup. This represents the current state of the spectrometer as reported in Publication IV (Chapter 7). cw-OPO: continuous-wave optical parametric oscillator, RF: radio frequency, EOM: electro-optic modulator, DC: direct current, AC: alternating current, FM: frequency modulation,  $\omega_m$ : (angular) modulation frequency.

MgO was positioned in the center of the cavity's long arm. When the pump beam ( $\omega_P$ ) passes through the crystal, some fraction of its intensity is converted into the lower-frequency signal ( $\omega_S$ ) and idler ( $\omega_I$ ) beams according to  $\omega_P = \omega_S + \omega_I$ , provided that quasi-phase matching is achieved at this particular PPLN crystal configuration. For this OPO system, the resulting signal and idler beams lie in the near-infrared and mid-infrared spectral regions, respectively, with different available NIR and MIR ranges depending on the specific OPO module.

Wavelength tuning of the signal and idler beams can be achieved in three different ways: (1) translational adjustment of the PPNL crystal by a turning screw, (2) angle-setting of an intracavity etalon, and (3) continuous piezoelectric fine-tuning of the seed laser. The intracavity etalon also acts as a frequency filter, since the angle of incidence influences both the absolute resonance frequencies and the free spectral range of the etalon. Piezoelectric tuning of the seed laser was realized by generating a high-voltage signal using a dedicated amplifier (PDL200, PiezoDrive) driven by a function generator (33220A, Agilent) and supplying it to a piezoelectric transducer attached to the seed laser fiber. The resulting piezoelectric strain causes slight changes in the (angular) pump laser frequency  $\omega_P$ , and thereby  $\omega_S$  and  $\omega_I$ . This approach provides a mode-hop-free tuning range of 100 GHz while scanning the applied voltage at 30 Hz, with decreasing tuning range for higher scanning frequencies.

In the experiments described in this work, only the MIR idler output beam was used for FM spectroscopic detection. A calcium fluoride ( $\text{CaF}_2$ ) beam splitter directed a small fraction of the idler output light towards a Michelson-type wavemeter (621A-IR, Bristol Instruments), which monitored the wavelength of the detection beam with an accuracy of  $6 \times 10^{-4} \text{ cm}^{-1}$ . The remaining MIR light was guided towards the EOM.

## Resonant Electro-Optic Modulator

The detection beam was subjected to frequency modulation by a resonant lithium tantalate ( $\text{LiTaO}_3$ ) electro-optic phase modulator (EO-T500T3-MWIR1, Qubig) with a resonance frequency of  $\nu_m = 489.0$  MHz and a high quality factor of  $Q = 285$ . Offering a large electro-optic coefficient of roughly  $r_{33} = 30$  pm/V, depending on the laser wavelength [1],  $\text{LiTaO}_3$  is a common material for Q-switches and phase/amplitude modulators. Thermoelectric temperature stabilization of the EOM to  $T = (25.0 \pm 0.1)$  °C ensured stability of the modulation parameters  $\nu_m$  and  $M$ . The resonance frequency of the EOM can be adjusted over about 10 MHz by changing the temperature within  $16^\circ\text{C} < T < 40^\circ\text{C}$  with a temperature coefficient of  $-0.33 \text{ MHz}/^\circ\text{C} < d\nu_m/dT < -0.43 \text{ MHz}/^\circ\text{C}$ . In fact, since this particular EOM does not have a tuning screw, the resonance frequency can only be set by changing the operating temperature. The EOM was driven by a high-power RF amplifier (ZHL-20W-13, Mini Circuits, 51.9 dB gain), which in turn was supplied with a modulation signal from the lock-in amplifier of up to  $-14.9$  dBm. This resulted in modulation power in the resonant EOM circuit of up to  $P_m = 5.0$  W, which is equal to the maximum input power recommended by the manufacturer.

In order to increase the achievable modulation depth, the phase modulator was arranged in double-pass configuration. For the first pass, the detection beam traveled through the  $\text{LiTaO}_3$  crystal slightly off-axis relative to the EOM input axis. Afterwards, it was reflected back by a mirror on a translational stage for a second pass. The transmitted frequency-modulated MIR detection beam had a slight spatial offset relative to the incident beam, and could be separated from it by a D-shaped pick-off mirror (see Fig. 3.1). To ensure proper overlap of the two phase modulation stages, the distance between the EOM and the mirror must be equal to an integer multiple of the half-wavelength of the modulation signal, which is 30.65 cm for  $\nu_m = 489.0$  MHz. Otherwise, the modulation waves would not be in phase and could even partially cancel each other out, as high frequency components from the first pass experience a shift towards lower frequencies on the second pass, and vice versa.

Two yttrium orthovanadate ( $\text{YVO}_4$ ) Glan-laser polarizers (Altechna) were placed in front and behind the EOM. Firstly, during normal operation of the FM spectrometer, the polarizer in front of the EOM was used to maximize the light intensity for the appropriate EOM polarization input angle. Secondly, as was alluded to in Section 2.2, phase modulators between crossed polarizers act as amplitude modulators [2], which allows for the adjustment of the demodulation phase angle to pure absorption ( $\theta = 0^\circ, 180^\circ$ ).

To this end, the first polarizer is slightly mismatched with regards to the intended polarization input angle of the EOM by  $\sim 2^\circ$ . Thus, the light traveling through the EOM exhibits two polarization components, one parallel and one perpendicular to the EOM input angle. Due to electro-optically induced birefringence, the two polarization components acquire a phase delay relative to each other, and the light experiences polarization modulation in phase with the modulation signal. This results in amplitude modulation of the frequency-modulated detection beam, which is converted into an FM signal after demodulation, with its intensity depending on the rotation angle of the second

polarizer. If the second polarizer is rotated back and forth by a few degrees in each direction, the magnitude of amplitude modulation seen by the FM detection-demodulation system changes accordingly. Since the total transmission of the Polarizer-EOM-Polarizer setup is a sine-squared function of the modulated phase delay [3], no change in amplitude modulation occurs at  $\theta = 0^\circ$  and  $\theta = 180^\circ$  when rotating the polarizer. Therefore, slight rotation of the second polarizer causes FM signal background undulations that vanish for in-phase demodulation. By adjusting the internal phase angle shift of the lock-in amplifier (see below) until the undulations disappear, the absolute demodulation phase angle can be set to pure absorption ( $\theta = 0^\circ, 180^\circ$ ).

### High-Bandwidth Mid-Infrared Photodetector

After traveling through the sample volume, e.g., a low-pressure flow reactor or the driven section of a shock tube, the MIR beam was detected by a photovoltaic mercury cadmium telluride (HgCdTe, MCT) detector (PVI-4TE-5, Vigo System). MCT is a common material for photovoltaic and photoconductive MIR detectors and can be produced with different mercury content  $x$  ( $\text{Hg}_x\text{Cd}_{1-x}\text{Te}$ ) [4, 5]. While the semiconductor CdTe has a room-temperature bandgap of 1.5 eV, the semimetal HgTe is essentially bandgap-free. By adjusting the composition ratio  $x$ , the detector material can be optimized for different spectral regions in the MIR. Compared to their counterparts in the visible spectral range, MIR photodiodes have much lower bandgaps and suffer from higher thermal noise, which often limits the detection sensitivity.

The MCT photodiode used in this work is part of an integrated detection module with preamplifier (FIP-10k-1G, Vigo System), active temperature control (PTCC-01-ADV, Vigo System), and DC signal monitor. To ensure stable detection performance and to minimize thermal noise, the active surface of the photodiode is kept at  $T = 196$  K by a four-stage thermoelectric cooling system. With a small active area of  $0.5 \times 0.5$  mm<sup>2</sup> and reverse bias voltage operation, the photodiode reaches a very fast response time of 100 ns.

A bias tee separates the DC and AC components of the measured signal intensity  $I_T(t)$ , with cut-off frequencies of  $f_{\text{DC}} = 2.3$  MHz and  $f_{\text{AC}} = 1.7$  MHz, respectively. After internal preamplification to a bandwidth of  $\Delta f_{\text{BW}} = 686$  MHz, the AC component was passed to the lock-in amplifier, while the DC signal was directly sent to a digital storage oscilloscope (MSO 8104A, Agilent) for recording. The photodiode-preamplifier system reaches a specific detectivity for the AC channel of  $D^* = 5.6 \times 10^9$  cm Hz<sup>1/2</sup> W<sup>-1</sup> at  $\lambda = 3.3$   $\mu\text{m}$  and the DC detector voltage response remains linear up to roughly 1 mW of incident optical power.

### Digital Lock-In Amplifier

In the experiments described in Publication I (Chapter 4), demodulation was performed using a conventional scheme assembled from several analog RF components, including directional coupler, phase shifter, frequency mixer, and two amplifiers. For all successive studies, the analog demodulation scheme was replaced by an all-digital lock-in amplifier (LIA, UHFLI, Zurich Instruments) with fast analog-to-digital conversion from DC up to 600 MHz at 1.8 GSa/s and 12-bit resolution. Digital signal processing avoids possible RF power mismatches and nonlinearities

of individual electronic components. It also allows for a variety of signal manipulation procedures, such as amplification, demodulation, and signal filtering, without the need for dedicated RF components, and thus without introducing additional noise or signal distortion into the detection system.

In general, for  $1f$  demodulation with conventional LIAs, all detected AC signal components with frequencies  $\nu_s$  are first supplied to a frequency mixer, which multiplies the measured signal with a reference signal of frequency  $\nu_m$ . The frequency mixing results in new signal components oscillating at  $\nu_s + \nu_m$  and  $\nu_s - \nu_m$ , which are then low-pass filtered at bandwidth  $\Delta f_{\text{LPF}} \ll \nu_m$ . Thus, all frequency components  $\nu_s$  that differ from  $\nu_m$  by more than  $\pm \Delta f_{\text{LPF}}$ , including higher harmonics of  $\nu_m$ , are suppressed in the demodulation process. For demodulation with the digital LIA, input AC signals are first digitized and then multiplied by a sine function in real time using a fast field-programmable gate array (FPGA). In this work, the maximum low-pass filter bandwidth of the digital LIA is  $\Delta f_{\text{LPF}} = 790.9$  kHz. At this bandwidth, the equivalent 10%-to-90% rise time is  $t_r = 0.35/\Delta f_{\text{LPF}} = 442$  ns, representing the overall time resolution of FM detection.

Since AC signals from the photodetector are fully digitized by the all-digital LIA, the practical implementation of signal demodulation is greatly simplified. Firstly, the absolute demodulation phase angle  $\theta$  can be conveniently adjusted by imposing an arbitrary digital phase shift. Secondly, the measured signals can be subjected to dual-phase demodulation without complicating the experimental setup or causing unintended signal attenuation. In dual-phase demodulation, the incoming AC signal is simultaneously demodulated at two different phase angles  $\theta$  and  $\theta + 90^\circ$ , which results in FM signals commonly referred to as  $X$  and  $Y$ , respectively. The absolute demodulation phase angle can be calculated via  $\theta = \arctan2(X, Y)$ , assuming negligible interference from in-phase and quadrature RAM components (see Section 2.2.1). At fixed detection frequency, the in-phase-quadrature (IQ) signal  $R = (X^2 + Y^2)^{1/2}$  has a constant amplitude regardless of the selected value for  $\theta$ . In principle, the  $\theta$ -independent  $R$  signal can be directly converted into FM-equivalent absorption using the FM working equation 2.27, provided that the corresponding  $\Delta f$  value at the given detection wavelength is known.

In addition to digital demodulation, the LIA was also used to generate the RF modulation signal at  $\nu_m = 489.0$  MHz, which is referenced to an internal temperature-stabilized quartz crystal oscillator with high frequency stability of 50 ppt over 1 s. All demodulated FM signals were converted into analog voltage signals of intensity  $I_{\text{FM}}$ , which can be scaled up to amplitudes of 10 V by adjusting the LIA output gain, and recorded by the digital storage oscilloscope (MSO 8104A, Agilent) for further analysis.

### Scanning Confocal Interferometer

In order to check the modulation index  $M$  of the EOM during operation, a scanning confocal interferometer with a free spectral range of  $\Delta f_{\text{FSR}}\nu = 3.0$  GHz was designed and built in house. The interferometer consists of a pair of custom-coated yttrium aluminium garnet (YAG) mirrors (Layertec) with custom coating, which are positioned at a distance equal to their radius of curvature of  $r = 25$  mm. With an average mirror reflectivity of  $R \approx 98.5\%$  in the range



$2500 \text{ cm}^{-1} \leq \tilde{\nu} \leq 5000 \text{ cm}^{-1}$ , the setup provides a finesse of  $\mathcal{F} \approx 200$  for optimal alignment. A piezo actuator (P-401-10, piezosystem jena) connected to one of the mirror mounts was supplied by ramp voltage signals provided by a function generator (33210A, Agilent) and amplified by a piezo driver (BPC303, Thorlabs). At maximum ramp amplitude, the mirror distance could be scanned by roughly  $10 \text{ }\mu\text{m}$ , corresponding to a frequency scan range of about  $20 \text{ GHz}$ . The intensity of the frequency-modulated MIR light transmitted by the scanning interferometer was measured by an AC-coupled lead(II) selenide (PbSe) photodetector (PDA20H-EC, Thorlabs) and recorded on the aforementioned digital storage oscilloscope.

Figure 3.2a shows an exemplary scanning interferometer transmission spectrum for determining the modulation depth of frequency-modulated light. Since the intensity ratio of the first-order sidebands to the carrier is equal to the ratio of the respective squared Bessel functions  $J_{\pm 1}(M)^2/J_0(M)^2$ , the modulation index  $M$  could be extracted in a straightforward manner.

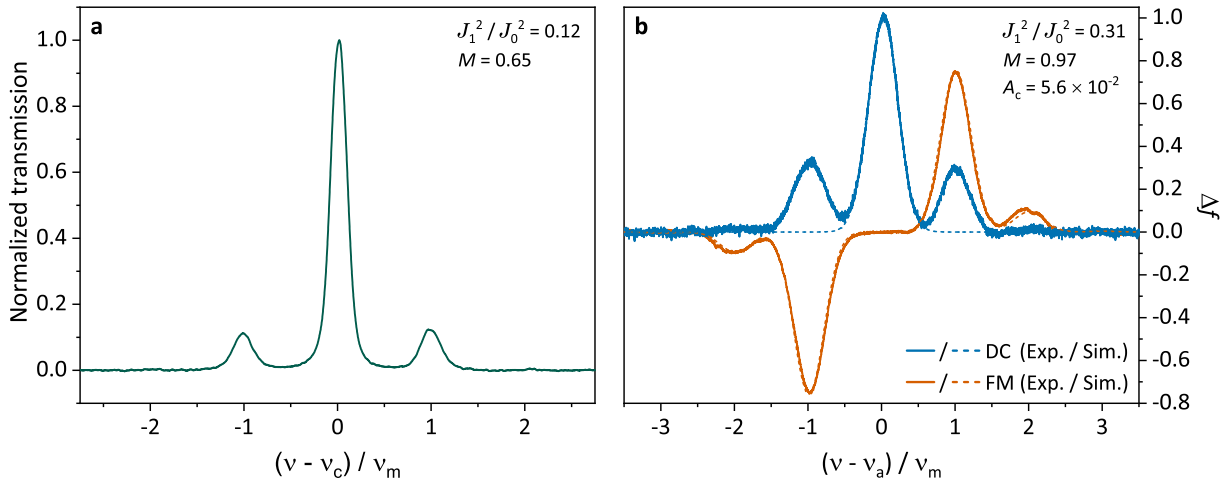


**Figure 3.2:** (a) Scanning interferometer transmission spectrum of frequency-modulated light at  $M = 0.65$ . (b) Conventional absorption spectrum (solid blue curve) and FM spectrum (solid orange curve) of the P(25)e rovibrational transition of  $\text{C}_2\text{H}_2$  in Ar at  $3233.08 \text{ cm}^{-1}$  ( $M = 0.97$ ,  $\theta = 0^\circ$ ,  $p = 32.1 \text{ Pa}$ ,  $T = 295 \text{ K}$ , 100 averages) alongside their simulated counterparts (dashed curves). The peak absorption at line center was  $A_c = 5.6 \times 10^{-2}$ . Since the conventional absorption spectrum was measured under frequency-modulated conditions, it shows sidebands at  $\nu_c \pm \nu_m$  (see main text).

### 3.2 Gain factor $G$ and Modulation Index $M$

Keeping in mind that the fractional absorption  $A$  caused by probing a spectral feature is connected to the measured signal intensities  $I_{\text{FM}}$  and  $I_0$  according to

$$A = \frac{2}{\Delta f} \frac{I_{\text{FM}}/G}{I_0} \quad (3.1)$$

it becomes clear that accurate knowledge of  $G$  and  $M$  is crucial for ensuring quantitative FM spectroscopic detection. While  $G$  only acts as a linear scaling factor,  $\Delta f$  is a complex function of several FM-related parameters, most importantly  $M$ , as already discussed in Section 2.1.4. The electronic gain factor  $G$  of the FM detection-demodulation system described in this work can be



separated into the variable and invariable components  $g$  and  $G_0$ , respectively, such that  $G = g G_0$ . While  $g$  covers the selected amplification for the LIA output, which can be freely adjusted up to amplitudes of 10 V,  $G_0$  accounts for constant effects on the demodulated signals, such as AC input loss and signal conversion during the demodulation process. By comparing conventional (DC) and FM absorption spectra at known modulation depth, and thereby  $\Delta f$ , the invariable gain factor  $G_0$  relative to the corresponding conventional absorption signal can be easily obtained at the selected  $g$  value (see Eq. 2.30).

As an alternative to the interferometer method, measured FM spectra can be fitted with  $\Delta f$  simulations to determine  $M$ . This works particularly well for narrow absorption lines with well-resolved FM signal sidebands ( $x_m > 1$ ) at sufficient modulation depths ( $M \gtrsim 0.6$ ). Figure 3.2b shows experimental (solid curves) and simulated (dashed curves) Doppler-limited spectra of a rovibrational  $\text{C}_2\text{H}_2$  line as an example. The DC spectrum (solid blue curve) was measured during EOM operation, and therefore some intensity was contained in the first-order sidebands at  $\nu_c \pm \nu_m$ . Consequently, the direct absorption (DC) spectrum resembles the intensity spectrum of frequency-modulated light, similar to the etalon trace in Fig. 3.2a. Because  $M$  is well-constrained by the intensity ratio of the DC spectrum as well as the FM lineshape (solid orange curve),  $G_0$  remains the only free parameter. Thus,  $G_0$  and  $M$  can be determined independently from the same DC/FM spectrum pair. For the current iteration of the FM detection-demodulation scheme, the invariable gain factor is  $G_0 = 1.23$ . At  $P_m = 5.0$  W and  $T = 25.0$  °C, the resonant  $\text{LiTaO}_3$  EOM described here provides a modulation index of  $M = 0.97$  at  $\nu_m = 489.0$  MHz for double-pass operation.

### 3.3 Shock Tube Apparatus

Shock-heating of gas mixtures has proven a prolific method in high-temperature gas-phase reaction kinetics [6, 7], most importantly for measurements of ignition delay times and concentration-time profiles of reactive species. Depending on the design and operation of the shock tube system [8] as well as the pre-shock conditions, a wide range of pressures and temperatures can be realized. Combined with a relatively straightforward procedure of deriving experimental conditions, the shock tube method represents a powerful tool in combustion research. Common drawbacks of shock tube experiments are the low repetition frequency of measurement and the limited shot-to-shot reproducibility of post-shock wave pressures and temperatures. However, such issues have been addressed by dedicated applications, e.g., high-repetition shock tubes [9, 10].

Figure 3.3 illustrates shock wave propagation in a pressure-driven apparatus. Shock tubes of this kind have high-pressure driver and low-pressure driven sections separated by a sacrificial burst diaphragm (see Fig. 3.3a), which spontaneously ruptures when the driver gas pressure is increased above a certain threshold. Starting from the diaphragm position ( $x = 0$ , see Fig. 3.3b), the shock wave (blue line) travels along the shock tube axis into the direction of the end wall.

A shock front represents a very thin region in which the fluid properties change rapidly, i.e., where a jump in flow velocity, pressure, and temperature occurs [11]. The flow velocities in front

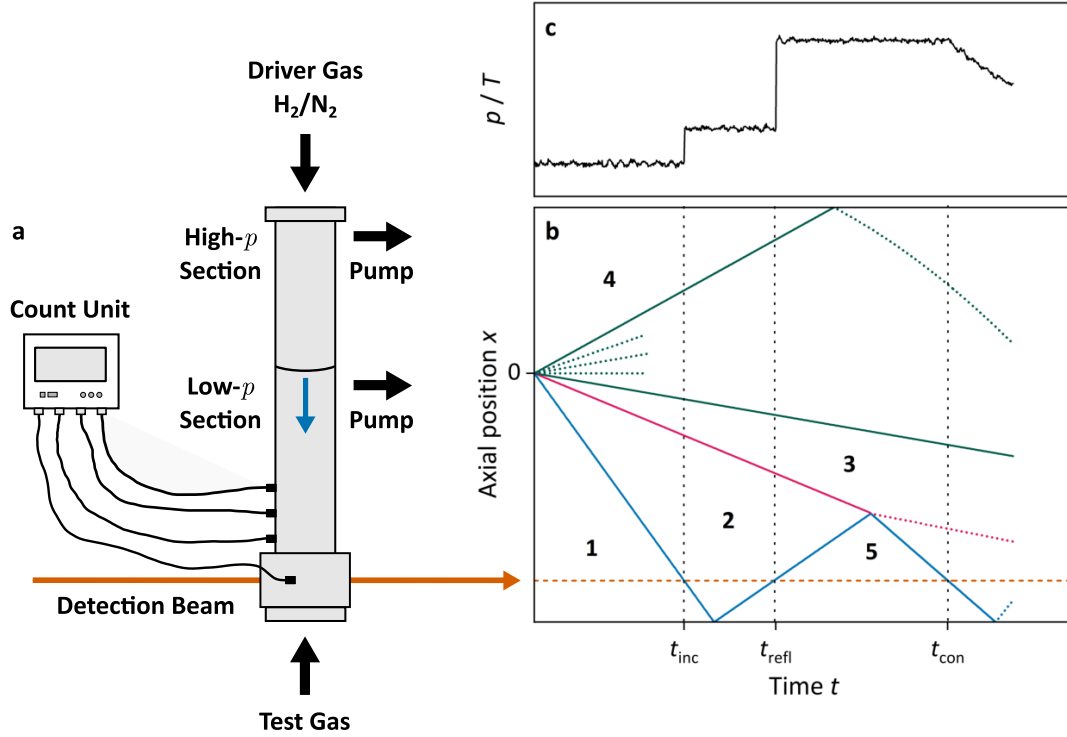


**Figure 3.3:** (a) Schematic of a pressure-driven shock tube. (b)  $x-t$  diagram showing the propagation of the shock wave (blue lines), the expansion-wave fan (green lines), and the contact surface (magenta lines). The numbered areas represent sections of the shock tube under initial pre-shock (1), incident wave (2), expanded driver gas (3), high-pressure driver gas (4), and reflected wave (5) conditions.  $t_{inc}$ ,  $t_{refl}$ , and  $t_{con}$  indicate the arrival of the incident, reflected, and contact surface-reflected wave at the observation point (dashed orange line), respectively. (c) Artificial  $p/T-t$  profile for illustration.

of (upstream) and behind (downstream) the shock wave are commonly referred to as  $u_1$  and  $u_2$ , respectively. Shock waves can only form when the upstream flow velocity  $u_1$  is larger than the speed of sound  $a_1$ , i.e., when the upstream flow is supersonic with the corresponding Mach number  $M_1 = u_1/a_1 > 1$ . Simultaneous to the shock wave propagation, a fan of expansion waves (green lines), which causes gradual changes in the state of the driver gas, spreads through the driver section, while the contact surface (magenta line), which is the interface between driver and driven gas, follows the shock front.

The arrival of the incident shock wave leads to rapid heating and compression of the test gas (see Fig. 3.3c). After passing the observation point (dashed orange line) and reflection at the end wall, the shock front travels through the test gas again, causing further heating/compression and bringing the test gas to rest. By assuming conservation of mass, momentum, and energy as well as ideal gas behavior, the relationship between pre-shock conditions ( $p_1$ ,  $T_1$ ) and post-incident shock conditions ( $p_2$ ,  $T_2$ ) conditions can be established via the so-called Rankine-Hugoniot equations [12]. Reflected-wave conditions ( $p_5$ ,  $T_5$ ) can be derived from incident-wave conditions ( $p_2$ ,  $T_2$ ) and the heat capacity ratio  $\gamma = c_p/c_V$ . In many applications, however, real gas effects also have to be taken into account by including the temperature dependency of  $c_p$ . For measurements behind the incident wave, the test gas is in motion relative to the laboratory reference frame. Thus, the

recorded time behind the incident wave  $t_{\text{lab}}$  has to be converted into actual reaction time  $t_{\text{rxn}}$  via  $t_{\text{rxn}} = t_{\text{lab}} \times \rho_2/\rho_1$ .

All shock tube experiments presented in this work (Publications III–V, Chapters 6, 7, and 8) were conducted with the Kiel shock tube setup, which has been used in several studies on the high-temperature reaction kinetics of HCO [13, 14], NCN [15–17], and HNO [18]. Since the shock tube has been described in detail elsewhere [13, 19], only a brief overview is given here. The Kiel shock tube is a pressure-driven apparatus with a stainless-steel body of 8.3 m total length, 81 mm inner diameter, and 10 mm wall thickness. It contains a 3.7 m long driver section and a 4.1 m long electro-polished driven section, separated by a sacrificial aluminium diaphragm. The diaphragm-holding connecting piece in the middle as well as the shock tube head with optical  $\text{CaF}_2$  windows and gas supply connections make up the rest of the total length. A combination of diaphragm and turbomolecular pumps evacuate the driven section down to pressures of  $p \approx 10^{-7}$  mbar.

$\text{H}_2/\text{N}_2$  mixtures of variable composition served as driver gas, with stronger shocks, and therefore higher post-shock temperatures and pressures, for higher mole fractions of the lower-mass species  $\text{H}_2$ . Incident shock wave velocities were measured using three piezoelectric sensors mounted flush with the shock tube walls at fixed distances, an additional sensor in the observation plane, and a count unit (see Fig. 3.3c). The sensors also provided values for the shock wave attenuation, which was typically around 1%/m. Incident and reflected shock wave conditions were calculated from shock wave velocities and attenuations as well as pre-shock conditions using a home-written one-dimensional frozen-chemistry code based on an iterative algorithm adopted from Gaydon and Hurlé [20]. Ideal shock wave propagation was assumed, but temperature-dependent thermodynamic properties of the shock-heated reactive gas mixtures were taken into account.

At typical pre-shock pressures of 20–100 mbar and with aluminum diaphragms of 50–100  $\mu\text{m}$  thickness, incident-wave conditions for the experiments of this work were within  $0.2 \text{ bar} \leq p_2 \leq 0.9 \text{ bar}$  and  $700 \text{ K} \leq T_2 \leq 2000 \text{ K}$  at Mach numbers of  $M_s \approx 3$ . Available time windows of measurement behind the incident and reflected shock waves were around 0.5 ms (reaction time frame) and 1 ms, respectively.

## 3.4 Calculation Methods

### Kinetic Profiles and Sensitivity Coefficients

The *Chemkin-II* package [21] was used for numerical simulations of concentration-time profiles in kinetic experiments. Unless stated otherwise in the respective publication, thermodynamic data were adopted in the form of NASA polynomials from Burcat [22] with updates from the ATcT database [23, 24]. For kinetic simulations regarding the reaction  $\text{NCN} + \text{H}$  (see Publication V, Chapter 8), the recent recommendation for the enthalpy of formation for  $^3\text{NCN}$  was taken into account [25]. All calculations assumed an adiabatic system at constant volume, allowing for minor changes of pressure and temperature due to chemical reactions.

Kinetic sensitivity analyses, which serve to identify the most important reactions for any arbitrary reactive species S at specified experimental conditions, were performed using the *SENKIN* routine

of *Chemkin-II* [26]. In *Chemkin-II*, reaction rate constants are given in terms of an extended Arrhenius expression

$$k_i = a_i A_i T^{n_i} \exp(-E_{ai}/RT) \quad (3.2)$$

with reaction index  $i$  and a scaling factor  $a_i$  used for sensitivity analysis, which is initially set to one. In order to gauge the impact of reaction  $i$ , its rate constant  $k_i$  is varied by slightly changing  $a_i$ , which causes reaction time-dependent variations in the species concentration  $[S]$ . The sensitivity coefficient of species  $S$  for reaction  $i$  is defined as

$$\sigma_i(S)' = \frac{\partial[S]}{\partial a_i} \quad (3.3)$$

and quantifies the extent to which the simulated profiles of the species of interest  $S$  are influenced by the respective reaction. Typically, it is useful to normalize the absolute sensitivity coefficient  $\sigma_i(S)'$  to some value of  $[S]$ . In this work, normalization of sensitivity coefficients was always performed with respect to the maximum species concentration  $[S]_{\max}$  over the entire reaction time, which provides coefficients relative to the starting point  $a_i = 1$ . Normalized sensitivity coefficients  $\sigma_i(S)$  are thus given by

$$\sigma_i(S) = \frac{a_i}{[S]_{\max}} \times \sigma_i(S)' = \frac{1}{[S]_{\max}} \times \frac{\partial[S]}{\partial \ln a_i} \quad (3.4)$$

By plotting  $\sigma_i(S)$  as functions of reaction time, high-impact reactions for the species of interest can be identified and appropriately considered in the kinetic analysis of measured profiles.

## FM Profiles

FM factors for quantitative analysis of detected species and spectral simulations were determined using the home-written *Fortran*-based simulation program *fmpromult*, which explicitly calculates absorption and dispersion contributions to  $\Delta f$  up to  $J_4(M)$  (see Eqs. 2.25 and 2.26). The program provides detection frequency-dependent  $\Delta f$  values from user-specified values for the modulation parameters  $\omega_m$ ,  $M$ , and  $\theta$  at given Gaussian, Lorentzian, or Voigt lineshapes. Calculations are performed either at constant Doppler and/or Lorentzian linewidths or at certain temperature and pressure values by using the molecular mass of the species as well as the pressure-broadening equation of the absorption line. Additionally, FM spectra can be simulated for several spectral lines with or without overlapping FM signals, potentially resulting in convoluted FM profiles (see Fig. 4.2d in Publication I).

## Allan Deviation

Sensitivity analysis based on Allan deviation was initially performed using an in-house *MATLAB* script, which calculates Allan deviation as function of the sampling interval time  $\tau$  for FM signal noise data recorded at constant sampling frequency  $f_s = 1/\tau_0$ . Allan deviation (ADEV) values in terms of  $I_{\text{FM}}$  were then converted into minimum detectable absorption  $A_{\min}(\tau)$ .

For Publications III–V, overlapping Allan deviation (OADEV) was used instead, since it provides better confidence levels of the results, especially at higher values for  $\tau$ . OADEV values were calculated with a *Python* script utilizing the *AllanTools* module [27]. As already mentioned in Section 2.3, since Allan analysis was initially developed to study the stability of atomic clocks, one distinguishes between "phase" data ( $x$ ) and "frequency" data ( $y$ ). Measured FM signal noise data was always supplied as "frequency" data to the Allan routines, since the FM signal intensity itself is the quantity of interest and not its time derivative.

## References

- [1] A. Yariv, P. Yeh in *Optical Waves in Crystals: Propagation and Control of Laser Radiation*, John Wiley & Sons, **1983**, Chapter 7 - Electro-Optics, 220 ff.
- [2] A. Yariv, P. Yeh in *Optical Waves in Crystals: Propagation and Control of Laser Radiation*, John Wiley & Sons, **1983**, Chapter 8 - Electro-optic Devices, 276 ff.
- [3] M. Bass in *Handbook of Optics. Vol. 2, Devices, Measurements, and Properties*. 2nd Edition, McGraw-Hill, **1995**, Chapter 13 - Electro-Optic Modulators.
- [4] P. Norton, HgCdTe infrared detectors, *Opto-Electron. Rev.* **2002**, 159–174.
- [5] A. Rogalski, HgCdTe infrared detector material: history, status and outlook, *Rep. Prog. Phys.* **2005**, *68*, 2267–2336, DOI [10.1088/0034-4885/68/10/R01](https://doi.org/10.1088/0034-4885/68/10/R01).
- [6] K. Bhaskaran, P. Roth, The shock tube as wave reactor for kinetic studies and material systems, *Prog. Energy Combust. Sci.* **2002**, *28*, 151–192, DOI [10.1016/S0360-1285\(01\)00011-9](https://doi.org/10.1016/S0360-1285(01)00011-9).
- [7] R. Hanson, D. Davidson, Recent advances in laser absorption and shock tube methods for studies of combustion chemistry, *Prog. Energy Combust. Sci.* **2014**, *44*, 103–114, DOI [10.1016/j.pecs.2014.05.001](https://doi.org/10.1016/j.pecs.2014.05.001).
- [8] M. Nishida in *Handbook of Shock Waves*, Academic Press, Burlington, **2001**, Chapter 4.1 - Shock Tubes, 553 ff. DOI [10.1016/B978-012086430-0/50012-9](https://doi.org/10.1016/B978-012086430-0/50012-9).
- [9] R. S. Tranter, P. T. Lynch, A miniature high repetition rate shock tube, *Rev. Sci. Instrum.* **2013**, *84*, 094102/1–11, DOI [10.1063/1.4820917](https://doi.org/10.1063/1.4820917).
- [10] A. Matsugi, A high-repetition-rate shock tube for transient absorption and laser-induced fluorescence studies of high-temperature chemical kinetics, *Rev. Sci. Instrum.* **2020**, *91*, 054101/1–9, DOI [10.1063/5.0007394](https://doi.org/10.1063/5.0007394).
- [11] G. Emanuel in *Handbook of Shock Waves*, Academic Press, Burlington, **2001**, Chapter 3.1 - Shock Waves in Gases, 185 ff. DOI [10.1016/B978-012086430-0/50005-1](https://doi.org/10.1016/B978-012086430-0/50005-1).
- [12] L. R. F. Henderson in *Handbook of Shock Waves*, Academic Press, Burlington, **2001**, Chapter 2 - General Laws for Propagation of Shock Waves Through Matter, 147 ff. DOI [10.1016/B978-012086430-0/50004-X](https://doi.org/10.1016/B978-012086430-0/50004-X).
- [13] M. Colberg, G. Friedrichs, Room temperature and shock tube study of the reaction  $\text{HCO} + \text{O}_2$  using the photolysis of glyoxal as an efficient HCO source, *J. Phys. Chem. A* **2006**, *110*, 160–170, DOI [10.1021/jp055168r](https://doi.org/10.1021/jp055168r).
- [14] G. Friedrichs, M. Colberg, J. Dammeier, T. Bentz, M. Olzmann, HCO formation in the thermal unimolecular decomposition of glyoxal: rotational and weak collision effects, *Phys. Chem. Chem. Phys.* **2008**, *10*, 6520–6533, DOI [10.1039/B809992H](https://doi.org/10.1039/B809992H).
- [15] J. Dammeier, N. Faßheber, G. Friedrichs, Direct measurements of the high temperature rate constants of the reactions  $\text{NCN} + \text{O}$ ,  $\text{NCN} + \text{NCN}$ , and  $\text{NCN} + \text{M}$ , *Phys. Chem. Chem. Phys.* **2012**, *14*, 1030–1037, DOI [10.1039/c1cp22123j](https://doi.org/10.1039/c1cp22123j).
- [16] N. Faßheber, J. Dammeier, G. Friedrichs, Direct measurements of the total rate constant of the reaction  $\text{NCN} + \text{H}$  and implications for the product branching ratio and the enthalpy of formation of NCN, *Phys. Chem. Chem. Phys.* **2014**, *16*, 11647–11657, DOI [10.1039/c4cp01107d](https://doi.org/10.1039/c4cp01107d).

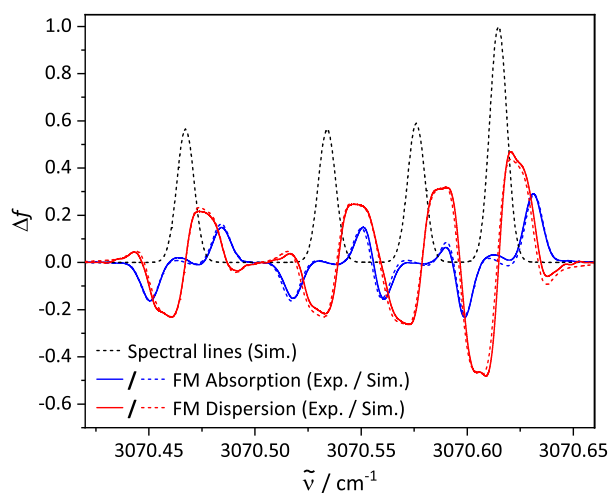
- 
- [17] S. Hesse, L. Nazari, G. Friedrichs, Investigation of the reactions  $\text{NCN} + \text{CH}_3$ ,  $\text{NCN} + \text{OH}$ , and  $\text{CH}_3 + \text{OH}$  behind shock waves, *Combust. Flame.* **2023**, 112646/1–14, DOI [10.1016/j.combustflame.2023.112646](https://doi.org/10.1016/j.combustflame.2023.112646).
- [18] N. Faßheber, M. C. Schmidt, G. Friedrichs, Quantitative HNO detection behind shock waves, *Proc. Combust. Inst.* **2017**, 36, 607–615, DOI [10.1016/j.proci.2016.05.035](https://doi.org/10.1016/j.proci.2016.05.035).
- [19] M. Colberg, PhD thesis, Christian-Albrechts-Universität zu Kiel, **2006**.
- [20] A. Gaydon, I. Hurle, *The Shock Tube in High-temperature Chemical Physics*, 1st Edition, Chapman and Hall, **1963**.
- [21] R. J. Kee, F. M. Ruply, J. A. Miller, Chemkin-II: A Fortran Chemical Kinetics Package for the Analysis of Gas-Phase Chemical Kinetics, tech. rep., Sandia National Laboratories, Livermore, California, Sandia Report SAND-89-8009, **1989**, DOI [10.2172/5681118](https://doi.org/10.2172/5681118).
- [22] E. Goos, A. Burcat, B. Ruscic, Extended Third Millenium Ideal Gas and Condensed Phase Thermochemical Database for Combustion with Updates from Active Thermochemical Tables, <http://burcat.technion.ac.il/dir>, **2009**.
- [23] B. Ruscic, R. E. Pinzon, G. von Laszewski, D. Kodeboyina, A. Burcat, D. Leahy, D. Montoy, A. F. Wagner, Active Thermochemical Tables: Thermochemistry for the 21st century, *J. Phys.: Conf. Ser.* **2005**, 16, 561–570, DOI [10.1088/1742-6596/16/1/078](https://doi.org/10.1088/1742-6596/16/1/078).
- [24] B. Ruscic, D. H. Bross, Active Thermochemical Tables (ATcT) enthalpies of formation values based on ver. 1.122r of the Thermochemical Network (2021), <https://atct.anl.gov/>, **2021**.
- [25] N. Lamoureux, P. Desgroux, M. Olzmann, G. Friedrichs, The story of NCN as a key species in prompt-NO formation, *Prog. Energ. Combust. Sci.* **2021**, 87, 100940/1–34, DOI [10.1016/j.pecs.2021.100940](https://doi.org/10.1016/j.pecs.2021.100940).
- [26] A. E. Lutz, R. J. Kee, J. A. Miller, SENKIN: A Fortran program for predicting homogeneous gas phase chemical kinetics with sensitivity analysis, Sandia National Laboratories, Livermore, California, Sandia Report SAND-87-8248, **1988**.
- [27] A. E. Wallin, D. Price, C. G. Carson, F. Meynadier, Y. Xie, E. Benkler, AllanTools 2019.9, <https://pypi.org/project/AllanTools/>, **2019**.

## CHAPTER 4

---

### Publication I: Single-Tone Mid-Infrared Frequency Modulation Spectroscopy for Sensitive Detection of Transient Species

---



Michael Stuhr<sup>a</sup>, Nancy Faßheber<sup>a</sup>, and Gernot Friedrichs<sup>a</sup>

<sup>a</sup>Institut für Physikalische Chemie, Christian-Albrechts-Universität zu Kiel, Max-Eyth-Straße 1, 24118 Kiel, Germany

*Opt. Express* **2019**, 27, 26499–26512, DOI [10.1364/oe.27.026499](https://doi.org/10.1364/oe.27.026499) (Editors' Pick).

Own Contributions:

- Prior to dissertation (M.Sc. thesis)
  - Initial setup of the single-tone MIR-FM spectrometer
  - FM spectra of CH<sub>4</sub> and FM detection of HCl
  - Preliminary data analysis
- During dissertation
  - Setup of scanning confocal interferometer
  - FM detection of OH radicals
  - Refined Allan sensitivity analysis
  - Final analysis and discussion of all data
  - Writing of paper draft



## Abstract

A single-tone mid-infrared frequency modulation (MIR-FM) spectrometer consisting of a cw-OPO-based laser system, a 500 MHz LiTaO<sub>3</sub> electro-optical modulator (EOM), and a high-bandwidth GaAs mid-infrared detector has been developed. In order to assess the instrument's sensitivity and time resolution, FM spectra of selected CH<sub>4</sub> transitions around 3070 cm<sup>-1</sup> were measured and the reaction Cl + CH<sub>4</sub> following the 193 nm excimer laser photolysis of oxalyl chloride was investigated by recording concentration-time profiles of HCl at 2925.90 cm<sup>-1</sup> in a low-pressure slow-flow reactor. Furthermore, OH radicals were generated by UV photolysis of H<sub>2</sub>O<sub>2</sub> and its transients were recorded at 3447.27 cm<sup>-1</sup>. The minimal detectable absorption of the spectrometer was determined to be  $A_{\min} = 4 \cdot 10^{-4}$  ( $\Delta f_{\text{BW}} = 1$  MHz,  $\tilde{\nu} = 3447$  cm<sup>-1</sup>) by using the Allan approach. Mainly due to thermal noise contributions of the easy-to-saturate photodetector, the detection limit is about a factor of 4 above the shot-noise limit. To the best of our knowledge, this work reports the first implementation of a single-tone MIR-FM spectrometer based on an external EOM modulation scheme and its use for the detection of transient molecular species.

## 4.1 Introduction

Since its first description by Bjorklund in 1980, laser-based frequency modulation spectroscopy (FMS) has proven to be a powerful tool for the detection of molecular species in both spectroscopic and reaction kinetics studies [1, 2]. FM techniques combine sub-microsecond time resolution with shot-noise limited sensitivity and are therefore particularly suitable for investigating short-lived species in the gas phase. In contrast to conventional absorption-based methods, FM spectroscopy is a derivative technique that is based on unequal absorption or dispersion of the sidebands in the frequency-modulated spectrum of the detection laser. In theory, intensity fluctuations of the light source and other forms of sideband-balanced effects such as broadband background absorption do not yield FM signal. An impressive example highlighting the combined advantages of the FM detection approach has been reported by Crofton and Peterson [3]. They were able to detect transient SiH<sub>2</sub> radicals (i.e., weak absorptions of a short-lived species) during the formation of particles (i.e., strong interfering and time-dependent background absorption) in a shock tube experiment (i.e., an experimental setup known to be prone to acoustic noise contributions).

Earlier, Sears and coworkers demonstrated the high sensitivity and high time resolution of FM spectroscopy for the detection of NH<sub>2</sub> and HCCl radicals in supersonic jets [4] and CN radicals in a low-pressure flow reactor [5]. Very recently, they used an FM detection scheme for detecting OH radicals in the near-infrared in a kinetic experiment [6]. Another example exploiting the excellent temporal response of FM spectroscopy is a study by Alagappan et al. [7], who investigated the collision dynamics of CN radicals with a time resolution of about 20 ns applying a 400 MHz modulation scheme.

The research groups of Wagner and Hanson pioneered the use of FM spectroscopy as a detection technique for shock tube studies. Such high-temperature studies are especially demanding with respect to quantitative determination of reactant concentrations, which are often in the range



of a few ppm that need to be detected with microsecond time resolution under harsh conditions (e.g., beam steering and pressure-induced birefringence in shock tube windows) in a real-time single-shot experiment [8–10]. Among the first species investigated with FM spectroscopy in shock tube experiments were  $\text{NH}_2$ ,  $^1\text{CH}_2$ , and  $\text{HCO}$  [11–14], more recently  $\text{HNO}$  has been detected as well [10].

So far, FM-based applications have mostly been limited to the visible and NIR regions, with more recent advances into the UV and VUV [15, 16]. The expansion of FM spectroscopy into the mid-infrared (MIR) region promises new detection options for many molecular species. Instead of relying on often weak absorption lines of overtone or combination bands observed in the NIR, detection on stronger fundamental rovibrational transitions in the MIR offers an increase in sensitivity. Our own interest lies in detection schemes for  $\text{HO}_2$ ,  $\text{CH}_3$ , and  $\text{HCN}$ . However, the limited bandwidth of MIR detectors and the low modulation efficiency of electro-optical modulators in the MIR (i.e., the high half-wave voltage, which is proportional to the detection wavelength) have made the widespread use of MIR-FM spectroscopy with external modulation largely unfeasible as yet. Moreover, the availability of reliable and robust cw-MIR laser sources was limited for a long time. Today, quantum cascade lasers (QCLs) and systems based on either difference frequency generation (DFG) or optical parametric oscillators (OPOs) are the most common MIR-light sources. Yet, there is a number of studies reporting the implementation of MIR-FM spectroscopy with approaches involving both external and direct modulation.

In the late nineties, Taatjes and coworkers introduced MIR-FM spectroscopy with external modulation for the detection of  $\text{HCl}$  in kinetic studies that were concerned with H-abstraction reactions [17, 18]. The low bandwidth of mid-infrared detectors available at the time required them to use the two-tone FM approach [19, 20], which limits the maximum achievable sensitivity [21] and makes quantitative measurements more difficult. In 2006, Borri et al. reported the implementation of single-tone MIR-FM spectroscopy with a current-modulated quantum cascade laser [22]. Shortly afterwards, Maddaloni et al. described a two-tone FM spectrometer based on DFG with a modulated diode laser achieving a signal-to-noise ratio improvement by a factor of 100 compared with the direct absorption setup [23]. Similarly, Lindsay et al. demonstrated a single-tone MIR-FM application by recording FM spectra of  $\text{CH}_4$  at  $3175\text{ cm}^{-1}$  using a cw-OPO-based laser system directly modulated with 153 MHz [24]. All three approaches employ direct modulation of the light source, resulting in undesirable amplitude modulation (AM) and reduced sensitivity. Chen et al. introduced the concept of modulating the frequency of a cw-quantum cascade laser by illuminating the front facet with 100 fs Ti:sapphire laser pulses, which also caused high levels of amplitude modulation [25]. This issue was later addressed by both all-optical and advanced electronic control schemes for AM suppression [26, 27], which holds the potential for future QCL-based FM spectroscopic applications.

Highly efficient electro-optical modulators with high-Q resonators, suitable for external modulation of MIR laser beams with sufficient modulation depth, have recently become commercially available. In addition, fast MIR detectors with up to 1 GHz bandwidth have entered the market, which enables the practical realization of single-tone MIR-FM spectroscopy. This work presents

the first measurements conducted with a newly established single-tone MIR-FM spectrometer taking advantage of external EOM modulation at 500 MHz. The results include FM spectra of CH<sub>4</sub> and concentration-time profiles of the stable species HCl and transient OH radicals. A sensitivity analysis of the detection scheme based on Allan variance was performed.

## 4.2 Theoretical Background

A brief outline of the principle behind FM spectroscopic methods is given here, whereas more detailed theoretical descriptions can be found elsewhere [1, 2, 21]. Frequency modulation of a monochromatic laser beam with the modulation frequency  $f_m$  leads to the emergence of discrete sidebands around the carrier frequency  $f_c$  (see upper part of Fig. 4.1), where the modulation index  $M$  is a measure for the modulation depth that determines the relative intensities of the carrier and the sidebands.  $M$  is defined as the ratio of the maximum induced frequency deviation to the modulation frequency  $f_m$ . The modulation of the laser frequency can be achieved either by direct modulation of the light source or by external modulation using an electro-optical modulator.

If a frequency-modulated beam passes through a sample that causes unequal absorption or dispersion of the opposing sidebands, an amplitude modulation of the electric field oscillating at the frequency  $f_m$  is induced. More generally, the effect of absorption and dispersion on the electric field is described by applying the complex transmission function  $T_n(\omega) = \exp(-\delta_n - i\phi_n)$  to the electric field, with  $\delta_n$  and  $\phi_n$  as the electric field coefficients for absorption and dispersion of the  $n$ th-order sideband, respectively. Using the angular frequencies  $\omega_c = 2\pi f_c$  and  $\omega_m = 2\pi f_m$ , the electric field  $E_T(t)$  of the transmitted amplitude-modulated light can be written as

$$E_T(t) = E_0 \exp(i\omega_c t) \sum_{n=-\infty}^{+\infty} T_n(\omega) J_n(M) \exp(in\omega_m t) \quad (4.1)$$

where  $J_n(M)$  is the  $n$ th-order Bessel function with the modulation index  $M$  as argument. At low modulation depths ( $M \ll 1$ ), only the first-order sidebands at  $f_c - f_m$  and  $f_c + f_m$  need to be considered ( $J_0 \approx 1$ ,  $J_{\pm 1} \approx \pm M/2$ ,  $J_{|n|>1} \approx 0$ ). The intensity of the transmitted light  $I_T(t)$  is proportional to the square modulus of the transmitted electric field  $E_T(t)$ . An expansion of  $|E_T(t)|^2$  yields a DC and an AC term, with the latter arising from the amplitude modulation induced by absorption or dispersion from interaction with the sample. After detection with a photodiode, the AC component can be converted to a low-bandwidth FM signal  $I_{\text{FM}}$  using a phase-sensitive demodulation scheme at  $f_m$ , resulting in the FM signal

$$I_{\text{FM}} = I_0 \cdot \Delta f \cdot \delta_c \cdot G = \frac{I_0}{2} \cdot \Delta f \cdot \alpha_c \cdot l \cdot G \quad (4.2)$$

where  $I_0 \propto E_0^2 \exp(-\delta_0) \approx E_0^2$  is the DC signal intensity,  $\Delta f$  the dimensionless FM factor at the given wavelength,  $l$  the absorption path length, and  $G$  the total gain of the demodulation circuit.  $\delta_c$  corresponds to a reference electric field attenuation coefficient, typically the line center attenuation of the absorption feature, with a narrow-band absorption coefficient  $\alpha_c = 2\delta_c/l$ . The

FM factor  $\Delta f$  is a function of  $f_m$ , the modulation index  $M$ , the phase angle of demodulation  $\theta$ , and the lineshape of the absorption feature.  $\Delta f$  can be understood as the ratio of differential sideband attenuation to carrier attenuation and is defined as

$$\Delta f = [A_{AC} \cos(\theta) + D_{AC} \sin(\theta)]/\delta_c \quad (4.3)$$

where  $A_{AC}$  and  $D_{AC}$  are the respective contributions from absorption and dispersion to the demodulated AC signal. In the limiting case of low modulation depth ( $M \ll 1$ ), where only the first-order sidebands are relevant,  $\Delta f$  is well below one. Assuming weak absorption and dispersion (i.e.,  $|\delta_0 - \delta_1| \ll 1$ ,  $|\phi_0 - \phi_1| \ll 1$ , etc.), the following approximations regarding  $A_{AC}$  and  $D_{AC}$  hold:

$$A_{AC} \approx M \cdot (\delta_{-1} - \delta_{+1}) \quad (4.4)$$

$$D_{AC} \approx M \cdot (\phi_{+1} - 2\phi_0 + \phi_{-1}) \quad (4.5)$$

Equations (4.4) and (4.5) reveal the derivative nature of FM spectroscopy. Equal absorption or dispersion of the different first-order frequency components of the FM beam do not yield an FM signal  $I_{FM}$ , hence demonstrating the immunity of FMS to broadband background absorption or dispersion.

For experiments at higher modulation depth ( $M \geq 0.5$ ) as performed in this work, signal contributions from higher order sidebands need to be taken into account by explicit summation over Bessel function-weighted terms resulting from the square modulus of Eq. (4.1) [2]. As it is the case for other narrow-bandwidth absorption methods as well, the lineshape needs to be known for quantitative detection. When  $M$ ,  $f_m$ ,  $G$ , and  $\theta$  are given, the wavelength dependent FM factor  $\Delta f$  can be calculated by rigorous treatment of the transmitted electric field  $E_T(t)$  according to Eq. (4.1). Conversely, the lineshape of the absorbing species can be recovered from an experimental FM spectrum [2, 28, 29].

The FM approach transfers absorption and dispersion information to a high frequency, which leads to a significant reduction of  $1/f$  noise and other forms of low-frequency noise. In principle, FM spectroscopic methods can accomplish shot-noise limited detection even on short timescales. In practice, however, the shot-noise limit is often not reached due to residual amplitude modulation (RAM). Generally, all contributions to amplitude modulation that do not stem from absorption or dispersion induced by the sample are referred to as RAM. Etalon effects, photorefractive scattering, and the mismatch of the polarization axes due to temperature fluctuations in the modulator crystal are the main factors contributing to RAM noise in applications with external frequency modulation [30]. Possible strategies for reducing RAM include tilting the EOM relative to the beam path, photorefractive erasure techniques, and active thermal stabilization of the modulator [31–33].

### 4.3 Experimental

Figure 4.1 shows a schematic of the experimental setup. Standard electronic radio frequency (RF) components (Mini Circuits) have been used in the modulation-demodulation circuitry. A combination of a fiber-coupled DFB pump laser (Koheras AdjustiK Y10 PM, NKT Photonics, 15 mW), an Yb-doped fiber amplifier (YAR-10K-1064-LP-SF, IPG Photonics, 10 W), and a continuous-wave optical parametric oscillator (cw-OPO, Argos SF-10, Lockheed Martin, modules B and C, >1.2 W idler power) was used as the narrow-bandwidth light source (<60 kHz linewidth). Only the idler output beam of the OPO module was used for detection and its wavelength was monitored with a wavemeter (Model 621, Bristol Instruments). For kinetic measurements, the frequency of the detection laser was kept fixed, shifted by  $f_m = 500$  MHz relative to the center of the respective absorption line in order to maximize the FM factor  $\Delta f$ . Spectral measurements were performed by applying a triangle-shaped voltage profile to the piezoelectric element in the pump laser that controls the emission wavelength.

A resonant LiTaO<sub>3</sub> electro-optical modulator (EO-T500T3-MIR, Qubig) was used for the modulation of the detection beam with  $f_m = 500$  MHz. According to the specified half-wave voltage of about 40 V/rad at  $\lambda = 4.5 \mu\text{m}$ , a modulation index of  $M \approx 0.5$  should be achievable at the maximum RF power rating of  $P_{\text{max}} = 5$  W. Since scanning etalons for the mid-infrared are not readily commercially available, the modulation index was initially estimated from the ratio of the first and second-order peaks in FM spectra measured at the highest RF power on the modulator. Later, a newly established self-made scanning etalon with custom-coated YAG mirrors ( $R \approx 98.5\%$ ,  $2500 \text{ cm}^{-1} \leq \tilde{\nu} \leq 5000 \text{ cm}^{-1}$ , Layertec) and a piezo actuator (P-401-10, piezosystem

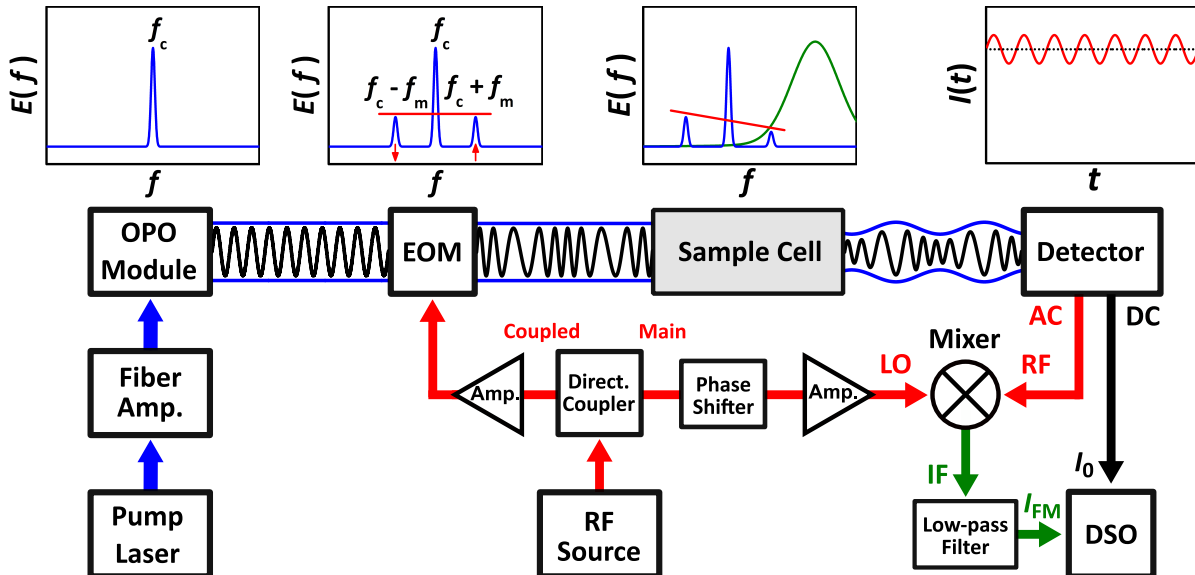


**Figure 4.1:** Schematic of the MIR-FM setup. OPO: optical parametric oscillator; EOM: electro-optical modulator; AC/DC: alternating/direct current; RF: radio frequency; LO: local oscillator; IF: intermediate frequency; DSO: digital storage oscilloscope.

jena) was used. Two YVO<sub>4</sub> polarizers, one in front of the EOM and one behind it, ensured that the beam polarization matched the required input polarization of the EOM and that the absolute phase angle was set to pure absorption ( $\theta = 0^\circ$  or  $180^\circ$ ; for details on the issue of setting the demodulation phase angle we refer to [13]).

The output of an RF source (Signal Generator 2023, Marconi Instruments) was split by a directional coupler (ZFDC-10-5-S+) and the resulting coupled and main signals were guided to the modulation line and the demodulation circuit, respectively. To set the power on the EOM and the local oscillator line of the demodulation circuit to appropriate levels, the RF source output power was adjusted and a set of attenuators (SAT series) as well as two amplifiers (ZHL-20W-13+, ZRI-700+) were used. After passing through an absorbing gas sample, the amplitude-modulated detection beam was focused onto a two-stage thermoelectrically cooled high-bandwidth GaAs detector (PVI-2TE-5, Vigo System) offering a fast time response ( $t_r \leq 0.7$  ns) and high detectivity ( $D_{\text{opt}}^* \geq 6 \cdot 10^{10}$  cm Hz<sup>1/2</sup> W<sup>-1</sup>). Within the detector module, the measured signal was pre-amplified and split into its AC and DC components with a bias tee. The AC signal was demodulated using a frequency mixer (ZFM-2000+), a phase shifter (JSPHS-661+), and a low-pass filter (SLP-1.9), after which the resulting FM signal was amplified and low-pass filtered to 1 MHz bandwidth using an additional amplifier (Model SR560, Stanford Research Systems). Both the FM signal and the DC signal were recorded with a digital storage oscilloscope (MSO 8104A, Agilent Technologies). The gain factor of the demodulation circuit  $G$  was determined by comparing the FM signal with the conventional absorption signal of a CH<sub>4</sub> sample measured at a known FM factor (see Eq. (4.2)), which yielded a value consistent with the total gain of the components in the demodulation circuit specified by the manufacturers.

All spectroscopic and kinetic experiments were conducted at room temperature in a 42 cm (CH<sub>4</sub> and HCl detection) or 18.5 cm (OH detection) long slow-flow gas cell equipped with quartz windows. An ArF excimer laser (RD-EXC-200, Radiant Dyes) was used as photolysis light source for the generation of Cl atoms and OH radicals by 193 nm photolysis of oxalyl chloride, (COCl)<sub>2</sub>, and H<sub>2</sub>O<sub>2</sub>, respectively. The output beam of the excimer laser was overlapped with and divided from the collinear detection laser beam using two dichroic mirrors, resulting in pulse energies of 20 – 39 mJ/pulse in the reactor. The chemicals used for the measurements were pure CH<sub>4</sub> (Air Liquide, 99.5%) and freshly distilled oxalyl chloride (Sigma-Aldrich, > 99%) in argon (Air Liquide, 99.999%). Gas mixtures of about 1% H<sub>2</sub>O<sub>2</sub> in argon were prepared by passing the carrier gas through a heated trap filled with solid adduct of H<sub>2</sub>O<sub>2</sub> and urea (Sigma-Aldrich, 97%) at a gas flow rate of 4 sccm,  $T = 50^\circ\text{C}$ , and  $p \leq 8.6$  mbar [34].

## 4.4 Results

In order to demonstrate the capabilities of the newly established MIR-FM spectrometer, we recorded (i) FM spectra of CH<sub>4</sub> at different modulation indices, (ii) time profiles of HCl formed by the reaction Cl + CH<sub>4</sub> following UV photolysis of oxalyl chloride, and (iii) OH transients produced by UV photolysis of H<sub>2</sub>O<sub>2</sub>. Moreover, in order to assess the sensitivity of the setup and

to reveal dominating noise sources, an Allan deviation analysis was conducted using FM signal noise recorded at different light power levels on the photodetector.

### Spectroscopic examples

Figure 4.2(b) shows FM spectra of the weak and spectroscopically isolated  $0200\ 1E \leftarrow 0000\ 1A_1$  transition of  $\text{CH}_4$  at  $\tilde{\nu}_0 = 3071.39\ \text{cm}^{-1}$  [35]. The individual spectra have been recorded with different modulation depths ( $0.20 < M < 0.69$ ) and the demodulation phase set to pure absorption. The scan rate and the number of scans used for averaging were  $0.77\ \text{cm}^{-1}\text{s}^{-1}$  and 16, respectively. For comparison, the directly measured absorption line, corresponding to a peak absorption of  $A_c = 3.9 \cdot 10^{-2}$ , is included in Fig. 4.2(b) as a black curve. A typical etalon trace of the frequency-modulated light at  $M = 0.60$  is shown in Fig. 4.2(a). Here, the vertical bars represent the exact positions of the carrier and sideband frequencies, which are not fully resolved by the scanning etalon setup. Note that the spectra in Fig. 4.2(b) have already been baseline corrected using previously recorded baseline signals. This was necessary due to recurrent undulations of the FM signal during wavelength scans, which we mostly attribute to minor polarization instabilities of the OPO laser system. An example trace of an uncorrected signal is shown in Fig. 4.2(c). Pronounced baseline effects only occurred when the detection laser wavelength was scanned, while for constant wavelengths the FM signal background exhibited only minor long-term drifts.

After baseline correction, high-quality derivative-like signals have been observed. Actually, as the high modulation frequency of 500 MHz already exceeded the width of the  $\text{CH}_4$  absorption line ( $\Delta\nu_{\text{HWHM}} = 140\ \text{MHz}$ ), instead of resembling a simple first derivative lineshape, the absorption peak is reproduced twice with positive and negative maxima at  $|\nu - \nu_0| \approx f_m = 500\ \text{MHz}$ . It is well-known from the literature [2, 21] and also directly follows from Eq. (4.4) that for  $f_m/\Delta\nu_{\text{HWHM}} > 1$  the FM signal originates from the direct interaction of a single sideband with the absorption feature, where the different signs of the signal reflect the relative phases of the opposing sidebands. For the experiment at the highest modulation index of  $M = 0.69$  in Fig. 4.2(b), a second-order peak at  $|\nu - \nu_0| \approx 1\ \text{GHz}$  emerges due to interaction of the second-order sideband with the spectral line.

More complicated FM spectra arise for the case of closely spaced absorption lines causing partial overlap of the corresponding FM signal contributions. An illustrative example with four  $\text{CH}_4$  absorption lines between  $3070.42\ \text{cm}^{-1}$  and  $3070.66\ \text{cm}^{-1}$  is shown in Fig. 4.2(d). The 16 times averaged FM spectra have been recorded with a scan rate of  $1.10\ \text{cm}^{-1}\text{s}^{-1}$  at a total pressure of  $p = 2.0\ \text{mbar}$  and a modulation index of  $M = 0.32$  by setting the demodulation phase angle  $\theta$  to either absorption (solid blue curve) or dispersion (solid red curve). Simulations of the absorption and dispersion FM spectra (dashed colored curves) based on Eqs. (4.2) and (4.3) as well as the conventional absorption spectrum (dashed black curve) were added for comparison. Apart from minor deviations, most notably around  $3070.63\ \text{cm}^{-1}$ , which can be attributed to small baseline issues and uncertainties of  $\theta$  and  $M$ , the simulated FM spectra are in excellent agreement with the experimental ones, demonstrating the reliable acquisition of FM spectra.

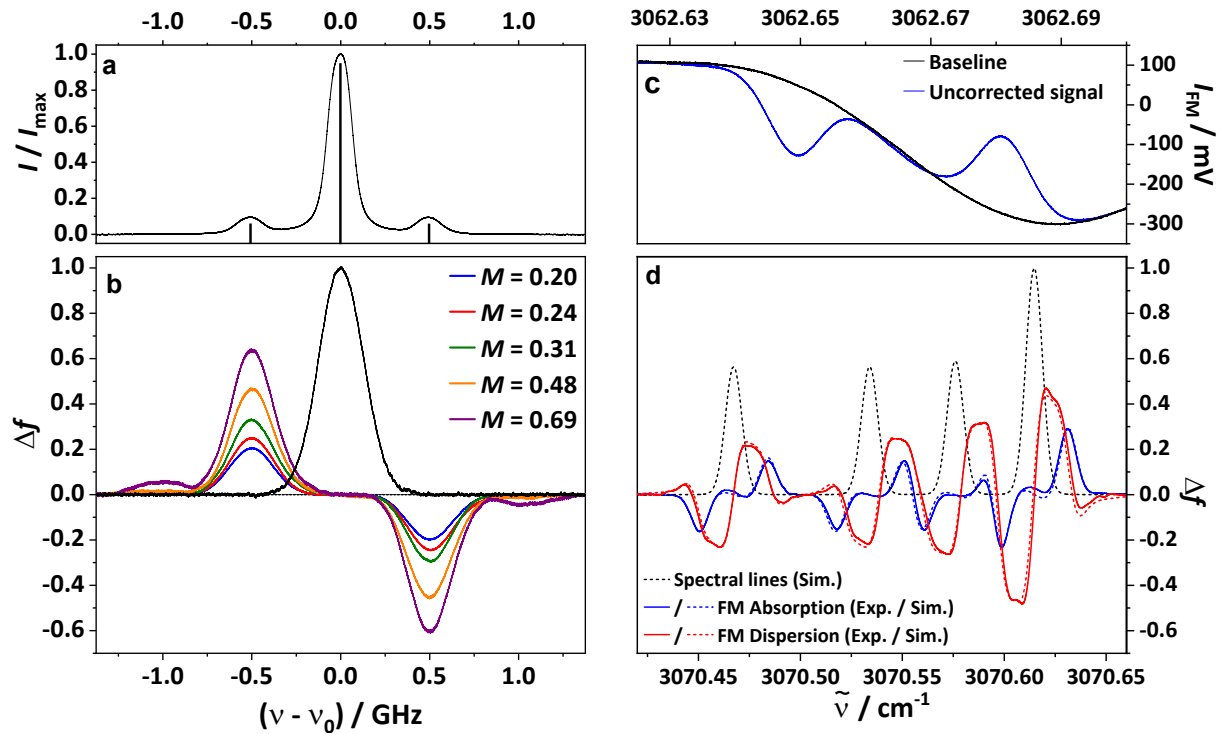
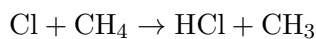


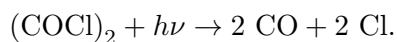
**Figure 4.2:** (a) Frequency spectrum of the modulated light at  $M = 0.60$ . (b) FM spectra of  $\text{CH}_4$  at different modulation indices and corresponding absorption spectra in units of the FM factor  $\Delta f$  ( $p = 1.5 \text{ mbar}$ ,  $\theta = 180^\circ$ ,  $\tilde{\nu}_0 = 3071.39 \text{ cm}^{-1}$ ,  $A_c = 3.9 \cdot 10^{-2}$ ). (c) Typical uncorrected FM signal (blue curve) and corresponding baseline (black curve). (d) Experimental (solid curves) and simulated (dashed curves) FM spectra of four closely spaced  $\text{CH}_4$  lines ( $p = 2.0 \text{ mbar}$ ,  $M = 0.32$ ,  $A_c = 5.2 \cdot 10^{-2}$  for the highest peak) as well as simulated direct absorption spectrum (dashed black curve).

## Reaction kinetics examples

Practical use of the new MIR-FM detection scheme for reaction kinetics studies has been demonstrated by the detection of a stable reaction product as well as a reactive transient radical. The formation of  $\text{HCl}$  from the reaction



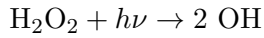
was observed on the R(1) line of its fundamental vibrational transition at  $2925.90 \text{ cm}^{-1}$ . Mixtures of 0.11% oxalyl chloride and varying mole fractions of  $\text{CH}_4$  in argon were passed through the sample cell at total pressures of  $8.6 \text{ mbar} \leq p \leq 31.0 \text{ mbar}$ . 193 nm photolysis of oxalyl chloride served as a source of  $\text{Cl}$  atoms [36] according to



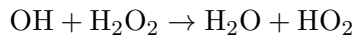
$\text{OH}$  radical transients have been detected at  $3447.27 \text{ cm}^{-1}$  on the P(3.5)e line of the fundamental vibrational transition from the  $X^2\Pi_{3/2}$  ground state [35]. Excimer laser photolysis of  $\sim 1\%$   $\text{H}_2\text{O}_2$



diluted in argon directly yields OH radicals with a quantum yield of  $\phi = 0.85$  [37].



A minor photodissociation channel also yields  $\text{H} + \text{HO}_2$  with a quantum yield of 0.15. Under the applied reaction conditions, generated OH radicals mainly react with excess  $\text{H}_2\text{O}_2$  according to the reaction



and, to a minor degree, undergo recombination. Representative examples for HCl and OH detection are shown in Figs. 4.3(a) and 4.3(b). Absorption cross sections for the conversion of the FM signals into absorption were adopted from the HITRAN database for both species [35]. High quality concentration-time profiles have been obtained, where both signal traces represent single-shot experiments with the electronic bandwidth set to  $\Delta f_{\text{BW}} = 1$  MHz. A moderate 10 point moving average was applied to the OH profile to further improve the signal-to-noise ratio.

Following photolysis at  $t = 0$ , Fig. 4.3(a) reveals the direct formation of HCl from the reaction  $\text{Cl} + \text{CH}_4$ . The small and short negative signal occurring over an interval of about  $1.5 \mu\text{s}$  is a typical measurement artifact caused by the intense excimer laser pulse. The inset in Fig. 4.3(a) highlights the noise level of the recorded profile, which is well below  $1 \cdot 10^{-3}$  for this experiment. The experimental data can be nicely represented by first-order kinetics (red curve in Fig. 4.3(a)), indicating pseudo-first order reaction conditions for the reaction  $\text{Cl} + \text{CH}_4$ . A kinetic pseudo-first order analysis of the experiments performed at varying mole fractions of the excess species

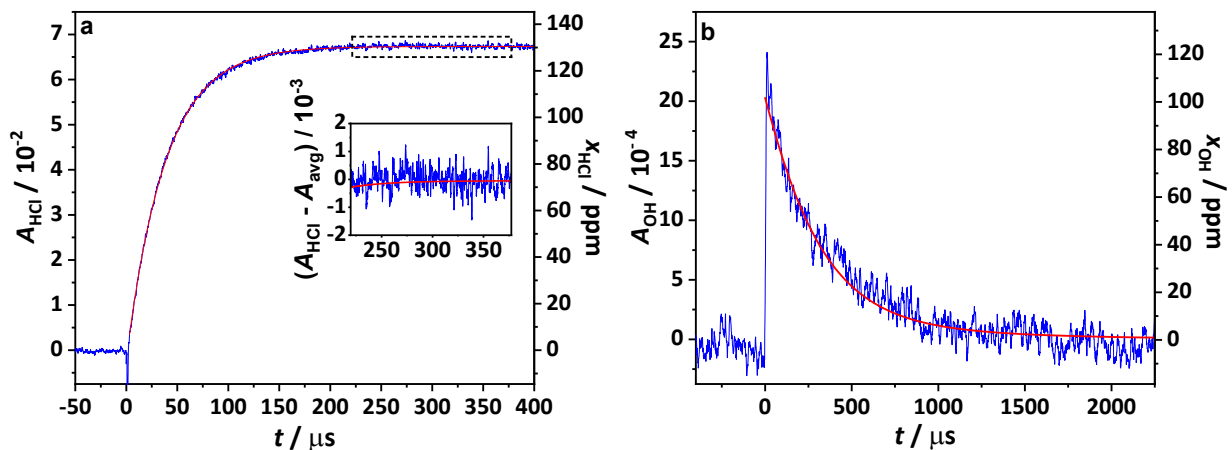


**Figure 4.3:** (a) HCl profile (blue curve) and single exponential fit (red curve) in units of absorbance and mole fraction at  $2925.90 \text{ cm}^{-1}$  ( $M = 0.48$ ,  $\Delta f_{\text{max}} = 0.45$ ,  $p = 31.0 \text{ mbar}$ ,  $\Delta f_{\text{BW}} = 1 \text{ MHz}$ ,  $P_0 = 0.6 \text{ mW}$ ). The inset shows the noise level on the recorded signal. (b) OH profile (blue curve) in units of absorbance and mole fraction at  $3447.90 \text{ cm}^{-1}$  ( $M = 0.48$ ,  $\Delta f_{\text{max}} = 0.45$ ,  $p = 8.6 \text{ mbar}$ ,  $\Delta f_{\text{BW}} = 1 \text{ MHz}$ , 10 point moving average,  $P_0 = 1.0 \text{ mW}$ ) and kinetic simulation (red curve) of the experimental profile based on rate constants adopted from Atkinson et al. [37] and Baulch et al. [38].



$\text{CH}_4$  yielded the expected linear trend and a bimolecular rate constant  $k_{\text{exp}} = (1.07 \pm 0.02) \cdot 10^{-13} \text{ cm}^3 \text{ molec}^{-1} \text{ s}^{-1}$ , which is in quantitative agreement with the recommended literature value of  $k_{\text{lit}} = (1.0 \pm 0.1) \cdot 10^{-13} \text{ cm}^3 \text{ molec}^{-1} \text{ s}^{-1}$  [39].

Figure 4.3(b) shows a typical kinetic profile of the transient OH radical. Following fast formation of OH from photodissociation of  $\text{H}_2\text{O}_2$ , the OH radical decay takes place on a timescale of several hundred microseconds. Next to loss of OH from the reaction  $\text{OH} + \text{H}_2\text{O}_2$ , a full kinetic analysis has to account for other reactions such as  $\text{OH} + \text{HO}_2$  as well. A numerical simulation of the profile (red curve in Fig. 4.3(b)) is in full agreement with the experimental trace. From the  $1\sigma$  standard deviation of the noise, one can estimate a minimum detectable single-shot absorbance of  $A_{\text{min}} = 1 \cdot 10^{-4}$  ( $\Delta f_{\text{BW}} = 1 \text{ MHz}$ , 10 point moving average). Based on the known absorption cross section of  $\sigma_{\text{OH}} = 5.2 \cdot 10^{-18} \text{ cm}^2 \text{ molec}^{-1}$  ( $T = 298 \text{ K}$ ,  $p = 8.6 \text{ mbar}$ ) [35], this yields a OH radical detection limit of  $\sim 4 \text{ ppm}$  for the specified conditions. Of course, the detection limit could be further improved to sub-ppm levels by signal-averaging procedures. Note that the OH detection presented in this work serves as an illustrative example for the detection of a transient species. In case of OH, due to more than two orders of magnitude higher absorption cross sections of its rovibrational  $A^2\Sigma^+ - X^2\Pi$  transitions at wavelengths around 308 nm, the detection limit achieved by sensitive UV laser absorption methods is even in the ppb range [15, 40].

### Allan sensitivity analysis

In this work, the preferred measure of sensitivity is the Allan deviation of the FM signal expressed in units of absorbance. Allan deviation is based on the two-sample variance of adjacent intervals of averaged data and was originally developed in order to investigate the frequency fluctuations of atomic clocks [41, 42].

Consider a data set of an arbitrary quantity  $y$  consisting of  $N$  data points measured with a sampling frequency  $f_s$ , so that individual points of data are evenly spaced by the time  $\tau_s = 1/f_s$  without any dead time. One can divide the data into  $K$  intervals of adjacent points, with  $k = N/K$  as the number of points in each interval and  $\tau = k \cdot \tau_s$  as the corresponding interval time period. The difference between the average  $\bar{y}_i$  for the  $i$ th interval and the average  $\bar{y}_{i+1}$  for the next interval is dependent on the selected averaging period  $\tau$  as well as the noise level affecting the quantity  $y$ . The Allan variance  $\sigma_A^2(\tau)$  is defined as the expectation value of the infinite time average of the sample variance regarding two adjacent intervals for a given value of  $\tau$ :

$$\langle \sigma_A^2(\tau) \rangle = \left\langle \frac{(\bar{y}_i - \bar{y}_{i+1})^2}{2} \right\rangle \quad (4.6)$$

Since any set of measured data is finite, an estimate for the Allan variance is used:

$$\sigma_A^2(\tau) = \frac{1}{2(K-1)} \sum_{i=0}^{K-1} (\bar{y}_i - \bar{y}_{i+1})^2 \quad (4.7)$$

The Allan deviation  $\sigma_A$  calculated from Eq. (4.7) with noise as input data can serve as the minimal

detectable signal of a detection system, corresponding to a signal-to-noise ratio of  $\text{SNR} = 1$ . As the Allan deviation is a measure for the signal difference between adjacent averaged intervals rather than the for the average deviation from the global mean, by determining  $\sigma_A$  at different averaging periods  $\tau$ , the Allan approach reveals the frequency range of present noise components. Hence, a sensitivity analysis in terms of Allan deviation is a convenient way to determine the minimal detectable signal as a function of the targeted effective time resolution.

An example of FM signal noise recorded at  $3071 \text{ cm}^{-1}$ , preamplified with  $\Delta f_{\text{BW}} = 1 \text{ MHz}$  (corresponding to a 10%-to-90% rise time of  $0.35 \mu\text{s}$ ), and sampled with the oscilloscope in intervals of  $\tau_s = 1 \mu\text{s}$  is shown in Fig. 4.4(a). Note that the signal is displayed on five different timescales to better illustrate the frequency dependence of the noise, where the individual segments of the signal noise with  $n > 0$  were offset from the zero line for better visualization.

On a small timescale ( $n \geq 3$ ), the signal noise appears to be statistical white noise, whereas on longer timescales ( $n \leq 1$ ) low-frequency signal undulations occur. The corresponding Allan plot in Fig. 4.4(b) shows a linear decrease of the Allan deviation  $\sigma_A$  with  $\sqrt{\tau}$  up to averaging periods of about  $40 \mu\text{s}$ , which is the expected  $\tau$ -dependence for white noise. For longer averaging periods  $\sigma_A$  starts to increase, with a maximum in the millisecond range. Since the noise on this timescale was very sensitive to tilting of the EOM relative to the beam path, it can most likely be attributed to RAM noise contributions. In contrast, we attribute the small shoulder at  $\tau \approx 10^{-4} \text{ s}$  to parasitic noise from the detection electronics.

Figure 4.5(a) shows the results of another typical Allan analysis of FM signal noise measured at  $\tilde{\nu} = 3447 \text{ cm}^{-1}$  with  $M = 0.48$  at four different light power levels  $P_0$ . Here, the Allan deviation is expressed in units of absorption, where the  $\tau$ -dependent Allan deviation in units of voltage was converted to the Allan deviation in terms of FM-equivalent absorption using Eq. (4.2). Overall, the Allan deviation decreases with increasing  $P_0$  and, for small values of  $\tau$ , decreases linearly with

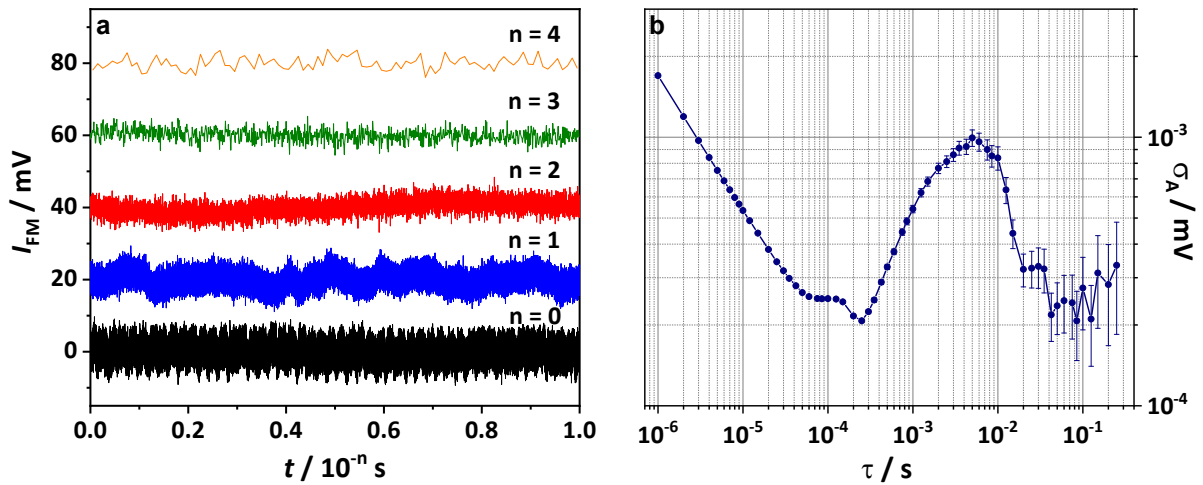


**Figure 4.4:** (a) Measured FM signal noise on five different timescales ( $M = 0.20$ ,  $P_0 = 480 \mu\text{W}$ ,  $\tilde{\nu} = 3071 \text{ cm}^{-1}$ ). The individual segments of FM noise were offset with 20 mV relative to each other for better visualization. (b) Corresponding Allan plot regarding  $I_{\text{FM}}$  with estimated errors.

increasing  $\sqrt{\tau}$ , although there is a slight curvature in all four Allan plots below  $10 \mu\text{s}$ . For the detection of transient species with  $\tau = 1 \mu\text{s}$  and at the highest value of  $P_0$ , the minimal detectable absorption is  $A_{\min} = 4 \cdot 10^{-4}$ . This is considerably lower than for conventional absorption-based techniques with dual-beam setups and multi-pass cells, which are limited to a noise-equivalent absorption of  $\sim 5 \cdot 10^{-6} \text{ Hz}^{-0.5}$  under ideal conditions, corresponding to a minimal detectable absorption of  $\sim 5 \cdot 10^{-3}$  at a comparable detection bandwidth of  $\Delta f_{\text{BW}} = 1 \text{ MHz}$  [43, 44]. More advanced methods using direct modulation schemes such as  $2f$  wavelength modulation absorption spectroscopy with DFG [45, 46] and interband cascade lasers [47] achieve minimal detectable absorption levels of  $> 1 \cdot 10^{-3}$  for the same bandwidth. Note that for the specific data shown in Fig. 4.5(a), the RAM noise at  $\tau \approx 3 \text{ ms}$  was much more pronounced than for the FM signal shown in Fig. 4.4(b). Clearly, careful optimization of the optical setup is necessary to reduce RAM noise components for sensitive detection of transients with concentration changes taking place on millisecond timescales.

Finally, in order to compare the achieved sensitivity with the theoretical shot-noise limit, Fig. 4.5(b) shows a log-log plot of  $A_{\min}$  values for  $\tau = 1 \mu\text{s}$  as a function of the incident light power  $P_0$  (diamond symbols). The expected shot-noise limit  $A_{\min}^{\text{SN}}$  [2] according to

$$A_{\min}^{\text{SN}} = \frac{4}{\Delta f_{\text{max}}} \left[ \left( \frac{P_0}{h\nu_c} \right) \frac{\eta}{\Delta f_{\text{BW}}} \right]^{-\frac{1}{2}} \quad (4.8)$$

with  $\Delta f_{\text{BW}} = 1 \text{ MHz}$ ,  $\Delta f_{\text{max}} = 0.45$ ,  $\nu_c = 1.03 \cdot 10^{14} \text{ Hz}$ , and  $\eta = 0.52$  is included in Fig. 4.5(b) as a dashed line with a slope of  $-0.5$  as well. Here,  $\Delta f_{\text{max}}$  is the maximum value of  $\Delta f$  in the FM spectrum,  $P_0$  is the light power on the detector,  $\nu_c$  is the frequency of the detection light,

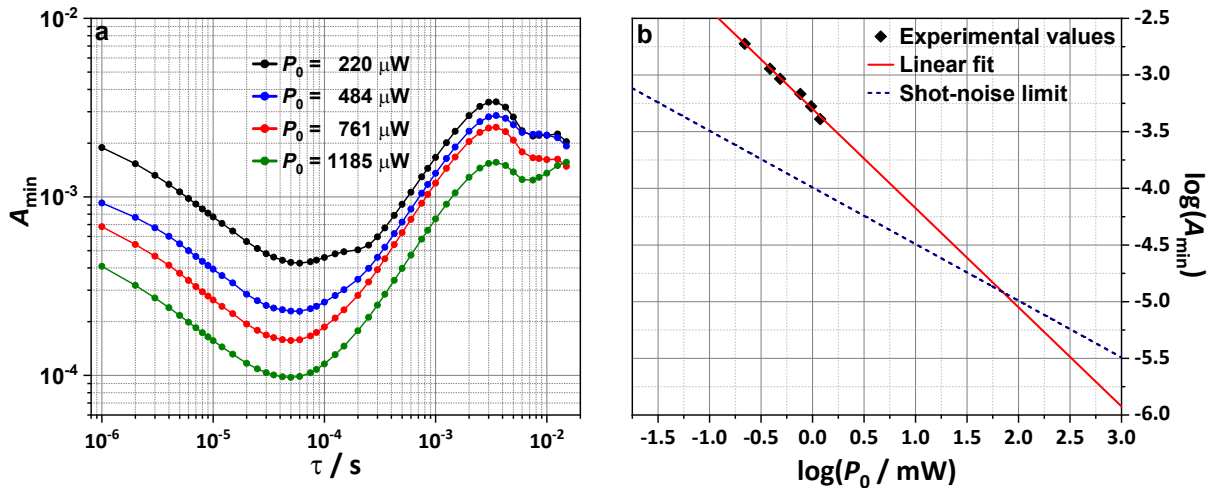


**Figure 4.5:** (a) Minimal detectable absorption  $A_{\min}$  derived from Allan analysis of FM signal noise at different light power levels  $P_0$  as function of the averaging period  $\tau$  ( $M = 0.48$ ,  $\Delta f_{\text{max}} = 0.45$ ,  $\tilde{\nu} = 3447 \text{ cm}^{-1}$ ). (b) log-log plot of experimental  $A_{\min}$  values at  $\tau = 1 \mu\text{s}$  versus light power  $P_0$  ( $M = 0.48$ ,  $\Delta f_{\text{max}} = 0.45$ ,  $\tilde{\nu} = 3447 \text{ cm}^{-1}$ ). The theoretical shot-noise limit is shown for comparison ( $\eta = 0.52$ ,  $\Delta f_{\text{BW}} = 1 \text{ MHz}$ ).

and  $\eta$  is the quantum efficiency of the photodetector. The assumed  $\Delta f_{\max}$  value corresponds to the appropriate value for OH detection at  $M = 0.48$ . At a power close to the saturation limit of the detector ( $\sim 1.2$  mW at  $\tilde{\nu} = 3447$  cm $^{-1}$ ) the achieved  $A_{\min}$  value is a factor of  $\sim 4$  above the corresponding shot-noise limit. The experimental values of  $A_{\min}$  in Fig. 4.5(b) are well represented by the solid red line with a slope of  $-0.9$ . Actually, for intensity-independent noise such as thermal noise, a slope of  $-1$  is expected and therefore we attribute the excessive noise to be dominated by thermal noise contributions from the photodetector, which is a common issue in the mid-infrared range. A simple linear extrapolation of the data reveals that the shot-noise limit would be reached at a power level of  $P_0 \approx 65$  mW. This corresponds to  $A_{\min} \approx 1.3 \cdot 10^{-5}$  for  $\tau = 1$   $\mu$ s and  $A_{\min} \approx 3.1 \cdot 10^{-6}$  for  $\tau = 50$   $\mu$ s, the latter relating to the  $\tau$  value of the minimum in the Allan plot in Fig. 4.5(a). These favorable numbers underline the high potential of MIR-FM spectroscopy as a sensitive detection method with high time resolution. Of course, the required light intensity, although easily accessible with the OPO laser system, is well beyond the saturation limit of the currently used photodetector. Moreover, optical saturation of the probed molecular rovibrational transition may become an issue at such high intensities.

## 4.5 Conclusion

The present study reports the first implementation of a single-tone MIR-FM detection scheme with external modulation. MIR-FMS holds high potential for sensitive detection of molecular species and is particularly useful for reaction kinetics applications as it allows to quantitatively measure concentration-time profiles of reactive species with microsecond time resolution. FM spectra and transient profiles of CH $_4$ , HCl, and OH radicals detected on selected transitions in the respective X-H stretch-vibrational bands around 3  $\mu$ m served as illustrative examples. A detection limit of  $A_{\min} = 4 \cdot 10^{-4}$  for  $\Delta f_{\text{BW}} = 1$  MHz was achieved using a resonant EOM with a modulation depth of  $M = 0.48$ . This detection limit is only about a factor of 4 higher than the shot-noise limit. Further improvements to the spectrometer are possible. A thermoelectrically cooled EOM in double-pass configuration is currently being implemented to further increase the modulation depth and to reduce RAM noise, which currently sets the sensitivity limit for measurements on longer timescales. Moreover, the photodetector will be replaced by a tailored model with multi-stage thermoelectrical cooling and a higher optical saturation limit. By combining higher modulation depth, reduced thermal noise, and higher detectable optical power, we expect to increase the overall sensitivity of the spectrometer by at least a factor of 5 and to approach the shot-noise limit. We also plan to demonstrate the use of MIR-FM spectroscopy for the detection of transient species under harsh shock tube conditions.

## Acknowledgments and Funding

We would like to thank the German Science Foundation (DFG) for financial support and the Cluster of Excellence FUTURE OCEAN at Kiel University for funding the laser system. N.F. thanks Kiel University for granting seed money for female PhD graduates.

## References

- [1] G. C. Bjorklund, Frequency-modulation spectroscopy: a new method for measuring weak absorptions and dispersions, *Opt. Lett.* **1980**, *5*, 15–17, DOI [10.1364/OL.5.000015](#).
- [2] G. Friedrichs, Sensitive Absorption Methods for Quantitative Gas Phase Kinetic Measurements. Part 1: Frequency Modulation Spectroscopy, *Z. Phys. Chem.* **2008**, *222*, 1–30, DOI [10.1524/zpch.2008.222.1.1](#).
- [3] M. W. Crofton, E. L. Petersen, Frequency modulation spectroscopy in a particle-forming environment for the detection of SiH<sub>2</sub>, *Proc. Combust. Inst.* **2005**, *30*, 1583–1589, DOI [10.1016/j.proci.2004.08.242](#).
- [4] B.-C. Chang, T. J. Sears, Transient frequency-modulation absorption spectroscopy of free radicals in supersonic free jet expansions, *Chem. Phys. Lett.* **1996**, *256*, 288–292, DOI [10.1016/0009-2614\(96\)00449-6](#).
- [5] S. W. North, R. Fei, T. J. Sears, G. E. Hall, CN radical reaction rate measurements by time-resolved FM spectroscopy, *Int. J. Chem. Kinet.* **1997**, *29*, 127–129, DOI [10.1002/\(SICI\)1097-4601\(1997\)29:2<127::AID-KIN6>3.0.CO;2-W](#).
- [6] J. P. A. Lockhart, E. C. Gross, T. J. Sears, G. E. Hall, Kinetic study of the OH + ethylene reaction using frequency-modulated laser absorption spectroscopy, *Int. J. Chem. Kinet.* **2019**, *51*, 412–421, DOI [10.1002/kin.21265](#).
- [7] A. Alagappan, M. L. Costen, K. G. McKendrick, Frequency modulated spectroscopy as a probe of molecular collision dynamics, *Spectrochim. Acta A* **2006**, *63*, 910–922, DOI [10.1016/j.saa.2005.10.050](#).
- [8] S. Song, D. M. Golden, R. K. Hanson, C. T. Bowman, A shock tube study of benzylamine decomposition: overall rate coefficient and heat of formation of the benzyl radical, *J. Phys. Chem. A* **2002**, *106*, 6094–6098, DOI [10.1021/jp0200851](#).
- [9] M. Colberg, G. Friedrichs, Room temperature and shock tube study of the reaction HCO + O<sub>2</sub> using the photolysis of glyoxal as an efficient HCO source, *J. Phys. Chem. A* **2006**, *110*, 160–170, DOI [10.1021/jp055168r](#).
- [10] N. Faßheber, M. C. Schmidt, G. Friedrichs, Quantitative HNO detection behind shock waves, *Proc. Combust. Inst.* **2017**, *36*, 607–615, DOI [10.1016/j.proci.2016.05.035](#).
- [11] J. Deppe, G. Friedrichs, A. Ibrahim, H.-J. Römmling, H. G. Wagner, The thermal decomposition of NH<sub>2</sub> and NH radicals, *Ber. Bunsenges. Phys. Chem.* **1998**, *102*, 1474–1485, DOI [10.1002/bbpc.199800016](#).
- [12] M. Votsmeier, S. Song, D. Davidson, R. Hanson, Sensitive detection of NH<sub>2</sub> in shock tube experiments using frequency modulation spectroscopy, *Int. J. Chem. Kinet.* **1999**, *31*, 445–453, DOI [10.1002/\(SICI\)1097-4601\(1999\)31:6<445::AID-KIN6>3.0.CO;2-4](#).
- [13] G. Friedrichs, H. G. Wagner, Quantitative FM spectroscopy at high temperatures: The detection of <sup>1</sup>CH<sub>2</sub> behind shock waves, *Z. Phys. Chem.* **2000**, *214*, 1723–1746, DOI [10.1524/zpch.2000.214.12.1723](#).
- [14] G. Friedrichs, J. T. Herbon, D. F. Davidson, R. K. Hanson, Quantitative detection of HCO behind shock waves: The thermal decomposition of HCO, *Phys. Chem. Chem. Phys.* **2002**, *4*, 5778–5788, DOI [10.1039/b205692e](#).
- [15] S. Wang, R. K. Hanson, Ultra-sensitive spectroscopy of OH radical in high-temperature transient reactions, *Opt. Lett.* **2018**, *43*, 3518–3521, DOI [10.1364/ol.43.003518](#).
- [16] U. Hollenstein, H. Schmutz, J. A. Agner, M. Sommariva, F. Merkt, Vacuum-ultraviolet frequency-modulation spectroscopy, *J. Chem. Phys.* **2017**, *146*, 014201/1–9, DOI [10.1063/1.4973011](#).
- [17] J. T. Farrell, C. A. Taatjes, Infrared frequency-modulation probing of Cl + C<sub>3</sub>H<sub>4</sub> (allene, propyne) reactions: kinetics of HCl production from 292 to 850 K, *J. Phys. Chem. A* **1998**, *102*, 4846–4856, DOI [10.1021/jp981265r](#).

- [18] C. A. Taatjes, Infrared frequency-modulation measurements of absolute rate coefficients for  $\text{Cl} + \text{HD} \rightarrow \text{HCl(DCl)} + \text{D(H)}$  between 295 and 700 K, *Chem. Phys. Lett.* **1999**, *306*, 33–40, DOI [10.1016/s0009-2614\(99\)00420-0](https://doi.org/10.1016/s0009-2614(99)00420-0).
- [19] G. R. Janik, C. B. Carlisle, T. F. Gallagher, Two-tone frequency-modulation spectroscopy, *J. Opt. Soc. Am. B* **1986**, *3*, 1070–1074, DOI [10.1364/JOSAB.3.001070](https://doi.org/10.1364/JOSAB.3.001070).
- [20] V. Avetisov, P. Kauranen, Two-tone frequency-modulation spectroscopy for quantitative measurements of gaseous species: theoretical, numerical, and experimental investigation of line shapes, *Appl. Opt.* **1996**, *35*, 4705–4723, DOI [10.1364/AO.35.004705](https://doi.org/10.1364/AO.35.004705).
- [21] J. A. Silver, Frequency-modulation spectroscopy for trace species detection: theory and comparison among experimental methods, *Appl. Opt.* **1992**, *31*, 707–717, DOI [10.1364/ao.31.000707](https://doi.org/10.1364/ao.31.000707).
- [22] S. Borri, S. Bartalini, P. D. Natale, M. Inguscio, C. Gmachl, F. Capasso, D. Sivco, A. Cho, Frequency modulation spectroscopy by means of quantum-cascade lasers, *Appl. Phys. B* **2006**, *85*, 223–229, DOI [10.1007/s00340-006-2343-6](https://doi.org/10.1007/s00340-006-2343-6).
- [23] P. Maddaloni, P. Malara, G. Gagliardi, P. D. Natale, Two-tone frequency modulation spectroscopy for ambient-air trace gas detection using a portable difference-frequency source around 3  $\mu\text{m}$ , *Appl. Phys. B* **2006**, *85*, 219–222, DOI [10.1007/s00340-006-2299-6](https://doi.org/10.1007/s00340-006-2299-6).
- [24] I. D. Lindsay, P. Groß, C. J. Lee, B. Adhimoolam, K.-J. Boller, Mid-infrared wavelength- and frequency-modulation spectroscopy with a pump-modulated singly-resonant optical parametric oscillator, *Opt. Express* **2006**, *14*, 12341–12346, DOI [10.1364/OE.14.012341](https://doi.org/10.1364/OE.14.012341).
- [25] G. Chen, C. G. Bethea, R. Martini, P. D. Grant, R. Dudek, H. C. Liu, High-speed all-optical modulation of a standard quantum cascade laser by front facet illumination, *Appl. Phys. Lett.* **2009**, *95*, 101104/1–3, DOI [10.1063/1.3223597](https://doi.org/10.1063/1.3223597).
- [26] C. Peng, H. Zhou, L. Zhu, T. Chen, Q. Liu, D. Wang, J. Li, Q. Peng, G. Chen, Z. Li, Purified frequency modulation of a quantum cascade laser with an all-optical approach, *Opt. Lett.* **2017**, *42*, 4506–4509, DOI [10.1364/ol.42.004506](https://doi.org/10.1364/ol.42.004506).
- [27] A. Shehzad, P. Brochard, R. Matthey, S. Blaser, T. Gresch, R. Maulini, A. Muller, T. Südmeyer, S. Schilt, Electrically-driven pure amplitude and frequency modulation in a quantum cascade laser, *Opt. Express* **2018**, *26*, 12306–12317, DOI [10.1364/oe.26.012306](https://doi.org/10.1364/oe.26.012306).
- [28] G. C. Bjorklund, M. D. Levenson, W. Lenth, C. Ortiz, Frequency modulation (FM) spectroscopy, *Appl. Phys. B* **1983**, *32*, 145–152, DOI [10.1007/bf00688820](https://doi.org/10.1007/bf00688820).
- [29] S. W. North, X. S. Zheng, R. Fei, G. E. Hall, Line shape analysis of Doppler broadened frequency-modulated line spectra, *J. Chem. Phys.* **1996**, *104*, 2129–2135, DOI [10.1063/1.470969](https://doi.org/10.1063/1.470969).
- [30] N. Wong, J. L. Hall, Servo control of amplitude modulation in frequency-modulation spectroscopy: demonstration of shot-noise-limited detection, *J. Opt. Soc. Am. B* **1985**, *2*, 1527–1533, DOI [10.1364/JOSAB.2.001527](https://doi.org/10.1364/JOSAB.2.001527).
- [31] M. Gehrtz, G. C. Bjorklund, E. A. Whittaker, Quantum-limited laser frequency-modulation spectroscopy, *J. Opt. Soc. Am. B* **1985**, *2*, 1510–1526, DOI [10.1364/JOSAB.2.001510](https://doi.org/10.1364/JOSAB.2.001510).
- [32] J. Sathian, E. Jaatinen, Reducing residual amplitude modulation in electro-optic phase modulators by erasing photorefractive scatter, *Opt. Express* **2013**, *21*, 12309–12317, DOI [10.1364/OE.21.012309](https://doi.org/10.1364/OE.21.012309).
- [33] W. Zhang et al., Reduction of residual amplitude modulation to  $1 \times 10^{-6}$  for frequency modulation and laser stabilization, *Opt. Lett.* **2014**, *39*, 1980–1983, DOI [10.1364/ol.39.001980](https://doi.org/10.1364/ol.39.001980).
- [34] W. Ludwig, B. Brandt, G. Friedrichs, F. Temps, Kinetics of the reaction  $\text{C}_2\text{H}_5 + \text{HO}_2$  by time-resolved mass spectrometry, *J. Phys. Chem. A* **2006**, *110*, 3330–3337, DOI [10.1021/jp0557464](https://doi.org/10.1021/jp0557464).
- [35] I. Gordon et al., The HITRAN2016 molecular spectroscopic database, *J. Quant. Spectrosc. Radiat. Transfer* **2017**, *203*, 3–69, DOI [10.1016/j.jqsrt.2017.06.038](https://doi.org/10.1016/j.jqsrt.2017.06.038).
- [36] A. V. Baklanov, L. N. Krasnoperov, Oxalyl Chloride - A Clean Source of Chlorine Atoms for Kinetic Studies, *J. Phys. Chem. A* **2001**, *105*, 97–103, DOI [10.1021/jp0019456](https://doi.org/10.1021/jp0019456).



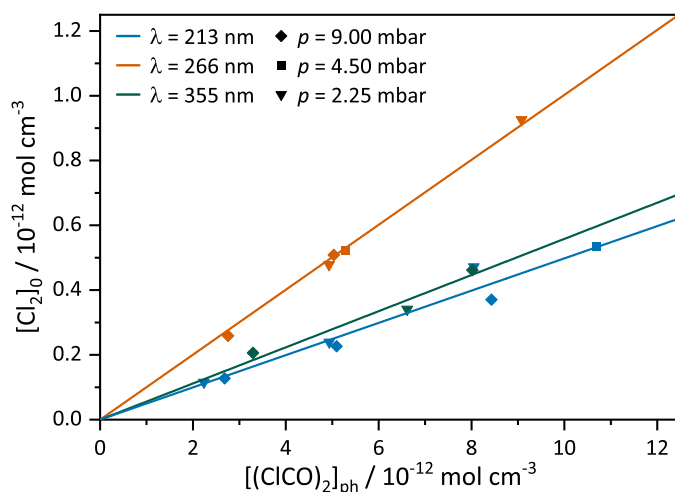
- [37] R. Atkinson, D. L. Baulch, R. A. Cox, J. N. Crowley, R. F. Hampson, R. G. Hynes, M. E. Jenkin, M. J. Rossi, J. Troe, Evaluated kinetic and photochemical data for atmospheric chemistry: Volume I - gas phase reactions of O<sub>x</sub>, HO<sub>x</sub>, NO<sub>x</sub>, and SO<sub>x</sub> species, *Atmos. Chem. Phys.* **2004**, *4*, 1461–1738, DOI [10.5194/acp-4-1461-2004](https://doi.org/10.5194/acp-4-1461-2004).
- [38] D. L. Baulch et al., Evaluated Kinetic Data for Combustion Modelling, *J. Phys. Chem. Ref. Data* **1992**, *21*, 411–734, DOI [10.1063/1.555908](https://doi.org/10.1063/1.555908).
- [39] R. Atkinson, D. L. Baulch, R. A. Cox, J. N. Crowley, R. F. Hampson, R. G. Hynes, M. E. Jenkin, M. J. Rossi, J. Troe, Evaluated kinetic and photochemical data for atmospheric chemistry: Volume II - gas phase reactions of organic species, *Atmos. Chem. Phys.* **2006**, *6*, 3625–4055, DOI [10.5194/acp-6-3625-2006](https://doi.org/10.5194/acp-6-3625-2006).
- [40] S. Wang, R. K. Hanson, High-sensitivity 308.6-nm laser absorption diagnostic optimized for OH measurement in shock tube combustion studies, *Appl. Phys. B* **2018**, *124*, 37/1–7, DOI [10.1007/s00340-018-6902-4](https://doi.org/10.1007/s00340-018-6902-4).
- [41] D. W. Allan, Statistics of atomic frequency standards, *Proc. IEEE* **1966**, *54*, 221–230, DOI [10.1109/PROC.1966.4634](https://doi.org/10.1109/PROC.1966.4634).
- [42] J. A. Barnes, A. R. Chi, L. S. Cutler, D. J. Healey, D. B. Leeson, T. E. McGunigal, J. A. Mullen, W. L. Smith, R. L. Sydnor, R. F. Vessot, et al., Characterization of frequency stability, *IEEE Trans. Instrum. Meas.* **1971**, 105–120, DOI [10.1109/TIM.1971.5570702](https://doi.org/10.1109/TIM.1971.5570702).
- [43] J. B. McManus, M. S. Zahniser, D. D. Nelson, J. H. Shorter, S. C. Herndon, D. Jervis, M. Agnese, R. McGovern, T. I. Yacovitch, J. R. Roscioli, Recent progress in laser-based trace gas instruments: performance and noise analysis, *Appl. Phys. B* **2015**, *119*, 203–218, DOI [10.1007/s00340-015-6033-0](https://doi.org/10.1007/s00340-015-6033-0).
- [44] J. Hodgkinson, R. P. Tatam, Optical gas sensing: a review, *Meas. Sci. Technol.* **2012**, *24*, 012004/1–59, DOI [10.1088/0957-0233/24/1/012004](https://doi.org/10.1088/0957-0233/24/1/012004).
- [45] P. Weibring, D. Richter, A. Fried, J. Walega, C. Dyroff, Ultra-high-precision mid-IR spectrometer II: System description and spectroscopic performance, *Appl. Phys. B* **2006**, *85*, 207–218, DOI [10.1007/s00340-006-2300-4](https://doi.org/10.1007/s00340-006-2300-4).
- [46] Y. Sakamoto, K. Tanaka, T. Asakawa, K. Tonokura, Wavelength Modulation Spectroscopy Detection of N<sub>2</sub>O Using a Direct-Bonded Quasi-Phase-Matched LiNbO<sub>3</sub>-Ridge-Waveguide Mid-Infrared Laser, *Jpn. J. Appl. Phys.* **2011**, *50*, 062401/1–4, DOI [10.1143/jjap.50.062401](https://doi.org/10.1143/jjap.50.062401).
- [47] W. Ren, L. Luo, F. K. Tittel, Sensitive detection of formaldehyde using an interband cascade laser near 3.6 μm, *Sens. Actuators B Chem.* **2015**, *221*, 1062–1068, DOI [10.1016/j.snb.2015.07.078](https://doi.org/10.1016/j.snb.2015.07.078).





## CHAPTER 5

### Publication II: UV Photolysis of Oxalyl Chloride: ClCO Radical Decomposition and Direct Cl<sub>2</sub> Formation Pathways



Michael Stuhr<sup>a</sup>, Sebastian Hesse<sup>a</sup>, Nancy Faßheber<sup>a</sup>, Marcel Wohler<sup>a</sup>, Mithun Pal<sup>a</sup>, Yasuyuki Sakai<sup>b</sup>, Patrick Hemberger<sup>c</sup>, and Gernot Friedrichs<sup>a</sup>

<sup>a</sup>Institute of Physical Chemistry, Kiel University, Max-Eyth-Straße 1, 24118 Kiel, Germany

<sup>b</sup>Carbon Recycling Energy Research Center, Ibaraki University, Nakanarusawa-cho 4-12-1, Hitachi 316-8511 Ibaraki, Japan

<sup>c</sup>Laboratory for Synchrotron Radiation and Femtochemistry, Paul Scherrer Institute, Forschungsstrasse 111, 5232 Villigen PSI, Switzerland

*submitted to Int. J. Chem. Kinet.*

#### Own Contributions:

- Planning of and participation in the measurement campaign at SLS
- Analysis and discussion of SLS data
- MIR-FM experiments at Kiel University
- Analysis and discussion of MIR-FM data
- Writing of paper draft

## Abstract

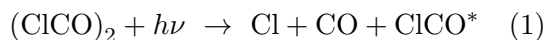
Oxalyl chloride,  $(\text{ClCO})_2$ , is widely used as a photolytic source of Cl atoms in reaction kinetics studies.  $(\text{ClCO})_2$  photolysis is typically assumed to produce Cl atoms with an overall yield of 2 via three-body dissociation,  $(\text{ClCO})_2 + h\nu \rightarrow \text{Cl} + \text{CO} + \text{ClCO}^*$ , followed by fast subsequent ClCO unimolecular decomposition of either the energetically excited  $\text{ClCO}^*$  fragment,  $\text{ClCO}^* \rightarrow \text{Cl} + \text{CO}$ , or the thermalized ClCO radical,  $\text{ClCO} + \text{M} \rightarrow \text{Cl} + \text{CO} + \text{M}$ . However, a recent study by Huang et al. (J. Phys. Chem. A 121 (2017) 2888–2895) suggests that UV photolysis of  $(\text{ClCO})_2$  at 248 nm directly yields  $\text{Cl}_2$  with a photolysis quantum yield of  $\phi(\text{Cl}_2) > 14\%$ . This new product pathway complicates the use of  $(\text{ClCO})_2$  as a clean source of Cl atoms and challenges the previously accepted photodissociation scheme. The purpose of the present work was two-fold. Firstly, the unimolecular decomposition of  $\text{ClCO}^*$  and ClCO radicals has been investigated in  $(\text{ClCO})_2/\text{C}_2\text{H}_6/\text{Ar}$  gas mixtures after UV photolysis at 266 nm and 355 nm. Cl atoms were captured by  $\text{C}_2\text{H}_6$  added in excess such that concentration-time profiles of HCl measured by means of mid-infrared frequency modulation (MIR-FM) spectroscopy reflect the temporally separated Cl formation pathways. The low-pressure thermal ClCO decomposition rate constant was determined to be  $k = (1.08 \pm 0.10) \times 10^{10} \text{ cm}^3 \text{ mol}^{-1} \text{ s}^{-1}$  at 295 K. Secondly, the photolysis quantum yield of direct  $\text{Cl}_2$  formation from  $(\text{ClCO})_2$  photofragmentation was studied with time-of-flight mass spectrometry (TOF-MS) using a photoelectron photoion coincidence (PEPICO) setup. Calibrated  $\text{Cl}_2$  concentration-time profiles were recorded and analyzed using kinetic simulations accounting for both direct and secondary formation of  $\text{Cl}_2$  from photolysis and reactions involving Cl, ClCO, and  $(\text{ClCO})_2$ , respectively. Direct  $\text{Cl}_2$  formation could be confirmed with wavelength-dependent quantum yields of  $\phi(\text{Cl}_2) = (5.0 \pm 1.6)\%$ ,  $(10.0 \pm 3.3)\%$ , and  $(5.6 \pm 2.0)\%$  at 213 nm, 266 nm, and 355 nm. Complementary quantum-chemical calculations of the potential energy diagram for ground-state photodissociation reveal a low-lying energy barrier for the formation of phosgene,  $\text{Cl}_2\text{CO}$ . We suggest that subsequent  $\text{Cl}_2$  and Cl formation from energetically excited  $\text{Cl}_2\text{CO}$  may actually play a key role for the overall photodissociation of  $(\text{ClCO})_2$ .

## 5.1 Introduction

UV photolysis of oxalyl chloride,  $(\text{ClCO})_2$ , has received considerable attention as “a clean source for chlorine atoms” [1] for gas-phase reaction kinetic applications.  $(\text{ClCO})_2$  features high vapor pressures at room temperature and high absorption cross sections in the UV spectral range, particularly at wavelengths below 250 nm.  $(\text{ClCO})_2$  photolysis has been widely used as Cl atom source for the generation of hydrocarbon radicals [2–5], silyl radicals [6], and even peroxy radicals [7] via subsequent H-abstraction reactions with hydrocarbons, silanes, and organic peroxides.

In an early study [8], Ahmed et al. used photofragment imaging of spin-orbit excited  $\text{Cl}^*$  ( $^2P_{1/2}$ ) and ground-state Cl ( $^2P_{3/2}$ ) atoms to study the UV photolysis of  $(\text{ClCO})_2$  at 235 nm. They identified slow and fast components of Cl formation and assigned them to primary Cl atoms from  $(\text{ClCO})_2$  photodissociation and secondary Cl atoms formed by ensuing decomposition of the chloroformyl radical, ClCO, respectively. Consequently, the first step of  $(\text{ClCO})_2$  photodissociation

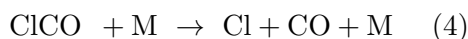
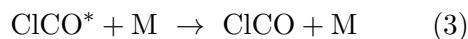
has been described as a three-body decomposition process yielding Cl atoms, CO, and ClCO:



Initially, due to the excess energy provided by the UV photon, vibrationally excited chloroformyl radicals ( $\text{ClCO}^*$ ) are formed, which can undergo fast unimolecular decomposition yielding Cl atoms and CO:



Already at mbar pressures,  $\text{ClCO}^*$  can also be collisionally deactivated to thermalized ClCO. Due to its low bond energy of  $\sim 30$  kJ/mol [9, 10], ClCO will undergo thermal decomposition even at room temperature, yielding Cl + CO as well.



The two-step photodissociation scheme via reactions 1 and 2 was later confirmed by Hemmi and Suits with photofragment translational spectroscopy using ArF excimer laser photolysis at 193 nm [11].  $\text{Cl}^+$  and  $\text{CO}^+$  ion signals showed a bimodal translational energy distribution, again implying two distinct contributions to the formation of Cl atoms and CO.

Baklanov and Krasnoperov introduced the practical use of  $(\text{ClCO})_2$  as a photolytic source of Cl atoms for gas-phase reaction kinetic studies [1, 6]. Using UV/Vis transient absorption spectroscopy, they measured the photodepletion of  $(\text{ClCO})_2$  and kinetic profiles of  $\text{Cl}_2$ . Observed  $\text{Cl}_2$  formation was attributed to recombination of Cl atoms. From  $\text{Cl}_2$  yields, a pressure-independent total photolysis yield of  $\phi_{\text{tot}}(\text{Cl}) = 2$  was reported for the overall Cl atom formation. Additionally, their study provided UV absorption cross sections of  $(\text{ClCO})_2$  at selected wavelengths between 193 nm and 390 nm.

Ghosh et al. studied the effects of photolysis wavelength (excimer laser photolysis at 193 nm, 248 nm, and 351 nm) and pressure (10 – 163 mbar) on the Cl atom yield by atomic resonance fluorescence [12]. Except at 193 nm, they could clearly distinguish direct Cl atom formation via reactions 1 and 2 from delayed Cl atom formation via reaction 4, hence enabling the rate constant determination of thermal ClCO decomposition in  $\text{N}_2$  and He buffer gas. They also recorded a continuous UV spectrum of  $(\text{ClCO})_2$  between 200 nm and 450 nm, with absorption cross sections in good agreement with the values from Ref. 1. Finally, Ghosh et al. reported pressure-independent total Cl atom yields  $\phi_{\text{tot}}(\text{Cl})$  of  $2.19 \pm 0.37$  and  $1.98 \pm 0.26$  at the photolysis wavelengths of 193 nm and 248 nm, respectively. Interestingly, a pronounced pressure dependence was found for photolysis at 351 nm. For example, in He buffer gas the total Cl atom yield decreased from  $2.17 \pm 0.33$  at 21.8 mbar to  $1.18 \pm 0.17$  at 163.2 mbar. Secondary chemistry that may consume Cl atoms should be negligible under their experimental conditions. Therefore, next to fast stabilization of photoexcited  $(\text{ClCO})_2$ , this finding may indicate a non-Cl forming pathway with collisional

stabilization of an intermediate as well, which has not been mentioned in their paper. It will become clear in the present work that this could be phosgene,  $\text{Cl}_2\text{CO}$ .

In an earlier study [13], Nicovich et al. investigated the formation of  $\text{ClCO}$  radicals by recombination of  $\text{Cl}$  and  $\text{CO}$  using time-resolved resonance fluorescence spectroscopy of  $\text{Cl}$  atoms. They also deduced the rate constant of the reverse reaction 4 as well as the enthalpy of formation of the  $\text{ClCO}$  radical. In agreement with Ref. 12, reaction 4 was found to be in the low-pressure regime up to the highest experimental pressure of about 300 mbar with a high rate constant around  $1 \times 10^{10} \text{ cm}^3 \text{ mol}^{-1} \text{ s}^{-1}$  in  $\text{N}_2$  at room temperature. This corresponds to a lifetime of merely 2.5 ms at 1 mbar.

Except for photolysis at 351 nm, all mentioned studies are consistent with a simple picture of photodissociation that follows the overall stoichiometric equation  $(\text{ClCO})_2 + h\nu \rightarrow 2 \text{ Cl} + 2 \text{ CO}$ , taking into account direct  $\text{Cl}$  formation from  $(\text{ClCO})_2$  photolysis and consecutive  $\text{Cl}$  formation from  $\text{ClCO}^*$  or  $\text{ClCO}$  decomposition. Thus, for many practical applications it has typically been assumed that  $(\text{ClCO})_2$  photolysis yields the desired  $\text{Cl}$  atoms with a photolysis yield of  $\phi_{\text{tot}}(\text{Cl}) = 2$ .

However, in a more recent study [14], Huang et al. investigated  $\text{Cl}_2$  formation after single-photon UV photolysis of  $(\text{ClCO})_2$  at 248 nm in  $(\text{ClCO})_2/\text{Ar}$  mixtures. They detected  $\text{Cl}_2$  on its weak  $\text{B}^3\Pi_{\text{ou}}^+ \leftarrow \text{X}^1\Sigma_{\text{g}}^+$  electronic transition at around 500 nm by cavity ring-down spectroscopy (CRDS). CRDS measurements were performed at low pressures of 55–120  $\mu\text{bar}$   $(\text{ClCO})_2$  without buffer gas. Their stated  $\text{Cl}_2$  concentrations correspond to an average value over the ringdown decay time of about 70  $\mu\text{s}$ . In fact, Huang et al. reported high total  $\text{Cl}_2$  concentrations, formally corresponding to a total  $\text{Cl}_2$  yield of  $0.8 \pm 0.4$ . Such high yields could not be fully attributed to secondary chemistry, most importantly to  $\text{Cl}_2$  from the reaction  $\text{Cl} + \text{ClCO} \rightarrow \text{Cl}_2 + \text{CO}$ . Quantum-chemical calculations of the ground state potential energy surface (PES) of  $(\text{ClCO})_2$  were therefore performed to identify potential direct  $\text{Cl}_2$ -forming dissociation pathways. A four-centered transition state with an energy barrier of 388.3 kJ/mol was identified, yielding  $\text{Cl}_2 + 2 \text{ CO}$  in a concerted  $\text{Cl}_2$  elimination step. According to their work,  $\text{Cl}$  atom formation proceeds via a roaming-like  $\text{Cl}$  atom shift rearrangement step, forming  $\text{ClC}(\text{O})\text{-COCl}$  with a 314.3 kJ/mol barrier. This rearrangement is followed by  $\text{O-Cl}$  bond dissociation to  $\text{ClC}(\text{O})\text{-CO} + \text{Cl}$ . Unexpectedly,  $\text{ClCO}$  radical formation was assumed to stem from an unusual alternative rearrangement step of the  $\text{ClC}(\text{O})\text{-COCl}$  intermediate, forming  $\text{ClCO-COCl}$  over an energy barrier of 573.2 kJ/mol and followed by  $\text{O-C}$  bond dissociation. The more likely  $\text{C-C}$  bond dissociation  $(\text{ClCO})_2 \rightarrow 2 \text{ ClCO}$  and direct  $\text{C-Cl}$  fission forming  $\text{ClC}(\text{O})\text{-CO} + \text{Cl}$  were apparently not considered. Based on an RRKM treatment, Huang et al. predicted a quantum yield of  $\phi(\text{Cl}_2) > 14\%$  for the  $\text{Cl}_2$ -forming channel. Note that including the neglected additional  $\text{C-C}$  bond dissociation channel would lower the branching fraction of  $\text{Cl}_2$  formation, hence this value should be probably seen as an upper limit. Most importantly, however, the results of Huang et al. suggest that direct formation of  $\text{Cl}_2$  is an active process in the UV photolysis of  $(\text{ClCO})_2$ , thereby calling the traditional picture of photodissociation outlined above into question.

In the present work, we aim to provide further insight into two key aspects of  $(\text{ClCO})_2$  photolysis

by revisiting ClCO formation followed by decomposition into Cl + CO and by investigating the role of direct Cl<sub>2</sub> formation proposed by Huang et al. [14]. To this end, two separate sets of experiments on the UV photolysis of (ClCO)<sub>2</sub> were conducted. Firstly, Cl atom formation and ClCO decomposition in (ClCO)<sub>2</sub>/C<sub>2</sub>H<sub>6</sub>/Ar mixtures after UV photolysis at 266 nm and 355 nm was investigated by means of mid-infrared frequency modulation (MIR-FM) detection of HCl. With C<sub>2</sub>H<sub>6</sub> in large excess, Cl atoms formed either by (ClCO)<sub>2</sub> photodissociation or by subsequent ClCO/ClCO\* decomposition were quickly and efficiently captured by an H-abstraction reaction with C<sub>2</sub>H<sub>6</sub>. In this way, the measured concentration-time profiles of HCl served as sensitive kinetic tracers for the two Cl-producing processes. The HCl profiles were analyzed with the help of kinetic simulations to derive the ClCO decomposition rate constant. Secondly, we quantified the formation of Cl<sub>2</sub> in photolysis experiments with (ClCO)<sub>2</sub>/Ar mixtures at wavelengths of 213 nm, 266 nm, and 355 nm. Kinetic profiles of Cl<sub>2</sub> were recorded with the photoelectron photoion coincidence spectroscopy (PEPICO) setup at the vacuum ultraviolet (VUV) beamline of the Swiss Light Source (SLS). The Cl<sub>2</sub> profiles were analyzed using kinetic simulations accounting for additional Cl<sub>2</sub> formation from secondary chemistry to extract the wavelength-dependent quantum yields of direct Cl<sub>2</sub> formation.

## 5.2 Experimental

### Gas mixtures and reaction mechanism

Several stock gas mixtures of (ClCO)<sub>2</sub> in Ar as buffer gas were prepared using the partial pressure method. To this end, liquid (ClCO)<sub>2</sub> (> 99%, Sigma-Aldrich) was subjected to several freeze-pump-thaw cycles for purification and then diluted with Ar (99.999%, Air Liquide). (ClCO)<sub>2</sub>/Ar mixtures with (ClCO)<sub>2</sub> mole fractions between 0.04% and 1.80% were prepared and introduced into the photolysis reactors of the two setups using calibrated mass flow controllers. For the experiments on ClCO decomposition, C<sub>2</sub>H<sub>6</sub> was added in excess to act as Cl-atom scavenger. This resulted in (ClCO)<sub>2</sub>/C<sub>2</sub>H<sub>6</sub>/Ar mixtures in the flow reactor with C<sub>2</sub>H<sub>6</sub>/Cl concentration ratios of > 800 to ensure pseudo-first order conditions for the scavenging reaction Cl + C<sub>2</sub>H<sub>6</sub> → HCl + C<sub>2</sub>H<sub>5</sub>. All experiments were conducted at an ambient temperature of  $T = 295$  K in the pressure range  $2.17 \text{ mbar} \leq p \leq 52.6 \text{ mbar}$ . The specific experimental conditions for individual measurements on ClCO decomposition and Cl<sub>2</sub> formation are shown in Tabs. A.1 and A.2 of the Supplementary Material, respectively.

Table 5.1 summarizes the rate constants of all reactions used in the kinetic simulations, which were performed with the Chemkin-II package [15] and thermodynamic data adopted from Goos et al. [16]. Most importantly, additional Cl<sub>2</sub> formation from post-photolysis chemistry had to be accounted for in order to extract reliable photolysis quantum yields for direct Cl<sub>2</sub> formation from (ClCO)<sub>2</sub> photofragmentation. Note that reactions 2 and 3 are meant to approximately capture the kinetics of ClCO\* during early reaction times. A more complete description would need to take into account the quantum-state resolved dynamics and kinetics of all accessible energy states of the ClCO\* radical, which is beyond the scope of this study.

Kinetic sensitivity coefficients  $\sigma(i, t)$  for reaction  $i$  at time  $t$  were normalized with respect to the maximum concentration of the species of interest, thus  $\sigma(i, t) = (\partial[X]/\partial \ln k_i)/[X]_{\max}$  with  $X = \text{HCl}$  or  $\text{Cl}_2$ . First, a more comprehensive reaction mechanism was tested – including secondary chemistry of the ethyl radical – but reactions with sensitivity coefficients of  $|\sigma(\text{HCl}, \text{Cl}_2)| < 1 \times 10^{-3}$  were considered negligible and thus not included in the reduced mechanism outlined in Tab. 5.1. The comparably low time resolution of the PEPICO setup of about 1 ms was accounted for in the simulations of the  $\text{Cl}_2$  profiles by convoluting the original signal with a suitable Maxwell-Boltzmann-type response function [5].

### ClCO decomposition

The room-temperature experiments on the decomposition of ClCO were performed in a low-pressure slow-flow reactor (2.7 cm inner diameter, 44 cm length) equipped with MIR and UV-transmissive  $\text{MgF}_2$  windows at pressures between 10 and 53 mbar. UV photolysis pulses at 355 nm ( $\sim 113$  mJ/pulse) and 266 nm ( $\sim 14$  mJ/pulse) were generated by a Nd:YAG laser (Quanta-Ray INDI-40-10, Spectra-Physics) using the 3rd and 4th harmonic, respectively. To optimize the overlap between the UV photolysis beam and the MIR detection beam (see below), iris diaphragms were placed on each side of the reactor through which both beams were guided.

MIR-FM laser spectroscopy served as quantitative detection method for HCl. Rather than probing the absolute attenuation of the laser light, FM-based methods use the differential attenuation of sidebands, which are generated by frequency modulation of the laser light. This way, the absorption information is encoded in a high frequency signal, thereby suppressing  $1/f$  intensity

**Table 5.1:** Reaction mechanism for the experiments on  $(\text{ClCO})_2$  photolysis. The rate constants are given in units of  $\text{cm}^3$ , mol, and s for  $T = 295$  K and  $M = \text{Ar}$ .

No.	Reaction	$k(295 \text{ K})$	Reference
1a	$(\text{ClCO})_2 + h\nu \rightarrow \text{Cl} + \text{CO} + \text{ClCO}^*$		
1b	$\rightarrow \text{Cl}_2 + 2 \text{ CO}$		
2	$\text{ClCO}^* \rightarrow \text{Cl} + \text{CO}$	see text	this work
3	$\text{ClCO}^* + \text{M} \rightarrow \text{ClCO} + \text{M}$	see text	this work
4	$\text{ClCO} + \text{M} \rightleftharpoons \text{Cl} + \text{CO} + \text{M}$	$1.1 \times 10^{10}$	this work
5 †	$\text{Cl} + \text{ClCO} \rightleftharpoons \text{Cl}_2 + \text{CO}$	$4.5 \times 10^{12}$	17
6	$\text{Cl} + \text{Cl} + \text{M} \rightleftharpoons \text{Cl}_2 + \text{M}$	$7.4 \times 10^{15}$	18
7	$\text{Cl} + (\text{ClCO})_2 \rightarrow \text{Cl}_2 + \text{CO} + \text{ClCO}$	$(0.5 - 1.5) \times 10^9$	this work
8	$\text{Cl} + \text{C}_2\text{H}_6 \rightleftharpoons \text{HCl} + \text{C}_2\text{H}_5$	$3.5 \times 10^{13}$	19
9a	$\text{Cl} + \text{C}_2\text{H}_5 \rightleftharpoons \text{C}_2\text{H}_5\text{Cl}$	$2.7 \times 10^{14}$	20
9b	$\rightleftharpoons \text{HCl} + \text{C}_2\text{H}_4$	$1.8 \times 10^{14}$	21
10	HCl diffusional loss	$(0.7 - 3.4) \times 10^2$	this work

†For kinetic analysis, the rate constant of reaction 5 was assumed to be equal for ClCO and  $\text{ClCO}^*$  (see Discussion). Only the forward reaction for  $\text{ClCO}^*$  was considered.

noise components and increasing the detection sensitivity of the laser absorption setup. For details on the underlying principles of FM spectroscopy and its practical application we refer to the literature [22, 23]. The MIR-FM detection system has been described in detail elsewhere [24, 25]. Briefly, MIR laser light was produced by a high-power continuous-wave optical parametric oscillator (cw-OPO, Argos 2400-SF-10, Lockheed Martin Aculight) with a linewidth of  $< 1$  MHz. The OPO system consists of an Yb-doped fiber seed laser (Koheras AdjustiK Y10 PM), an Yb-doped fiber amplifier (YAR-10K-1064-LP-SF, IPG Photonics), and an OPO resonator. The MIR idler output of the OPO was used for detection and its wavelength was monitored by a wavemeter (621A-IR, Bristol Instruments) with an accuracy of  $6 \times 10^{-4} \text{ cm}^{-1}$ . A resonant 489 MHz LiTaO<sub>3</sub> electro-optic modulator (EO-T500T3-MWIR1, Qubig) in double-pass configuration served as the frequency modulator. Temperature stabilization of the EOM ensured a constant modulation depth being applied to the detection beam. Two YVO<sub>4</sub> Glan-laser polarizers were placed in front of and behind the EOM. The first polarizer was used to match the polarization angle of the detection beam to the EOM input polarization axis and the second polarizer was used to set the demodulation phase angle to pure absorption by a well-established procedure [23, 26]. The modulated MIR beam passed through the slow-flow reactor via the MgF<sub>2</sub> windows and was then focused onto a fast thermoelectrically cooled HgCdTe detector (PVI-4TE-5, Vigo System), which provided the DC light intensity signal and the AC signal containing the absorption information. An all-digital 600 MHz lock-in amplifier (UHFLI, Zurich Instruments) was used for demodulation of the AC detector signal to yield the FM signal. The 489 MHz RF output signal of the lock-in amplifier was supplied to a high-power amplifier and then used to drive the EOM. All DC and FM signal traces were recorded on a digital storage oscilloscope (MSO 8104A, Agilent).

MIR-FM detection of HCl was performed on the P(7) rovibrational transition at  $2727.78 \text{ cm}^{-1}$ , since more intense transitions such as P(3) and R(2) were not within the accessible scan range of our laser system. Using the P(7) linestrength from the HITRAN database [27] and simulations of the FM lineshape, which accounted for both Doppler- and pressure-broadening effects, the measured FM signals were converted into mole fractions. The pressure-broadening coefficient for Ar of the P(7) line was taken from Boulet et al. [28]. For this set of experiments, (ClCO)<sub>2</sub> photolysis fractions had to be estimated from the known absorption cross sections of (ClCO)<sub>2</sub> [12]. A software tool based on the formalism described in Ref. 29 was used to check for uniform energy fluence throughout the reactor and to estimate the absolute number of absorbed photons.

### Direct Cl<sub>2</sub> formation

All experiments on the quantum yield of direct Cl<sub>2</sub> formation were performed with the PEPICO setup at the VUV beamline [30] of the Swiss Light Source at room temperature. The PEPICO setup has been described in detail elsewhere [31, 32] and only a brief outline is given here. A side-sampled flow reactor (8.8 mm inner diameter, 55 cm length) was supplied with (ClCO)<sub>2</sub>/Ar mixtures at pressures between 2.17 and 9.15 mbar using calibrated mass flow controllers. For this set of experiments, the 3rd, 4th, and 5th harmonics of a Nd:YAG laser (Q-SMART 850, Quantel) were used for generating UV photolysis pulses at 355 nm ( $\sim 70 \text{ mJ/pulse}$ ), 266 nm ( $\sim 26 \text{ mJ/pulse}$ ),



and 213 nm ( $\sim 5$  mJ/pulse), respectively. The laser pulses were coupled into the flow reactor through two quartz windows along its long axis. Effective photolysis energies in the reactor were taken as the mean of the measured photolysis pulse energies in front and behind the flow reactor. The  $(\text{ClCO})_2/\text{Ar}$  mixtures were introduced into the ionization chamber of the PEPICO setup by effusion through the side hole of the reactor (225  $\mu\text{m}$  diameter). After ionization by the VUV beam from the SLS synchrotron (photon energy set by a monochromator to 11.7 eV), ion optics guided the ions and electrons onto two delay-line detectors to record photoelectron-photoion coincidences. Taking advantage of the time-of-flight mass-spectrometric (TOF-MS) capabilities of the PEPICO setup, time-resolved mass spectra after UV photolysis and VUV ionization were recorded in 250  $\mu\text{s}$  intervals.

The time-dependent  $\text{Cl}_2^+$  mass signals were converted into concentration-time profiles using a calibration procedure. To this end, calibration gas with  $(200 \pm 4)$  ppm  $\text{Cl}_2$  in  $\text{N}_2$  (All-in-Gas) was further diluted in Ar (99.999%, Air Liquide) to produce gas mixtures with varying mole fractions of  $\text{Cl}_2$ . Note that the calibration gas mixtures used  $\text{N}_2/\text{Ar}$  as buffer gas, while the  $(\text{ClCO})_2$  mixtures for the photolysis experiments used pure Ar. This goes along with a difference in the effusion rates from the reactor into the ionization chamber, which leads to higher  $\text{Cl}_2^+$  mass signals for the  $\text{N}_2/\text{Ar}$ -based calibration measurements compared to the photolysis experiments in Ar at the same  $\text{Cl}_2$  concentration. The effusion effect on the  $\text{Cl}_2^+$  ion signals in the calibration measurements was corrected by using the square roots of molecular weights of  $\text{N}_2$  and Ar (Graham's law). Additionally, the effects of pressure and VUV beam intensity fluctuations on the signals were accounted for as well.

$(\text{ClCO})_2$  photolysis fractions were deduced from the depletion of the  $\text{ClCO}^+$  mass signals after photolysis, which represented the most intense fragment signals of  $(\text{ClCO})_2^+$  at a VUV photon energy of 11.7 eV. A typical profile is shown in Fig. A.1 in the Supplementary Material. The first 10 ms after the photolysis pulse were excluded from this analysis to ensure that the  $\text{ClCO}^+$  mass signals for determining the photolysis fraction did not include contributions from  $\text{ClCO}$  formed by  $(\text{ClCO})_2$  photolysis. Photolysis fractions estimated from the weaker parent ion signals or from the measured pulse energies and UV cross sections using the software tool (*vide supra*) were consistent with the  $\text{ClCO}^+$  photodepletion values within  $\pm 14\%$  on average.

Complementary quantum-chemical calculations were performed using Gaussian 16 (Revision C.01) [33]. The optimized geometries, vibrational frequencies, and energies of reactants, products, and transition states were calculated by the G4 composite method [34]. All stationary points were confirmed by one imaginary frequency for transition states and by zero imaginary frequencies for local minima, respectively. Intrinsic reaction coordinate (IRC) calculations were performed to confirm that the optimized transition states connect reactants and products.

### 5.3 Results

In this section, we first present the experimental  $\text{HCl}$  profiles measured with MIR-FM spectroscopy along with the resulting rate constant  $k_4$  of reaction  $\text{ClCO} + \text{M} \rightarrow \text{Cl} + \text{CO} + \text{M}$ . Then, the



experimental  $\text{Cl}_2$  profiles from TOF-MS measurements are discussed and the photolysis quantum yields for direct  $\text{Cl}_2$  formation  $\phi(\text{Cl}_2)$  are presented for all three photolysis wavelengths.

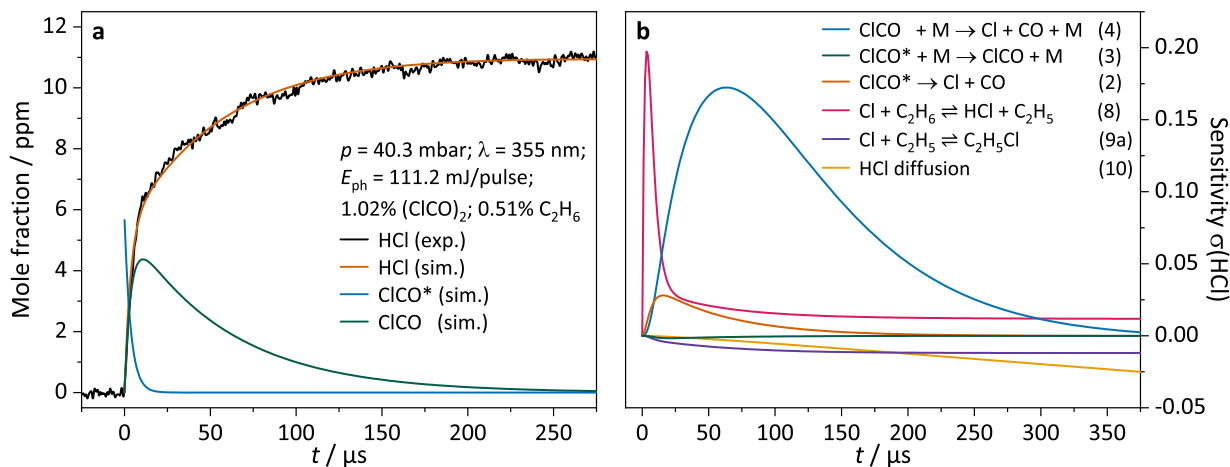
### ClCO decomposition

Figure 5.1 illustrates the formation of HCl after  $(\text{ClCO})_2$  photolysis at 355 nm observed by MIR-FM spectroscopy. In Fig. 5.1a, a typical experimental HCl profile (black curve) is shown alongside simulated profiles of HCl (orange curve),  $\text{ClCO}^*$  (blue curve), and  $\text{ClCO}$  (green curve).

Under the experimental conditions of this study, the formation of HCl can be roughly separated into two phases. The transition between the two phases occurs at around  $10 \mu\text{s}$  for the particular profile in Fig. 5.1a. Initially, HCl formation is driven by "prompt" Cl atoms from  $(\text{ClCO})_2$  photolysis (reaction 1) and fast unimolecular  $\text{ClCO}^*$  decomposition (reaction 2). Afterwards, HCl is almost exclusively formed by capturing Cl atoms from thermal  $\text{ClCO}$  decomposition (reaction 4). Diffusional loss of HCl out of the photolysis volume, which plays a minor role for modeling the fast HCl formation, was treated approximately by assuming a first-order loss process on a ms time scale.

The HCl sensitivity plot in Fig. 5.1b reveals that the HCl profile is highly sensitive to the rate constant  $k_4$  of the target reaction  $\text{ClCO} + \text{M}$  for reaction times of  $t > 10 \mu\text{s}$ . It can be seen from the simulated  $\text{ClCO}$  profile in Fig. 5.1a that the  $\text{ClCO}$  concentration peaks at around  $10 \mu\text{s}$  and subsequently follows a single exponential decay. The well-studied H-abstraction reaction 8,  $\text{Cl} + \text{C}_2\text{H}_6 \rightarrow \text{HCl} + \text{C}_2\text{H}_5$ , is the most important reaction right after the arrival of the UV pulse, showing that this reaction is rate-limiting for HCl formation at  $t < 10 \mu\text{s}$ .

Nevertheless, the initial fast increase in the HCl signal still contains information on the relative  $\text{ClCO}^*$  loss by fast unimolecular decomposition (reaction 2) and collisional stabilization to  $\text{ClCO}$  (reaction 3). In particular, the mole fraction level at the transition point between fast and slow HCl formation, which is found at  $\sim 6$  ppm for the experiment shown in Fig. 5.1a, is governed



**Figure 5.1:** (a) Kinetic HCl profile (black, average of 100 photolysis events) alongside simulated profiles of HCl (orange),  $\text{ClCO}^*$  (blue), and  $\text{ClCO}$  (green) at a photolysis wavelength of 355 nm and  $p = 40.3$  mbar. (b) Sensitivity coefficients  $\sigma(\text{HCl})$  for the same profile.

by the ratio  $r$  of the corresponding rate constants,  $r = k_3[M]/k_2$ . At low pressures, nearly all ClCO\* decomposes quickly to Cl + CO, whereas at sufficiently high pressure most ClCO\* is deactivated and then forms Cl on a much slower time scale. Even at high pressures, as a result of the instantaneous Cl formation from (ClCO)<sub>2</sub> photolysis (reaction 1), a fast HCl component will still be observed and the mole fraction of the transition point will correspond to about half of the maximum possible HCl yield.

An example of a kinetic HCl profile for (ClCO)<sub>2</sub> photolysis at 266 nm is shown in Fig. 5.2a. It can be clearly seen that the transition point from fast to slow HCl formation kinetics is found at a much higher relative mole fraction value than for the experiment at 355 nm. This is consistent with the higher internal excitation of the generated ClCO\* fragment at 266 nm, which should lead to a higher specific rate constant for unimolecular ClCO\* decomposition and a less efficient collisional stabilization to energy levels below the dissociation threshold. For all experiments, approximate values for the rate constant ratio  $r$  were obtained by fitting the initial increase and transition point by holding the rate constant of reaction 8 at its literature value. The obtained data are included in Tab. A.1 in the Supplementary Material. Corresponding rate constant ratios  $r$  are plotted as function of the experimental density in Fig. A.2 and are included in Fig. 5.7 as well. For (ClCO)<sub>2</sub> photolysis at 355 nm, the data points nicely follow the expected linear increase of the rate constant ratio  $r = k_3[M]/k_2$  with increasing pressure. Although the much lower values for 266 nm photolysis are fully consistent with a more dominant unimolecular decomposition of ClCO\*, the rate constant ratio turns out to be essentially independent of pressure. Obviously, for the much higher internal excitation of the ClCO\*, the simplified kinetic treatment with energy-independent  $k_2$  and collisional deactivation by a one-step (strong) collision event described by  $k_3$  is not valid anymore. Instead, the collisional deactivation of the molecule will proceed via several consecutive (weak) collision events. A full master equation analysis would be needed to model the state-dependent relaxation and decomposition of the ClCO radical, but such an analysis was not possible due to the very limited available data.

In contrast to the initial fast increase of the HCl profile, the slow HCl formation component is not rate-limited by reaction 8 and therefore reflects the unimolecular decomposition of the thermalized ClCO molecule,  $\text{ClCO} + \text{M} \rightarrow \text{Cl} + \text{CO} + \text{M}$ , with rate constant  $k_4$ . The high sensitivity coefficients for this reaction (blue curve in Fig. 5.1b) and the strong deviations of the simulated HCl profiles by multiplying or dividing the best-fit  $k_4$  values by a factor of 1.5 (dashed orange curves in Fig. 5.2a) indicate that the direct measurement of  $k_4$  was possible by fitting the HCl profiles based on the reaction mechanism outlined in Tab. 5.1. Figure 5.2b shows the individual pseudo-first order rate constants  $k'_4 = k_4[M]$  for photolysis at 266 nm (blue symbols) and 355 nm (orange symbols). Both data sets essentially agree, with the  $k'_4$  values for photolysis at 266 nm being merely 8% higher on average than the values for 355 nm. A pseudo-first order fit of the combined dataset (black line) provided the rate constant  $k_4 = (1.08 \pm 0.10) \times 10^{10} \text{ cm}^3 \text{ mol}^{-1} \text{ s}^{-1}$  for  $\text{M} = \text{Ar}$  and  $T = 295 \text{ K}$ . No deviation from linearity was observed in the studied pressure range and the  $k_4$  value reported in this work thus represents the low-pressure limited rate constant. The error margins for  $k_4$  were estimated by varying each considered error-prone quantity within

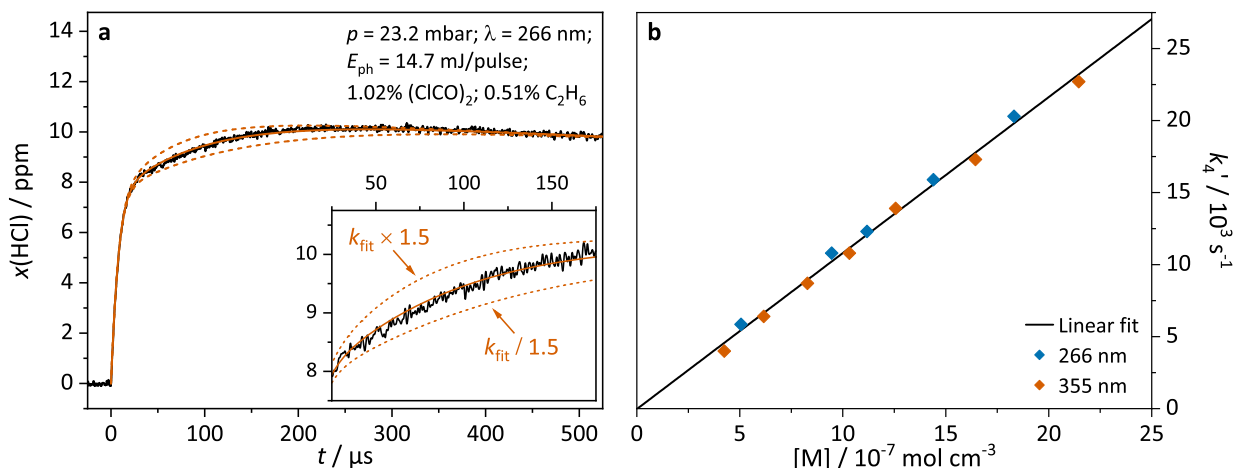


**Figure 5.2:** (a) Experimental (black, average of 100 photolysis events) and simulated (orange) kinetic HCl profiles at a photolysis wavelength of 266 nm and  $p = 23.2$  mbar. The inset shows the pseudo-first order region of ClCO decomposition. (b) Pseudo-first order plot for the decomposition reaction  $\text{ClCO} + \text{M}$  with Ar buffer gas after  $(\text{ClCO})_2$  photolysis at 266 nm (blue symbols) and 355 nm (orange symbols). The black line represents the linear fit to all data points.

its uncertainty range and then readjusting  $k_4$  to reproduce the HCl profile as closely as possible. Relative uncertainties in pressure ( $\sim 1\%$ ),  $k_8$  (20%, estimated from the Arrhenius plot in Ref. 19), the ratio  $r = k_3[\text{M}]/k_2$  (20%, estimated from HCl profile fitting), the first-order HCl diffusion loss rate (10%), and the data scatter in Fig. 5.2b (1.5%, corresponding to  $1\sigma$  standard error of the data scatter relative to the linear fit) were taken into account. We allowed for error compensation by adding all individual relative uncertainties for  $k_4$  in quadrature, resulting in a low relative uncertainty of  $\pm 9\%$  in  $k_4$ . Since all Cl forming reaction steps are of first or pseudo-first order, including the reaction  $\text{ClCO} + \text{M}$ , uncertainties in the initial Cl atom concentration only effected the absolute HCl yield but not the overall shape of the HCl profile. Therefore,  $k_4$  as well as the determined  $r$  value were not affected by uncertainties in the initial  $(\text{ClCO})_2$  concentrations or the assumed photolysis fractions.

### Direct $\text{Cl}_2$ formation

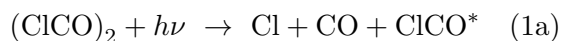
Figure 5.3 illustrates the results of a typical TOF-MS measurement using PEPICO at flow reactor pressure  $p = 4.49$  mbar. Since  $(\text{ClCO})_2$  photolysis was performed at a repetition rate of 10 Hz, a maximum observation time of 100 ms was available, where  $t = 0$  marks the photolysis pulse. The mass spectrum in Fig. 5.3a shows the isotope peak pattern of the parent ion peaks and signals of the three main fragment ions  $\text{Cl}_2\text{CO}^+$ ,  $\text{ClC}(\text{O})\text{-CO}^+$ , and  $\text{ClCO}^+$  right before the photolysis pulse (blue bars,  $-22$  ms to  $-2$  ms). Figure 5.3b displays the signal intensity differences relative to the pre-photolysis data at early (orange bars, 2 ms to 22 ms) and late (green bars, 45 ms to 65 ms) reaction times.

In addition to reduced parent and fragment ion signals due to  $(\text{ClCO})_2$  depletion,  $\text{Cl}_2$  formation is clearly visible in Fig. 5.3b. The  $\text{Cl}_2^+$  ion signal is higher for late reaction times, which suggests significant contributions from post-photolysis chemistry. Interestingly, for late reaction times, there

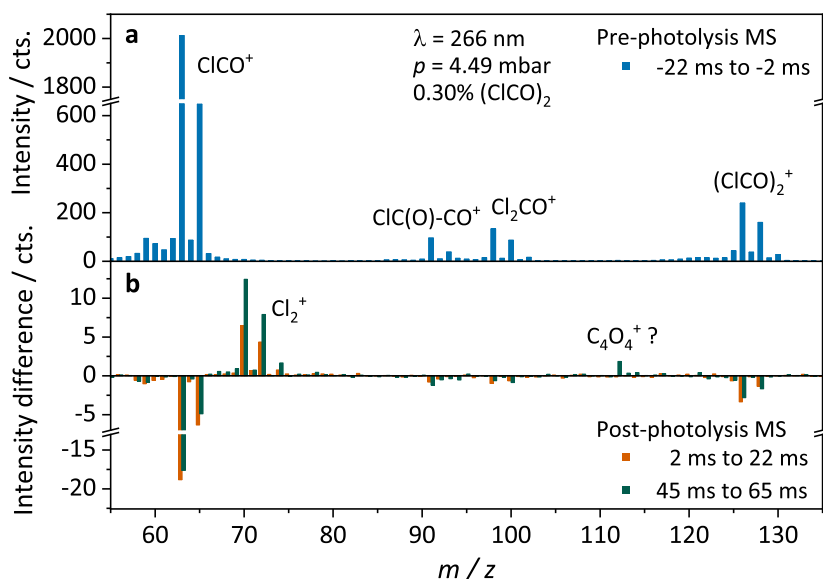
is also a mass peak at  $m/z$  112 without discernible Cl isotope pattern. We tentatively ascribe this signal to  $C_4O_4^+$  ions, which may result from recombination products from reactions involving  $(ClCO)_2$  and/or  $ClC(O)-CO$  (see below).

Figure 5.4 shows examples for kinetic  $Cl_2$  profiles (black curves) extracted from the time-dependent TOF-MS data at photolysis wavelengths of 213 nm (a), 266 nm (b), and 355 nm (c). The intense photolysis pulse caused short negative signal artifacts around  $t = 0$  for photolysis wavelengths of 213 nm and 266 nm.

Following the photolysis pulse, the  $Cl_2$  signals show step-like features within the time resolution of the TOF-MS system. This initial step can be ascribed to direct  $Cl_2$  formation according to reaction 1b as proposed by Huang et al.[14]:



Channel 1a leads to the reactive photolysis products  $Cl$  and  $ClCO^*$ , while channel 1b directly produces the low-reactivity products  $Cl_2$  and  $CO$ . In this work, the corresponding photolysis quantum yield for channel 1b is denoted  $\phi(Cl_2)$ . As discussed and quantified in the preceding section and depending on the rate constant ratio  $r = k_3[M]/k_2$ , some fraction of the  $ClCO^*$  radicals will dissociate according to reaction 2, whereas the rest is thermalized to  $ClCO$  in reaction 3. During the next few ms, a small additional amount of secondary  $Cl_2$  is then formed due to reaction 5,  $Cl + ClCO$ . The amount of secondary  $Cl_2$  from this reaction critically depends on the thermal lifetime of the  $ClCO$ , which is accurately known from the rate constant measurements of reaction 4 outlined above. In the further course of reaction, a slow and steady increase of the



**Figure 5.3:** (a) Typical time-of-flight mass spectrum (blue columns) measured at 11.7 eV before the UV photolysis pulse. (b) Difference TOF-MS spectrum for early (orange columns) and late (green columns) reaction times relative to the pre-photolysis signal level.

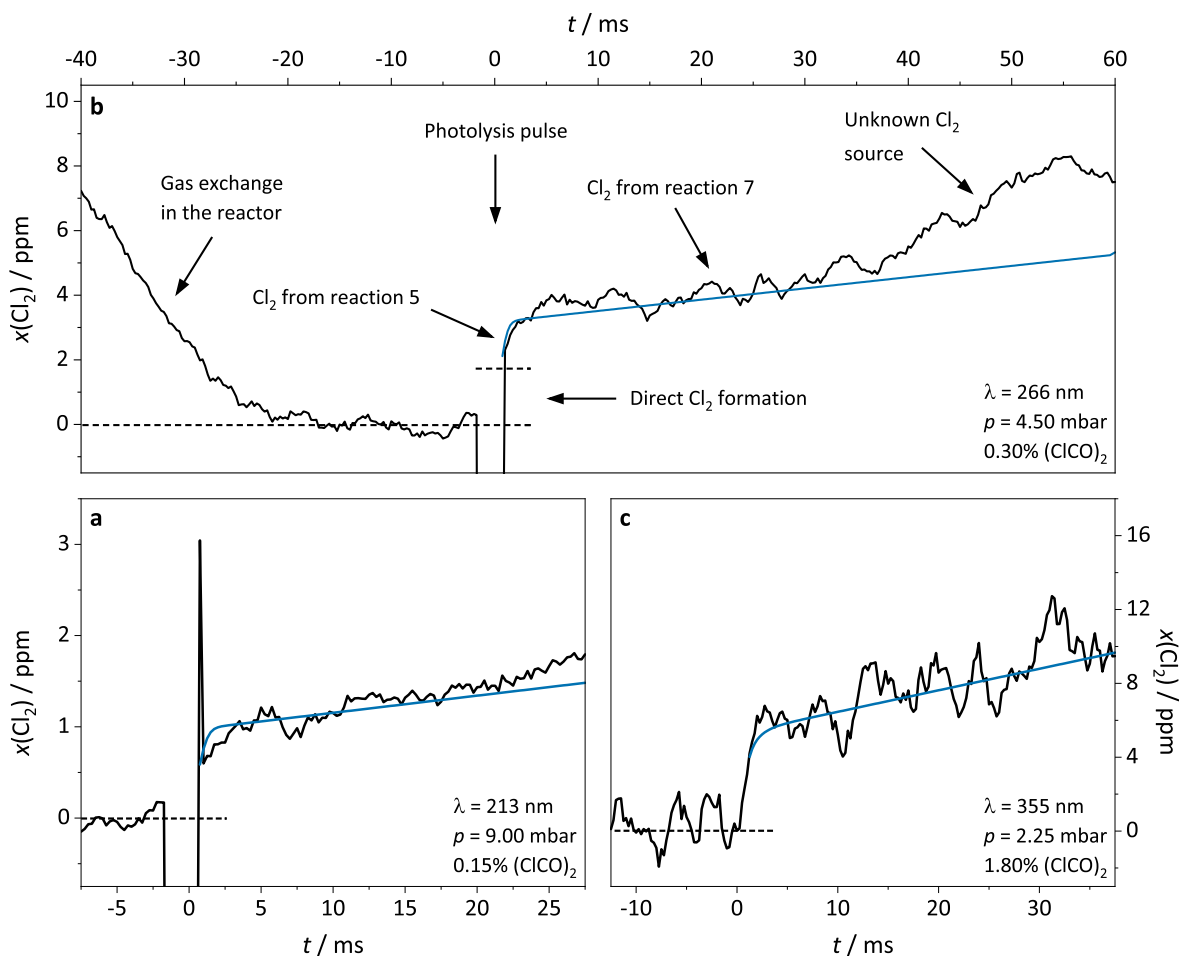
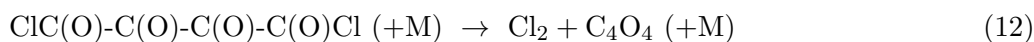
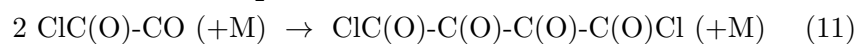
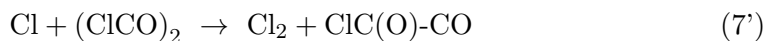


**Figure 5.4:** Experimental (black) and simulated (blue) kinetic  $\text{Cl}_2$  profiles at photolysis wavelengths of (a) 213 nm (average of 90000 photolysis events), (b) 266 nm (14400), and (c) 355 nm (117000) at different initial  $(\text{ClCO})_2$  concentrations and total pressures.

$\text{Cl}_2$  signal is observed. This slow component of secondary  $\text{Cl}_2$  formation is due to  $\text{Cl} + (\text{ClCO})_2$  (reaction 7), whereas  $\text{Cl}$  atom recombination (reaction 6) is too slow to significantly contribute to observed  $\text{Cl}_2$  levels. Many measured kinetic profiles also exhibit another delayed increase in  $\text{Cl}_2$  concentration, like the one shown in Fig. 5.4b at  $t \approx 40 \text{ ms}$ . Finally, the  $\text{Cl}_2$  signal starts to vanish at  $t \approx 60 \text{ ms}$  because the flowing reaction mixture in the side-sampled reactor is being replaced by fresh gas.

The extent of delayed  $\text{Cl}_2$  formation depends on the concentration of  $(\text{ClCO})_2$ , hence it is tempting to ascribe it to some secondary bimolecular reaction of a species that is formed in a reaction with  $(\text{ClCO})_2$ . Tentatively, such a reaction sequence may be formulated as follows:



On the one hand this somewhat speculative reaction sequence yields the thermodynamically unstable [35]  $C_4O_4$ , which could also explain the observed weak  $m/z$  112 signal in the mass spectra (see Fig. 5.3b). On the other hand, both the delayed  $Cl_2$  as well as the  $m/z$  112 signal could also be fragment peaks of  $ClC(O)-C(O)-C(O)-C(O)Cl$  or other higher  $C_xO_yCl_z$  species from unknown secondary chemistry. In principle, fragment peaks may be identified, for example, by a translational energy component of the photoelectrons different from the one following photoionization of  $Cl_2$  itself. However, this could not be confirmed by the detected photoelectron images for early and late  $Cl_2$  signals (see Fig. A.3 in the Supplementary Material), which all seem to be consistent with the  $Cl_2$  photoionization reference image within their experimental uncertainty.

Since the reason for delayed  $Cl_2$  formation remains unclear, we have focused the following kinetic analysis on the the first  $\sim 30$  ms of the  $Cl_2$  transients. The main aim of this analysis was to determine quantum yield values  $\phi(Cl_2)$  for the direct  $Cl_2$  channel from the initial step-like feature rather than a full description of secondary chemistry. All simulations of  $Cl_2$  profiles were performed by adjusting  $\phi(Cl_2)$  to represent the measured concentrations as closely as possible, while also allowing for secondary  $Cl_2$  formation via reactions 5–7.

Values for the ratio  $r = k_3[M]/k_2$  have been adopted from the MIR-FMS results for photolysis at 355 nm and 266 nm (see Fig. A.2 in the Supplementary Material). However, for photolysis at 213 nm, an estimated pressure-independent ratio of  $r = 0.2$  was used, which is in line with the overall wavelength trend. As already mentioned above, the rate constant ratio  $r = k_3[M]/k_2$  determines the branching of the  $ClCO^*$  radical into  $Cl + CO$  and  $ClCO$ , and thereby influences secondary  $Cl_2$  formation from  $Cl/ClCO/ClCO^*$  chemistry. In this way,  $r$  controls (i) the "prompt"  $Cl$  atom yield  $\phi_{ph}(Cl)$ , which includes direct  $Cl$  from photolysis and from  $ClCO^*$  decomposition, but does not include  $Cl$  from the thermal  $ClCO$  decomposition, and (ii) the  $ClCO$  radical yield  $\phi(ClCO)$  from collisional stabilization of  $ClCO^*$ . Thus,  $\phi_{ph}(Cl)$  and  $\phi(ClCO)$  are constrained to  $(1 - \phi(Cl_2)) \times (r + 2)/(r + 1)$  and  $(1 - \phi(Cl_2)) \times r/(r + 1)$ , respectively. As an example, consider an arbitrarily selected value of  $\phi(Cl_2) = 0.05$  at  $p = 4.5$  mbar. In this case, the fast component of the  $Cl$  atom yield is  $\phi_{ph}(Cl) = 1.32/1.41/1.74$  and the  $ClCO$  yield is  $\phi(ClCO) = 0.58/0.49/0.16$  for photolysis at 355/266/213 nm. This results in a total  $Cl$  atom yield of  $\phi_{tot}(Cl) = \phi_{ph}(Cl) + \phi(ClCO) = 1.90$ , and direct  $Cl_2$  formation with  $\phi(Cl_2) = 0.05$  accounts for the remaining chlorine.

Figure 5.5 illustrates the kinetic analysis of a typical  $Cl_2$  signal after  $(ClCO)_2$  photolysis at 266 nm in more detail. The corresponding sensitivity plot in Figure 5.5b reveals that secondary  $Cl_2$  formation is dominated by the overall lifetime of  $ClCO$  (fast component, determined by reactions 4 and 5) and reaction 7 (slow component). The assumed ratio  $r = k_3[M]/k_2$  is less important because a lower  $Cl$  atom yield from reaction 2 is mainly compensated by a higher  $ClCO$  radical yield from reaction 3. Direct  $Cl_2$  formation described by  $\phi(Cl_2)$  does not appear in the sensitivity plot, since it was set by adjusting the initial  $Cl_2$  concentration (see Fig. 5.4b).

In Fig. 5.5a, the blue curve corresponds to the best-fit simulation using  $\phi(Cl_2)$  as the adjustable parameter. Alternative simulations with varying values for  $\phi(Cl_2)$  (dashed orange curves) and  $k_5$  (dashed green curves) reveal the influence of these two quantities. Both  $\phi(Cl_2)$  and  $k_5$  have a similar effect on the  $Cl_2$  profile by essentially causing a shift in the predicted total  $Cl_2$  concentration.

Therefore, if  $\phi(\text{Cl}_2)$  is assumed to be too high, this can be at least partially compensated by a lower value for  $k_5$ . Since associated minor changes in the initial gradient are difficult to recognize – due to the photolysis pulse artefact, the necessary convolution of the simulated profiles with the TOF-MS time response function, and the quite pronounced noise in the signal – such uncertainties need to be accounted for in the error analysis.

Despite the rather moderate signal-to-noise ratio of the  $\text{Cl}_2$  profiles, the kinetic analysis yielded reliable values for the photolysis quantum yield  $\phi(\text{Cl}_2)$  (fitting of the initial step and early plateau value) and an estimate for the rate constant of reaction 7,  $\text{Cl} + (\text{ClCO})_2$  (fitting of the slow increase). Taking into account all profiles, approximate rate constant values for reaction 7 of  $k_7 \approx (0.5 - 1.5) \times 10^9 \text{ cm}^3 \text{ mol}^{-1} \text{ s}^{-1}$  have been obtained, which are fully consistent with the upper limit of  $k_7 < 2.4 \times 10^{10} \text{ cm}^3 \text{ mol}^{-1} \text{ s}^{-1}$  reported by Baklanov and Krasnoperov [1].

Figure 5.6 illustrates the best-fit results of the initial  $\text{Cl}_2$  concentrations for all experiments as function of the concentration of photolyzed  $(\text{ClCO})_2$ . The individual data points were measured for  $(\text{ClCO})_2$  photolysis at 213 nm (blue symbols), 266 nm (orange symbols), and 355 nm (green symbols) at different initial  $(\text{ClCO})_2$  concentrations and total pressures. For all three photolysis wavelengths, the data show a linear trend without discernible pressure dependence, hence confirming a robust extrapolation of measured  $\text{Cl}_2$  concentrations to  $t = 0$ . The slopes of the zero-point straight lines in Fig. 5.6 correspond to the quantum yield values of direct  $\text{Cl}_2$  formation, which are  $\phi(\text{Cl}_2) = (5.0 \pm 1.6)\%$  for 213 nm,  $(10.0 \pm 3.3)\%$  for 266 nm, and  $(5.6 \pm 2.0)\%$  for 355 nm.

The reported errors are based on a detailed uncertainty analysis. Uncertainties in  $k_4$  (9%, see above),  $k_5$  (40%, estimated from the Arrhenius plot in Ref. 17), and the ratio  $r$  (20% for 266 nm and 355 nm, factor 3 for 213 nm), were considered by varying their assumed values and re-adjusting  $\phi(\text{Cl}_2)$  in the kinetic simulations. The scatter of the  $\phi(\text{Cl}_2)$  data in Fig. 5.6 is 3% on average ( $1\sigma$  standard error). Additionally, estimated uncertainties in the initial  $(\text{ClCO})_2$  concentrations (5%),

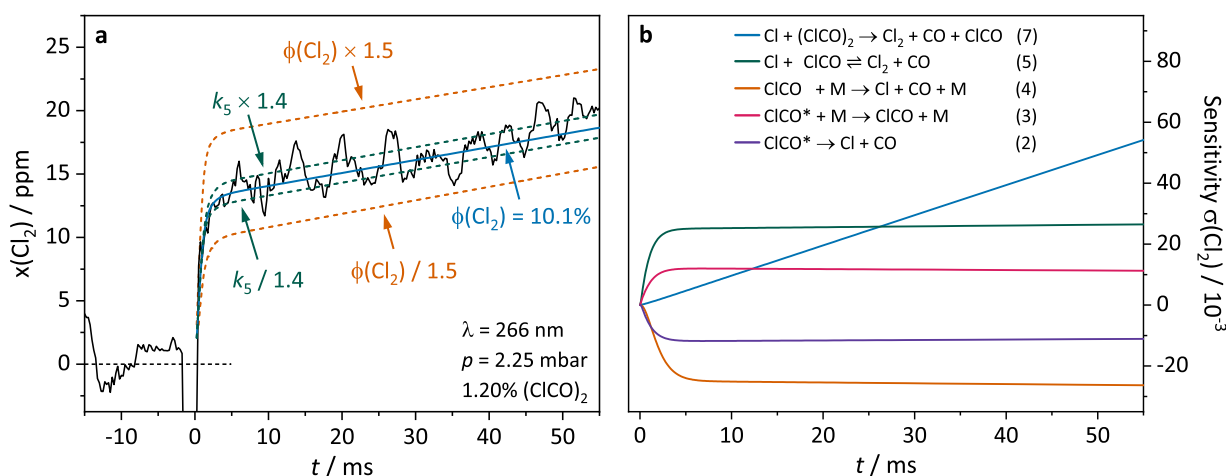


**Figure 5.5:** (a) Experimental (black, average of 36000 photolysis events) and simulated (blue) kinetic  $\text{Cl}_2$  profile at a photolysis wavelength of 266 nm. Alternative simulations with different values for  $\phi(\text{Cl}_2)$  (dashed orange curves) and  $k_5$  (dashed green curves) are included as well. (b) Sensitivity coefficients  $\sigma(\text{Cl}_2)$  for the same profile.



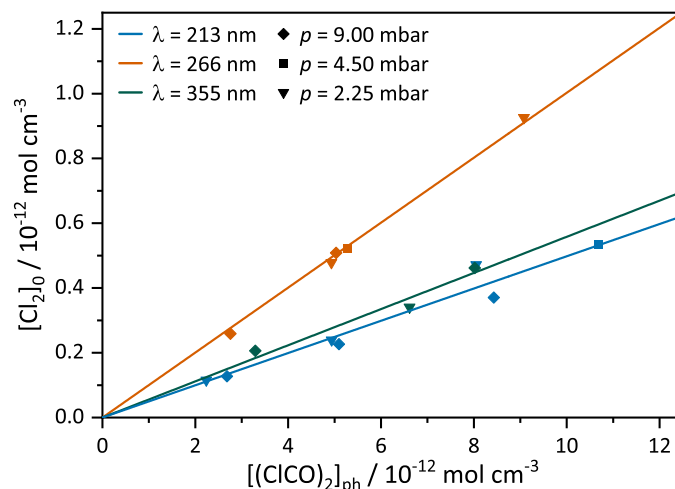


**Figure 5.6:** Quantum yield plot for  $(\text{ClCO})_2$  photolysis at 213 nm (blue), 266 nm (orange), and 355 nm (green).  $[(\text{ClCO})_2]_{\text{ph}}$  denotes the concentration of photolyzed  $(\text{ClCO})_2$  as determined from the depletion of the  $(\text{ClCO})_2$  TOF-MS signal.  $[\text{Cl}_2]_0$  is the initial  $\text{Cl}_2$  concentration determined by the kinetic analysis of the transient  $\text{Cl}_2$  profiles. Individual data points at different pressures are shown as symbols alongside zero-point linear fits for all three wavelengths. The slopes correspond to  $\phi(\text{Cl}_2)$  at the respective wavelengths.

photolysis fractions (7% on average), and the  $\text{Cl}_2$  calibration factor (2%), have been accounted for as well. They were added in quadrature, thereby allowing for error compensation of these three contributions. The total uncertainty for  $\phi(\text{Cl}_2)$  was calculated by adding this quadrature component and the individual contributions for  $k_4$ ,  $k_5$ ,  $r$ , and the scatter.  $k_5$  represents the largest source of the total uncertainty (contributing up to 18% to the relative error), followed by the uncertainty of the  $(\text{ClCO})_2$  photolysis fraction (7%, with one-to-one impact on  $\phi(\text{Cl}_2)$ ).

## 5.4 Discussion

### Thermal ClCO decomposition

Nicovich et al. [13] performed laser photolysis experiments on  $\text{Cl}_2/\text{CO}/\text{M}$  mixtures ( $\text{M} = \text{N}_2$ ,  $\text{CO}$ ,  $\text{Ar}$ ,  $\text{CO}_2$ ) and detected kinetic profiles of  $\text{Cl}$  atoms by time-resolved resonance fluorescence spectroscopy. Temperature- and pressure-dependent measurements (185–260 K, 19–266 mbar) of the equilibration kinetics of the reaction  $\text{Cl} + \text{CO} + \text{M} \rightleftharpoons \text{ClCO} + \text{M}$  could be described by the Arrhenius expressions  $k_{-4} = (3.8 \pm 1.3) \times 10^{13} \times \exp[-(810 \pm 70) \text{ K}/T] \text{ cm}^6 \text{ mol}^{-2} \text{ s}^{-1}$  and  $k_4 = (2.5 \pm 1.9) \times 10^{14} \times \exp[-(2960 \pm 160) \text{ K}/T] \text{ cm}^3 \text{ mol}^{-1} \text{ s}^{-1}$  for  $\text{N}_2/\text{CO}$  buffer gas mixtures, corresponding to  $k_4(295 \text{ K}) \approx 1.1 \times 10^{10} \text{ cm}^3 \text{ mol}^{-1} \text{ s}^{-1}$ . Nicovich et al. also reported relative collision efficiency of  $\beta(\text{N}_2) : \beta(\text{Ar}) = 1.0 : 0.8$ , which are partially based on a study of Clark et al. [36]. The latter also investigated the reverse reaction  $\text{Cl} + \text{CO} + \text{M}$  in  $\text{Ar}$  buffer gas in a discharge flow reactor with  $\text{Cl}$  profiles inferred from measured  $\text{Cl}_2$  red afterglow intensities. Direct measurements of the forward rate constant  $k_4$  have been performed by Ghosh et al. [12]. Similar to the present study, the  $(\text{ClCO})_2$  photolysis experiments showed a secondary  $\text{Cl}$  atom formation that can be ascribed to the thermal decomposition of collisionally stabilized



ClCO radicals. For photolysis wavelengths of 248 nm and 351 nm and pressures from 10.4 to 163.2 mbar, Ghosh et al. were able to extract rate constants from the Cl profiles measured by atomic resonance fluorescence, yielding  $k_4(294 \text{ K}) = 1.0 \times 10^{10} \text{ cm}^3 \text{ mol}^{-1} \text{ s}^{-1}$  in  $\text{N}_2$  buffer gas, and  $k_4(298 \text{ K}) = 8.4 \times 10^9 \text{ cm}^3 \text{ mol}^{-1} \text{ s}^{-1}$  in He buffer gas. Taking into account the somewhat different relative collision efficiencies of  $\text{N}_2$ , Ar, and He, all previous values are in very good agreement with our data for Ar buffer gas,  $k_4(295 \text{ K}) = (1.08 \pm 0.10) \times 10^{10} \text{ cm}^3 \text{ mol}^{-1} \text{ s}^{-1}$ .

### Collisional stabilization of ClCO\*

Data for the wavelength- and pressure-dependent rate constant ratio of ClCO\* collisional deactivation and unimolecular ClCO\* decomposition,  $r = k_3[\text{M}]/k_2$ , is sparse. Our results can only be compared with approximate values derived from the reported Cl atom yields  $\phi_{\text{ph}}(\text{Cl})$  and  $\phi_{\text{tot}}(\text{Cl})$  of Ghosh et al. [12]. Here,  $\phi_{\text{tot}}(\text{Cl})$  corresponds to the total Cl atom yield, including Cl atoms from thermal decomposition of collisionally stabilized ClCO, and  $\phi_{\text{ph}}(\text{Cl})$  denotes the "prompt" Cl yield from direct photolysis (reaction 1a and 2). For example, Ghosh et al. determined  $\phi_{\text{ph}}(\text{Cl}) = (1.74 \pm 0.32)$  and  $\phi_{\text{tot}}(\text{Cl}) = (2.04 \pm 0.36)$  ( $2\sigma$  precision) for 248 nm photolysis of oxalyl chloride in He buffer gas at a total pressure of 33.5 mbar, corresponding to  $r = (\phi_{\text{tot}} - \phi_{\text{ph}})/(\phi_{\text{ph}} - \phi_{\text{tot}}/2) = (2.04 - 1.74)/(1.74 - 2.04/2) = 0.42$ . Note that  $r = \infty$  corresponds to complete collisional stabilization of ClCO\* ( $\phi_{\text{ph}} = \phi_{\text{tot}}/2$ ) and that  $r = 0$  indicates that all ClCO\* undergoes direct unimolecular decomposition ( $\phi_{\text{ph}} = \phi_{\text{tot}}$ ).

Figure 5.7 summarizes results for  $r = k_3[\text{M}]/k_2$  from this work (filled symbols) in comparison with values calculated from the work of Ghosh et al. (open symbols) [12]. The approximate  $r$

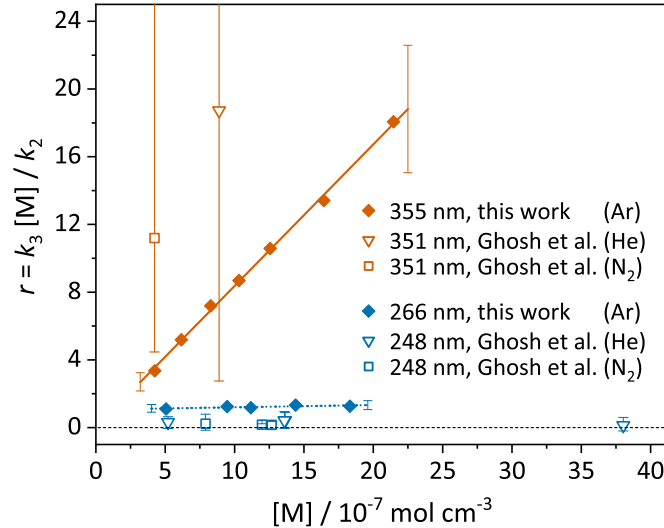


**Figure 5.7:** Rate constant ratio  $r = k_3[\text{M}]/k_2$  as function of  $[\text{M}]$  for  $(\text{ClCO})_2$  photolysis at 266 nm (blue) and 355 nm (orange) in Ar buffer gas from this work (closed symbols). Comparison with data measured at 248 nm (blue) and 351 nm (orange) in  $\text{N}_2$  or He buffer gas from the work of Ghosh et al. (open symbols) [12]. The values for  $r$  from Ref. 12 were calculated with  $r = (\phi_{\text{tot}}(\text{Cl}) - \phi_{\text{ph}}(\text{Cl})) / (\phi_{\text{ph}}(\text{Cl}) - \phi_{\text{tot}}(\text{Cl})/2)$ .  $\phi_{\text{tot}}(\text{Cl})$  corresponds to the total Cl atom yield and  $\phi_{\text{ph}}(\text{Cl})$  to the "prompt" Cl atom yield from reactions 1a and 2. The error bars stem from the analysis of the kinetic HCl profiles (this work) and the reported  $1\sigma$  uncertainty levels of  $\phi_{\text{tot}}(\text{Cl})$  and  $\phi_{\text{ph}}(\text{Cl})$  (Ref. 12).

values derived from the original Ghosh et al. data fall into the range  $0 < r < 1.4$  for 248 nm photolysis and  $2.7 < r < \infty$  for 351 nm photolysis. The wide range of values results from their reported uncertainties for  $\phi_{\text{tot}}(\text{Cl})$  and  $\phi_{\text{tot}}(\text{Cl})$ , where we already accounted for a reduced  $1\sigma$  uncertainty level instead of  $2\sigma$ . On average,  $r \approx 0.27$  (248 nm,  $12.8 \text{ mbar} \leq p \leq 93.6 \text{ mbar}$ ) and  $r \approx 15$  (351 nm,  $p = 10.4$  and  $21.9 \text{ mbar}$ ) is obtained. These indirectly derived values are essentially consistent with our results. Both show the expected, significant decrease of collisional stabilization of the  $\text{ClCO}^*$  intermediate with decreasing photolysis wavelength.

Whereas the  $\mu\text{s}$  time resolution of our experiments uncovered the fast  $\text{ClCO}^*/\text{ClCO}$  kinetics and yielded reliable results for the pressure dependence of the deactivation step (reaction 3), the focus of the Ghosh et al. study was more on the quantification of the total Cl quantum yield. For 193 nm and 248 nm photolysis, their data are consistent with  $\phi_{\text{tot}}(\text{Cl}) \approx 2$ . However, for 351 nm photolysis in  $\text{N}_2$ , with  $\phi_{\text{tot}}(\text{Cl}) = (1.83 \pm 0.16)$  at  $p = 10.4 \text{ mbar}$  and  $\phi_{\text{tot}}(\text{Cl}) = (0.88 \pm 0.06)$  at  $p = 148.1 \text{ mbar}$ , a pronounced decrease of the total Cl atom yield was observed, consistent with Stern-Volmer collisional quenching of the photoexcited  $(\text{ClCO})_2$  molecule. Here, we would like to point out that an alternative interpretation is also possible, namely the collisional stabilization of a rapidly formed photoproduct such as phosgene,  $\text{Cl}_2\text{CO}$  (see below).

### Direct $\text{Cl}_2$ formation

Although our obtained direct Cl formation photolysis quantum yields of  $\phi(\text{Cl}_2)$  of  $(5.0 \pm 1.6)\%$  at 213 nm,  $(10.0 \pm 3.3)\%$  at 266 nm, and  $(5.6 \pm 2.0)\%$  at 355 nm are below the lower limit of  $\phi(\text{Cl}_2) > 14\%$  determined by Huang et al. [14] for 248 nm photolysis, they still support direct  $\text{Cl}_2$  formation as an active process in the UV photodecomposition of  $(\text{ClCO})_2$ . As already outlined in the Introduction in more detail, their combined experimental/theoretical value was based on an incomplete PES, making lower  $\text{Cl}_2$  yields more likely.

In order to clarify the issue of direct  $\text{Cl}_2$  formation, we have completed the ground-state potential energy diagram by considering additional bond-fission and molecular elimination channels. By limiting ourselves to the ground-state potential, we implicitly assume that a rapid relaxation process of electronically excited  $(\text{ClCO})_2$  takes place after photoexcitation. Although this approach has already been used successfully many times [37–39], it is clear that excited-state photodynamics can become very important, especially at higher excitation energies. Thus, the following discussion offers only basic orientation on possible reaction channels and branching fractions.

Initially, CCSD(T)/cc-pVTZ//B3LYP/cc-pVTZ calculations have been performed for the stationary points of the PES, hence the same level of theory used by Huang et al. [14]. However, since this method yielded a  $\text{ClCO}$  bond dissociation energy of 13.4 kJ/mol, which is not compatible with the value of 31.3 kJ/mol calculated from accurate thermodynamic data taken from the ATcT database [10], we instead proceeded with the G4 composite method. A comparison of G4 and CCSD(T) energies of reactants, intermediates, transition states, and products can be found in Tab. A.3 in the Supplementary Material, e.g., yielding a  $\text{ClCO}$  bond dissociation energy of 25.8 kJ/mol. The G4 formation enthalpies for  $(\text{ClCO})_2$ ,  $\text{Cl}_2\text{CO}$  and  $\text{ClCO}$  also agree well with the corresponding literature values (see Tab. A.4 in the Supplementary Material). Figure 5.8 shows

the G4 potential energy diagram for the photofragmentation of  $(\text{ClCO})_2$ , the photon energies for photolysis at 213 nm (561.6 kJ/mol), 266 nm (449.7 kJ/mol), and 355 nm (337.0 kJ/mol) are indicated as colored dashes as well. Structures for the transition states TS1–5 are provided in Fig. A.4 and Tab. A.5 in the Supplementary Material.

The right side of Fig. 5.8 depicts the Cl and  $\text{Cl}_2$  formation pathways discussed by Huang et al. [14], including the roaming-like Cl atom shift rearrangement via TS1 (302.5 kJ/mol) to  $\text{ClC(O)-COCl}$ , followed by several steps finally forming  $2 \text{ Cl} + 2 \text{ CO}$ .  $\text{Cl}_2$  elimination can take place over TS3 with an energy barrier of 401.5 kJ/mol. We did not include the high-energy alternative Cl-forming pathways with energy barriers well above 500 kJ/mol that can be safely neglected. Instead, on the left side of Fig. 5.8, we added the barrierless C-C bond dissociation pathway forming two  $\text{ClCO}$  radicals (280.5 kJ/mol) that can undergo subsequent C-Cl bond dissociation to yield  $\text{Cl} + \text{CO}$ . Most importantly, we have identified a low-lying decomposition pathway with a barrier of merely 161.6 kJ/mol forming phosgene,  $\text{Cl}_2\text{CO}$ , and  $\text{CO}$  via TS4. This reaction channel is characterized by a Cl-transfer and simultaneous C-C bond cleavage via a three-centered transition state. Despite the entropically demanding tight TS structure, due to the comparably low energy barrier (118.9 kJ/mol lower than the competing barrierless C-C bond fission with loose TS structure), highly vibrationally excited  $(\text{ClCO})_2$  from the photolysis will decompose to form phosgene to a large extent. In turn,  $\text{Cl}_2\text{CO}$  can undergo C-Cl bond fission (306.3 kJ/mol) yielding Cl atoms or  $\text{Cl}_2$  elimination can take place via TS5 (339.5 kJ/mol). Note that the barrier height of TS5 is 62 kJ/mol lower than  $\text{Cl}_2$  formation via TS3, the latter of which was discussed as the main  $\text{Cl}_2$ -forming channel by Huang et al.

Both for photodissociation at 213 nm (561.6 kJ/mol) and 266 nm (449.7 kJ/mol), four Cl and two  $\text{Cl}_2$  forming pathways are energetically accessible on the ground-state PES. The product branching fractions critically depend on the specific rate constants and exact energy barriers of

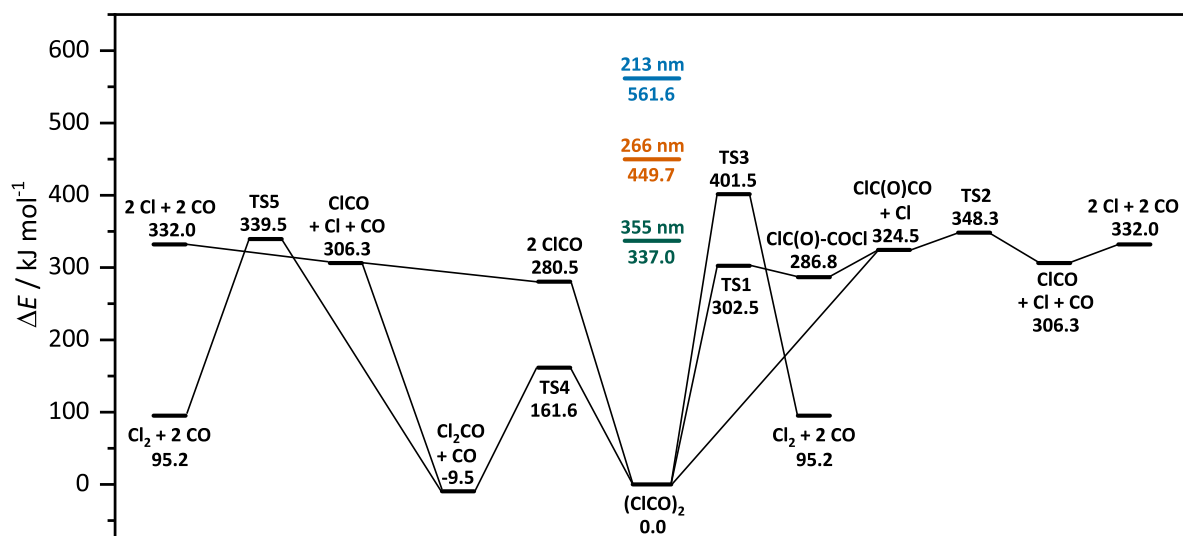


**Figure 5.8:** Ground-state potential energy diagram for the photofragmentation of  $(\text{ClCO})_2$ . Energies were calculated on the G4 level of theory.

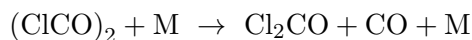
the different channels as well as the energy partitioning of the resulting intermediates that may undergo further decomposition. At sufficiently high pressure, they are also influenced by collisional energy transfer processes. Keeping in mind that photodissociation from electronically excited states may become important as well, we refrained from a detailed RRKM-type analysis to predict quantitative channel branching fractions. Qualitatively, the presented PES is well compatible with a competitive  $\text{Cl}_2$  formation from  $\text{Cl}_2\text{CO}$  via TS5, which is only 33.2 kJ/mol above the lowest-lying Cl atom forming C-C bond fission channel.

Note, however, that the energy barrier for direct  $\text{Cl}_2$  formation via TS5 (339.5 kJ/mol) and even more so via TS3 (401.5 kJ/mol) is higher than the energy provided by a 355 nm (337.0 kJ/mol) photon. Therefore, the experimentally obtained quantum yield of  $(5.6 \pm 2.0)\%$  for direct  $\text{Cl}_2$  formation at 355 nm is puzzling. Next to uncertainties in the G4 energy calculations, this finding may also indicate a yet unidentified, fast  $\text{Cl}_2$  formation pathway from secondary chemistry. In principle, this could be the reaction  $\text{Cl} + \text{ClCO}^*$  which might be faster due to the excited ClCO radical. In order to check for possible bias, we have estimated the maximum reasonable contribution of this reaction to the observed  $\text{Cl}_2$  yield as follows: First, with the rate constant ratio  $r = k_3[\text{M}]/k_2$  kept fixed, the smallest possible  $k_2$  value still compatible with the measured HCl concentration-time profiles was chosen to maximize the lifetime of the  $\text{ClCO}^*$  radical in the numerical simulations. Second, the rate constant of the reaction  $\text{Cl} + \text{ClCO}^*$  was set equal to the Lennard-Jones collision rate constant  $k = 1.8 \times 10^{14} \text{ cm}^3 \text{ mol}^{-1} \text{ s}^{-1}$ , which has been estimated based on Lennard-Jones parameters of Cl ( $\sigma = 3.55 \text{ \AA}$ ,  $\epsilon/k_B = 75 \text{ K}$ ) and OCS ( $\sigma = 4.13 \text{ \AA}$ ,  $\epsilon/k_B = 335 \text{ K}$ ). This corresponds to a 40-fold increase of the rate constant compared to  $k_5$  for ClCO. In this way, about 25–40% of the fast  $\text{Cl}_2$  formation could be attributed to this reaction, thereby reducing the photolysis quantum yield of direct  $\text{Cl}_2$  formation to  $\phi_{\min}(\text{Cl}_2) = 3.0\%$  at 213 nm, 7.1% at 266 nm, and 4.2% at 355 nm. This would be a significant effect on the quantum yield results. However, since this calculation is a very conservative estimate of the maximum possible bias, we take these values rather as confirmation that a noticeable influence of these secondary species can actually almost be ruled out. The general statement that photolysis leads directly to chlorine would not change either.

## Role of $\text{Cl}_2\text{CO}$

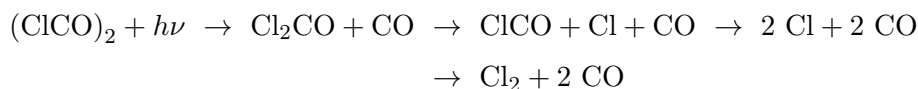
The potential energy diagram in Fig. 5.8 shows that the unexpectedly low barrier for phosgene formation makes this reaction channel the most likely dissociation channel on the ground-state potential energy surface. Even though excited-state photochemistry may prevail for deep UV photolysis, it is nevertheless surprising that little attention has been paid to this potential photodissociation channel so far. It is known from a few experimental studies that  $(\text{ClCO})_2$  decomposition yields phosgene. Pola [40] observed  $\text{Cl}_2\text{CO}$  by infrared spectroscopy in  $\text{SF}_6$ -sensitized  $(\text{ClCO})_2$  decomposition experiments. Since the addition of the radical scavenger NO did not change the resulting  $\text{Cl}_2\text{CO}$  yields, it was concluded that  $(\text{ClCO})_2$  reacts to  $\text{Cl}_2\text{CO}$  and

CO in a concerted manner:

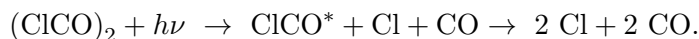


Also, in a matrix-isolation study by Schroeder et al. [41], UV photolysis of  $(\text{ClCO})_2$  was found to generate  $\text{Cl}_2\text{CO}$  and CO. Moreover, UV photodissociation experiments of phosgene at 235 nm have been performed by Maul et al. [42]. In their TOF-MS study, Cl atoms were detected by resonance-enhanced multiphoton ionization (REMPI) in two spin-orbit states. A detailed analysis of the kinetic energy spectra revealed that photodissociation is dominated by the concerted three-body process,  $\text{Cl}_2\text{CO} \rightarrow 2 \text{Cl} + \text{CO}$ , rather than the fast consecutive reaction sequence  $\text{Cl}_2\text{CO} \rightarrow \text{ClCO} + \text{Cl} \rightarrow 2 \text{Cl} + \text{CO}$ . However, the authors also mention the possibility of  $\text{Cl}_2$  formation via  $\text{Cl}_2\text{CO} \rightarrow \text{Cl}_2 + \text{CO}$ , but were not able to draw any conclusions with regard to the importance of this  $\text{Cl}_2$  elimination channel.

Combining the few experimental results with our findings of the respective energy barriers, it is well conceivable that a reaction sequence according to



can contribute to both the overall Cl atom and  $\text{Cl}_2$  photodissociation yields. Such a photodissociation mechanism would be in stark contrast with the previous interpretation of the photodynamics to be fully dominated by the sequence [8, 11]



Unfortunately, the experimental design of this study did not aim at elucidating the role of phosgene in the photodissociation of oxalyl chloride. Indications for phosgene as an intermediate would first and foremost be expected from the measured mass spectra (see Fig. 5.3) following  $(\text{ClCO})_2$  photolysis at a wavelength of 355 nm. Because of the low excess energy remaining in the  $\text{Cl}_2\text{CO}$  fragment for 355 nm excitation (with regard to the subsequent decomposition, see Fig. 5.8), there is the possibility to collisionally stabilize the  $\text{Cl}_2\text{CO}$  intermediate. However, the corresponding mass peaks at  $m/z$  98, 100, and 102 (see Fig. 5.3) are attributable to the fragment peaks of the excess species oxalyl chloride. Nevertheless, a detailed analysis of the photolysis-induced signal depletion of the fragment peaks  $\text{ClCO}^+$  and  $\text{Cl}_2\text{CO}^+$ , which should be the same for all  $(\text{ClCO})_2$  related mass peaks, actually provides a first hint at the  $\text{Cl}_2\text{CO}$  intermediate. Whereas the average ratio of signal depletion of the  $\text{Cl}_2\text{CO}^+$  and  $\text{ClCO}^+$  mass signals is equal to 1 within uncertainty limits ( $2\sigma$  error of the mean value) for 213 nm ( $1.10 \pm 0.16$ ) and 266 nm ( $0.97 \pm 0.21$ ), it is well below 1 for 355 nm photolysis ( $0.21 \pm 0.29$ ). This indicates an additional signal contribution to the  $\text{Cl}_2\text{CO}$  signal – most likely stemming from the  $\text{Cl}_2\text{CO}$  intermediate itself. Clearly, further experiments are needed to specifically investigate and constrain the contribution of the phosgene dissociation pathway.

## 5.5 Summary

In this work, two key aspects regarding the UV photolysis of  $(\text{ClCO})_2$  have been investigated. Firstly, the unimolecular  $\text{ClCO}$  decomposition was investigated at 295 K in Ar buffer gas by kinetic analysis of  $\text{HCl}$  profiles measured in  $(\text{ClCO})_2/\text{C}_2\text{H}_6/\text{Ar}$  mixtures after UV photolysis at 266 nm and 355 nm. We derived a rate constant of  $k_4(295 \text{ K}) = (1.08 \pm 0.10) \times 10^{10} \text{ cm}^3 \text{ mol}^{-1} \text{ s}^{-1}$  in Ar buffer gas, which is in very good agreement with previous studies. The analysis of the  $\text{HCl}$  profiles also provided values for the rate constant ratio between collisional relaxation and unimolecular decomposition of the  $\text{ClCO}^*$  radical.

Secondly, the direct  $\text{Cl}_2$  formation channel of  $(\text{ClCO})_2$  photolysis raised by Huang et al. [14] was studied using measured  $\text{Cl}_2$  concentrations in  $(\text{ClCO})_2/\text{Ar}$  mixtures after UV photolysis at 213 nm, 266 nm, and 355 nm. A comprehensive kinetic analysis of the  $\text{Cl}_2$  profiles yielded photolysis quantum yields  $\phi(\text{Cl}_2)$  of  $(5.0 \pm 1.6)\%$  at 213 nm,  $(10.0 \pm 3.3)\%$  at 266 nm, and  $(5.6 \pm 2.0)\%$  at 355 nm. While earlier studies on the UV photolysis of  $(\text{ClCO})_2$  were compatible with  $\phi_{\text{tot}}(\text{Cl}) = 2$ , the results of our work strongly suggest that direct formation of  $\text{Cl}_2$  is an active process in the UV photodecomposition of  $(\text{ClCO})_2$ . However, our photolysis quantum yields are lower than the value of  $\phi(\text{Cl}_2) > 14\%$  provided by Huang et al. [14] for 248 nm photolysis, which in retrospect should probably be regarded as an upper limit. It is expected that  $\phi(\text{Cl}_2)$  strongly depends on the accessible decomposition pathways at a given excess energy and hence photolysis wavelength. The ground-state potential energy diagram reveals that both  $\text{Cl}_2$  and  $\text{Cl}$  can be formed by the decomposition of energetically excited phosgene, which has not previously been considered as a key intermediate for the photodissociation of  $(\text{ClCO})_2$ .

Further experimental and theoretical work is needed to complete the picture of the wavelength- and pressure-dependent absolute quantum yields of all photoproducts. Such studies should focus on the phosgene intermediate, on the relative contributions of ground-state and excited-state photodissociation, and on photolysis experiments over a wide range of wavelengths.

## Acknowledgments and Funding

Part of this work was performed at the VUV beamline of the Swiss Light Source (Paul Scherrer Institute, PSI) under Proposal No. 20190780. We are grateful to have received a poster award at the 12th International Conference on Chemical Kinetics (ICCK) in Hefei (China), which motivated us to submit this paper to the ICCK special conference issue. We would also like to thank Friedrich Temps and Joachim Gripp (Kiel University) for providing the Nd:YAG photolysis laser and technical support, respectively.

## References

- [1] A. V. Baklanov, L. N. Krasnoperov, Oxalyl Chloride - A Clean Source of Chlorine Atoms for Kinetic Studies, *J. Phys. Chem. A* **2001**, *105*, 97–103, DOI [10.1021/jp0019456](https://doi.org/10.1021/jp0019456).
- [2] E. V. Shafir, I. R. Slagle, V. D. Knyazev, Kinetics of the Self-Reaction of  $\text{C}_2\text{H}_5$  Radicals, *J. Phys. Chem. A* **2003**, *107*, 6804–6813, DOI [10.1021/jp034876e](https://doi.org/10.1021/jp034876e).
- [3] A. Matsugi, A. Miyoshi, Kinetics of the self-reactions of benzyl and o-xyllyl radicals studied by cavity ring-down spectroscopy, *Chem. Phys. Lett.* **2012**, *521*, 26–30, DOI [10.1016/j.cplett.2011.11.043](https://doi.org/10.1016/j.cplett.2011.11.043).



- [4] O. Welz, M. P. Burke, I. O. Antonov, C. F. Goldsmith, J. D. Savee, D. L. Osborn, C. A. Taatjes, S. J. Klippenstein, L. Sheps, New Insights into Low-Temperature Oxidation of Propane from Synchrotron Photoionization Mass Spectrometry and Multiscale Informatics Modeling, *J. Phys. Chem. A* **2015**, *119*, 7116–7129, DOI [10.1021/acs.jpca.5b01008](https://doi.org/10.1021/acs.jpca.5b01008).
- [5] D. Schleier, P. Constantinidis, N. Faßheber, I. Fischer, G. Friedrichs, P. Hemberger, E. Reusch, B. Sztáray, K. Voronova, Kinetics of the  $\alpha$ -C<sub>3</sub>H<sub>5</sub> + O<sub>2</sub> reaction, investigated by photoionization using synchrotron radiation, *Phys. Chem. Chem. Phys.* **2018**, *20*, 10721–10731, DOI [10.1039/c7cp07893e](https://doi.org/10.1039/c7cp07893e).
- [6] A. V. Baklanov, L. N. Krasnoperov, UV Absorption Spectrum and Rate Constant for Self-Reaction of Silyl Radicals, *J. Phys. Chem. A* **2001**, *105*, 4917–4922, DOI [10.1021/jp0041981](https://doi.org/10.1021/jp0041981).
- [7] J. Zádor, H. Huang, O. Welz, J. Zetterberg, D. L. Osborn, C. A. Taatjes, Directly measuring reaction kinetics of  $\cdot$ QOOH – a crucial but elusive intermediate in hydrocarbon autoignition, *Phys. Chem. Chem. Phys.* **2013**, *15*, 10753–10760, DOI [10.1039/c3cp51185e](https://doi.org/10.1039/c3cp51185e).
- [8] M. Ahmed, D. Blunt, D. Chen, A. G. Suits, UV photodissociation of oxalyl chloride yields four fragments from one photon absorption, *J. Chem. Phys.* **1997**, *106*, 7617–7624, DOI [10.1063/1.473764](https://doi.org/10.1063/1.473764).
- [9] B. Ruscic, R. E. Pinzon, G. von Laszewski, D. Kodeboyina, A. Burcat, D. Leahy, D. Montoy, A. F. Wagner, Active Thermochemical Tables: Thermochemistry for the 21st century, *J. Phys.: Conf. Ser.* **2005**, *16*, 561–570, DOI [10.1088/1742-6596/16/1/078](https://doi.org/10.1088/1742-6596/16/1/078).
- [10] B. Ruscic, D. H. Bross, Active Thermochemical Tables (ATcT) enthalpies of formation values based on ver. 1.122r of the Thermochemical Network (2021), <https://atct.anl.gov/>, **2021**.
- [11] N. Hemmi, A. G. Suits, Photodissociation of Oxalyl Chloride at 193 nm Probed via Synchrotron Radiation, *J. Phys. Chem. A* **1997**, *101*, 6633–6637, DOI [10.1021/jp970786w](https://doi.org/10.1021/jp970786w).
- [12] B. Ghosh, D. K. Papanastasiou, J. B. Burkholder, Oxalyl chloride, ClC(O)C(O)Cl: UV/vis spectrum and Cl atom photolysis quantum yields at 193, 248, and 351 nm, *J. Chem. Phys.* **2012**, *137*, 164315/1–12, DOI [10.1063/1.4755769](https://doi.org/10.1063/1.4755769).
- [13] J. M. Nicovich, K. D. Kreutter, P. H. Wine, Kinetics and thermochemistry of ClCO formation from the Cl + CO association reaction, *J. Chem. Phys.* **1990**, *92*, 3539–3544, DOI [10.1063/1.457862](https://doi.org/10.1063/1.457862).
- [14] T.-K. Huang, B.-J. Chen, K.-C. Lin, L. Lin, B.-J. Sun, A. H. H. Chang, Cl<sub>2</sub> Elimination in 248 nm Photolysis of (COCl)<sub>2</sub> Probed with Cavity Ring-Down Absorption Spectroscopy, *J. Phys. Chem. A* **2017**, *121*, 2888–2895, DOI [10.1021/acs.jpca.6b12810](https://doi.org/10.1021/acs.jpca.6b12810).
- [15] R. J. Kee, F. M. Ruply, J. A. Miller, Chemkin-II: A Fortran Chemical Kinetics Package for the Analysis of Gas-Phase Chemical Kinetics, tech. rep., Sandia National Laboratories, Livermore, California, Sandia Report SAND-89-8009, **1989**, DOI [10.2172/5681118](https://doi.org/10.2172/5681118).
- [16] E. Goos, A. Burcat, B. Ruscic, Extended Third Millennium Ideal Gas Thermochemical Database with updates from Active Thermochemical Tables, <http://garfield.chem.elte.hu/Burcat/burcat.html>, last access Nov. 2023, **2016**.
- [17] D. Baulch, J. Duxbury, S. Grant, D. Montague, Evaluated Kinetic Data for High Temperature Reactions; Volume 4: Homogeneous Gas Phase Reactions of Halogen-and Cyanide-Containing Species, *J. Phys. Chem. Ref. Data* **1981**, *10*, 343–345.
- [18] H. Hippler, J. Troe, Flash photolysis study of the recombination of chlorine atoms in the presence of various inert gases and NO, *Int. J. Chem. Kinet.* **1976**, *8*, 501–510, DOI [10.1002/kin.550080404](https://doi.org/10.1002/kin.550080404).
- [19] M. G. Bryukov, I. R. Slagle, V. D. Knyazev, Kinetics of Reactions of Cl Atoms with Ethane, Chloroethane, and 1, 1-Dichloroethane, *J. Phys. Chem. A* **2003**, *107*, 6565–6573, DOI [10.1021/jp0275138](https://doi.org/10.1021/jp0275138).
- [20] R. Timonen, K. Kalliorinne, J. Koskikallio, Kinetics of Reactions of Methyl and Ethyl Radicals with Chlorine in the Gas Phase Studied by Photochlorination of Methane. *Acta Chem. Scand.* **1986**, *40*, 459–466, DOI [10.3891/acta.chem.scand.40a-0459](https://doi.org/10.3891/acta.chem.scand.40a-0459).

- [21] P. W. Seakins, E. L. Woodbridge, S. R. Leone, A laser flash photolysis, time-resolved Fourier transform infrared emission study of the reaction  $\text{Cl} + \text{C}_2\text{H}_5 \rightarrow \text{HCl}(\text{v}) + \text{C}_2\text{H}_4$ , *J. Phys. Chem.* **1993**, *97*, 5633–5642, DOI [10.1021/j100123a029](https://doi.org/10.1021/j100123a029).
- [22] J. A. Silver, Frequency-modulation spectroscopy for trace species detection: theory and comparison among experimental methods, *Appl. Opt.* **1992**, *31*, 707–717, DOI [10.1364/ao.31.000707](https://doi.org/10.1364/ao.31.000707).
- [23] G. Friedrichs, Sensitive Absorption Methods for Quantitative Gas Phase Kinetic Measurements. Part 1: Frequency Modulation Spectroscopy, *Z. Phys. Chem.* **2008**, *222*, 1–30, DOI [10.1524/zpch.2008.222.1.1](https://doi.org/10.1524/zpch.2008.222.1.1).
- [24] M. Stuhr, N. Faßheber, G. Friedrichs, Single-tone mid-infrared frequency modulation spectroscopy for sensitive detection of transient species, *Opt. Express* **2019**, *27*, 26499–26512, DOI [10.1364/oe.27.026499](https://doi.org/10.1364/oe.27.026499).
- [25] M. Stuhr, G. Friedrichs, Mid-infrared Frequency Modulation Detection of HCN and Its Reaction with O Atoms behind Shock Waves, *J. Phys. Chem. A* **2022**, *126*, 9485–9496, DOI [10.1021/acs.jpca.2c06817](https://doi.org/10.1021/acs.jpca.2c06817).
- [26] G. Friedrichs, H. G. Wagner, Quantitative FM spectroscopy at high temperatures: The detection of  $^1\text{CH}_2$  behind shock waves, *Z. Phys. Chem.* **2000**, *214*, 1723–1746, DOI [10.1524/zpch.2000.214.12.1723](https://doi.org/10.1524/zpch.2000.214.12.1723).
- [27] I. Gordon et al., The HITRAN2016 molecular spectroscopic database, *J. Quant. Spectrosc. Radiat. Transfer* **2017**, *203*, 3–69, DOI [10.1016/j.jqsrt.2017.06.038](https://doi.org/10.1016/j.jqsrt.2017.06.038).
- [28] C. Boulet, P.-M. Flaud, J.-M. Hartmann, Infrared line collisional parameters of HCl in argon, beyond the impact approximation: Measurements and classical path calculations, *J. Chem. Phys.* **2004**, *120*, 11053–11061, DOI [10.1063/1.1714794](https://doi.org/10.1063/1.1714794).
- [29] D. F. Davidson, A. Y. Chang, R. K. Hanson, Laser photolysis shock tube for combustion kinetics studies, *Symp. (Int.) Combust.* **1989**, *22*, 1877–1885, DOI [10.1016/S0082-0784\(89\)80202-4](https://doi.org/10.1016/S0082-0784(89)80202-4).
- [30] M. Johnson, A. Bodi, L. Schulz, T. Gerber, Vacuum ultraviolet beamline at the Swiss Light Source for chemical dynamics studies, *Nucl. Instrum. Methods Phys. Res. Sect. A* **2009**, *610*, 597–603, DOI [10.1016/j.nima.2009.08.069](https://doi.org/10.1016/j.nima.2009.08.069).
- [31] A. Bodi, P. Hemberger, T. Gerber, B. Sztáray, A new double imaging velocity focusing coincidence experiment:  $i^2\text{PEPICO}$ , *Rev. Sci. Instrum.* **2012**, *83*, 083105/1–8, DOI [10.1063/1.4742769](https://doi.org/10.1063/1.4742769).
- [32] B. Sztáray, K. Voronova, K. G. Torma, K. J. Covert, A. Bodi, P. Hemberger, T. Gerber, D. L. Osborn, CRF-PEPICO: Double velocity map imaging photoelectron photoion coincidence spectroscopy for reaction kinetics studies, *J. Chem. Phys.* **2017**, *147*, 013944/1–10, DOI [10.1063/1.4984304](https://doi.org/10.1063/1.4984304).
- [33] M. J. Frisch et al., Gaussian-16 Revision C.01, Gaussian Inc. Wallingford CT, **2016**.
- [34] L. A. Curtiss, P. C. Redfern, K. Raghavachari, Gaussian-4 theory, *J. Chem. Phys.* **2007**, *126*, 084108/1–12, DOI [10.1063/1.2436888](https://doi.org/10.1063/1.2436888).
- [35] H. Jiao, H.-S. Wu, Are Neutral Oxocarbons Stable?, *J. Org. Chem.* **2003**, *68*, 1475–1479, DOI [10.1021/jo026243m](https://doi.org/10.1021/jo026243m).
- [36] T. C. Clark, M. A. A. Clyne, D. H. Stedman, Mechanism of formation of triatomic molecules in atomic combination reactions. Part 1. – Formation of ClNO and ClCO in reactions of atomic chlorine, *Trans. Faraday Soc.* **1966**, *62*, 3354–3365, DOI [10.1039/tf9666203354](https://doi.org/10.1039/tf9666203354).
- [37] D. U. Andrews, B. R. Heazlewood, A. T. Maccarone, T. Conroy, R. J. Payne, M. J. T. Jordan, S. H. Kable, Photo-tautomerization of acetaldehyde to vinyl alcohol: a potential route to tropospheric acids, *Science* **2012**, *337*, 1203–1206, DOI [10.1126/science.1220712](https://doi.org/10.1126/science.1220712).
- [38] H. Fan, P.-Y. Tsai, K.-C. Lin, C.-W. Lin, C.-Y. Yan, S.-W. Yang, A. H. H. Chang, Molecular elimination of  $\text{Br}_2$  in photodissociation of  $\text{CH}_2\text{BrC}(\text{O})\text{Br}$  at 248 nm using cavity ring-down absorption spectroscopy, *J. Chem. Phys.* **2012**, *137*, 214304/1–10, DOI [10.1063/1.47673462](https://doi.org/10.1063/1.47673462).



- 
- [39] I. Sadiek, G. Friedrichs, Y. Sakai, Ab Initio and RRKM/Master Equation Analysis of the Photolysis and Thermal Unimolecular Decomposition of Bromoacetaldehyde, *J. Phys. Chem. A* **2021**, *125*, 8282–8293, DOI [10.1021/acs.jpca.1c04347](https://doi.org/10.1021/acs.jpca.1c04347).
- [40] J. Pola, IR laser driven decomposition of oxalyl chloride in presence of radical scavengers: Evidence for molecular mechanism, *Collect. Czechoslov. Chem. Commun.* **1982**, *47*, 3258–3260, DOI [10.1135/cccc19823258](https://doi.org/10.1135/cccc19823258).
- [41] W. Schroeder, M. Monnier, G. Davidovics, A. Allouche, P. Verlaque, J. Pourcin, H. Bodot, Ultraviolet photoisomerizations and FT-IR investigations of matrix isolated oxalyl halide conformers, *J. Mol. Struct.* **1989**, *197*, 227–242, DOI [10.1016/0022-2860\(89\)85165-8](https://doi.org/10.1016/0022-2860(89)85165-8).
- [42] C. Maul, T. Haas, K.-H. Gericke, F. J. Comes, Spin selectivity in the ultraviolet photodissociation of phosgene, *J. Chem. Phys.* **1995**, *102*, 3238–3247, DOI [10.1063/1.468634](https://doi.org/10.1063/1.468634).

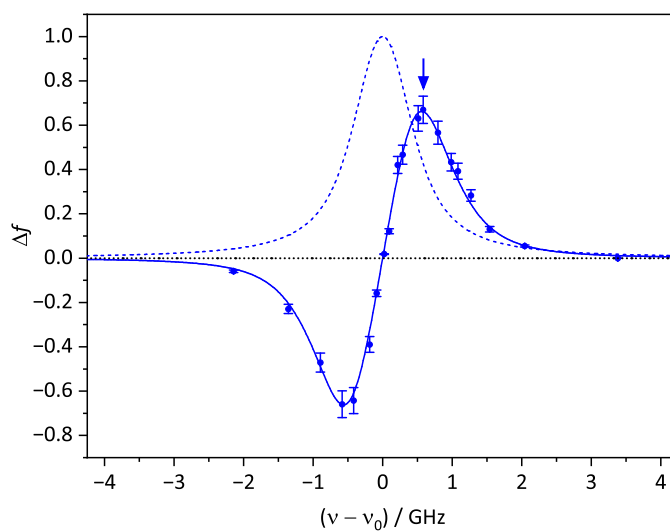


## CHAPTER 6

---

### Publication III: Quantitative and Sensitive Mid-Infrared Frequency Modulation Detection of HCN behind Shock Waves

---



Michael Stuhr<sup>a</sup>, Sebastian Hesse<sup>a</sup>, and Gernot Friedrichs<sup>a</sup>

<sup>a</sup>Institut für Physikalische Chemie, Christian-Albrechts-Universität zu Kiel, Max-Eyth-Straße 1, 24118 Kiel, Germany

*Fuels* **2021**, 2, 437–447, DOI [10.3390/fuels2040025](https://doi.org/10.3390/fuels2040025).

Own Contributions:

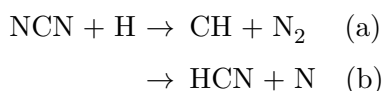
- Shock tube experiments
- Quantitative HCN detection
- Data analysis and discussion
- Writing of paper draft

## Abstract

Despite its key role for the study and modeling of nitrogen chemistry and  $\text{NO}_x$  formation in combustion processes, HCN has only rarely been detected under high-temperature conditions. Here, we demonstrate quantitative detection of HCN behind incident and reflected shock waves using a novel sensitive single-tone mid-infrared frequency modulation (mid-IR-FM) detection scheme. The temperature-dependent pressure broadening of the P(26) line in the fundamental CH stretch vibration band was investigated in the temperature range  $670 \text{ K} \leq T \leq 1460 \text{ K}$ , yielding a pressure-broadening coefficient for argon of  $2\gamma_{\text{Ar}}^{296 \text{ K}} = (0.093 \pm 0.007) \text{ cm}^{-1}\text{atm}^{-1}$  and a temperature exponent of  $n_{\text{Ar}} = 0.67 \pm 0.07$ . The sensitivity of the detection scheme was characterized by means of an Allan analysis, showing that HCN detection on the ppm mixing ratio level is possible at typical shock wave conditions. In order to demonstrate the capability of mid-IR-FM spectroscopy for future high-temperature reaction kinetic studies, we also report the first successful measurement of a reactive HCN decay profile induced by its reaction with oxygen atoms.

## 6.1 Introduction

Hydrogen cyanide (HCN) is formed by gas phase combustion reactions and during devolatilization of fuels containing organic nitrogen, e.g., biomass residues [1, 2]. The present work, which is based on the authors' contribution to the virtual 10th European Combustion Meeting 2021 [3], is motivated by the important role of HCN in thermochemical processes and as a key intermediate for modeling nitrogen chemistry in combustion, in particular for prompt-NO formation [1, 4]. Prompt-NO formation is initiated by the reaction  $\text{CH} + \text{N}_2 \rightarrow \text{NCN} + \text{H}$  [5] and the fate of the NCN radical is largely determined by the branching ratio of its subsequent reaction with H atoms [4]:



Whereas the reverse association/rearrangement channel (a) to  $\text{CH} + \text{N}_2$  exhibits a slightly negative temperature dependence, the forward channel (b) yields the so-called Fenimore products  $\text{HCN} + \text{N}$  in an activation-controlled reaction step [6–8]. As a result, the branching becomes highly temperature-dependent and switches from the  $\text{HCN} + \text{N}$  channel at high temperatures to the  $\text{CH} + \text{N}_2$  channel at low temperatures, going along with other non-Fenimore routes for NCN consumption by reactions with  $\text{H}_2$  and O atoms [4, 9, 10]. Although there is general agreement about the importance of this so-called prompt-NO switch and the HCN intermediate for  $\text{NO}_x$  modeling, significant disagreement between experiment and flame modeling studies on the one hand and theoretical rate constant predictions on the other hand remains. For example, at a typical flame temperature of 2000 K, experimental data and flame modeling results [7, 11] are consistent with a forward branching fraction of about 70%, but theory [6, 8] predicts a much lower value of about 20%. In order to resolve this issue, measurements of the branching ratio by

monitoring HCN concentration-time profiles as a direct product of the reaction  $\text{NCN} + \text{H}$  are required.

However, in contrast to quantitative detection schemes for the educt species NCN [12–14], reliable high-temperature detection of HCN is difficult and suitable detection schemes are sparse. Ex-situ detection of absolute HCN concentrations in low-pressure flames using near-infrared cavity ring down spectroscopy has been performed by Lamoureux et al. [15, 16]. Similarly, Gersen et al. determined HCN concentrations in fuel-rich methane/air flames using near-infrared wavelength modulation spectroscopy and microprobe gas sampling [17]. Measurements in the mid-infrared (mid-IR) spectral region are preferable, since the absorption line strengths in the fundamental band of the CH stretch vibration enable considerably higher sensitivity, which is especially relevant for single-shot shock tube measurements that require high time resolution and sensitivity. In-situ detection of HCN in the mid-IR range was realized with polarization spectroscopy in flames at atmospheric pressure by Sun et al. [18] and with degenerate four-wave mixing spectroscopy during straw gasification by Hot et al. [19], respectively. Both groups have chosen the P(20) rovibrational line in the  $\nu_1$  band for their measurements.

Early studies by Hanson and coworkers [20, 21] investigated the pressure broadening of several rovibrational transitions of HCN in the  $\nu_1$  band at room temperature and of the P(10) line behind shock waves using tunable diode laser spectroscopy. For species detection in the mid-IR, pressure broadening often becomes comparable to Doppler broadening at typical shock wave conditions such that the determination of accurate pressure-broadening coefficients is crucial for quantitative HCN detection. However, to the best of our knowledge and due to the limited sensitivity of conventional detection schemes, kinetic profiles of HCN have not been measured behind shock waves so far.

Frequency modulation (FM) spectroscopy offers high sensitivity and  $\mu\text{s}$  time resolution even under harsh experimental conditions [22]. FM detection schemes for shock tube applications have been successfully implemented for shock tube experiments targeting the detection of  $\text{NH}_2$  [23],  $^1\text{CH}_2$  [24], HCO [25], and OH [26] on electronic transitions in the VIS and UV spectral range. Very recently, we established single-tone frequency modulation spectroscopy in the mid-IR [27] aiming at sensitive detection of various species on their fundamental rovibrational transitions.

In this work, we report the first FM detection of HCN behind shock waves. As a prerequisite for quantitative HCN detection to measure the branching fraction of the reaction  $\text{NCN} + \text{H}$ , the high-temperature pressure-broadening coefficient of argon was determined. The spectroscopically isolated and high- $J$  P(26) absorption line at  $3228.049\text{ cm}^{-1}$  in the  $\nu_1$  CH stretch vibration band was selected to ensure high sensitivity under high-temperature conditions. Moreover, to demonstrate the capability of  $\mu\text{s}$  time-resolved detection behind shock waves, first kinetic profiles of HCN during its oxidation by oxygen atoms were recorded as well. For sure, future studies on this and other bimolecular reactions of HCN as well as on the important isomerization step of HCN to hydrogen isocyanide (HNC) [28] will benefit from the availability of a sensitive HCN detection scheme as outlined in this work.

## 6.2 Experimental

The cw-OPO-laser based FM spectrometer with external modulation of the laser beam using a resonant, single-frequency electro-optic modulator and analog demodulation electronics has been described in Ref. 27. For an outline of the operation principle of the time-resolved FM spectrometer we refer to Ref. 22. Important for a sensitive FM detection scheme for high-temperature shock tube applications is a high modulation frequency (comparable to the Doppler- and pressure-broadened linewidth of the probed absorption line) in combination with strong modulation (expressed in terms of the modulation index  $M$ , with a preferable value of  $M \geq 1$ ). Both these requirements have only recently become technically feasible in the MIR with the availability of efficient single-frequency electro-optic modulators and fast HgCdTe heterostructure photovoltaic detectors, the latter also offering a sufficiently high optical saturation power to allow for near shot-noise limited detection. Compared to the earlier version of the setup in Ref. 27, by now we have implemented several modifications to further enhance the spectrometer performance; these will be described in more detail elsewhere. Briefly, a new temperature-stabilized electro-optic modulator (EO-500T3-MWIR1, Qubig) was used to modulate the laser beam in double-pass configuration at a frequency of  $\nu_m = 489$  MHz, yielding a modulation index of  $M = 1.0$  and thus a very high value for a system operating in the mid-IR. Reduction of thermal noise contributions was achieved by a photodetector with two additional thermo-electric cooling stages (PVI-4TE-5, Vigo System), increasing the specific detectivity of the photodetector by 70% to  $D^* = 1.41 \times 10^{11} \text{ cm Hz}^{0.5} \text{ W}^{-1}$ . Finally, the analog demodulation electronics have been replaced by an all-digital 600 MHz lock-in amplifier (UHFLI, Zurich Instruments) that also served as the modulation frequency source. The low-pass of the demodulated signal was set to a bandwidth of 790 kHz, equivalent to a 10%-to-90% signal rise time of about 500 ns, hence ensuring a sufficiently fast time response to temporally resolve  $\mu\text{s}$  concentration transients.

The pressure-driven stainless-steel Kiel shock tube with an inner diameter of 81 mm has been described in detail elsewhere [29]. Shock wave conditions were calculated with a frozen chemistry/real gas code with shock wave velocities and shock wave damping measured with four fast piezoelectric sensors. Gas mixtures were prepared in a stainless-steel gas mixing system equipped with glass storage flasks and were further diluted with argon using calibrated mass flow controllers. Before the shock tube experiment, the low-pressure section of the shock tube was flushed for about 6 min with the sample gas mixture to reduce possible adsorption effects on the shock tube wall. The following gases were used as supplied (Air Liquide): HCN (calibrated mixture of  $969 \text{ ppm} \pm 29 \text{ ppm}$  in  $\text{N}_2$ ), argon as the main buffer gas (99.999%) to dilute the HCN stock mixture using mass flow controllers, variable mixtures of  $\text{H}_2/\text{N}_2$  as driver gas (both 99.999%), and  $\text{N}_2\text{O}$  (99.999%) as high-temperature source for oxygen atoms.

## 6.3 Results and Discussion

The P(26) transition at  $3228.049 \text{ cm}^{-1}$  in the  $\nu_1$  CH stretch band of HCN was selected for sensitive detection. The curves in Figure 6.1 illustrate the temperature-dependent linestrengths of selected

rovibrational transitions with different rotational quantum number  $J$  as calculated using the parameters included in the HITRAN database [30]. While at temperatures below 1100 K some HCN lines, including the P(8), P(15), and P(19) transitions shown in Figure 6.1, offer somewhat higher intensities than the selected P(26) line, due to several hot band transitions located close to the respective line centers, they are not fully spectroscopically isolated. In fact, selecting the high- $J$  P(26) line represents a compromise between a high linestrength at high temperatures and spectroscopic isolation to ensure that the recorded FM signal originates only from the absorption line of interest.

### Pressure Broadening Coefficient

Three sets of shock tube experiments were conducted to derive the temperature-dependent pressure-broadening coefficient  $2\gamma_{\text{Ar}}$  for argon. For each set with HCN mole fractions of 200 ppm, 350 ppm, and 500 ppm, respectively, the pressure and temperature behind the incident or reflected wave were kept approximately constant ( $\Delta p/p = 3.0\%$  and  $\Delta T/T = 3.0\%$ ). The experimental conditions are summarized in Table 6.1.

In order to measure the complete FM profile of the absorption line under the respective conditions, several shock tube experiments at different fixed wavelengths around the line center were performed. The linewidth of the single-frequency OPO laser system was about  $2 \times 10^{-6} \text{ cm}^{-1}$ , much below the Doppler width of  $0.014 \text{ cm}^{-1}$  (FWHM at  $T = 1000 \text{ K}$ ). Therefore, the resulting FM profile can be derived from a purely Doppler- and pressure-broadened Voigt lineshape, since convolution with the laser lineshape function is not necessary.

Example traces of HCN absorption during two shock tube experiments are shown in Figure 6.2. The blue traces in Figures 6.2b,e depict the measured pressures during the shock tube experiments

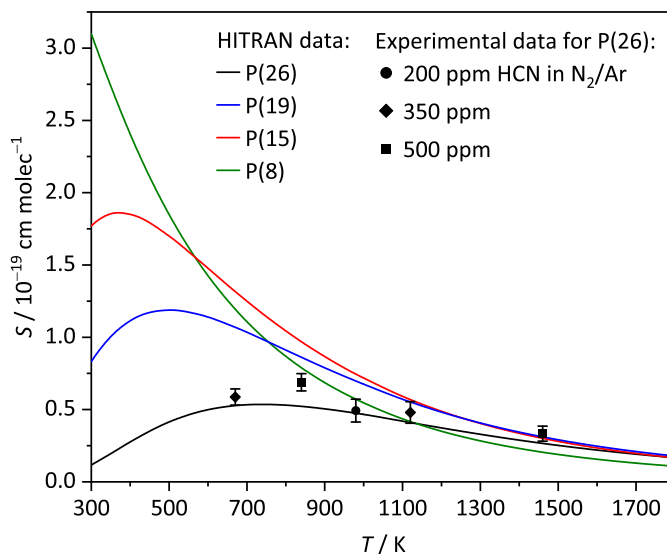


**Figure 6.1:** Temperature-dependent linestrengths  $S$  for several rovibrational transitions in the P-branch of the  $\nu_1$  band of HCN. HITRAN database [30] predictions (curves) are compared to experimental data obtained for the P(26) transition (symbols).

**Table 6.1:** Experimental conditions for FM line profile measurements behind incident (inc.) and reflected (refl.) shock waves and the corresponding total Lorentzian linewidths  $2\Gamma_{\text{total}}$  (FWHM).

	Data Set	$x_{\text{HCN}}$ / ppm	$T$ / K	$p$ / bar	$2\Gamma_{\text{total}}$ / $\text{cm}^{-1}$
1	inc.	200	980	0.54	0.0279
	refl.	200	1830	2.39	— *
2	inc.	350	670	0.32	0.0240
	refl.	350	1120	1.22	0.0631
3	inc.	500	840	0.21	0.0254
	refl.	500	1460	0.98	0.0484

\* Not used for analysis, see text.

and the black traces in Figures 6.2a,d represent the corresponding absorption signals. Note that, for the sake of clarity, FM equivalent absorption (as calculated from the finally derived lineshape parameters of this work) is shown instead of the raw FM signal.

Following the arrival of the incident and reflected shock wave, the signals exhibit step-like features reflecting the temperature- and pressure-dependent absorption cross section and the change of total density. The stable plateau signals indicate that HCN is thermally stable under the experimental conditions. For experiments with a laser wavelength close to the maximum of the absorption line, pre-shock absorption was observed as well and needed to be properly taken into account to correctly set the baseline of the signal. In contrast, due to the much narrower linewidth at pre-shock conditions, for measurements in the outer wings of the absorption line no such baseline correction was necessary. Figure 6.2c shows the measured FM profiles for data set 2 with 350 ppm HCN under incident ( $T \approx 670$  K,  $p \approx 0.32$  bar) and reflected ( $T \approx 1120$  K,  $p \approx 1.22$  bar) shock wave conditions as well as the corresponding simulated derivative-like FM lineshapes (solid curves) and the underlying conventional Voigt absorption line profiles (dashed curves). The errors for the individual data points were estimated from the uncertainties of pressure and temperature as well as from the FM signal noise. Figure 6.2f shows equivalent results for the experiments performed with an HCN mole fraction of 200 ppm. For this data set, the measured FM signals behind the reflected wave in Figure 6.2d were too weak to yield reliable lineshape data, leaving in total five distinct FM profiles with a given pressure/temperature combination to determine the pressure broadening by argon. All data in Figures 6.2c,f are shown in terms of the FM factor  $\Delta f$  as defined in Ref. 22:

$$I_{\text{FM}} = \frac{I_0}{2} \times \Delta f \times \alpha_c \times l \times G \quad (6.1)$$

Here,  $I_0$  and  $I_{\text{FM}}$  correspond to the measured signal levels of the total laser intensity and the demodulated FM intensity, respectively.  $l$  is the absorption length and  $G$  an electronic gain factor accounting for the amplification and losses of the FM signal in the demodulation circuitry. Briefly, the FM factor  $\Delta f$  can be understood as the relative FM signal measured at a given detection wavelength, normalized to the conventional narrow bandwidth absorption coefficient  $\alpha_c$  at the



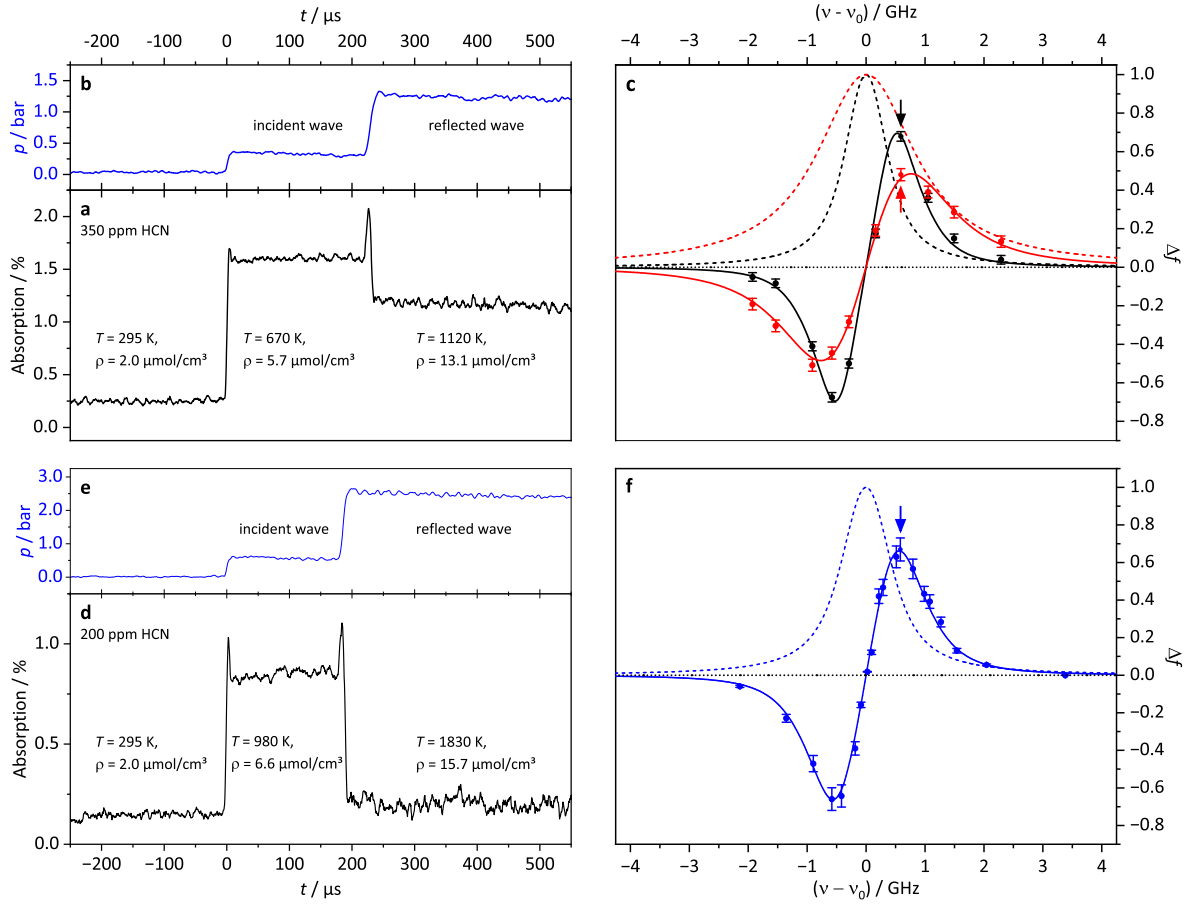


**Figure 6.2:** Typical measured HCN traces (a + d, 2 MHz sampling rate, 20 points moving average), the corresponding pressure traces (b + e), and the resulting line profiles (c + f) for the P(26) absorption line at  $\tilde{\nu} = 3228.049$   $\text{cm}^{-1}$ . The data points extracted from the experiments shown in the left plots are highlighted in the right plots with arrows. The solid and dashed curves in the right plots correspond to the simulated FM profiles and their respective underlying absorption lineshapes for  $T \approx 670$  K and  $p \approx 0.32$  bar (black), for  $T \approx 1120$  K and  $p \approx 1.22$  bar (red), and for  $T \approx 980$  K and  $p \approx 0.54$  bar (blue).

line center. Its actual value depends on the modulation index  $M$ , the ratio of the modulation frequency  $\nu_m$  and absorption linewidth, and on the demodulation phase angle. The latter was set to a value corresponding to a pure absorption signal in our case. As it is outlined in more detail in Ref. 22, for a given laser frequency  $\nu$  and a known modulation index  $M$ , the FM factor can be directly calculated from the corresponding absorption line profile in a straightforward manner. For a phase angle set to pure absorption, the FM factor is given as follows:

$$\Delta f = 2 \times \left[ \sum_{n=0}^{\infty} J_n(M) J_{n+1}(M) (\alpha_{-n-1} - \alpha_{n+1} + \alpha_{-n} - \alpha_n) \right] / \alpha_c \quad (6.2)$$

Here,  $\alpha_i$  corresponds to the narrow-bandwidth value of the absorption coefficient at the spectral position of the  $n$ -th sideband of the frequency-modulated laser beam at  $\nu_0 \pm n \nu_m$ , weighted according to their corresponding Bessel function values  $J_n(M)$ .  $\alpha_c$  is the absorption coefficient

at line center, which is introduced for the purpose of normalization. As becomes clear from Equation (6.2), for higher  $M$  values, the resulting FM signal exhibits contributions from higher sidebands. In the limiting case  $M \ll 1$ , however, it simply represents the difference in absorption measured at the first-order sidebands at  $(\nu_0 + \nu_m)$  and  $(\nu_0 - \nu_m)$  which explains the overall derivative nature of the observed FM profile.

By combining the absorption values of all HCN traces for each data set in Table 6.1, the FM line profiles for incident and reflected wave conditions were fitted iteratively by a Voigt lineshape model. The Lorentzian width  $2\Gamma_{\text{total}}$  was used as the sole adjustable parameter, which sensitively depends on total pressure and temperature. Contributions of  $\text{N}_2$  and HCN to the Lorentzian linewidth were subtracted using literature values for their pressure-broadening coefficients and temperature exponents [31, 32] and assuming the usual mole fraction weighted additivity rule,  $\Gamma_{\text{total}} = \sum_i x_i \Gamma_i$ . The temperature dependence of the full-width broadening coefficient  $2\gamma$  is expressed as

$$2\gamma_i(T) = 2\gamma_i^{296\text{K}} \left( \frac{296 \text{ K}}{T} \right)^{n_i} \quad (6.3)$$

In the case of HCN, the unknown temperature exponent was assumed to be  $n_{\text{HCN}} = 1$ , which is consistent with earlier results reported for the P(10) line [21].

As it turns out, the significant increase of the broadening of the absorption line behind the reflected wave (see Figure 6.2c) is predominantly due to the higher pressure behind the reflected wave instead of the temperature-related increase of the Doppler-broadening contribution. Figure 6.3 shows a log-log plot of the determined argon-broadening coefficients. A linear fit of the data according to Equation (6.3) yields the temperature exponent of  $n_{\text{Ar}} = 0.67 \pm 0.07$  from the slope and the full-width room-temperature pressure-broadening coefficient of  $2\gamma_{\text{Ar}}^{296 \text{ K}} = (0.093 \pm 0.007) \text{ cm}^{-1} \text{ atm}^{-1}$  from the intercept. These results compare well with values for the temperature exponent of the P(10) line ( $0.63 \pm 0.06$ ) and the argon-broadening coefficients for the lines between P(1) ( $0.162 \text{ cm}^{-1} \text{ atm}^{-1}$ ) and P(18) ( $0.099 \text{ cm}^{-1} \text{ atm}^{-1}$ ) reported in Refs. [20, 21].

Altogether, these data reveal the expected clear trend of lower pressure broadening with increasing rotational excitation, which is typically ascribed to the lower rotational transition probabilities resulting from the more widely spaced rotational levels at higher  $J$  values [33]. The calculated integrated linestrengths  $S$  for the P(26) transition are included in Figure 6.1 as symbols. On average, these data are 17% higher than the values predicted from the HITRAN database [30] with the highest deviation occurring for the experiments with the largest HCN mole fractions of 500 ppm. Note that higher HCN mole fractions go along with higher  $\text{N}_2$  content as well, corresponding to a mole fraction of up to 52%  $\text{N}_2$  in the shock-heated gas mixtures in case of the 500 ppm HCN experiments. The reason for using an HCN/ $\text{N}_2$  stock gas mixture instead of HCN/argon was simply due to its commercial availability. Handling of the highly toxic HCN is difficult and therefore we have refrained from preparing our own stock gas mixtures from pure HCN gas.

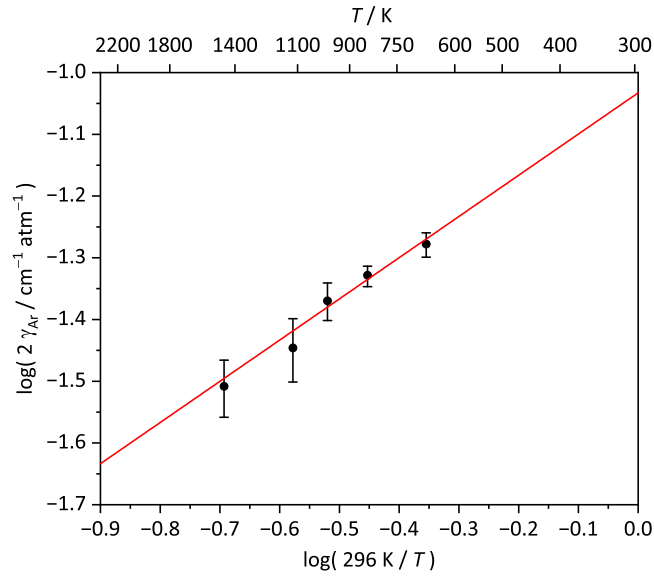


**Figure 6.3:** log-log plot for the temperature dependence of the argon-broadening coefficient  $2\gamma_{\text{Ar}}$ . Experimental data (black symbols) including errors estimated from the Voigt fits and a linear fit according to Equation (6.3) (red line).

In order to validate the HCN content in the gas mixtures, complementary measurements of the undiluted HCN/N<sub>2</sub> mixture were performed at room temperature for five intense lines between P(8) to P(21) using standard FTIR spectroscopy (Vertex 80, Bruker). On average, the linestrengths derived from the FTIR data were 6% higher than the HITRAN values, which, however, cannot fully account for the difference between our data and the HITRAN prediction as seen in Figure 6.1. We tentatively ascribe the remaining moderate discrepancy to non-idealities and uncertainties in the calculated shock wave parameters. Although non-idealities resulting from vibrational relaxation effects of shock-heated N<sub>2</sub>-containing gas mixtures should remain small for the conditions used in this work [34], the clear trend of higher deviations for increasing N<sub>2</sub> content is evident. Whereas the data point with 200 ppm HCN is in agreement with the HITRAN prediction within error limits, the experiments at 500 ppm deviate by up to 30%.

### HCN Detection Limit

The HCN detection limit of the mid-IR-FM setup can be estimated from an Allan analysis of the FM signal baseline noise using the overlapping Allan deviation as the preferred measure of sensitivity [35]. To this end, pure FM signal noise was recorded under normal lab conditions without shock tube operation and was then subjected to an overlapping Allan analysis procedure. The calculated values for the overlapping Allan deviation as function of the averaging period  $\tau$ , corresponding to the time resolution of the detection system, were converted to the respective absorption values  $A = \alpha_c \times l$  using the standard FM Equation (6.1) with the FM factor  $\Delta f$  calculated using Equation (6.2). As shown in Ref. 22, FM factors on the order of  $\Delta f \approx 1$  correspond to the best sensitivity that can be achieved with an FM detection scheme. With  $\Delta f \approx 0.6$  as obtained in this work (see Figures 6.2c,f), thanks to the combination of high modulation index

and high modulation frequency, the current version of our FM spectrometer already comes close to this optimum. Figure 6.4 shows the resulting Allan plot, assuming  $\Delta f = 0.6$ .

For an effective time resolution of  $\tau = 500$  ns, the minimum detectable absorption is  $A_{\min} = 3 \times 10^{-4}$ . With increasing averaging time,  $A_{\min}$  initially decreases with  $\tau^{-0.5}$ , indicating that statistical noise components such as thermal and/or shot noise of the photodetector prevails. The lowest detectable absorption of  $A_{\min} = 3 \times 10^{-5}$  is achieved at a time response of  $\tau = 100 \mu\text{s}$ . These favorable values demonstrate the high detection sensitivity of FM spectroscopy even on the short timescales, as they are required for experiments behind shock waves. Another advantage of the derivative nature of FM spectroscopy for shock tube applications stems from the fact that typical shock tube-induced acoustic and pressure-induced noise components are significantly reduced, resulting in a more stable baseline compared to conventional difference amplification laser absorption schemes [36]. Note that the increase of the Allan deviation for time resolutions  $\tau > 100 \mu\text{s}$ , and hence the loss of sensitivity on longer timescales, is due to well-known residual amplitude modulation (RAM) effects in FM spectroscopy [37] that typically cause baseline undulations in the kHz range. These are of minor concern for shock tube applications since the necessary time resolutions are in the range of 1–20  $\mu\text{s}$  and the total experimental test time window is limited to at most a few ms anyway.

Using the linestrengths from the HITRAN database and the argon-broadening parameters derived in this work, the HCN detection limit at  $T = 1000$  K and  $p = 0.4$  bar is about 3 ppm for  $\tau = 10 \mu\text{s}$  and single-pass shock tube detection with  $l = 81$  mm. This demonstrates the high potential of mid-IR-FM spectroscopy for quantitative detection of HCN under shock wave conditions. However, towards higher temperatures and pressures, the rapidly decreasing Boltzmann

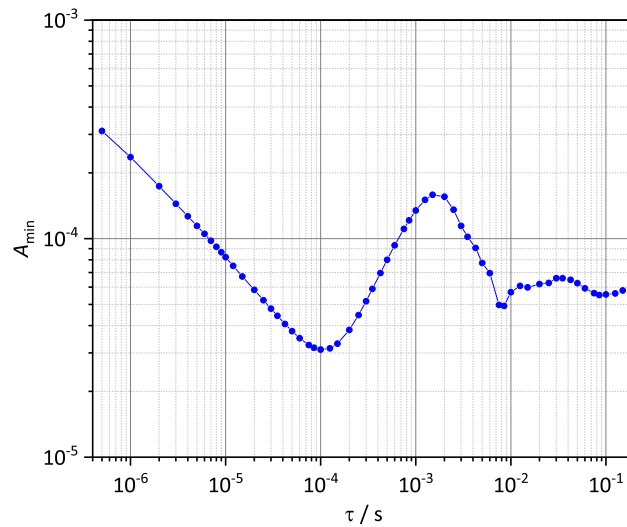


**Figure 6.4:** Minimum detectable absorption as function of the time resolution  $\tau$  for typical measurement conditions (790 kHz bandwidth, 700  $\mu\text{W}$  light power on the detector,  $I_0 = 1.2$  V,  $\Delta f = 0.6$ ,  $G = 200$ ,  $\tilde{\nu} = 3228.05 \text{ cm}^{-1}$ ).

population of individual rotational states (going along with lower linestrengths, see Figure 6.1) as well as the increasing linewidths (see Figure 6.2c) significantly reduce the attainable detection limit. For example, at  $T = 2500$  K and  $p = 1.6$  bar the HCN detection limit increases to 28 ppm. A second overlapping Allan analysis was conducted using FM signal noise measured behind the reflected wave in pure argon. For realistic time resolutions of  $\tau \leq 20$   $\mu$ s, this analysis yielded detection limits that are a factor of 2 higher than the  $A_{\min}$  values shown in Figure 6.4, most likely due to additional technical noise contributions caused by the propagating shock wave.

### Kinetic HCN Profile

To further demonstrate the capability of mid-IR-FM spectroscopy to enable sensitive kinetic studies behind shock waves, first reactive concentration-time profiles of HCN during the reaction  $\text{HCN} + \text{O}$  were recorded. Here, the thermal decomposition of  $\text{N}_2\text{O}$  according to  $\text{N}_2\text{O} + \text{M} \rightarrow \text{N}_2 + \text{O} + \text{M}$  served as an effective source of O atoms at temperatures  $T > 1500$  K. Figure 6.5 illustrates, to the best of our knowledge for the first time, a kinetic profile of HCN behind shock waves. The signal was obtained with a gas mixture of 500 ppm HCN and 2.0%  $\text{N}_2\text{O}$  in  $\text{N}_2$ /argon at a temperature of 1638 K and a pressure of 1.24 bar behind the reflected shock wave. The sigmoidal HCN profile with accelerated loss towards longer reaction times is due to the ever-increasing O atom concentration during the experiment resulting from the rather slow  $\text{N}_2\text{O}$  decomposition. For this particular kinetic HCN profile, the standard deviation of the noise behind the reflected wave corresponds to a detection limit of about 20–25 ppm. This is consistent with the detection limit of 21 ppm derived from the Allan analysis for reflected wave conditions mentioned in the previous section. A more systematic study targeting the determination of the high-temperature rate constant of the reaction  $\text{HCN} + \text{O}$  is currently underway and will be published elsewhere.

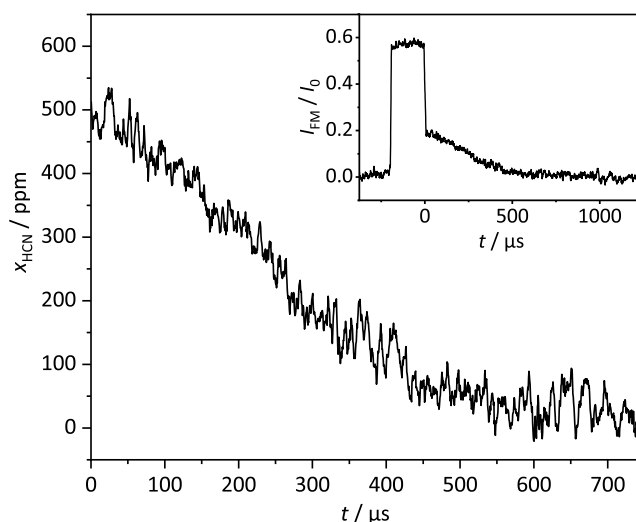


**Figure 6.5:** Kinetic profile of HCN during the reaction  $\text{HCN} + \text{O}$  behind the reflected shock wave (500 ppm HCN, 2.0%  $\text{N}_2\text{O}$ ,  $T = 1638$  K,  $p = 1.24$  bar, 2 MHz sampling rate, 10 points moving average). The inset shows the baseline-corrected and  $I_0$ -normalized FM signal for pre-shock, incident wave, and reflected wave conditions.  $t = 0$  marks the arrival of the reflected shock wave.

## 6.4 Conclusions

Single-tone mid-IR-FM spectroscopy has been demonstrated as a suitable and sensitive laser absorption method for the detection of HCN in shock tube experiments. As a prerequisite for quantitative high-temperature detection of HCN, we have determined the argon pressure-broadening parameters for the P(26) line in the  $\nu_1$  band of HCN. A detection limit as low as 3 ppm at  $T = 1000$  K and  $p = 400$  mbar for single-pass shock tube detection ( $l = 81$  mm) was achieved. Furthermore, the first reactive profiles of HCN behind reflected shock waves were recorded. The outcome of this study serves as a basis for future reaction kinetic studies of HCN reactions and, in particular, paves the way for the determination of the HCN yield and with it the temperature-dependent branching ratio of the reaction  $\text{NCN} + \text{H}$ , which is key for prompt-NO modeling.

## Acknowledgments and Funding

The authors like to acknowledge the financial support of the German Science Foundation (DFG) through projects FR1529/4-2 and FR1529/7-1, as well as the Cluster of Excellence EC-80 "Future Ocean" at Kiel University for making available the OPO laser system.

## References

- [1] P. Glarborg, J. A. Miller, B. Ruscic, S. J. Klippenstein, Modeling nitrogen chemistry in combustion, *Prog. Energy Combust. Sci.* **2018**, *67*, 31–68, DOI [10.1016/j.pecs.2018.01.002](https://doi.org/10.1016/j.pecs.2018.01.002).
- [2] D. Schmid, O. Karlström, P. Yrjas, Release of  $\text{NH}_3$ , HCN and NO during devolatilization and combustion of washed and torrefied biomass, *Fuel* **2020**, *280*, 118583/1–7, DOI [10.1016/j.fuel.2020.118583](https://doi.org/10.1016/j.fuel.2020.118583).
- [3] M. Stuhr, S. Hesse, G. Friedrichs, Quantitative and Sensitive Mid-Infrared Frequency Modulation Detection of HCN behind Shock Waves, *10th European Combustion Meeting 2021*, Poster (Online).
- [4] N. Lamoureux, P. Desgroux, M. Olzmann, G. Friedrichs, The story of NCN as a key species in prompt-NO formation, *Prog. Energ. Combust. Sci.* **2021**, *87*, 100940/1–34, DOI [10.1016/j.pecs.2021.100940](https://doi.org/10.1016/j.pecs.2021.100940).
- [5] L. Moskaleva, M. Lin, The spin-conserved reaction  $\text{CH} + \text{N}_2 \rightarrow \text{H} + \text{NCN}$ : A major pathway to prompt NO studied by quantum/statistical theory calculations and kinetic modeling of rate constant, *Proc. Combust. Inst.* **2000**, *28*, 2393–2401, DOI [10.1016/s0082-0784\(00\)80652-9](https://doi.org/10.1016/s0082-0784(00)80652-9).
- [6] W.-S. Teng, L. V. Moskaleva, H.-L. Chen, M. C. Lin, Ab Initio Chemical Kinetics for  $\text{H} + \text{NCN}$ : Prediction of NCN Heat of Formation and Reaction Product Branching via Doublet and Quartet Surfaces, *J. Phys. Chem. A* **2013**, *117*, 5775–5784, DOI [10.1021/jp402903t](https://doi.org/10.1021/jp402903t).
- [7] N. Faßheber, J. Dammeier, G. Friedrichs, Direct measurements of the total rate constant of the reaction  $\text{NCN} + \text{H}$  and implications for the product branching ratio and the enthalpy of formation of NCN, *Phys. Chem. Chem. Phys.* **2014**, *16*, 11647–11657, DOI [10.1039/c4cp01107d](https://doi.org/10.1039/c4cp01107d).
- [8] S. J. Klippenstein, M. Pfeifle, A. W. Jasper, P. Glarborg, Theory and modeling of relevance to prompt-NO formation at high pressure, *Combust. Flame* **2018**, *195*, 3–17, DOI [10.1016/j.combustflame.2018.04.029](https://doi.org/10.1016/j.combustflame.2018.04.029).
- [9] N. Faßheber, N. Lamoureux, G. Friedrichs, The rate constant of the reaction  $\text{NCN} + \text{H}_2$  and its role in NCN and NO modeling in low pressure  $\text{CH}_4/\text{O}_2/\text{N}_2$ -flames, *Phys. Chem. Chem. Phys.* **2015**, *17*, 15876–15886, DOI [10.1039/c5cp01414j](https://doi.org/10.1039/c5cp01414j).

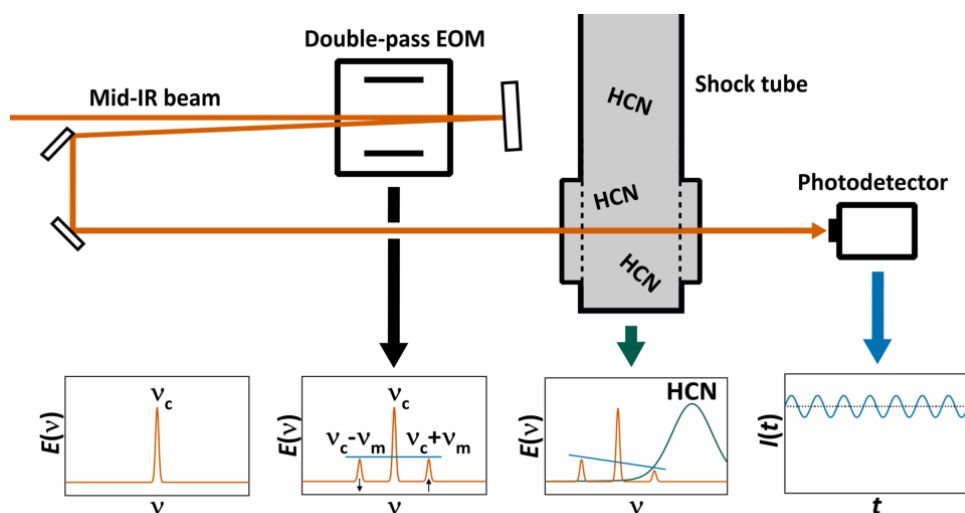
- [10] J. Dammeier, N. Faßheber, G. Friedrichs, Direct measurements of the high temperature rate constants of the reactions  $\text{NCN} + \text{O}$ ,  $\text{NCN} + \text{NCN}$ , and  $\text{NCN} + \text{M}$ , *Phys. Chem. Chem. Phys.* **2012**, *14*, 1030–1037, DOI [10.1039/c1cp22123j](https://doi.org/10.1039/c1cp22123j).
- [11] N. Lamoureux, H. E. Merhubi, L. Pillier, S. de Persis, P. Desgroux, Modeling of NO formation in low pressure premixed flames, *Combust. Flame* **2016**, *163*, 557–575, DOI [10.1016/j.combustflame.2015.11.007](https://doi.org/10.1016/j.combustflame.2015.11.007).
- [12] J. Dammeier, G. Friedrichs, Thermal Decomposition of  $\text{NCN}_3$  as a High-Temperature NCN Radical Source: Singlet-Triplet Relaxation and Absorption Cross Section of  $\text{NCN}(^3\Sigma)$ , *J. Phys. Chem. A* **2010**, *114*, 12963–12971, DOI [10.1021/jp1043046](https://doi.org/10.1021/jp1043046).
- [13] N. Lamoureux, C. M. Western, X. Mercier, P. Desgroux, Reinvestigation of the spectroscopy of the transition of the NCN radical at high temperature: Application to quantitative NCN measurement in flames, *Combust. Flame* **2013**, *160*, 755–765, DOI [10.1016/j.combustflame.2012.12.009](https://doi.org/10.1016/j.combustflame.2012.12.009).
- [14] N. Faßheber, L. Bornhorst, S. Hesse, Y. Sakai, G. Friedrichs, The Reaction  $\text{NCN} + \text{H}_2$ : Quantum Chemical Calculations, Role of  $^1\text{NCN}$  Chemistry, and  $^3\text{NCN}$  Absorption Cross Section, *J. Phys. Chem. A* **2020**, *124*, 4632–4645, DOI [10.1021/acs.jpca.0c02631](https://doi.org/10.1021/acs.jpca.0c02631).
- [15] N. Lamoureux, H. E. Merhubi, X. Mercier, J. Pauwels, P. Desgroux, HCN quantitative measurement in a laminar low pressure flame at 1036 nm using pulsed CRDS technique, *Proc. Combust. Inst.* **2013**, *34*, 3557–3564, DOI [10.1016/j.proci.2012.06.067](https://doi.org/10.1016/j.proci.2012.06.067).
- [16] N. Lamoureux, H. E. Merhubi, L. Gasnot, C. Schoemaecker, P. Desgroux, Measurements and modelling of HCN and CN species profiles in laminar  $\text{CH}_4 / \text{O}_2 / \text{N}_2$  low pressure flames using LIF/CRDS techniques, *Proc. Combust. Inst.* **2015**, *35*, 745–752, DOI [10.1016/j.proci.2014.05.126](https://doi.org/10.1016/j.proci.2014.05.126).
- [17] S. Gersen, A. Mokhov, H. Levinsky, Diode laser absorption measurement and analysis of HCN in atmospheric-pressure, fuel-rich premixed methane/air flames, *Combust. Flame* **2008**, *155*, 267–276, DOI [10.1016/j.combustflame.2008.04.006](https://doi.org/10.1016/j.combustflame.2008.04.006).
- [18] Z. Sun, Z. Li, A. Konnov, M. Aldén, Quantitative HCN measurements in  $\text{CH}_4/\text{N}_2\text{O}/\text{O}_2/\text{N}_2$  flames using mid-infrared polarization spectroscopy, *Combust. Flame* **2011**, *158*, 1898–1904, DOI [10.1016/j.combustflame.2011.03.008](https://doi.org/10.1016/j.combustflame.2011.03.008).
- [19] D. Hot, R. L. Pedersen, W. Weng, Y. Zhang, M. Aldén, Z. Li, Spatially and temporally resolved IR-DFWM measurement of HCN released from gasification of biomass pellets, *Proc. Combust. Inst.* **2019**, *37*, 1337–1344, DOI [10.1016/j.proci.2018.07.105](https://doi.org/10.1016/j.proci.2018.07.105).
- [20] P. L. Varghese, R. K. Hanson, Tunable diode laser measurements of spectral parameters of HCN at room temperature, *J. Quant. Spectrosc. Radiat. Transfer* **1984**, *31*, 545–559, DOI [10.1016/0022-4073\(84\)90060-8](https://doi.org/10.1016/0022-4073(84)90060-8).
- [21] A. Chang, R. Hanson, Shock-tube study of HCN self-broadening and broadening by argon for the P(10) line of the  $\nu_1$  band at 3  $\mu\text{m}$ , *J. Quant. Spectrosc. Radiat. Transfer* **1985**, *33*, 213–217, DOI [10.1016/0022-4073\(85\)90150-5](https://doi.org/10.1016/0022-4073(85)90150-5).
- [22] G. Friedrichs, Sensitive Absorption Methods for Quantitative Gas Phase Kinetic Measurements. Part 1: Frequency Modulation Spectroscopy, *Z. Phys. Chem.* **2008**, *222*, 1–30, DOI [10.1524/zpch.2008.222.1.1](https://doi.org/10.1524/zpch.2008.222.1.1).
- [23] J. Deppe, G. Friedrichs, A. Ibrahim, H.-J. Römming, H. G. Wagner, The thermal decomposition of  $\text{NH}_2$  and  $\text{NH}$  radicals, *Ber. Bunsenges. Phys. Chem.* **1998**, *102*, 1474–1485, DOI [10.1002/bbpc.199800016](https://doi.org/10.1002/bbpc.199800016).
- [24] G. Friedrichs, H. G. Wagner, Quantitative FM spectroscopy at high temperatures: The detection of  $^1\text{CH}_2$  behind shock waves, *Z. Phys. Chem.* **2000**, *214*, 1723–1746, DOI [10.1524/zpch.2000.214.12.1723](https://doi.org/10.1524/zpch.2000.214.12.1723).
- [25] G. Friedrichs, J. T. Herbon, D. F. Davidson, R. K. Hanson, Quantitative detection of HCO behind shock waves: The thermal decomposition of HCO, *Phys. Chem. Chem. Phys.* **2002**, *4*, 5778–5788, DOI [10.1039/b205692e](https://doi.org/10.1039/b205692e).



- [26] S. Wang, R. K. Hanson, Ultra-sensitive spectroscopy of OH radical in high-temperature transient reactions, *Opt. Lett.* **2018**, *43*, 3518–3521, DOI [10.1364/ol.43.003518](https://doi.org/10.1364/ol.43.003518).
- [27] M. Stuhr, N. Faßheber, G. Friedrichs, Single-tone mid-infrared frequency modulation spectroscopy for sensitive detection of transient species, *Opt. Express* **2019**, *27*, 26499–26512, DOI [10.1364/oe.27.026499](https://doi.org/10.1364/oe.27.026499).
- [28] P. Glarborg, P. Marshall, Importance of the Hydrogen Isocyanide Isomer in Modeling Hydrogen Cyanide Oxidation in Combustion, *Energy Fuels* **2017**, *31*, 2156–2163, DOI [10.1021/acs.energyfuels.6b02085](https://doi.org/10.1021/acs.energyfuels.6b02085).
- [29] M. Colberg, G. Friedrichs, Room temperature and shock tube study of the reaction  $\text{HCO} + \text{O}_2$  using the photolysis of glyoxal as an efficient HCO source, *J. Phys. Chem. A* **2006**, *110*, 160–170, DOI [10.1021/jp055168r](https://doi.org/10.1021/jp055168r).
- [30] I. Gordon et al., The HITRAN2016 molecular spectroscopic database, *J. Quant. Spectrosc. Radiat. Transfer* **2017**, *203*, 3–69, DOI [10.1016/j.jqsrt.2017.06.038](https://doi.org/10.1016/j.jqsrt.2017.06.038).
- [31] V. M. Devi, D. Benner, M. Smith, C. Rinsland, S. W. Sharpe, R. Sams, A multispectrum analysis of the  $\nu_1$  band of  $\text{H}^{12}\text{C}^{14}\text{N}$ : Part I. Intensities, self-broadening and self-shift coefficients, *J. Quant. Spectrosc. Radiat. Transfer* **2003**, *82*, 319–341, DOI [10.1016/s0022-4073\(03\)00161-4](https://doi.org/10.1016/s0022-4073(03)00161-4).
- [32] C. Rinsland, V. M. Devi, M. Smith, D. C. Benner, S. W. Sharpe, R. L. Sams, A multispectrum analysis of the  $\nu_1$  band of  $\text{H}^{12}\text{C}^{14}\text{N}$ : Part II. Air- and  $\text{N}_2$ -broadening, shifts and their temperature dependences, *J. Quant. Spectrosc. Radiat. Transfer* **2003**, *82*, 343–362, DOI [10.1016/s0022-4073\(03\)00162-6](https://doi.org/10.1016/s0022-4073(03)00162-6).
- [33] D. R. Rao, T. Oka, Dicke narrowing and pressure broadening in the infrared fundamental band of HCl perturbed by Ar, *J. Mol. Spectrosc.* **1987**, *122*, 16–27, DOI [10.1016/0022-2852\(87\)90215-3](https://doi.org/10.1016/0022-2852(87)90215-3).
- [34] J. P. Appleton, Shock-Tube Study of the Vibrational Relaxation of Nitrogen Using Vacuum-Ultraviolet Light Absorption, *J. Chem. Phys.* **1967**, *47*, 3231–3240, DOI [10.1063/1.1712381](https://doi.org/10.1063/1.1712381).
- [35] W. J. Riley, *Handbook of Frequency Stability Analysis*, US Department of Commerce, National Institute of Standards and Technology (NIST), **2008**.
- [36] M. Votsmeier, S. Song, D. Davidson, R. Hanson, Sensitive detection of  $\text{NH}_2$  in shock tube experiments using frequency modulation spectroscopy, *Int. J. Chem. Kinet.* **1999**, *31*, 445–453, DOI [10.1002/\(SICI\)1097-4601\(1999\)31:6<445::AID-KIN6>3.0.CO;2-4](https://doi.org/10.1002/(SICI)1097-4601(1999)31:6<445::AID-KIN6>3.0.CO;2-4).
- [37] J. A. Silver, Frequency-modulation spectroscopy for trace species detection: theory and comparison among experimental methods, *Appl. Opt.* **1992**, *31*, 707–717, DOI [10.1364/ao.31.000707](https://doi.org/10.1364/ao.31.000707).

## CHAPTER 7

### Publication IV: Mid-Infrared Frequency Modulation Detection of HCN and Its Reaction with O Atoms behind Shock Waves



Michael Stühr<sup>a</sup> and Gernot Friedrichs<sup>a</sup>

<sup>a</sup>Institut für Physikalische Chemie, Christian-Albrechts-Universität zu Kiel, Max-Eyth-Straße 1, 24118 Kiel, Germany

Reprinted with permission from

*J. Phys. Chem. A* **2022**, 126, 50, 9485–9496, DOI [10.1021/acs.jpca.2c06817](https://doi.org/10.1021/acs.jpca.2c06817).

Copyright 2022 American Chemical Society.

Own Contributions:

- Shock tube experiments
- Advanced aspects of quantitative FM detection
- Allan sensitivity analysis
- Data analysis and discussion
- Writing of paper draft

## Abstract

Hydrogen cyanide (HCN) is the primary cyanide species in combustion processes and plays a key role in the formation of  $\text{NO}_x$  in the combustion of fossil fuels, nitrogen-containing biofuels, and blended hydrocarbon-ammonia mixtures. Robust, sensitive, and time-resolved in-situ laser diagnostic methods are needed to gain insight into the combustion chemistry of HCN. Mid-infrared frequency modulation spectroscopy (MIR-FMS) has recently been established as such a quantitative technique for HCN detection behind shock waves. With a minimum detectable fractional absorption of  $2 \times 10^{-4}$  at a time resolution of  $5 \mu\text{s}$ , an improved spectrometer design enabled the detection of HCN behind shock waves down to the ppm mole fraction level. An Allan noise analysis revealed that a further improvement toward shot-noise limited detection should be possible when fast mid-infrared photodetectors with higher saturation limit will become available. HCN kinetic profiles in the presence of  $\text{O}(^3\text{P})$  atoms from thermal  $\text{N}_2\text{O}$  decomposition have been measured in the temperature range  $1448 \text{ K} < T < 1954 \text{ K}$ . The determined total rate constants for the key HCN oxidation reaction  $\text{HCN} + \text{O}$ ,  $k/(\text{cm}^3 \text{ mol}^{-1} \text{ s}^{-1}) = 1.88 \times 10^{14} \exp(-64.5 \text{ kJ mol}^{-1}/RT)(+28\%, -37\%)$ , turn out to be largely consistent with previous measurements. These data complete the set of available rate constant studies, by now covering the temperature range from  $450 \text{ K} < T < 2500 \text{ K}$  and relying on the detection of almost all feasible reactant and product species.

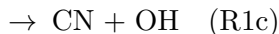
## 7.1 Introduction

Hydrogen cyanide (HCN) is considered the predominant cyanide species in combustion processes. It is formed by devolatilization of fuels with organically bound nitrogen, thermal decomposition of hydrocarbon amines, and by the reactions of  $\text{NO}$  with  $\text{CH}_x$  radicals [1]. In the combustion of nitrogen-free fuels,  $\text{N}_2$  from the combustion air serves as the nitrogen source and HCN plays a key role as a precursor for nitrogen oxide ( $\text{NO}_x$ ) formation. Here, it is mainly generated in the prompt- $\text{NO}$  initiation sequence  $\text{CH} + \text{N}_2 \rightarrow \text{NCN} + \text{H} \rightarrow \text{HCN} + \text{N}$  [2].

In light of global attempts to reduce carbon dioxide and  $\text{NO}_x$  emissions, high-temperature nitrogen chemistry continues to be in the focus of reaction kinetics research. Next to the combustion of nitrogen-rich biomass, ammonia ( $\text{NH}_3$ ) has gathered considerable attention both as a carbon-free hydrogen carrier as well as a renewable fuel for internal combustion engines [3]. Besides the need for green ammonia production [4], two other issues still hamper the practical use of  $\text{NH}_3$  as fuel. First, ammonia-based combustion entails high emissions of  $\text{NO}_x$ , especially under lean conditions [5]. Second, combustion of pure  $\text{NH}_3$  in air suffers from low flame speeds and limited flame stability, which represents a substantial obstacle for the use of  $\text{NH}_3$  as fuel in many applications [6, 7]. A possible solution to the latter problem is the addition of  $\text{H}_2$  or hydrocarbons like  $\text{CH}_4$  in order to increase the laminar burning velocity [8, 9]. However, the combustion of hydrocarbon- $\text{NH}_3$  blends opens up nitrogen-carbon cross-chemistry, again leading to the formation of amines and cyanides.

In conventional hydrocarbon-air combustion processes, the primary path of HCN removal is its

oxidation by O atoms [1, 10]:



The nitrogen-containing product species of reaction R1 then proceed further into the direction of  $\text{NO}_x$  via various reaction sequences involving H atoms, O atoms, OH radicals, and/or  $\text{O}_2$  [10, 11]. At higher temperatures, HCN is also in fast equilibrium with hydrogen isocyanide (HNC). Recently, Glarborg et al. [12] re-examined HNC combustion chemistry and concluded that HCN-HNC isomerization plays a role in HCN removal under fuel-rich conditions, since it offers an additional oxidation pathway initiated by the reaction  $\text{HNC} + \text{OH}$ .

Robust diagnostic methods for the high-temperature in-situ detection of HCN facilitate further insight into combustion chemistry of hydrocarbon-air fuels, blended fuels containing ammonia, and nitrogen-containing biofuels. However, HCN detection techniques rarely fulfill the stringent requirements for high-temperature reaction kinetics studies, where kinetic profiles are recorded at low concentrations and on short time scales. In that regard, frequency modulation spectroscopy (FMS) offers both high time resolution and high detection sensitivity [13]. The derivative nature of FM-based detection schemes also makes them very suitable for harsh conditions as they occur in shock tube measurements, which suffer from specific shock-related issues like beam steering noise related to density gradients in the boundary layer, pressure-induced birefringence in the optical windows, and acoustic vibrations from shock tube operation. As yet, most FM detection schemes for shock tube applications have targeted comparably strong electronic transitions in the visible range for recording concentration-time profiles of three-atomic radical species, including the amidogen radical  $\text{NH}_2$  [14]. FM detection of HNO, another key species for modeling nitrogen chemistry, has been reported more recently as well [15].

For HCN, with electronic transitions lying in the difficult-to-access vacuum-UV at wavelengths well below 200 nm [16], quantitative detection has been mostly accomplished in the mid-infrared (MIR) spectral range on fundamental CH stretch vibrational transitions. Recent notable examples of laser-spectroscopic in-situ MIR HCN detection are based on polarization spectroscopy [17] and degenerate four-wave mixing spectroscopy [18]. These two methods were employed to investigate HCN emission levels from  $\text{CH}_4\text{-N}_2\text{O-O}_2\text{-N}_2$  flames and gasified biomass, respectively. Reports on spectroscopic detection of HCN behind shock waves are scarce. In early work of Brupbacher and Kern [19, 20], who recorded the first kinetic profiles of HCN (and DCN) behind shock waves by detecting the CH stretch band emission centered at  $(3.0 \pm 0.1) \mu\text{m}$  (mostly referred to as the  $\nu_1$  band), equimolar mixtures of 1–2% HCN/ $\text{D}_2$  or  $\text{C}_2\text{N}_2/\text{H}_2$  in argon were shock-heated to investigate the isotope exchange mechanism and the formation of HCN, respectively. Later, Chang and Hanson [21] investigated the pressure broadening of the P(10) line in the  $\nu_1$  band using tunable diode laser spectroscopy. For shock tube detection in the MIR, pressure broadening is often comparable to Doppler broadening such that the determination of accurate pressure-broadening

coefficients becomes crucial for quantitative HCN detection. Very recently, targeting the HCN bending vibration band at  $14\text{ }\mu\text{m}$ , Elkhazraji et al. [22, 23] developed a versatile and widely tunable MIR laser absorption diagnostics that is based on a pulsed difference-frequency generation scheme between a  $\text{CO}_2$  gas laser and an external-cavity quantum cascade laser. With a time resolution of about  $67\text{ }\mu\text{s}$ , set by the  $15\text{ kHz}$  repetition frequency of the laser system, and a minimum detectable absorbance of about  $1\%$ , both the rate constant and HCN yield of the thermal decomposition of isoxazole were measured in single-pulse shock tube experiments.

In a preceding study on HCN detection behind shock waves, we have established a new detection scheme in the  $\nu_1$  CH stretch vibration band using single-tone mid-infrared frequency modulation spectroscopy (MIR-FMS) [24]. Therein, the temperature-dependent pressure broadening of the P(26) rovibrational line has been investigated under shock wave conditions and it was shown that MIR-FM detection of HCN on the ppm mixing ratio level and with  $\mu\text{s}$  time resolution is possible. A first kinetic HCN profile had been included as well.

The aim of the present work is 2-fold. First, the current implementation of the single-tone MIR-FM spectrometer is described in detail and the detection limit of the system is characterized based on an FM signal noise analysis by calculating the overlapping Allan deviation. Moreover, minimal detectable absorption values were determined at different light power levels on the photodetector in order to estimate the minimum required light power to achieve shot-noise limited detection. Second, a detailed rate constant study for the reaction  $\text{HCN} + \text{O}$  demonstrates the suitability of the detection scheme for kinetic measurements under shock tube conditions. Despite its importance for modeling the HCN oxidation in combustion processes, relatively few high-temperature studies have been performed on the reaction  $\text{HCN} + \text{O}$  as yet. Previous studies targeted the rate constants of the different reaction channels by monitoring reaction products such as H atoms ( $k_{\text{R1a}}$ ) [25], NH and CN ( $k_{\text{R1b}}$ ,  $k_{\text{R1c}}$ ) [26], and NCO ( $k_{\text{R1a}}$ ) [27]. Roth et al. [25] also measured O atom reactant profiles to infer the total rate constant. In this sense, by providing direct measurements of the total rate constant by detecting the reactant HCN, our study closes the circle of available experimental high-temperature data.

## 7.2 Experimental

### Frequency Modulation Spectrometer

Figure 7.1 shows a schematic of the experimental setup used for sensitive and time-resolved HCN detection behind shock waves. By implementing a new modulation scheme and replacing the analog with an all-digital demodulation, the spectrometer is a significant development of the former MIR-FM system described in Ref. 28.

A high-power narrow-bandwidth continuous-wave optical parametric oscillator (cw-OPO) served as the MIR laser light source. It consists of a fiber-coupled distributed feedback (DFB) seed laser (Koheras AdjustiK Y10 PM, NKT Photonics,  $1064\text{ nm}$ ,  $15\text{ mW}$ ) in combination with an Yb-doped fiber amplifier (YAR-10K-1064-LP-SF, IPG Photonics,  $10\text{ W}$ ), which in turn pumped the OPO resonator (Argos SF-10, Lockheed Martin, module B,  $> 1.2\text{ W}$  idler power). The output of the

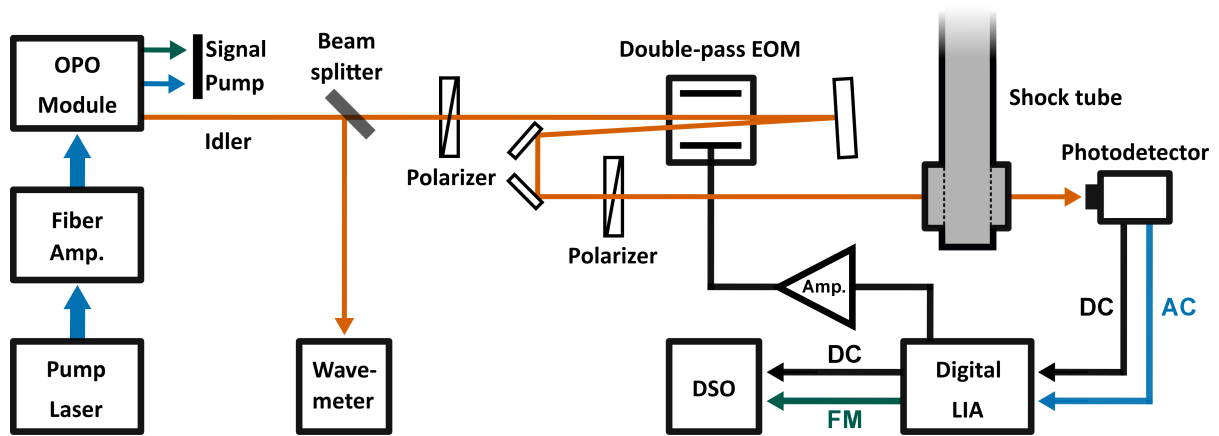


**Figure 7.1:** Schematic of the single-tone mid-infrared frequency modulation detection system. Amp.: amplifier, OPO: optical parametric oscillator, EOM: electro-optic modulator, LIA: lock-in amplifier, DSO: digital storage oscilloscope.

OPO can be fine-tuned by adjusting both the PPLN (periodically poled lithium niobate) crystal as well as the exact seed laser output frequency and the idler output wavelength was monitored by a wavemeter with  $6 \times 10^{-4} \text{ cm}^{-1}$  accuracy (621A-IR, Bristol Instruments).

Single-tone frequency modulation of the MIR detection beam was accomplished using a resonant  $\text{LiTaO}_3$  electro-optical modulator (EO-T500T3-MWIR1, Qubig) with a modulation frequency of  $\nu_m = 489 \text{ MHz}$  and thermo-electric temperature stabilization ( $T = 25.0 \pm 0.1 \text{ }^\circ\text{C}$ ). The EOM was operated in double-pass configuration with the detection beam being subject to frequency modulation on both passes. In order to ensure optimal phase overlap between the two passes, the distance between the EOM and the mirror behind it had to be set to the half-wavelength of the EOM modulation frequency, here about 30.7 cm. This configuration resulted in a modulation depth corresponding to a modulation index of  $M = 1.0$ , which is comparatively high for an MIR application. Thanks to the temperature stabilization of the EOM and the high frequency stability of the RF source, the modulation index remained practically constant for all experiments. Nevertheless, the modulation index was regularly checked with an in-house designed confocal scanning etalon with custom-coated YAG mirrors ( $R \approx 98.5\%$ ,  $2500 \text{ cm}^{-1} < \tilde{\nu} < 5000 \text{ cm}^{-1}$ , Layertec) and a piezo actuator (P-401-10, piezosystem jena). A  $\text{YVO}_4$  Glan-laser polarizer (Altechna) was placed in front of the EOM to match the polarization angle of the MIR laser beam to the specified input polarization plane of the EOM. The addition of an identical polarizer behind the EOM allows one to set the demodulation phase angle to pure absorption ( $\theta = 0^\circ, 180^\circ$ , in-phase). This phase setting method, which relies on the fact that the EOM acts as an amplitude modulator between crossed polarizers resulting in a quadrature FM signal, is explained in further detail in Refs. 29 and 13.

After passing through the shock tube via a pair of  $\text{CaF}_2$  windows, the modulated MIR beam was focused onto a fast photovoltaic  $\text{HgCdTe}$  detector with four-stage thermo-electric cooling (PVI-4TE-5, Vigo System, 686 MHz bandwidth). A built-in bias-tee separates the AC components caused by absorption or dispersion from the DC signal. Demodulation of the AC signal was

performed with an all-digital 600 MHz lock-in amplifier (UHFLI, Zurich Instruments) with the low-pass filter set to the highest possible bandwidth of  $\Delta f_{\text{BW}} = 790$  kHz, which corresponds to a 10%-to-90% rise time and hence time resolution  $t_r \approx 0.35/\Delta f_{\text{BW}}$  of around 500 ns. A high power amplifier (ZHL-20W-13, Mini Circuits, 51.9 dB gain), taking the 489 MHz RF signal from the lock-in-amplifier as input, served as driver for the EOM. Finally, the FM and DC signal traces were recorded on a digital storage oscilloscope (MSO 8104A, Agilent Technologies).

FM detection of HCN was performed on the P(26) transition in the  $\nu_1$  CH stretch band at  $3228.049 \text{ cm}^{-1}$ . As explained in our previous work in more detail [24], the selection of this transition combines a relatively high absorption cross section over the studied temperature range with spectral separation. Unlike other absorption lines in the same branch, it is well separated from hot band transitions that could otherwise cause interference [30]. Raw FM signal intensities can be converted to fractional absorption and hence HCN concentration using the FM working equation

$$\frac{I_{\text{FM}}/G}{I_0} = \frac{\Delta f}{2} \sigma_c c l. \quad (7.1)$$

Here,  $I_{\text{FM}}$  and  $I_0$  are the measured FM signal (after demodulation) and the total intensity signal (without absorbing sample), respectively.  $\sigma_c$  is the narrow-bandwidth absorption cross section at line center,  $c$  the concentration of the absorbing species,  $l$  the absorption path length,  $\Delta f$  the FM factor, and  $G$  the electronic gain or amplification factor of the FM signal relative to the  $I_0$  signal.  $G$  can be directly determined from the specification of all electronic components or by a direct comparison of the obtained FM signal with a normal absorption signal. For overall low fractional absorption  $A$ , Beer-Lambert's law yields

$$A = \frac{\Delta I/G'}{I_0} = \sigma_c c l, \quad (7.2)$$

where  $\Delta I = I_0 - I$  corresponds to the intensity absorbed by the sample, which is typically measured by a difference amplification scheme with a gain of  $G'$ . Compared to such a conventional absorption setup, the only additional quantity needed to perform a quantitative FM experiment is the FM factor  $\Delta f$ , which is a useful measure for the efficiency of an FM detection scheme. It can be pre-calculated for a known line profile of the probed absorption transition and is a function of  $T$ ,  $p$ ,  $M$ , and the ratio  $x_m$  of the modulation frequency  $\nu_m$  and the full width at half maximum (FWHM) of the absorption feature  $\Delta\nu_{\text{FWHM}}$ . For in-phase demodulation,  $\Delta f$  is given by

$$\Delta f = \frac{2}{\sigma_c} \times \sum_{n=0}^{\infty} J_n(M) J_{n+1}(M) (\sigma_{-n-1} - \sigma_{n+1} + \sigma_{-n} - \sigma_n), \quad (7.3)$$

with  $\sigma_i$  corresponding to the narrow-bandwidth value of the absorption cross section at the spectral position of the  $i$ -th sideband of the frequency-modulated laser beam, weighted according to their corresponding Bessel function values  $J_i(M)$ . For details of the underlying FM theory and the



concept of calculating FM factors we refer to the literature [13, 29, 31]. Note, however, that for the limiting case of a small modulation index ( $M \lesssim 0.3$ ), the FM factor is simply given by the difference of the absorptions probed by the lower and upper first side bands of the frequency-modulated light,  $\Delta f = M(\sigma_{-1} - \sigma_{+1})/\sigma_c$ , and thus  $\Delta f = M$  for  $x_m > 1$ . For a practical measurement of a concentration-time profile at a fixed detection wavelength, it is important to consider the resulting derivative-like lineshape. To maximize the absorption-induced FM signal, the carrier frequency of the detection beam needs to be shifted by  $\Delta\nu_{\text{opt}}$  from the absorption line center. The corresponding maximum FM factor is termed  $\Delta f_{\text{max}}$ .

## Shock Tube and Gas Mixtures

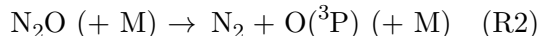
The experiments were conducted in the pressure-driven Kiel shock tube, an electropolished stainless steel tube with a total length of 8 m, a test section length of 4.4 m and an inner diameter of 81 mm. It is described in more detail in Ref. 32. Prior to each experiment, the test section of the shock tube was evacuated to pressures  $< 10^{-6}$  mbar by a combination of a turbomolecular and diaphragm pump. It was flushed with the particular gas mixture for 6 minutes to minimize possible adsorption effects at the shock tube walls. A calibrated mixture of HCN in  $\text{N}_2$  ( $969 \text{ ppm} \pm 29 \text{ ppm}$ ), pure  $\text{N}_2\text{O}$  ( $> 99.998\%$ ), and argon ( $99.999\%$ ) as balance gas were used to prepare reaction gas mixtures with variable compositions using calibrated mass flow controllers (Area FC-7700CU, Advanced Energy Industries). As the experiments were performed with 350 ppm and 500 ppm HCN, the reaction gas mixtures contained relatively large  $\text{N}_2$  fractions of 36.1% and 51.6%, respectively. All gases (Air Liquide) were used as supplied.

Incident and reflected wave conditions were derived from the initial pre-shock wave conditions in the test section and the shock wave velocities measured by three piezo-electric sensors (M113A21, PCB Piezotronics). The calculations were performed by a frozen-chemistry code accounting for temperature-dependent heat capacities and shock wave damping, which was typically around 1%/m. Instantaneous rotational and vibrational equilibration has been assumed for all molecular species. Whereas the vibrational relaxation times of  $\text{N}_2\text{O}$  are known to be well below 1  $\mu\text{s}$  for all temperatures and pressures used in this study [33], it cannot be completely ruled out that vibrational relaxation of  $\text{N}_2$  takes place on the time scale of the kinetic experiments. For example, by completely neglecting its vibrational relaxation, up to 5% higher initial temperatures would be expected behind the reflected shock wave for a 51.6%  $\text{N}_2$  gas mixture, which is significantly higher than the typically assumed  $\pm 1\%$  temperature uncertainty from the shock speed determination. Actually, expected relaxation times for  $\text{N}_2$  in a pure  $\text{N}_2$  bath gas [34] are 0.42 s for a typical incident shock (850 K, 0.5 bar) and 1.4 ms for a typical reflected shock (1700 K, 1.25 bar) experiment. However, the high  $\text{N}_2\text{O}$  content in the reaction gas mixtures (1.5% to 4%) considerably reduces the relaxation time by efficient near-resonant  $\text{N}_2\text{O}$ - $\text{N}_2$  vibrational energy transfer collisions. Relying on experimentally measured data for  $\text{N}_2(\text{v} = 1)/\text{N}_2\text{O}(\nu_3)$  energy transfer probabilities [35] and Lennard-Jones  $\text{N}_2/\text{N}_2\text{O}$  collision frequencies, we estimate the  $\text{N}_2$  vibrational relaxation times to be on the order of 5  $\mu\text{s}$  to 50  $\mu\text{s}$ . Hence, these are much shorter than the observed reaction time scales of 0.5–1 ms and close to the few  $\mu\text{s}$  time resolution of the conducted experiments in most

cases. Depending on the temperature, pressure, and  $\text{N}_2\text{O}$  content, the longest relaxation times are expected for the incident shock wave experiments at 1.5%  $\text{N}_2\text{O}$  mixing ratio level.

### Oxygen Atom Precursor and Reaction Mechanism

The thermal decomposition of  $\text{N}_2\text{O}$  served as the source for oxygen atoms, which are formed in their  $^3\text{P}$  ground state:



For simplicity, we refer to  $\text{O}(^3\text{P})$  as  $\text{O}$  throughout this work. Reaction R2 has been investigated over a wide range of temperatures and pressures in several studies [36–39]. Recently, Mulvihill et al. [40] measured the low-pressure rate constant of reaction R2 in the temperature range  $1546 \text{ K} < T < 2230 \text{ K}$  using  $\text{N}_2\text{O}$  laser absorption spectroscopy on the  $\text{P}(33)\text{e}$  transition in the  $\nu_3$  NN stretch band. We adopted the recommended Arrhenius expression, which was based on their measured accurate rate constants with a low uncertainty level of about 9% and low-temperature data from earlier studies. With densities of  $\rho < 1.1 \times 10^{-5} \text{ mol cm}^{-3}$ , all experiments conducted in the present work lie in the low-pressure region of the unimolecular decomposition of  $\text{N}_2\text{O}$  [37]. Collision efficiencies for gases other than argon (i.e.,  $\text{N}_2$  and  $\text{N}_2\text{O}$  that were present in significant amounts) were adopted from the literature as outlined in Tab. 7.1.

The detailed GDFkin3.0<sup>®</sup>\_NOMech2.0 [11] flame mechanism was used as a starting point to identify potentially important secondary chemistry for the simulation of the kinetic  $\text{HCN}$  profiles. For sensitivity analysis, sensitivity coefficients  $\sigma(i, t)$  for reaction  $i$  at time  $t$  were normalized with respect to the maximum concentration of  $\text{HCN}$  over the time history, resulting in  $\sigma(i, t) = (\partial[\text{HCN}]/\partial \ln k_i)/[\text{HCN}]_{\text{max}}$ . For the final mechanism outlined in Tab. 7.1, only 14 reactions with sensitivity coefficients of  $|\sigma(\text{HCN})| > 5 \times 10^{-3}$  needed to be considered. The corresponding rate constant expressions were updated with recent literature recommendations and thermodynamic data for all species were adopted from the ATcT database (version 1.122r) [54, 55]. Numerical simulations have been performed with the Chemkin-II package [56].

**Table 7.1:** Reduced reaction mechanism and Arrhenius parameters for the analysis of the shock tube experiments on HCN + O. Rate constants are given in the form  $k = A T^n \exp(-E_a/RT)$  in units of  $\text{cm}^3$ , mol, s, K, and kJ.  $k_0$  and  $k_\infty$  refer to the low-pressure and high-pressure limit rate constants of reaction R2, respectively.

No.	Reaction	$A$	$n$	$E_a$	Ref.	$T$ range / K
R1	HCN + O $\rightarrow$ products	$1.88 \times 10^{14}$	0.00	64.5	This work	1448–1954
R1a	$\rightleftharpoons$ NCO + H		See text		10, 41	
R1b	$\rightleftharpoons$ NH + CO		See text		10, 41	
R1c	$\rightleftharpoons$ CN + OH		See text		10, 41	
R2	N <sub>2</sub> O ( + M) $\rightleftharpoons$ N <sub>2</sub> + O ( + M)	$k_0$ $1.04 \times 10^{15}$ $k_\infty$ $1.26 \times 10^{12}$	0.00 0.00	250.2 262.0	40 37	850–2500 1570–3100
	collision efficiencies: Ar = 1.0, N <sub>2</sub> = $1.7 \pm 0.3$ , N <sub>2</sub> O = 2.0					37, 42, 43*
R3a	N <sub>2</sub> O + O $\rightleftharpoons$ NO + NO	$9.15 \times 10^{13}$	0.00	115.8	44	1370–4080
R3b	$\rightleftharpoons$ N <sub>2</sub> + O <sub>2</sub>	$3.69 \times 10^{12}$	0.00	66.7	44	1075–3340
R4	HCN + M $\rightleftharpoons$ HNC + M	$1.60 \times 10^{26}$	–3.23	216.9	12, 41	1000–2000
R5a	HCN + OH $\rightleftharpoons$ CN + H <sub>2</sub> O	$3.92 \times 10^6$	1.83	43.1	45	500–2000
R5b	$\rightleftharpoons$ HOCN + H	$3.19 \times 10^4$	2.45	50.7	46	298–2840
R6	HNC + O $\rightleftharpoons$ NH + CO	$4.60 \times 10^{12}$	0.00	9.2	47	1500–2400
R7a	HNC + OH $\rightleftharpoons$ HNCO + H	$3.60 \times 10^{12}$	0.00	–2.0	12, 48	250–2500
R7b	$\rightleftharpoons$ CN + H <sub>2</sub> O	$3.00 \times 10^2$	3.16	44.4	12	250–2500
R8a	N <sub>2</sub> O + H $\rightleftharpoons$ N <sub>2</sub> + OH	$2.20 \times 10^{14}$	0.00	70.1	49	1000–2000
R8b	$\rightleftharpoons$ NO + NH	$6.69 \times 10^{22}$	–2.16	155.6	49	1000–2000
R9	N <sub>2</sub> O + NCO $\rightleftharpoons$ N <sub>2</sub> + NO + CO	$9.04 \times 10^{13}$	0.00	116.4	50	500–2500
R10	NCO + O $\rightleftharpoons$ NO + CO	$4.52 \times 10^{13}$	0.00	0.0	50	500–2500
R11	NCO + NCO $\rightleftharpoons$ N <sub>2</sub> + CO + CO	$1.81 \times 10^{13}$	0.00	0.0	50	500–2500
R12a	NCO + NO $\rightleftharpoons$ N <sub>2</sub> + CO <sub>2</sub>	$5.79 \times 10^{18}$	–1.97	4.7	51	300–3000
R12b	$\rightleftharpoons$ N <sub>2</sub> O + CO	$6.41 \times 10^{16}$	–1.34	3.0	51	300–3000
R13	NH + O $\rightleftharpoons$ NO + H	$7.00 \times 10^{13}$	0.00	0.0	52	250–3000
R14	OH + OH $\rightleftharpoons$ H <sub>2</sub> O + O	$3.57 \times 10^4$	2.40	8.8	53	290–2380

\* The estimate for the collision efficiency of N<sub>2</sub>O is based on the study of Röhrig et al. [37], taking into account earlier results of Johnston et al. [43].

## 7.3 Results and Discussion

### HCN Detection System

**Allan Analysis:** In order to characterize the sensitivity of the MIR-FM detection scheme, an Allan noise analysis has been conducted. Overlapping Allan deviation (OADEV) served as the defining quantity of detection sensitivity [57]. The analysis was based on pure FM signal noise recorded without shock tube operation at a sampling rate of 2 MHz to match the minimum time resolution of 500 ns given by the demodulation electronics. An overlapping Allan deviation routine was applied to the FM signal noise data to calculate OADEV values at various sampling intervals  $\tau$ , which can be converted to the respective minimal detectable fractional absorption values  $A_{\min}$  using the FM working equation outlined above.

Voigt line profiles for the conversion of fractional absorption values to HCN mole fractions were calculated from line strengths and pressure-broadening parameters for the P(26) transition taken from the HITRAN database (line strengths) [30], our previous study on HCN detection (Ar parameters) [24], and a study by Rinsland et al. (N<sub>2</sub> parameters) [58]. At 1700 K and 1.2 bar, the Voigt linewidth in pure argon is  $\Delta\nu_{\text{Voigt}}^{\text{FWHM}} = 1.27$  GHz and the pressure broadening of the bath gas accounts for  $\sim 80\%$  to the total linewidth. For a modulation index of  $M = 1.0$  and a modulation frequency of  $\nu_m = 489$  MHz, the corresponding FM factor is  $\Delta f_{\max} = 0.63$  reached

at a frequency offset of  $\Delta\nu_{\text{opt}} = 0.61$  GHz. The exact quantities, which need to be known for a quantitative calibration-free detection, are a distinct function of temperature and pressure.

Figure 7.2 illustrates the line center absorption cross section  $\sigma_c$  as well as the FM detection parameters  $\Delta\nu_{\text{opt}}$  and  $\Delta f_{\text{max}}$  as a function of temperature for two representative pressures of 0.4 and 1.2 bar. The observed trends for  $\sigma_c$  in Fig. 7.2a are both a result of the temperature dependence of the line strength and the temperature and pressure dependencies of the line profile, whereas the frequency shift  $\Delta\nu_{\text{opt}}$  in Fig. 7.2b and the FM factor  $\Delta f_{\text{max}}$  in Fig. 7.2c only depend on the line profile function. With high  $\Delta f_{\text{max}}$  values of 0.35–0.75, the FM system provides sensitive HCN detection. Even higher FM factors could be achieved with a higher modulation index, which is, however, not technically feasible as yet. The much lower absorption cross sections and FM factors for a pressure increase from 0.4 bar to 1.2 bar underline the fact that careful consideration of pressure-broadening effects is very important for MIR-FM detection. For example, as calculated from the ratios of  $\sigma_c$  and  $\Delta f_{\text{max}}$ , at  $T = 1000$  K the FM detection sensitivity is about a factor of 3.1 lower at 1.2 bar as compared to 0.4 bar. In a standard non-modulated laser absorption experiment, the factor becomes 2.4, since only the ratio of  $\sigma_c$  matters.

The black curve in the Allan plot shown in Fig. 7.3a represents the minimum detectable HCN mole fraction for a typical temperature and pressure of 1700 K and 1.2 bar (corresponding to  $\Delta f_{\text{max}} = 0.63$ ). Using the same noise data, the orange curve reflects the close-to-ideal situation with an FM factor of  $\Delta f_{\text{max}} = 1.0$ ; the corresponding Allan curve is simply shifted to lower detection limits according to the ratio of the FM factors. Starting with the minimal sampling interval of  $\tau = 500$  ns, which is equivalent to a single point of the measured FM signal noise and the 10%-to-90% rise time of the detection system, the OADEV values initially decrease with  $\tau^{-1/2}$ . This is the expected behavior for noise with frequency-independent power spectral density (white noise), such as thermal or shot noise. At  $\tau = 500$  ns, the HCN detection limit (for  $T = 1700$  K and  $p = 1.2$  bar) is 29 ppm, corresponding to a minimum detectable absorption of  $A_{\text{min}} = 3.6 \times 10^{-4}$ . This detection limit is further improved with data point averaging (corresponding to a lower time resolution) down to  $A_{\text{min}} = 3.6 \times 10^{-5}$  (2.9 ppm) reached at  $\tau = 100$   $\mu$ s. Beyond  $\tau = 100$   $\mu$ s, the sensitivity of the MIR-FM detection scheme is again reduced due to residual amplitude modulation (RAM) effects that are well-known to limit FM-based applications in the kHz range [13, 28, 59]. They are of minor concern for most shock tube applications that require time resolutions in the  $\mu$ s range and exhibit maximum test times behind the reflected shock wave of typically 1 ms.

The noise analysis of pure FM noise does not yet account for extra noise components from shock tube operation. As it will become clear from the shock tube data presented below, however, the resulting baseline instabilities were not particularly pronounced. The blue curve in Fig. 7.3a represents an Allan analysis of the baseline noise of a typical shock tube experiment behind the reflected shock wave. Whereas already at short times shock tube operation does add some noise (about a factor of 1.5 in Fig. 7.3a), more significant baseline undulations occur on longer time scales and impair the effective detection sensitivity by a factor of about 2. For a typical time resolution of  $\tau = 5$   $\mu$ s, the minimum detectable fractional absorption is  $A_{\text{min}} \approx 2 \times 10^{-4}$ . This value is about 5–10 times lower than the typical detection sensitivity of  $A_{\text{min}} \approx (1 - 2) \times 10^{-3}$

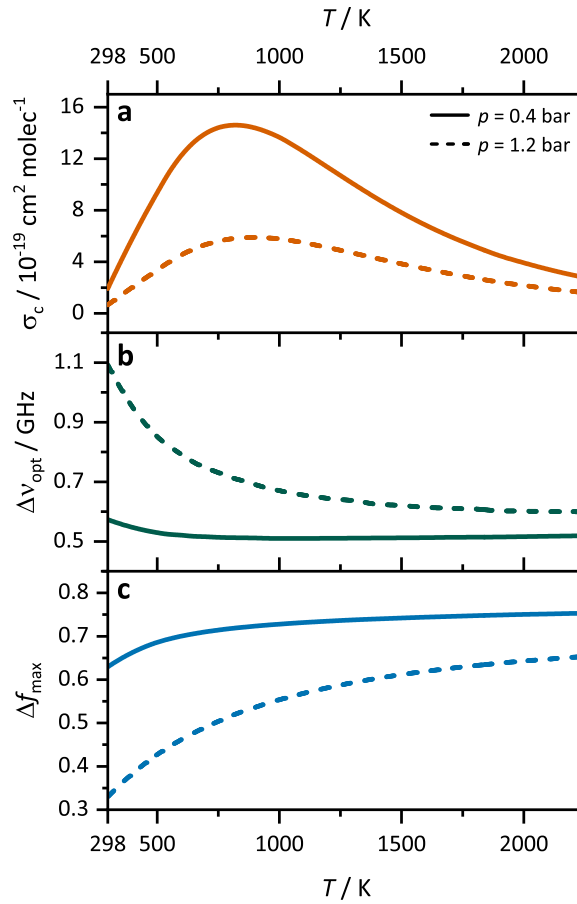


**Figure 7.2:** HCN line center absorption cross section  $\sigma_c$  (bath gas argon, P(26) line at  $\tilde{\nu}_c = 3228.049 \text{ cm}^{-1}$ ) and FM detection parameters  $\Delta \nu_{\text{opt}}$  and  $\Delta f_{\text{max}}$ , calculated for  $M = 1.0$  and  $\nu_m = 489 \text{ MHz}$ .

reported for conventional single- and dual-beam absorption setups using low-noise single-frequency MIR diode lasers [60, 61].

**Shot-Noise Limit:** FM-based applications in the visible range routinely achieve shot-noise limited detection sensitivity [13]. This requires the light power on the photodetector  $P$  to be high enough to overcome laser excess and thermal noise. Due to lower band gaps in the photoactive material of the detectors, the latter often dominates and is more difficult to overcome in MIR-based systems. Whereas the absorption signal scales with  $P$ , shot noise increases with the square root of the number of photons. Consequently, the minimal detectable absorption of a shot noise limited detection scheme scales with  $P^{-1/2}$ . In contrast, thermal noise is power-independent, hence the detection limit of thermal-noise limited detection systems scales with  $P^{-1}$ . Clearly, higher power levels on the photodetector are advantageous, but are limited both by optical saturation of the probed absorption transition and saturation of the detector electronics in practical applications.

Figure 7.3b illustrates the trend of experimental detection limits determined from the measured FM noise level at different light powers (black circles).  $A_{\text{min}}$  values were calculated for  $\tau = 1 \mu\text{s}$  and  $\Delta f_{\text{max}} = 0.6$  using the standard FM working equations. At the highest used light power of

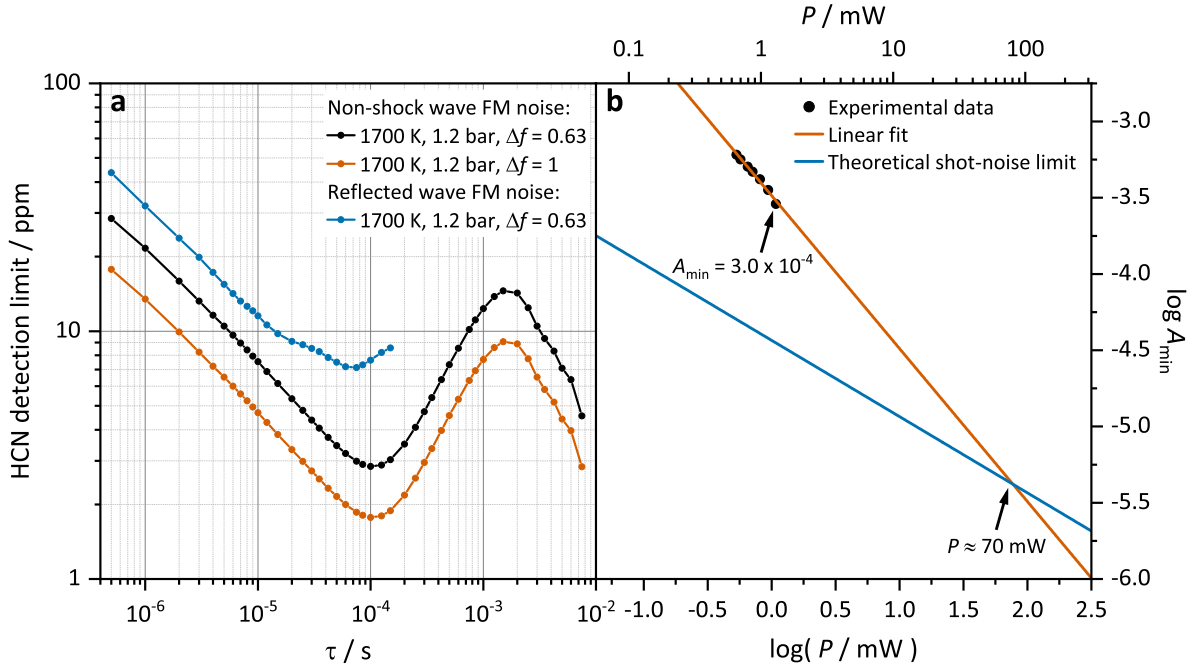


**Figure 7.3:** (a) HCN detection limits ( $M = 1.0$ ,  $\nu_m = 489 \text{ MHz}$ ,  $T = 1700 \text{ K}$ ,  $p = 1.2 \text{ bar}$ , bath gas argon) as function of the sampling interval  $\tau$  (equal to the time resolution). The black and orange curves are based on pure FM baseline noise without shock tube operation, the blue curve reflects typical noise characteristics of a reflected shock wave experiment. (b) log-log plot of experimental  $A_{\min}$  values ( $\tau = 1 \mu\text{s}$ ,  $\Delta f = 0.6$ ) versus the light power  $P_0$  on the photodetector (symbols and orange line). The corresponding theoretical shot-noise limit is shown for comparison as well (blue line).

1.08 mW, which is still in the linear regime of the HgCdTe detector (up to 1.2 mW, full saturation at 1.6 mW), the minimal detectable absorption reaches a value of  $A_{\min} = 3.0 \times 10^{-4}$ . This is still about 8 times higher than the shot-noise limit  $A_{\min}^{\text{SN}}$  derived from the following equation [13, 31]:

$$A_{\min}^{\text{SN}} = \frac{4}{\Delta f_{\max}} \left[ \eta \left( \frac{P}{h\nu_c} \right) \tau \right]^{-1/2} \quad (7.4)$$

Here,  $h$  is Planck's constant and  $\eta$  the quantum efficiency of the detector at light frequency  $\nu_c$ . The orange line in Fig. 7.3b represents a linear fit to the experimental  $A_{\min}$  values and the blue line indicates the corresponding shot-noise limit  $A_{\min}^{\text{SN}}$  with a slope of  $-0.5$  on the logarithmic scale. With a slope of  $-1.0$ , the experimental  $A_{\min}$  values clearly suggest that the current implementation of the MIR-FM detection system is still limited by thermal noise contributions. Simple extrapolation reveals that  $P \approx 70 \text{ mW}$  would be needed to reach a shot-noise limited situation, which would correspond to an excellent detection limit of  $A_{\min} < 5 \times 10^{-6}$  at a time resolution of  $1 \mu\text{s}$ . However, besides the problem of optical saturation that may easily become significant at such high light powers [62], to the best of our knowledge, MIR photodetectors that combine such a high saturation limit with the required high bandwidths around 500 MHz are not available. Therefore, future implementations shall also explore two-tone FM schemes that offer shot-noise limited detection capability with lower detector bandwidth requirements [63].

### HCN + O Rate Constant

In order to determine the total rate constant for the reaction  $\text{HCN} + \text{O}$ , 24 shock tube experiments were performed in the temperature range  $1448 \text{ K} < T < 1954 \text{ K}$ . Four of those experiments were conducted behind the incident wave and the other 20 behind the reflected wave. A summary of the experimental conditions and the resulting values for  $k_{\text{R1}}$  are included in Table 7.2.

With HCN detection capability down to the ppm mole fraction level, the present MIR-FM detection system allows one to perform direct rate constant measurements behind shock waves. Nevertheless, as a compromise between detection sensitivity and time resolution, the kinetic profiles were smoothed by adjacent averaging with a 10-point window to a time resolution of  $5 \mu\text{s}$ . With a detection sensitivity of  $A_{\text{min}} \approx 2 \times 10^{-4}$ , this corresponds to a detection limit of about 15 ppm HCN for an experiment at  $T = 1700 \text{ K}$  and  $p = 1.2 \text{ bar}$  (see blue curve in Fig. 7.3a).

**Data Analysis:** Figure 7.4 shows an example of a kinetic HCN profile measured by shock heating a gas mixture containing 350 ppm HCN and 1.5%  $\text{N}_2\text{O}$ . The plot in Fig. 7.4a reflects the raw FM signal. Due to the low pressure and hence low HCN concentration in the pre-shock reaction gas mixture ( $T = 293 \text{ K}$ ,  $p = 22 \text{ mbar}$ ) as well as the unfavorable FM factor at these conditions, the expected FM response of HCN is almost zero such that the pre-shock signal can be used as a baseline. Following the arrival of the incident shock wave ( $T = 908 \text{ K}$ ,  $p = 0.23 \text{ bar}$ ), a step-like HCN signal is observed and the signal plateau reflects the thermal stability of HCN and  $\text{N}_2\text{O}$  at this temperature. The slight increase of the HCN signal during the first few tens of  $\mu\text{s}$  may indicate the delayed vibrational equilibration of  $\text{N}_2$ . This time scale is consistent with an estimated  $30 \mu\text{s}$  vibrational relaxation time based on literature results for  $\text{N}_2\text{O}/\text{N}_2$  near-resonant vibrational energy transfer [35] and the 1.5%  $\text{N}_2\text{O}$  mole fraction (see Experimental section). It causes the experimental temperature to decrease by about 10 K, going along with a slight increase of the HCN absorption cross section. With the arrival of the reflected wave at  $t = 0$  ( $T = 1632 \text{ K}$ ,  $p = 1.07 \text{ bar}$ ), the signal is about halved, which is mainly due to the temperature dependence of the absorption cross section and the FM factor (see Fig. 7.2). For data analysis, the initial FM signal was set equal to HCN mole fractions in the reaction gas mixture. However, the resulting conversion factors were found to be consistent with the calculated factors based on  $\sigma_c$  and  $\Delta f_{\text{max}}$  within  $\pm 8\%$ . This good agreement confirms the reliability of the detection system for quantitative and sensitive MIR-FM detection of HCN.

The reflected wave initiates the thermal decomposition of  $\text{N}_2\text{O}$  and subsequently the oxidation of HCN according to reaction R1. Figure 7.4b shows the corresponding HCN profile in terms of mole fractions (black curve) as well as the simulated HCN (blue curve) and O atom (solid magenta curve) profiles. The pronounced induction period of the HCN decay reveals that the reaction does not follow pseudo-first order kinetics and that accurate modeling of the intermediate O atom concentration level is important for the determination of the rate constant of the  $\text{HCN} + \text{O}$  reaction. At the experimental conditions of this study, the decomposition of  $\text{N}_2\text{O}$  is indeed slow and also sets the lower limit for the experimentally feasible temperature range. For example, the thermal  $\text{N}_2\text{O}$  half-life time of about 5 ms for the experiment shown in Fig. 7.4, which represents



**Table 7.2:** Experimental shock wave conditions and total rate constants  $k_{\text{R1}}$  for the reaction  $\text{HCN} + \text{O}$ .

$T$ / K	$p$ / bar	$\rho \times 10^{-6}$ / mol cm <sup>-3</sup>	$x(\text{HCN})^\dagger$ / ppm	$x(\text{N}_2\text{O})$ / %	$k_{\text{R1}} \times 10^{-12}$ / cm <sup>3</sup> mol <sup>-1</sup> s <sup>-1</sup>
1448	1.18	9.91	500	2.0	0.9
1480	1.04	8.52	500	2.0	1.0
1502	1.08	8.64	500	2.0	0.9
* 1584	0.43	3.26	350	1.5	1.6
1605	1.41	10.69	500	2.0	1.5
1608	1.27	9.50	500	4.0	1.3
1632	1.07	7.86	350	1.5	2.1
1647	1.26	9.19	500	2.0	1.3
1656	1.10	7.95	350	3.0	2.2
* 1664	0.47	3.39	350	3.0	2.3
1666	1.25	9.02	500	2.0	1.8
1700	1.38	9.88	500	4.0	1.4
1716	1.35	9.45	500	2.0	1.9
* 1716	0.45	3.16	350	1.5	2.4
1732	1.44	10.01	500	4.0	1.6
1741	0.96	6.69	350	1.5	2.1
1743	1.38	9.55	500	2.0	2.3
1764	1.21	8.26	350	1.5	2.3
1772	1.14	7.82	350	3.0	2.9
1777	1.21	8.28	350	1.5	2.6
* 1821	0.49	3.20	350	2.0	3.2
1824	1.49	9.83	500	2.0	2.4
1867	1.53	9.96	500	2.0	2.4
1954	1.42	8.75	350	1.5	3.7

\* Experiments behind incident shock waves.

† Since the 969 ppm HCN stock gas mixture contained  $\text{N}_2$  as balance gas, the reaction gas mixtures with 350/500 ppm HCN, next to  $\text{N}_2\text{O}$  and Ar, also contained 36.1/51.6%  $\text{N}_2$ .

a measurement at an intermediate temperature of 1632 K, already exceeds the maximum about 1 ms measurement time window behind the reflected wave. The actual O atom profile reflects the interplay of slow O atom formation from  $\text{N}_2\text{O}$  thermal decomposition and the fast consecutive  $\text{N}_2\text{O} + \text{O}$  reaction. For an unperturbed simulation (dashed magenta curve in Fig. 7.4b, without HCN), the O atom mole fraction remains much smaller (about 275 ppm at  $t = 700 \mu\text{s}$ ) than the initial  $\text{N}_2\text{O}$  mole fraction of 15000 ppm. In the presence of HCN (solid magenta curve), O atom consumption by reaction R1 induces a further decrease of the resulting O atom mole fraction level.

Two additional examples for experimental HCN profiles are shown in Fig. 7.5 together with the corresponding sensitivity analyses. The experiment at higher temperature in Fig. 7.5c exhibits a noticeably higher noise level than the experiment in Fig. 7.5a, revealing that the temperature dependence of the absorption cross section of the probed P(26) line limits the accessible temperature range. For example, the HCN profile in Fig. 7.5c has a noise level of around 35 ppm, which would increase to roughly 63 ppm at 2500 K assuming a similar FM signal noise level. Best-fit simulations of the HCN profiles in Fig. 7.5 using  $k_{\text{R1}}$  as the adjustable parameter (solid blue curves) nicely reproduce the shape of the experimental profiles. In contrast, simulations with  $k_{\text{R1}}$  multiplied or divided by a factor of 2 (dashed blue curves) deviate significantly from the experiment, indicating

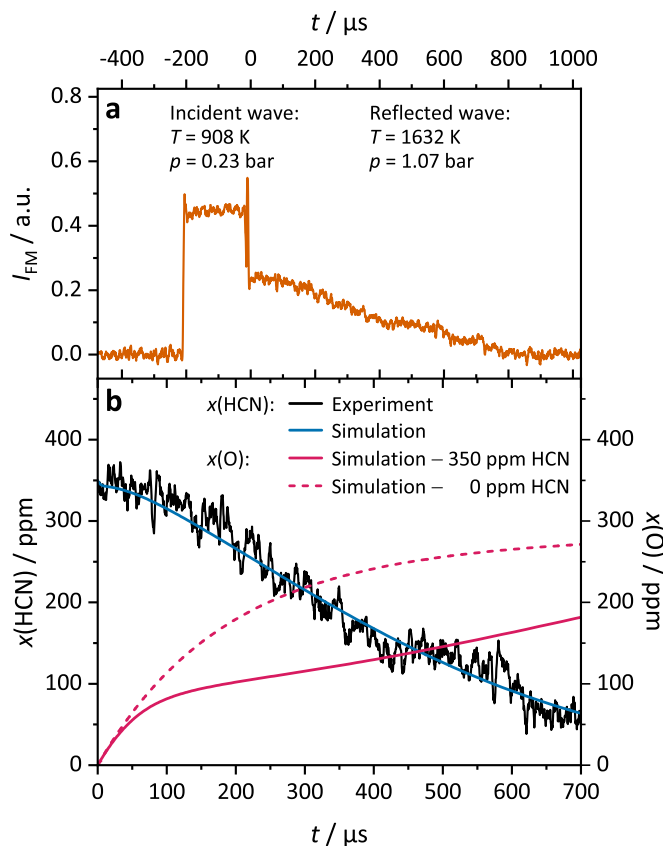


**Figure 7.4:** Kinetic profile of HCN in terms of (a) the raw FM signal  $I_{\text{FM}}$  and (b) HCN mole fractions behind the reflected shock wave ( $T = 1632 \text{ K}$ ,  $p = 1.07 \text{ bar}$ , 350 ppm HCN, 1.5%  $\text{N}_2\text{O}$ ). The curves depict the results of a numerical simulation for HCN (solid blue) and O atoms (solid magenta); a simulated O atom profile in the absence of HCN is shown as well (dashed magenta).

that a sensitive determination of  $k_{\text{R1}}$  was possible.

Sensitivity coefficients  $\sigma(\text{HCN})$  for the most important reactions are shown in Figs. 7.5b and 7.5d. Both reaction R1 (sum of the reaction channels R1a and R1b) and reaction R2 show similar and high sensitivities, but the two reaction channels of the consecutive reaction  $\text{N}_2\text{O} + \text{O}$  (reaction R3) are important as well. Clearly, the extracted  $k_{\text{R1}}$  values strongly rely on the accurate treatment of the O atom yield set by  $k_{\text{R2}}$  and  $k_{\text{R3}}$ . Here, rate constant values for  $k_{\text{R3a}}$  and  $k_{\text{R3b}}$  were based on the recommendation by Meagher and Anderson [44]. In contrast to the O atom yield, the assumed branching ratio for reaction R1 turned out to be of minor importance. We have adopted the branching fractions reported by Glarborg et al. [10] (80%, 20%, and  $< 1\%$  for channels R1a, R1b, and R1c at  $T = 1700 \text{ K}$ ), but simulations with the recommendation by Dean and Bozzelli [41] (placing an about 10% higher weight on channel R1b) changed the simulated HCN mole fractions by less than 1 ppm over the entire reaction profile, which is well below the noise level. Note that the H atoms formed in the main reaction channel R1a are fully captured by reaction R8,  $\text{N}_2\text{O} + \text{H}$ , such that the possible reaction  $\text{HCN} + \text{H}$  does not play a role.

As already mentioned in the Introduction, the isomerization of HCN to HNC (reaction R4) opens up additional oxidation routes towards  $\text{NO}_x$  [12, 64]. Under the experimental conditions

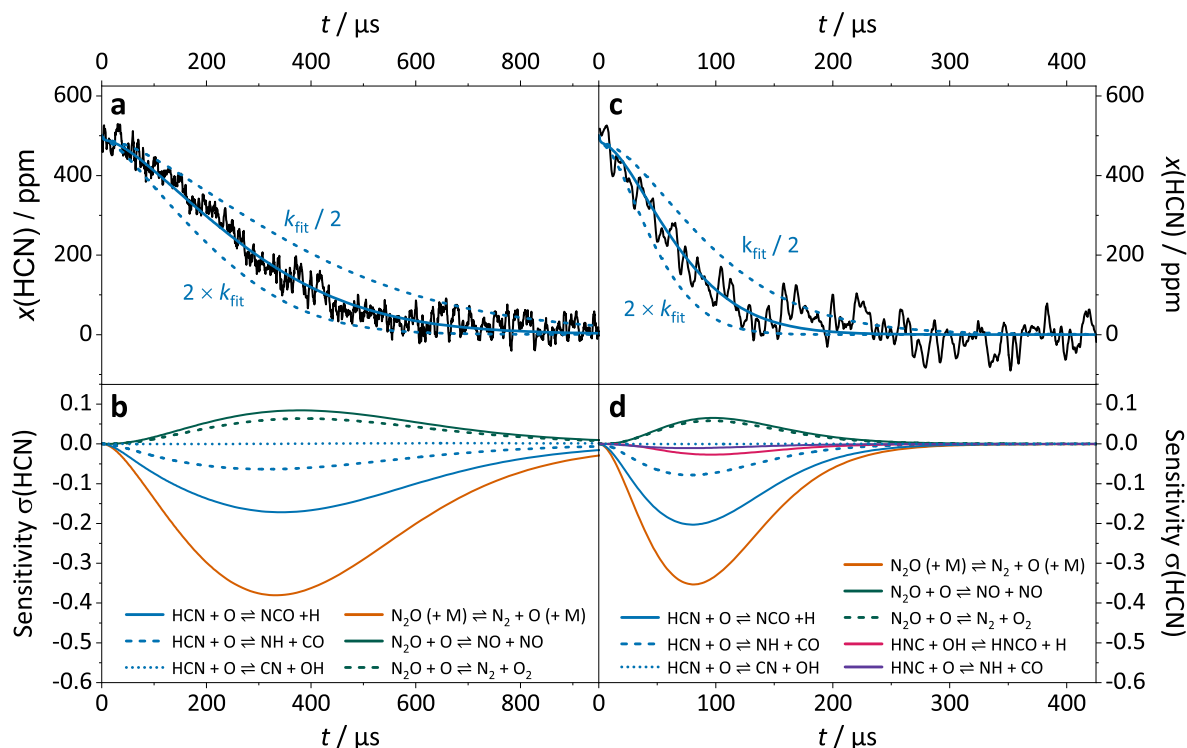


**Figure 7.5:** Experimental and simulated HCN profiles at 1666 K, 1.25 bar (a) and 1867 K, 1.55 bar (c). Simulations with  $k_{\text{R1}}$  divided or multiplied by a factor of 2 are shown as well. The corresponding sensitivity coefficients  $\sigma(\text{HCN})$  for the most relevant reactions are shown in (b) and (d).

studied in this work, HCN-HNC equilibration is established within a few microseconds and the equilibrium lies firmly on the side of HCN ( $\sim 99\%$  at 1448 K,  $\sim 95\%$  at 1954 K). HNC oxidation only starts to contribute to HCN/HNC loss at the highest experimental temperatures (see magenta and purple curves in Fig. 7.5d).

Rate constant results for  $k_{\text{R1}}$  are listed in Table 7.2 and are included in the Arrhenius plot in Fig. 7.6 as black symbols. Filled circles correspond to measurements behind reflected waves and open circles to measurements behind incident waves. The latter have been performed at a factor of about 3 lower total pressure and overall concentration levels, yielding about 20% higher rate constant values on average. Secondary chemistry and the assumed experimental temperature that critically determines the O atom yield may explain this minor discrepancy. In particular, the delayed  $\text{N}_2$  equilibration, which is more significant at the lower pressures behind the incident wave, may have caused a slight systematic underestimation of the assumed experimental temperature. Of course, the remaining difference may also indicate a real pressure dependence of the rate constant, however, according to the theoretical calculations of Miller et al. [65], this is not expected. These authors performed a detailed rate constant study on the chemically activated complex-forming reaction using statistical theories, but a full master-equation analysis of the pressure dependence has not been performed as yet.

For deriving uncertainty levels for  $k_{\text{R1}}$ , the scatter of the data points in terms of the standard error of  $\pm 4\%$ , the uncertainties in the rate constants for  $\text{N}_2\text{O} + \text{M}$  ( $\pm 9\%$ , derived from the uncertainties

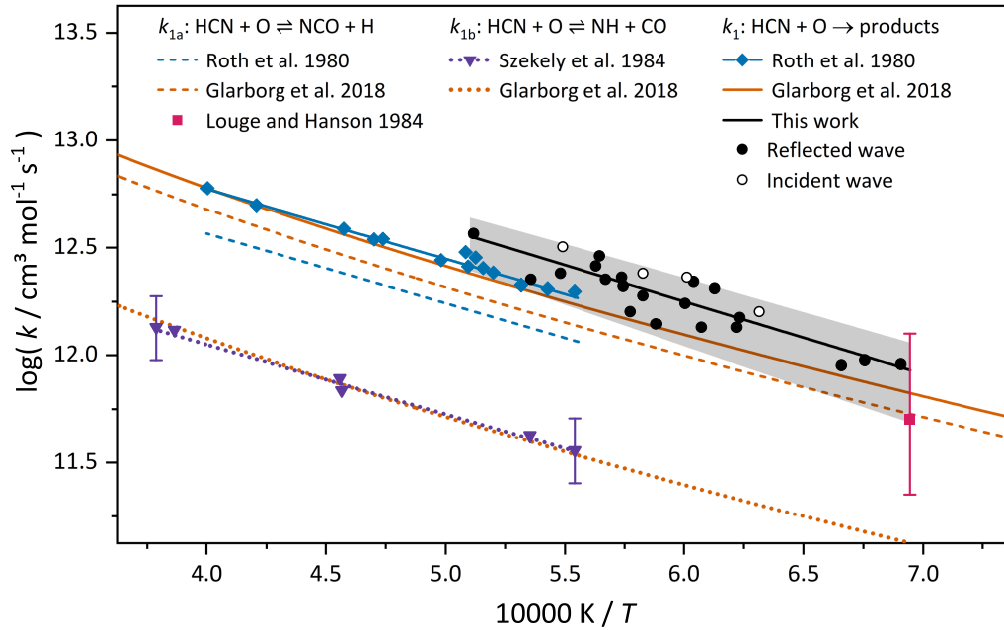


**Figure 7.6:** Arrhenius plot for reaction R1,  $\text{HCN} + \text{O}$ . Experimental total rate constants from measurements behind incident (open black circles) and reflected shock wave (solid black circles), corresponding Arrhenius expression (black line), and uncertainty range (grey area). Selected literature data for  $k_{\text{R1a}}$ ,  $k_{\text{R1b}}$ , and  $k_{\text{R1}}$  have been adopted from Refs. 10, 25–27.

in the Arrhenius parameters in Ref. 40) and  $\text{N}_2\text{O} + \text{O}$  ( $\pm 20\%$ , estimated), the uncertainties of the experimental temperature ( $-0.5\%$  to  $+1.5\%$ , including the potential underestimation of the assumed effective experimental temperature due to the delayed  $\text{N}_2$  equilibration), the uncertainty due to the error in the  $\text{N}_2$  collision efficiency ( $\pm 11\%$  for mixtures with  $51.6\%$   $\text{N}_2$ ), as well as the uncertainties of the initial concentrations of  $\text{N}_2\text{O}$  ( $\pm 2\%$ ) and  $\text{HCN}$  ( $\pm 5\%$ ) were taken into account. Since our experimental rate constants show no significant dependence on the  $\text{N}_2\text{O}$  mole fraction, potential errors in the collision efficiency of  $\text{N}_2\text{O}$  were considered negligible.

In simulations of  $\text{HCN}$  profiles performed at 1448 K, 1700 K, and 1954 K, the values for the respective quantities were varied within their assumed uncertainty limits and  $k_{\text{R1}}$  was re-adjusted to best reproduce the  $\text{HCN}$  profile. All individual uncertainties for  $k_{\text{R1}}$  were added in quadrature to allow for partial error compensation, resulting in a weakly temperature-dependent, asymmetric relative uncertainty of  $\Delta k_1/k_1 = (+28\%, -37\%)$  on average, with increasing uncertainties towards lower temperatures. Interestingly, despite the relatively low uncertainty of the experimental temperature of  $-0.5\%/+1.5\%$ , with up to  $36\%$ , the temperature contributed most to the overall uncertainty. This is due to the high activation energy of  $E_{\text{A}} = 250 \text{ kJ/mol}$  for the thermal decomposition of  $\text{N}_2\text{O}$  [40]. The uncertainty range of the rate constant data for  $k_{\text{R1}}$  is visualized as the grey area in Fig. 7.6. Overall, the data are best represented by the following Arrhenius expression (black line).

$$k_{\text{R1}}/(\text{cm}^3 \text{ mol}^{-1} \text{ s}^{-1}) = 1.88 \times 10^{14} \exp(-64.5 \text{ kJ mol}^{-1}/RT) \quad (+28\%, -37\%)$$

**Comparison with Literature:** Figure 7.6 compares the rate constant results for  $k_{\text{R1}}$  of the present study with available experimental high-temperature shock tube data and a recent recommendation by Glarborg et al. [10]. Channel-specific rate constants  $k_{\text{R1a}}$  and  $k_{\text{R1b}}$  are included in the plot as well. Channel R1c exhibits much lower rate constants with a branching fraction below 1% and, for the sake of clarity, is not included in the graph.

By means of atom resonance absorption spectroscopy (ARAS), Roth et al. [25] monitored H and O atom concentration-time profiles at temperatures  $1800 \text{ K} \leq T \leq 2500 \text{ K}$  using low concentration mixtures of HCN (25 to 200 ppm) and  $\text{N}_2\text{O}$  (5 to 40 ppm). They were able to deduce the total rate constant from the O-ARAS profile (blue diamond symbols and solid blue line) and the branching fraction of the H atom forming main reaction channel (62.5%, dashed blue line) from the H-ARAS experiments. From today's view, the remaining 37.5% shall be mainly attributed to the  $\text{NH} + \text{CO}$  forming reaction channel R1b. Szekely et al. [26] deduced  $k_{\text{1b}}$  values from NH laser absorption measurements at  $1800 \text{ K} \leq T \leq 2600 \text{ K}$ . Their data and Arrhenius expression are shown as purple triangle symbols and dotted purple line, and, referenced to the total rate constant of Ref. 25, yield a branching fraction of 20%. Szekely et al. also measured CN profiles, but due to the low CN yield were only able to estimate an upper limit for  $k_{\text{R1c}}$  (not shown in Fig. 7.6). In the same working group, Louge and Hanson [27] developed a laser absorption diagnostic tool for NCO detection behind shock waves. By comparison of NCO profiles measured for mixtures of  $\text{C}_2\text{N}_2/\text{N}_2\text{O}/\text{O}_2$  and  $\text{HCN}/\text{N}_2\text{O}/\text{O}_2$  as well as by detailed modeling, they were able to derive a relative rate constant estimate for  $k_{\text{R1a}}$ . Referenced to the rate constant of the reaction  $\text{C}_2\text{N}_2 + \text{O} \rightarrow \text{CN} + \text{NCO}$ , they reported a single value of  $k_{\text{R1a}} = 10^{11.7(-0.35, +0.40)}$  for  $T = 1440 \text{ K}$  (magenta square symbol).

The rate constants from all previous experimental studies, including the results of two additional sets of measurements at lower temperatures by Davies and Thrush [66] (450-650 K, discharge flow reactor, O atom detection by chemiluminescence) and Perry and Melius [67] (540-900 K, discharge flow reactor, O atom detection by chemiluminescence, laser-induced fluorescence detection of NCO) are well reproduced by the Glarborg et al. [10] recommendation (orange curves). For the two main reaction channels R1a and R1b, they adopted the previous Miller and Bowman recommendation [68], which in turn was based on the results of statistical rate constant calculations of Perry and Melius [67] and Miller et al. [65]. Actually, in order to reproduce the experimental rate constant studies, the transition state energies for the initial  $\text{HC(O)N}$  complex forming step were scaled by 6–11 kJ/mol within the error limits of the applied BAC-MP4 method in Refs. 67 and 65. Using a similar scaling for the transition state barrier of the H abstraction reaction channel R1c resulted in  $k_{\text{R1c}}$  values well above the upper limit determined by Szekely et al. [26]. Therefore, Dean and Bozzelli[41] recommended a much lower rate constant using QRRK methodology and the original BAC-MP4 barrier. Their rate constant expression for  $k_{\text{R1c}}$ , which has been adopted by Glarborg et al., makes this reaction channel unimportant up to very high temperatures (0.3% at  $T = 3000 \text{ K}$ ).

In a nutshell, although the theoretical treatments are in reasonable agreement with previous experimental results, to the best of our knowledge, a state-of-the-art rate constant prediction based on high-level quantum-chemical calculations is not available as yet. In this light, we consider our

new rate constant data a valuable addition to the existing experimental data set. They are largely consistent with the previous experimental studies and the Glarborg et al. [10] recommendation, but yield  $\sim 30\%$  and  $\sim 50\%$  higher rate constants at the lowest and highest temperature of this study, respectively.

## 7.4 Summary

We have demonstrated the application of single-tone MIR-FM spectroscopy for sensitive high-temperature detection of HCN behind shock waves. Using the thermal decomposition of  $\text{N}_2\text{O}$  as the source of atomic oxygen, the total rate constant  $k_{\text{R1}}$  of the reaction  $\text{HCN} + \text{O}$  has been determined for temperatures between 1448 K and 1954 K. The obtained Arrhenius expression

$$k_{\text{R1}}/(\text{cm}^3 \text{ mol}^{-1} \text{ s}^{-1}) = 1.88 \times 10^{14} \exp(-64.5 \text{ kJ mol}^{-1}/RT) \quad (+28\%, -37\%)$$

bridges the gap between previous low-temperature discharge-flow reactor measurements of Davies and Thrush [66] and Perry and Melius [67] ( $T < 900 \text{ K}$ ) and the shock tube measurements of Roth et al. [25] ( $T > 1800 \text{ K}$ ). Despite the fact that our rate constants are up to 50% higher than previous recommendations, keeping in mind that all rate constant studies relied on detailed modeling of the measured kinetic profiles, the overall agreement of the experimental studies is remarkable. Including our new measurements, kinetic profiles of almost all involved reactant and product species have been analyzed for the reaction  $\text{HCN} + \text{O}$  by now. With HCN (this work), O [25, 66, 67], NCO [27, 67], H [25], NH [26], and CN [26] profiles available, the total rate constant and the branching fractions (perhaps with the exception of the minor  $\text{CN} + \text{OH}$  channel) of this important reaction seem to be well set.

The MIR-FM detection system enables sensitive and quantitative detection of HCN behind shock waves. The Allan sensitivity analysis of the FM signal noise yielded minimum detectable absorption values of  $A_{\text{min}} \approx (0.8 - 1.3) \times 10^{-4}$  at a time resolution of  $\tau = 5 \mu\text{s}$ , somewhat reduced by shock-induced noise contributions to  $A_{\text{min}} \approx 2 \times 10^{-4}$  at  $\tau = 5 \mu\text{s}$  behind reflected shock waves. This high sensitivity allowed us to detect HCN down to the ppm level. Further improvements of the detection system may become possible with the availability of photodetectors with higher saturation limit, and future MIR detection of other nitrogen species such as HNC and  $\text{NH}_3$  may prove useful to get further insight into the combustion chemistry of nitrogen species. Whereas the present paper focused on the characterization of the new detection system and a first rate constant study, for the sake of completeness it should be mentioned that we have already completed another high temperature shock tube study [69] that relied on the quantitative detection capability. Therein, by simultaneous monitoring of HCN and NCN concentration-time profiles, the absolute yield of HCN in the reaction  $\text{NCN} + \text{H}$  has been determined.

## Acknowledgments and Funding

The setup of the MIR-FM spectrometer was possible thanks to financial support of the German Science Foundation (DFG) through project FR1529/7-1.

## References

- [1] P. Dagaut, P. Glarborg, M. Alzueta, The oxidation of hydrogen cyanide and related chemistry, *Prog. Energy Combust. Sci.* **2008**, *34*, 1–46, DOI [10.1016/j.pecs.2007.02.004](https://doi.org/10.1016/j.pecs.2007.02.004).
- [2] N. Lamoureux, P. Desgroux, M. Olzmann, G. Friedrichs, The story of NCN as a key species in prompt-NO formation, *Prog. Energy Combust. Sci.* **2021**, *87*, 100940/1–34, DOI [10.1016/j.pecs.2021.100940](https://doi.org/10.1016/j.pecs.2021.100940).
- [3] H. Kobayashi, A. Hayakawa, K. K. A. Somarathne, E. C. Okafor, Science and technology of ammonia combustion, *Proc. Combust. Inst.* **2019**, *37*, 109–133, DOI [10.1016/j.proci.2018.09.029](https://doi.org/10.1016/j.proci.2018.09.029).
- [4] G. Chehade, I. Dincer, Progress in green ammonia production as potential carbon-free fuel, *Fuel* **2021**, *299*, 120845/1–34, DOI [10.1016/j.fuel.2021.120845](https://doi.org/10.1016/j.fuel.2021.120845).
- [5] A. Hayakawa, T. Goto, R. Mimoto, T. Kudo, H. Kobayashi, NO formation/reduction mechanisms of ammonia/air premixed flames at various equivalence ratios and pressures, *Mech. Eng. J.* **2015**, *2*, 14-00402/1–10, DOI [10.1299/mej.14-00402](https://doi.org/10.1299/mej.14-00402).
- [6] A. Hayakawa, T. Goto, R. Mimoto, Y. Arakawa, T. Kudo, H. Kobayashi, Laminar burning velocity and Markstein length of ammonia/air premixed flames at various pressures, *Fuel* **2015**, *159*, 98–106, DOI [10.1016/j.fuel.2015.06.070](https://doi.org/10.1016/j.fuel.2015.06.070).
- [7] A. Hayakawa, Y. Arakawa, R. Mimoto, K. K. A. Somarathne, T. Kudo, H. Kobayashi, Experimental investigation of stabilization and emission characteristics of ammonia/air premixed flames in a swirl combustor, *Int. J. Hydrogen Energy* **2017**, *42*, 14010–14018, DOI [10.1016/j.ijhydene.2017.01.046](https://doi.org/10.1016/j.ijhydene.2017.01.046).
- [8] M. Zhang, Z. An, L. Wang, X. Wei, B. Jianayihan, J. Wang, Z. Huang, H. Tan, The regulation effect of methane and hydrogen on the emission characteristics of ammonia/air combustion in a model combustor, *Int. J. Hydrogen Energy* **2021**, *46*, 21013–21025, DOI [10.1016/j.ijhydene.2021.03.210](https://doi.org/10.1016/j.ijhydene.2021.03.210).
- [9] W. S. Chai, Y. Bao, P. Jin, G. Tang, L. Zhou, A review on ammonia, ammonia-hydrogen and ammonia-methane fuels, *Renew. Sust. Energy Rev.* **2021**, *147*, 111254/1–16, DOI [10.1016/j.rser.2021.111254](https://doi.org/10.1016/j.rser.2021.111254).
- [10] P. Glarborg, J. A. Miller, B. Ruscic, S. J. Klippenstein, Modeling nitrogen chemistry in combustion, *Prog. Energy Combust. Sci.* **2018**, *67*, 31–68, DOI [10.1016/j.pecs.2018.01.002](https://doi.org/10.1016/j.pecs.2018.01.002).
- [11] N. Lamoureux, H. E. Merhubi, L. Pillier, S. de Persis, P. Desgroux, Modeling of NO formation in low pressure premixed flames, *Combust. Flame* **2016**, *163*, 557–575, DOI [10.1016/j.combustflame.2015.11.007](https://doi.org/10.1016/j.combustflame.2015.11.007).
- [12] P. Glarborg, P. Marshall, Importance of the Hydrogen Isocyanide Isomer in Modeling Hydrogen Cyanide Oxidation in Combustion, *Energy Fuels* **2017**, *31*, 2156–2163, DOI [10.1021/acs.energyfuels.6b02085](https://doi.org/10.1021/acs.energyfuels.6b02085).
- [13] G. Friedrichs, Sensitive Absorption Methods for Quantitative Gas Phase Kinetic Measurements. Part 1: Frequency Modulation Spectroscopy, *Z. Phys. Chem.* **2008**, *222*, 1–30, DOI [10.1524/zpch.2008.222.1.1](https://doi.org/10.1524/zpch.2008.222.1.1).
- [14] J. Deppe, G. Friedrichs, A. Ibrahim, H.-J. Römmling, H. G. Wagner, The thermal decomposition of  $\text{NH}_2$  and  $\text{NH}$  radicals, *Ber. Bunsenges. Phys. Chem.* **1998**, *102*, 1474–1485, DOI [10.1002/bbpc.199800016](https://doi.org/10.1002/bbpc.199800016).
- [15] N. Faßheber, M. C. Schmidt, G. Friedrichs, Quantitative HNO detection behind shock waves, *Proc. Combust. Inst.* **2017**, *36*, 607–615, DOI [10.1016/j.proci.2016.05.035](https://doi.org/10.1016/j.proci.2016.05.035).
- [16] J. A. Nuth, S. Glicker, The vacuum ultraviolet spectra of  $\text{HCN}$ ,  $\text{C}_2\text{N}_2$ , and  $\text{CH}_3\text{CN}$ , *J. Quant. Spectrosc. Radiat. Transfer* **1982**, *28*, 223–231, DOI [10.1016/0022-4073\(82\)90025-5](https://doi.org/10.1016/0022-4073(82)90025-5).
- [17] Z. Sun, Z. Li, A. Konnov, M. Aldén, Quantitative HCN measurements in  $\text{CH}_4/\text{N}_2\text{O}/\text{O}_2/\text{N}_2$  flames using mid-infrared polarization spectroscopy, *Combust. Flame* **2011**, *158*, 1898–1904, DOI [10.1016/j.combustflame.2011.03.008](https://doi.org/10.1016/j.combustflame.2011.03.008).



- [18] D. Hot, R. L. Pedersen, W. Weng, Y. Zhang, M. Aldén, Z. Li, Spatially and temporally resolved IR-DFWM measurement of HCN released from gasification of biomass pellets, *Proc. Combust. Inst.* **2019**, *37*, 1337–1344, DOI [10.1016/j.proci.2018.07.105](https://doi.org/10.1016/j.proci.2018.07.105).
- [19] J. M. Brupbacher, R. D. Kern, Reaction of hydrogen cyanide and deuterium behind reflected shock waves, *J. Phys. Chem.* **1972**, *76*, 285–291, DOI [10.1021/j100647a001](https://doi.org/10.1021/j100647a001).
- [20] J. M. Brupbacher, R. D. Kern, Reaction of cyanogen and hydrogen behind reflected shock waves, *J. Phys. Chem.* **1973**, *77*, 1329–1335, DOI [10.1021/j100630a003](https://doi.org/10.1021/j100630a003).
- [21] A. Chang, R. Hanson, Shock-tube study of HCN self-broadening and broadening by argon for the P(10) line of the  $\nu_1$  band at 3  $\mu\text{m}$ , *J. Quant. Spectrosc. Radiat. Transfer* **1985**, *33*, 213–217, DOI [10.1016/0022-4073\(85\)90150-5](https://doi.org/10.1016/0022-4073(85)90150-5).
- [22] A. Elkhazraji, M. Adil, B. Giri, M. Mhanna, N. Abualsaud, A. A. Alsulami, M. K. Shakfa, M. Marangoni, A. Farooq, A laser diagnostic for HCN detection in mid-infrared, *Technical Digest Series (OSA)* **2022**, paper ATu4I.2, presented at CLEO, 2022, DOI [10.1364/CLEO\\_AT.2022.ATu4I.2](https://doi.org/10.1364/CLEO_AT.2022.ATu4I.2).
- [23] A. Elkhazraji, M. Adil, M. Mhanna, N. Abualsaud, A. A. Alsulami, M. K. Shakfa, M. Marangoni, B. Giri, A. Farooq, A mid-IR laser diagnostic for HCN detection, *Proc. Combust. Inst.* **2022**, paper 1E12, presented at the 39th Int. Symp. on Combustion 2022, DOI [10.1016/j.proci.2022.09.054](https://doi.org/10.1016/j.proci.2022.09.054).
- [24] M. Stuhr, S. Hesse, G. Friedrichs, Quantitative and Sensitive Mid-Infrared Frequency Modulation Detection of HCN behind Shock Waves, *Fuels* **2021**, *2*, 437–447, DOI [10.3390/fuels2040025](https://doi.org/10.3390/fuels2040025).
- [25] P. Roth, R. Löhr, H. D. Hermanns, Stoßwellenmessungen zur Kinetik der Reaktion  $\text{HCN} + \text{O}$ , *Ber. Bunsenges. Phys. Chem.* **1980**, *84*, 835–840, DOI [10.1002/bbpc.19800840903](https://doi.org/10.1002/bbpc.19800840903).
- [26] A. Szekely, R. K. Hanson, C. T. Bowman, Shock tube study of the reaction between hydrogen cyanide and atomic oxygen, *Symp. (Int.) Combust.* **1985**, *20*, 647–654, DOI [10.1016/S0082-0784\(85\)80554-3](https://doi.org/10.1016/S0082-0784(85)80554-3).
- [27] M. Y. Louge, R. K. Hanson, Shock tube study of NCO kinetics, *Symp. (Int.) Combust.* **1985**, *20*, 665–672, DOI [10.1016/S0082-0784\(85\)80556-7](https://doi.org/10.1016/S0082-0784(85)80556-7).
- [28] M. Stuhr, N. Faßheber, G. Friedrichs, Single-tone mid-infrared frequency modulation spectroscopy for sensitive detection of transient species, *Opt. Express* **2019**, *27*, 26499–26512, DOI [10.1364/oe.27.026499](https://doi.org/10.1364/oe.27.026499).
- [29] G. Friedrichs, H. G. Wagner, Quantitative FM spectroscopy at high temperatures: The detection of  $^1\text{CH}_2$  behind shock waves, *Z. Phys. Chem.* **2000**, *214*, 1723–1746, DOI [10.1524/zpch.2000.214.12.1723](https://doi.org/10.1524/zpch.2000.214.12.1723).
- [30] I. Gordon et al., The HITRAN2016 molecular spectroscopic database, *J. Quant. Spectrosc. Radiat. Transfer* **2017**, *203*, 3–69, DOI [10.1016/j.jqsrt.2017.06.038](https://doi.org/10.1016/j.jqsrt.2017.06.038).
- [31] G. C. Bjorklund, M. D. Levenson, W. Lenth, C. Ortiz, Frequency modulation (FM) spectroscopy, *Appl. Phys. B* **1983**, *32*, 145–152, DOI [10.1007/bf00688820](https://doi.org/10.1007/bf00688820).
- [32] M. Colberg, G. Friedrichs, Room temperature and shock tube study of the reaction  $\text{HCO} + \text{O}_2$  using the photolysis of glyoxal as an efficient HCO source, *J. Phys. Chem. A* **2006**, *110*, 160–170, DOI [10.1021/jp055168r](https://doi.org/10.1021/jp055168r).
- [33] C. J. S. M. Simpson, K. B. Bridgman, T. R. D. Chandler, Shock-Tube Study of Vibrational Relaxation in Nitrous Oxide, *J. Chem. Phys.* **1968**, *49*, 509–513, DOI [10.1063/1.1670104](https://doi.org/10.1063/1.1670104).
- [34] R. C. Millikan, D. R. White, Systematics of Vibrational Relaxation, *J. Chem. Phys.* **1963**, *39*, 3209–3213, DOI [10.1063/1.1734182](https://doi.org/10.1063/1.1734182).
- [35] J. F. Roach, W. R. Smith, Shock-Tube Study of Vibration-Vibration Energy Exchange in  $\text{N}_2$ - $\text{N}_2\text{O}$  Mixtures, *J. Chem. Phys.* **1969**, *50*, 4114–4115, DOI [10.1063/1.1671677](https://doi.org/10.1063/1.1671677).
- [36] J. E. Johnsson, P. Glarborg, K. Dam-Johansen, Thermal dissociation of nitrous oxide at medium temperatures, *Symp. (Int.) Combust.* **1992**, *24*, 917–923, DOI [10.1016/s0082-0784\(06\)80109-8](https://doi.org/10.1016/s0082-0784(06)80109-8).

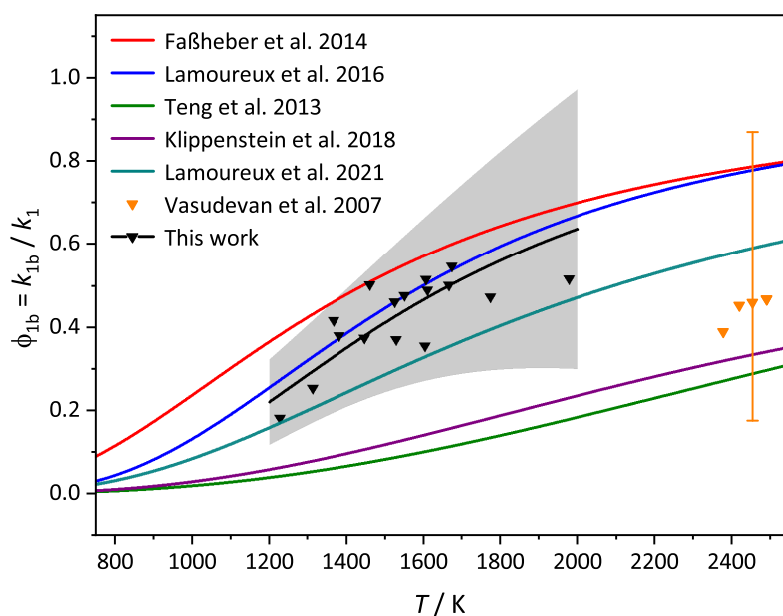
- [37] M. Röhrig, E. L. Petersen, D. F. Davidson, R. K. Hanson, The pressure dependence of the thermal decomposition of  $\text{N}_2\text{O}$ , *Int. J. Chem. Kinet.* **1996**, *28*, 599–608, DOI [10.1002/\(SICI\)1097-4601\(1996\)28:8<599::AID-KIN5>3.0.CO;2-Q](https://doi.org/10.1002/(SICI)1097-4601(1996)28:8<599::AID-KIN5>3.0.CO;2-Q).
- [38] S. Javoy, R. Mevel, C. E. Paillard, A study of  $\text{N}_2\text{O}$  decomposition rate constant at high temperature: Application to the reduction of nitrous oxide by hydrogen, *Int. J. Chem. Kinet.* **2009**, *41*, 357–375, DOI [10.1002/kin.20401](https://doi.org/10.1002/kin.20401).
- [39] T. V. Pham, T. J. Tsay, M. C. Lin, Thermal decomposition of  $\text{N}_2\text{O}$  near 900 K studied by FTIR spectrometry: Comparison of experimental and theoretical  $\text{O}(^3\text{P})$  formation kinetics, *Int. J. Chem. Kinet.* **2020**, *52*, 632–644, DOI [10.1002/kin.21388](https://doi.org/10.1002/kin.21388).
- [40] C. R. Mulvihill, S. A. Alturaifi, E. L. Petersen, A shock-tube study of the  $\text{N}_2\text{O} + \text{M} \rightleftharpoons \text{N}_2 + \text{O} + \text{M}$  ( $\text{M} = \text{Ar}$ ) rate constant using  $\text{N}_2\text{O}$  laser absorption near  $4.6\ \mu\text{m}$ , *Combust. Flame* **2021**, *224*, 6–13, DOI [10.1016/j.combustflame.2020.10.040](https://doi.org/10.1016/j.combustflame.2020.10.040).
- [41] A. M. Dean, J. W. Bozzelli in *Combustion Chemistry of Nitrogen*, In: *Gas-Phase Combustion Chemistry* (Ed. W.C. Gardiner), Springer, New York, **2000**, pp. 125–341, DOI [10.1007/978-1-4612-1310-9\\_2](https://doi.org/10.1007/978-1-4612-1310-9_2).
- [42] P. Glarborg, J. E. Johnsson, K. Dam-Johansen, Kinetics of homogeneous nitrous oxide decomposition, *Combust. Flame* **1994**, *99*, 523–532, DOI [10.1016/0010-2180\(94\)90045-0](https://doi.org/10.1016/0010-2180(94)90045-0).
- [43] H. S. Johnston, Interpretation of the Data on the Thermal Decomposition of Nitrous Oxide, *J. Chem. Phys.* **1951**, *19*, 663–667, DOI [10.1063/1.1748328](https://doi.org/10.1063/1.1748328).
- [44] N. E. Meagher, W. R. Anderson, Kinetics of the  $\text{O}(^3\text{P}) + \text{N}_2\text{O}$  Reaction. 2. Interpretation and Recommended Rate Coefficients, *J. Phys. Chem. A* **2000**, *104*, 6013–6031, DOI [10.1021/jp994471n](https://doi.org/10.1021/jp994471n).
- [45] S. T. Wooldridge, R. K. Hanson, C. T. Bowman, Simultaneous laser absorption measurements of CN and OH in a shock tube study of  $\text{HCN} + \text{OH} \rightarrow \text{products}$ , *Int. J. Chem. Kinet.* **1995**, *27*, 1075–1087, DOI [10.1002/kin.550271105](https://doi.org/10.1002/kin.550271105).
- [46] W. Tsang, J. T. Herron, Chemical Kinetic Data Base for Propellant Combustion I. Reactions Involving NO,  $\text{NO}_2$ , HNO,  $\text{HNO}_2$ , HCN and  $\text{N}_2\text{O}$ , *J. Phys. Chem. Ref. Data* **1991**, *20*, 609–663, DOI [10.1063/1.555890](https://doi.org/10.1063/1.555890).
- [47] M. C. Lin, Y. He, C. F. Melius, Implications of the  $\text{HCN} \rightarrow \text{HNC}$  process to high-temperature nitrogen-containing fuel chemistry, *Int. J. Chem. Kinet.* **1992**, *24*, 1103–1107, DOI [10.1002/kin.550241208](https://doi.org/10.1002/kin.550241208).
- [48] A. J. C. Bunkan, Y. Tang, S. R. Sellevåg, C. J. Nielsen, Atmospheric Gas Phase Chemistry of  $\text{CH}_2\text{NH}$  and HNC. A First-Principles Approach, *J. Phys. Chem. A* **2014**, *118*, 5279–5288, DOI [10.1021/jp5049088](https://doi.org/10.1021/jp5049088).
- [49] J. W. Bozzelli, A. Y. Chang, A. M. Dean, Analysis of the reactions  $\text{H} + \text{N}_2\text{O}$  and  $\text{NH} + \text{NO}$ : Pathways and rate constants over a wide range of temperature and pressure, *Symp. (Int.) Combust.* **1994**, *25*, 965–974, DOI [10.1016/s0082-0784\(06\)80733-2](https://doi.org/10.1016/s0082-0784(06)80733-2).
- [50] W. Tsang, Chemical Kinetic Data Base for Propellant Combustion. II. Reactions Involving CN, NCO, and HNCO, *J. Phys. Chem. Ref. Data* **1992**, *21*, 753–791, DOI [10.1063/1.555914](https://doi.org/10.1063/1.555914).
- [51] M. C. Lin, Y. He, C. F. Melius, Theoretical aspects of product formation from the  $\text{NCO} + \text{NO}$  reaction, *J. Phys. Chem.* **1993**, *97*, 9124–9128, DOI [10.1021/j100138a010](https://doi.org/10.1021/j100138a010).
- [52] N. Cohen, K. R. Westberg, Chemical Kinetic Data Sheets for High-Temperature Reactions. Part II, *J. Phys. Chem. Ref. Data* **1991**, *20*, 1211–1311, DOI [10.1063/1.555901](https://doi.org/10.1063/1.555901).
- [53] M. S. Wooldridge, R. K. Hanson, C. T. Bowman, A shock tube study of the  $\text{OH} + \text{OH} \rightarrow \text{H}_2\text{O} + \text{O}$  reaction, *Int. J. Chem. Kinet.* **1994**, *26*, 389–401, DOI [10.1002/kin.550260402](https://doi.org/10.1002/kin.550260402).
- [54] B. Ruscic, R. E. Pinzon, G. von Laszewski, D. Kodeboyina, A. Burcat, D. Leahy, D. Montoy, A. F. Wagner, Active Thermochemical Tables: Thermochemistry for the 21st century, *J. Phys.: Conf. Ser.* **2005**, *16*, 561–570, DOI [10.1088/1742-6596/16/1/078](https://doi.org/10.1088/1742-6596/16/1/078).
- [55] B. Ruscic, D. H. Bross, Active Thermochemical Tables (ATcT) enthalpies of formation values based on ver. 1.122r of the Thermochemical Network (2021), <https://atct.anl.gov/>, **2021**.

- [56] R. J. Kee, F. M. Ruply, J. A. Miller, Chemkin-II: A Fortran Chemical Kinetics Package for the Analysis of Gas-Phase Chemical Kinetics, tech. rep., Sandia National Laboratories, Livermore, California, Sandia Report SAND-89-8009, **1989**, DOI [10.2172/5681118](https://doi.org/10.2172/5681118).
- [57] W. J. Riley, *Handbook of Frequency Stability Analysis*, US Department of Commerce, National Institute of Standards and Technology (NIST), **2008**.
- [58] C. Rinsland, V. M. Devi, M. Smith, D. C. Benner, S. W. Sharpe, R. L. Sams, A multispectrum analysis of the  $\nu_1$  band of  $\text{H}^{12}\text{C}^{14}\text{N}$ : Part II. Air- and  $\text{N}_2$ -broadening, shifts and their temperature dependences, *J. Quant. Spectrosc. Radiat. Transfer* **2003**, *82*, 343–362, DOI [10.1016/s0022-4073\(03\)00162-6](https://doi.org/10.1016/s0022-4073(03)00162-6).
- [59] E. A. Whittaker, M. Gehrtz, G. C. Bjorklund, Residual amplitude modulation in laser electro-optic phase modulation, *J. Opt. Soc. Am. B* **1985**, *2*, 1320–1326, DOI [10.1364/josab.2.001320](https://doi.org/10.1364/josab.2.001320).
- [60] S. Wang, E. E. Dames, D. F. Davidson, R. K. Hanson, Reaction Rate Constant of  $\text{CH}_2\text{O} + \text{H} = \text{HCO} + \text{H}_2$  Revisited: A Combined Study of Direct Shock Tube Measurement and Transition State Theory Calculation, *J. Phys. Chem. A* **2014**, *118*, 10201–10209, DOI [10.1021/jp5085795](https://doi.org/10.1021/jp5085795).
- [61] R. Sur, S. Wang, K. Sun, D. F. Davidson, J. B. Jeffries, R. K. Hanson, High-sensitivity interference-free diagnostic for measurement of methane in shock tubes, *J. Quant. Spectrosc. Radiat. Transfer* **2015**, *156*, 80–87, DOI [10.1016/j.jqsrt.2015.01.023](https://doi.org/10.1016/j.jqsrt.2015.01.023).
- [62] I. Sadiq, G. Friedrichs, Saturation dynamics and working limits of saturated absorption cavity ringdown spectroscopy, *Phys. Chem. Chem. Phys.* **2016**, *18*, 22978–22989, DOI [10.1039/c6cp01966h](https://doi.org/10.1039/c6cp01966h).
- [63] J. A. Silver, Frequency-modulation spectroscopy for trace species detection: theory and comparison among experimental methods, *Appl. Opt.* **1992**, *31*, 707–717, DOI [10.1364/ao.31.000707](https://doi.org/10.1364/ao.31.000707).
- [64] N. Faßheber, N. Lamoureux, G. Friedrichs, The rate constant of the reaction  $\text{NCN} + \text{H}_2$  and its role in NCN and NO modeling in low pressure  $\text{CH}_4/\text{O}_2/\text{N}_2$ -flames, *Phys. Chem. Chem. Phys.* **2015**, *17*, 15876–15886, DOI [10.1039/c5cp01414j](https://doi.org/10.1039/c5cp01414j).
- [65] J. A. Miller, C. Parrish, N. J. Brown, A statistical-theoretical investigation of the thermal rate coefficient and branching ratio for the reaction  $\text{O} + \text{HCN} \rightarrow \text{products}$ , *J. Phys. Chem.* **1986**, *90*, 3339–3345, DOI [10.1021/j100406a008](https://doi.org/10.1021/j100406a008).
- [66] P. B. Davies, B. A. Thrush, Reactions of oxygen atoms with hydrogen cyanide, cyanogen chloride and cyanogen bromide, *Trans. Faraday Soc.* **1968**, *64*, 1836–1843, DOI [10.1039/tf9686401836](https://doi.org/10.1039/tf9686401836).
- [67] R. A. Perry, C. F. Melius, The rate and mechanism of the reaction of HCN with oxygen atoms over the temperature range 540 – 900 K, *Symp. (Int.) Combust.* **1985**, *20*, 639–646, DOI [10.1016/S0082-0784\(85\)80553-1](https://doi.org/10.1016/S0082-0784(85)80553-1).
- [68] J. A. Miller, C. T. Bowman, Mechanism and modeling of nitrogen chemistry in combustion, *Prog. Energ. Combust. Sci.* **1989**, *15*, 287–338, DOI [10.1016/0360-1285\(89\)90017-8](https://doi.org/10.1016/0360-1285(89)90017-8).
- [69] M. Stühr, S. Hesse, G. Friedrichs, Branching fraction measurement of the prompt-NO switch reaction  $\text{NCN} + \text{H}$ , *Proc. Combust. Inst.* **2023**, *39*, 147–156, DOI [10.1016/j.proci.2022.07.146](https://doi.org/10.1016/j.proci.2022.07.146).



## CHAPTER 8

### Publication V: Branching Fraction Measurement of the Prompt-NO Switch Reaction $\text{NCN} + \text{H}$



Michael Stuhr<sup>a</sup>, Sebastian Hesse<sup>a</sup>, and Gernot Friedrichs<sup>a</sup>

<sup>a</sup>Institut für Physikalische Chemie, Christian-Albrechts-Universität zu Kiel, Max-Eyth-Straße 1, 24118 Kiel, Germany

*Proc. Combust. Inst.* **2023**, 39, 147–156, DOI [10.1016/j.proci.2022.07.146](https://doi.org/10.1016/j.proci.2022.07.146).

#### Own Contributions:

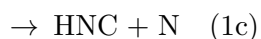
- $\text{NCN}_3$  synthesis (together with S. Hesse)
- Shock tube experiments (together with S. Hesse)
- Recording and analysis of kinetic HCN profiles
- Analysis and discussion of rate constant data
- Writing of paper draft

## Abstract

The branching fraction  $\phi$  of the prompt-NO switch reaction  $\text{NCN} + \text{H}$  (1), essentially yielding either  $\text{CH} + \text{N}_2$  (1a) or  $\text{HCN} + \text{N}$  (1b), is key for modeling prompt-NO formation in flames. Large discrepancies exist between available experimental data and flame modeling studies on the one hand and high-level theoretical predictions on the other hand, resulting in factor of 5 uncertainty for  $\phi_{1b}$  at  $T = 1500$  K. By simultaneous monitoring of NCN and HCN concentration-time profiles during the reaction  $\text{NCN} + \text{H}$  at temperatures  $1200 \text{ K} < T < 2000 \text{ K}$  behind shock waves,  $\phi_{1b}$  has been directly measured for the first time. Thermal decomposition of cyanogen azide ( $\text{NCN}_3$ ) and ethyl iodide ( $\text{C}_2\text{H}_5\text{I}$ ) served as sources for NCN radicals and H atoms. NCN has been detected by UV laser absorption at 329.130 nm and HCN detection was accomplished by mid-infrared frequency modulation spectroscopy at  $3228.049 \text{ cm}^{-1}$ . Kinetic simulations provided both the total rate constant  $k_1$  from the NCN and  $k_{1b}$  from the HCN profiles. In order to account for a side reaction of residual BrCN from  $\text{NCN}_3$  synthesis, a rough estimate for the rate constant of the reaction  $\text{BrCN} + \text{H}$  was inferred from the experiments as well. The measured rate constants for  $k_1$  confirm earlier results (Faßheber et al., Phys. Chem. Chem. Phys. 16 (2014) 11647) and  $k_{1b}$  follows the Arrhenius expression  $k_{1b}/(\text{cm}^3 \text{ mol}^{-1} \text{ s}^{-1}) = 4.2 \times 10^{14} \exp(-38.2 \text{ kJ mol}^{-1}/RT)$  with moderate uncertainties of  $\pm(37 - 49\%)$ . The branching fraction increases with temperature, yielding  $\phi_{1b} = 0.22 (\pm 46\%)$  at 1200 K,  $0.47 (\pm 42\%)$  at 1600 K, and  $0.63 (\pm 53\%)$  at 2000 K. The corresponding prompt-NO switch temperature of  $T_S = 1670 \text{ K}$  ( $\phi_{1b} = 0.5$ ) shows that the reaction  $\text{NCN} + \text{H}$  advances towards the Fenimore products  $\text{HCN} + \text{N}$  already at typical temperatures of hydrocarbon/air flames, in stark contrast to the most recent theoretical estimate reporting  $T_S = 3235 \text{ K}$ .

## 8.1 Introduction

The prompt-NO mechanism is an important pathway for the formation of nitrogen oxides ( $\text{NO}_x$ ) in hydrocarbon combustion, especially under fuel-rich conditions [1]. Prompt-NO formation is initiated primarily by the reaction  $\text{CH} + \text{N}_2 \rightarrow \text{NCN} + \text{H}$  [2], accordingly the fate of the cyanonitrene (NCN) radical plays a key role for prompt-NO modeling [3]. Except at very high temperatures, NCN flame chemistry is dominated by its triplet electronic ground state ( $^3\text{NCN}$ ). However, in reaction kinetics studies NCN is typically formed in its electronically excited singlet state ( $^1\text{NCN}$ ) first such that singlet-triplet relaxation and singlet chemistry may become important as well [3, 4]. In hydrocarbon/air flames, NCN is primarily consumed by the title reaction  $\text{NCN} + \text{H}$  [5], which is known to proceed through four possible product channels [6, 7]:



Here, channel 1a represents the reverse reaction of the prompt-NO initiation step, whereas the forward channel 1b yields the Fenimore products  $\text{HCN} + \text{N}$  and therefore proceeds into the direction of  $\text{NO}_x$ . There is general agreement in the literature that reaction 1a, taking place on a doublet potential energy surface (PES) by a complex association-isomerization process without overall effective energy barrier, dominates at low flame temperatures and that channel 1b, taking place on a quartet PES as an activation-controlled process, starts to compete toward higher flame temperatures [1, 6–9]. The other two channels are only expected to play a significant role under specific conditions, channel 1c at temperatures above 2500 K and channel 1d at elevated pressures below 1000 K [7]. Therefore, in a simplified view applicable to typical flame conditions, channels 1c and 1d can be neglected and the fate of NCN is largely determined by the so-called prompt-NO switch, i.e., the branching of channels 1a and 1b with branching fractions  $\phi_{1b} = k_{1b}/k_1 \approx 1 - \phi_{1a}$ .

In their recent review on NCN flame chemistry, Lamoureux et al. [3] highlighted the central role of the prompt-NO switch for overall  $\text{NO}_x$  modeling and introduced the associated concept of the prompt-NO switch temperature  $T_S$ . The latter simply represents the temperature where the branching of the reaction  $\text{NCN} + \text{H}$  switches between channel 1a (dominating at  $T < T_S$ ) and channel 1b (dominating at  $T > T_S$ ), hence  $k_{1a}(T_S) = k_{1b}(T_S)$  and  $\phi_{1b} = 0.5$ .

Despite the fact that the branching has been addressed in a number of studies, considerable discrepancies between experimental and flame modeling results on the one hand and theoretical calculations on the other hand remain. The shock tube study by Faßheber et al. [8] provided experimental values for the total rate constant  $k_1$  over a wide temperature range of  $962 \text{ K} < T < 2425 \text{ K}$ . Arrhenius expressions for  $k_{1a}$  and  $k_{1b}$  could be inferred from their data as well, yielding a relatively low value of  $T_S = 1440 \text{ K}$ . Lamoureux et al. [9] modeled prompt-NO formation in low-pressure premixed flames with respect to experimental concentration profiles of several relevant species, including NCN and NO. Their analysis is consistent with  $T_S = 1630 \text{ K}$ , again showing that channel 1b significantly contributes to  $\text{NO}_x$  formation at moderate temperatures. Such low  $T_S$  values are in stark contrast to the results of the high-level quantum-chemical kinetic studies of Teng et al. [6] and Klippenstein et al. [7], reporting a much higher prompt-NO switch temperature of 3415 K and 3235 K, respectively. For a temperature of 1500 K, a branching fraction of merely  $\phi_{1b} = 0.1$  is predicted, whereas the experimental/flame model results support a branching fraction of about  $\phi_{1b} = 0.5$ . It is the main objective of this paper to address this striking discrepancy by a direct measurement of the branching fraction  $\phi_{1b}$ .

As of yet, the only experimental study of channel 1b has been reported by Vasudevan et al. [10] who inferred five individual  $k_{1b}$  rate constant values from combined modeling of CH and NCN species profiles measured in shock-heated ethane/nitrogen/helium/argon gas mixtures at temperatures between 2378 K and 2492 K. Although not reported in their work, in retrospect it is possible to extract a branching fraction value from their  $k_{1b}$  data by calculating  $k_{1a}$  values from their reported rate constant expression for  $k_{-1a}$  of the reverse reaction  $\text{CH} + \text{N}_2 \rightarrow \text{NCN} + \text{H}$ . As further outlined in Section A of the Supplementary Material,  $\phi_{1b} = 0.46^{+0.41}_{-0.29}$  is obtained for a temperature of 2450 K. Clearly, channel 1b is operative at this high temperature, but the uncertainty of the obtained branching fraction is too high to draw any conclusions with respect to



the aforementioned discrepancy.

Here, we strike to derive temperature-dependent branching fractions at lower temperatures by simultaneous monitoring of  $^3\text{NCN}$  and HCN concentration-time profiles behind shock waves, the first yielding values for  $k_1$  and the second constraining the HCN yield and thereby  $k_{1b}$ . High-temperature detection of  $^3\text{NCN}$  by laser absorption spectroscopy in the UV is well established and has been used extensively for shock tube experiments involving  $^3\text{NCN}$  [4, 8, 11]. Recently, thanks to improvements in mid-infrared frequency modulation spectroscopy (MIR-FMS) [12, 13], quantitative and time-resolved detection of HCN behind shock waves on the ppm level has become feasible as well.

## 8.2 Experimental

The rate constants  $k_{1b}$  and  $k_1$  were determined by simultaneous laser absorption detection of HCN and  $^3\text{NCN}$  in shock-heated gas mixtures of cyanogen azide ( $\text{NCN}_3$ , source of  $\text{NCN}$  radicals) and ethyl iodide ( $\text{C}_2\text{H}_5\text{I}$ , source of  $\text{H}$  atoms). All measurements were performed behind incident shock waves with the Kiel shock tube apparatus, an aluminum burst membrane-operated electropolished stainless-steel shock tube with an inner diameter of 81 mm and a 4.4 m long test section. It is described in detail in Ref. 14. Shock wave conditions were calculated with a frozen chemistry code with shock wave velocities and damping measured with four fast piezoelectric sensors. The two separate laser detection systems, a UV frequency-doubled ring-dye laser-based difference amplification scheme and a frequency modulation MIR-OPO system, were arranged in perpendicular single-pass configuration of the laser beams through four optical ports in the shock tube head.

Time-resolved HCN detection for shock tube applications has recently been established by using single-tone MIR-FMS [12] in the fundamental  $\nu_1$  CH stretch vibration band. As a prerequisite for quantitative HCN detection under typical shock wave conditions, the high-temperature pressure-broadening parameters of the observed P(26) transition line at  $3228.049\text{ cm}^{-1}$  were determined in a previous study [13]. Temperature-dependent line strength data were taken from the HITRAN database [15]. For a more detailed description of the MIR-FM detection scheme we refer to Refs. [12, 13]. Under typical experimental conditions used in this work, the minimal detectable absorption of  $2.5 \times 10^{-4}$  at a time resolution of  $1\text{ }\mu\text{s}$  corresponds to HCN mole fractions of about 5–15 ppm, depending on temperature and pressure.

Kinetic profiles of the  $^3\text{NCN}$  radical were recorded using UV laser absorption spectroscopy at 329.130 nm. At this wavelength, the  $Q_1$  band head of the  $^3\Sigma^+(010) - ^3\Pi(010)$  vibrationally excited transition forms an intense absorption feature ideal for sensitive high-temperature detection. This approach to  $^3\text{NCN}$  detection is well established in our laboratory [4, 8, 11] and is explained in detail in the recent  $\text{NCN}$  review [3]. Most importantly, a previous discrepancy of published absorption cross section values has been recently resolved. In this work, the Doppler-limited high-temperature expression  $\sigma_{\text{NCN}} / (\text{cm}^2 \text{ mol}^{-1}) = 2.63 \times 10^9 \exp(-1.96 \times 10^{-3} \times T/\text{K}) (\pm 22\%)$  was used [4].

The highly toxic and explosive substance  $\text{NCN}_3$  was synthesized from sodium azide ( $\text{NaN}_3$ ,

Merck, 99%) and cyanogen bromide (BrCN, Sigma-Aldrich, 97%) using a variant of a procedure described by Milligan et al. [16], yielding a gas mixture of NCN<sub>3</sub>, non-reacted BrCN, and N<sub>2</sub> as side product from NCN<sub>3</sub> decomposition [4]. It has been shown in previous work [11, 17] that the mole fraction of residual BrCN after synthesis can be below 4%, however, for the particular synthesis performed in this study, the BrCN content was 16% as measured by FTIR spectroscopy. This was most likely due to insufficient grinding of NaN<sub>3</sub> prior to its exposure to BrCN during synthesis. Gas mixtures of NCN<sub>3</sub> and C<sub>2</sub>H<sub>5</sub>I (Alfa Aesar, 98%) in argon (Air Liquide, 99.999%) were prepared barometrically and further diluted with argon as needed using calibrated mass flow controllers. In order to minimize decomposition of NCN<sub>3</sub> in the supply lines [4] and to avoid concentration errors from adsorption effects of the precursors on the inner shock tube wall, the low-pressure section of the shock tube was flushed with the reactant gas mixtures for 6 minutes before each shock tube experiment. Nevertheless, as determined from the <sup>3</sup>NCN absorption levels in the respective shock wave experiments, NCN<sub>3</sub> mole fractions in the shock tube were around 10% lower than targeted. This uncertainty level is in accord with our experience with the difficult handling of NCN<sub>3</sub> gas mixtures [3, 4].

Numerical simulations of the reaction system were performed with the CHEMKIN-II package using a reduced reaction mechanism built from the GDFkin3.0 mechanism [9] as a starting point. Updated thermochemistry has been included, for example for <sup>3</sup>NCN ( $\Delta_f H_{298K}^\circ = 451$  kJ/mol [3]), and the mechanism was supplemented with additional reactions for NCN/NCN<sub>3</sub> chemistry [2, 4, 11, 17], the thermal decomposition of C<sub>2</sub>H<sub>5</sub>I [18], as well as some iodine chemistry. Since hydrogen and iodine atoms are formed in similar amounts from C<sub>2</sub>H<sub>5</sub>I decomposition, in particular the not yet investigated potential side reaction NCN + I needs a closer look. Ab initio calculations have been performed for feasible reaction products on the M062X/def2-TZVP DFT level of theory that allows for treatment of iodine thermochemistry (see Section B of the Supplementary Material). The results have been validated by comparison with thermochemical data from the literature. In contrast to the reaction NCN + H, the available analogous reaction channels for NCN + I are either endothermic or lead to only weakly-bound association products that quickly re-dissociate to the reactants. We therefore conclude that the reaction NCN + I cannot compete with the reaction NCN + H and hence plays a negligible role. The most important reactions for the analysis of the experiments in this work are included in Tab. 8.1, the full mechanism and the thermodynamic data of the involved species are provided in Sections C and D of the Supplementary Material, respectively.

<sup>1</sup>NCN chemistry is expected to be different from <sup>3</sup>NCN chemistry, both in terms of rate constants and spin restricted formation of specific products, however, due to the lack of kinetic data (except for a few cases [4, 24]), it has been accounted for by simply duplicating the <sup>3</sup>NCN reactions with the same rate constants. Such an approximate treatment is possible in cases where the singlet-triplet relaxation time is short compared to the <sup>3</sup>NCN lifetime, but may introduce some inaccuracies otherwise.

**Table 8.1:** Arrhenius parameters for the most important reactions of this work. Rate constants are given in the form  $k = A T^n \exp(-E_a/RT)$  in units of  $\text{cm}^3$ , mol, s, kJ, and K. In cases where rate constants for  $^1\text{NCN}$  and  $^3\text{NCN}$  reactions were assumed to be equal, NCN represents both species; but for  $^1\text{NCN}$  only the forward reactions were included. The full mechanism is provided in Section C of the Supplementary Material.

No.	Reaction		$A$	$n$	$E_a$	Ref.	$T$ range
1	$\text{NCN} + \text{H}$	$\rightarrow$ products	See text			[8]	962–2425
1a	$\text{NCN} + \text{H}$	$\rightleftharpoons \text{CH} + \text{N}_2$	See text				
1b		$\rightleftharpoons \text{HCN} + \text{N}$	$4.2 \times 10^{14}$	0.00	38.2	This work	1200–2000
2	$\text{NCN}_3$	$\rightarrow ^1\text{NCN} + \text{N}_2$	$4.9 \times 10^9$	0.00	71.0	[17]	617–927
3	$^1\text{NCN} + \text{M}$	$\rightarrow ^3\text{NCN} + \text{M}$	$6.5 \times 10^{11}$	0.00	29.2	*	860–1820
4	$\text{NCN} + \text{M}$	$\rightleftharpoons \text{C} + \text{N}_2 + \text{M}$	$8.9 \times 10^{14}$	0.00	260.0	[11]	2012–3248
5	$\text{NCN} + \text{NCN}$	$\rightleftharpoons \text{CN} + \text{CN} + \text{N}_2$	$1.1 \times 10^{13}$	0.00	11.7	[4]	1050–2500
6	$\text{NCN} + \text{C}$	$\rightleftharpoons \text{CN} + \text{CN}$	$5.3 \times 10^{14}$	0.00	20.0	*	860–1820
7	$\text{NCN} + \text{CH}$	$\rightleftharpoons \text{HCN} + \text{CN}$	$3.2 \times 10^{13}$	0.00	–3.6	[2]	2000–4000
8a	$\text{C}_2\text{H}_5\text{I}$	$\rightleftharpoons \text{C}_2\text{H}_5 + \text{I}$	$3.4 \times 10^{13}$	0.00	203.5	[18]	950–1400
8b	$\text{C}_2\text{H}_5\text{I}$	$\rightleftharpoons \text{C}_2\text{H}_4 + \text{HI}$	$4.7 \times 10^{13}$	0.00	225.9	[18]	950–1400
9	$\text{C}_2\text{H}_5 + \text{M}$	$\rightleftharpoons \text{C}_2\text{H}_4 + \text{H} + \text{M}$	$1.0 \times 10^{18}$	0.00	139.7	[18]	950–1400
10	$\text{C}_2\text{H}_5\text{I} + \text{H}$	$\rightarrow \text{C}_2\text{H}_5 + \text{HI}$	$1.0 \times 10^{15}$	0.00	21.6	[18]	950–1400
11	$\text{HI} + \text{H}$	$\rightarrow \text{H}_2 + \text{I}$	$6.6 \times 10^{13}$	0.00	4.1	[18]	950–1400
12	$\text{C}_2\text{H}_4 + \text{H}$	$\rightleftharpoons \text{C}_2\text{H}_3 + \text{H}_2$	$5.4 \times 10^{14}$	0.00	62.4	[19]	700–2000
13	$\text{CN} + \text{H}_2$	$\rightarrow \text{HCN} + \text{H}$	$3.0 \times 10^5$	2.45	9.4	[20]	940–1860
14	$\text{HCN} + \text{H}$	$\rightarrow \text{CN} + \text{H}_2$	$3.7 \times 10^{14}$	0.00	104.0	[21]	300–2500
15	$\text{CN} + \text{M}$	$\rightleftharpoons \text{C} + \text{N} + \text{M}$	$2.5 \times 10^{14}$	0.00	590.3	[22]	500–2500
16	$\text{CH} + \text{H}$	$\rightleftharpoons \text{C} + \text{H}_2$	$3.7 \times 10^{14}$	0.01	22.3	[23]	800–2000
17	$\text{BrCN} + \text{H}$	$\rightarrow \text{HCN} + \text{Br}$	See text				

\* Estimation based on joint consideration of previous work on NCN chemistry of our group as well as on yet unpublished CN profiles measured during  $\text{NCN}_3$  decomposition.

### 8.3 Results and Discussion

Sixteen simultaneous  $^3\text{NCN}$  and HCN measurements have been performed in the temperature range  $1200 \text{ K} < T < 2000 \text{ K}$ . The experimental conditions and the determined values of  $k_{1b}$  and  $k_1$  for each experiment are listed in Tab. B.2 in the Supplementary Material (Section E). In comparison with the previous study on the total rate constant  $k_1$ , which was based on NCN detection only [8], the experiments in this work used significantly higher concentrations of  $\text{NCN}_3$  in order to bring the resulting HCN mole fractions to a detectable level. Note that the absorption cross section of HCN lies in the range of  $(2.4\text{--}6) \times 10^5 \text{ cm}^2/\text{mol}$ , while the one of  $^3\text{NCN}$  is in the range of  $(5\text{--}20) \times 10^7 \text{ cm}^2/\text{mol}$ . Therefore, despite the high sensitivity of the MIR-FM detection scheme,  $^3\text{NCN}$  could be detected with much better signal-to-noise ratio. Although  $\text{C}_2\text{H}_5\text{I}$  was used in 5–24 excess with respect to  $\text{NCN}_3$ , true pseudo-first order conditions were not established. We refrained from further increasing  $\text{C}_2\text{H}_5\text{I}$  mole fractions to ensure that secondary ethyl iodide chemistry remained at a tolerable level.

#### Data Evaluation

Figure 8.1 illustrates a typical experiment at 1674 K and 457 mbar with initial mole fractions of 98 ppm  $\text{NCN}_3$  and 802 ppm  $\text{C}_2\text{H}_5\text{I}$ . Residual BrCN and  $\text{N}_2$  from  $\text{NCN}_3$  synthesis, in this case

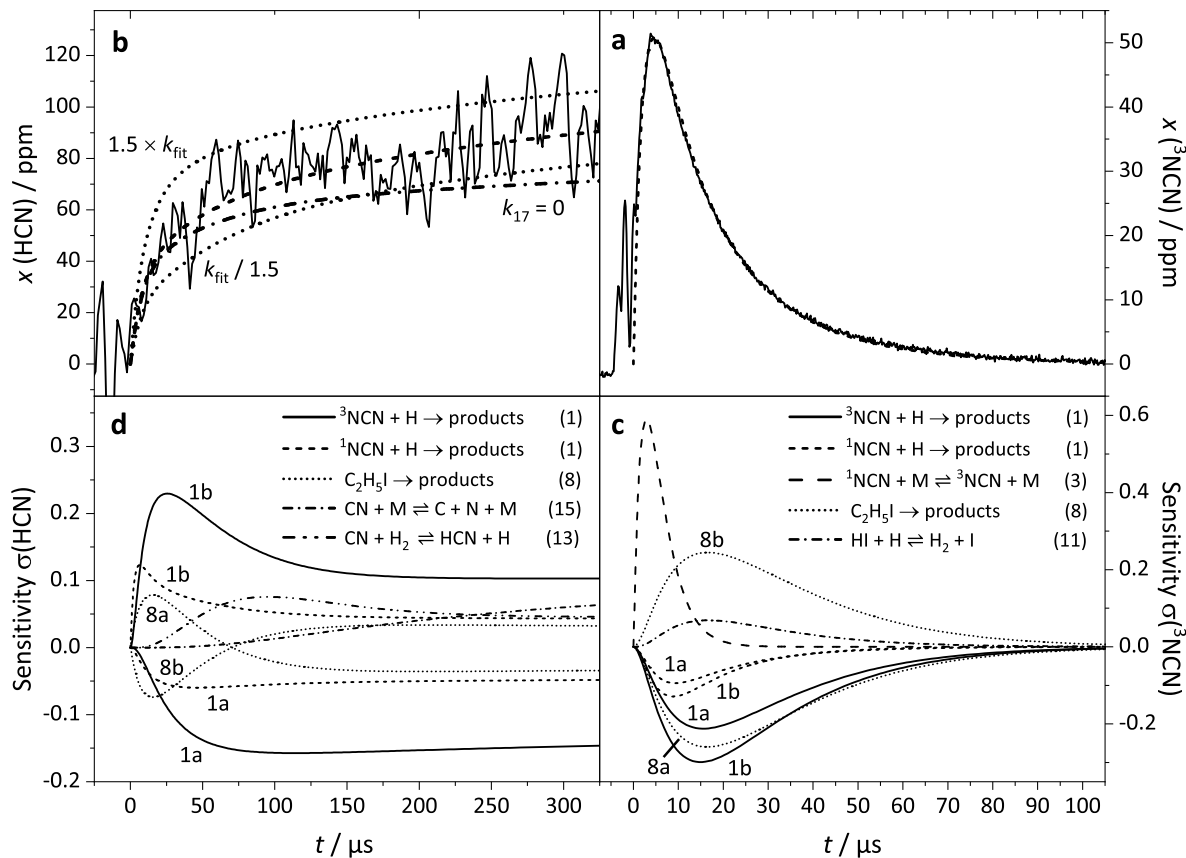


**Figure 8.1:** Example kinetic profiles of  $^3\text{NCN}$  (a) and HCN (b) at 1674 K and 457 mbar with 98 ppm  $\text{NCN}_3$  and 802 ppm  $\text{C}_2\text{H}_5\text{I}$  in comparison with numerical simulations. The corresponding sensitivity coefficients (normalized with respect to the maximum concentration of  $^3\text{NCN}$  or HCN) are shown for the simulation with  $k_{17} = 0$  in subfigures (c) and (d). In Figs. 8.1a and 8.1b, the dashed curves represent the best-fit simulations to the experimental profiles.

33 ppm and 49 ppm, were present as well. Another experimental profile at a lower temperature is included in Section F of the Supplementary Material as Fig. B.1. Moreover, all experimental and simulated profiles of both  $^3\text{NCN}$  and HCN are available in a separate ASCII file (see Section G of the Supplementary Material). In Figure 8.1, the concentration-time profiles of  $^3\text{NCN}$  (Fig. 8.1a) and HCN (Fig. 8.1b) are shown as solid curves alongside corresponding sensitivity coefficients  $\sigma$  for both species (Fig. 8.1c and Fig. 8.1d). Here, the sensitivity coefficient  $\sigma(i,j)$  for species  $i$  and reaction  $j$  was normalized with respect to the maximum concentration  $[i]_{\text{max}}$  over the time history,  $\sigma(i,j) = 1/[i]_{\text{max}}(\partial[i]/\partial \ln k_j)$ .

Thermal decomposition of  $\text{NCN}_3$  first yields  $^1\text{NCN}$  radicals, followed by fast collision-induced intersystem crossing to  $^3\text{NCN}$  [17]. As can be seen in Fig. 8.1a, following the Schlieren signal indicating the arrival of the incident shock wave, the  $^3\text{NCN}$  concentration quickly reaches its maximum after about 5  $\mu\text{s}$ . The ensuing decay of the  $^3\text{NCN}$  concentration due to reaction 1,  $\text{NCN} + \text{H}$ , proceeds on a slower timescale, resulting in a quasi-single exponential decay with detectable  $^3\text{NCN}$  signal for about 100  $\mu\text{s}$ . Due to the comparatively high  $\text{NCN}_3$  concentrations used in the experiments, the recorded  $^3\text{NCN}$  profiles have a high signal-to-noise ratio and thus

allow for reliable determination of  $k_1$ . Allowing for a minor baseline offset behind the incident shock wave, which we attribute to slight shock-induced misalignment of the optical setup, the simulated  $^3\text{NCN}$  profile in Fig. 8.1a (dashed curve) nicely reproduces the experiment.

Figure 8.1c shows the corresponding sensitivity analysis. As expected, the highest sensitivity coefficients  $\sigma(^3\text{NCN})$  are found for the singlet-triplet relaxation of  $\text{NCN}$ , the thermal decomposition of the H-precursor ethyl iodide, and the target reaction  $\text{NCN} + \text{H}$ . Since two channels of reaction 1 are taken into account and both  $^3\text{NCN}$  and  $^1\text{NCN}$  can react with hydrogen atoms, four different sensitivity coefficients for  $\text{NCN} + \text{H}$  appear in the plot. Similarly, both ethyl iodide decomposition channels 8a ( $\text{C}_2\text{H}_5 + \text{I}$ ) and 8b ( $\text{C}_2\text{H}_4 + \text{HI}$ ) appear in Fig. 8.1c because the branching fraction of reaction 8 critically determines the yield of hydrogen atoms via reaction 9,  $\text{C}_2\text{H}_5 \rightarrow \text{C}_2\text{H}_4 + \text{H}$ . Also reaction 11,  $\text{HI} + \text{H}$ , turns out to be important because it reduces the amount of hydrogen atoms available for the target reaction  $\text{NCN} + \text{H}$ . In contrast, varying the branching fraction of  $^3\text{NCN} + \text{H}$  had no discernable effect on the simulated  $^3\text{NCN}$  profiles, which implies that the products of reaction 1 are insignificant for the decay of  $^3\text{NCN}$ . Consequently, an accurate determination of  $k_1$  is possible.

Figure 8.1b shows the kinetic  $\text{HCN}$  profile recorded during the same shock wave experiment. As can be seen from the comparatively low signal-to-noise ratio, the  $\text{HCN}$  detection sensitivity was the main limiting factor of the experiments conducted in this work. For the kinetic analysis of the  $\text{HCN}$  profiles,  $k_{1b}$  was used as the main fitting parameter and  $k_{1a} = k_1 - k_{1b}$  was calculated using the corresponding  $k_1$  value from the  $^3\text{NCN}$  profile fit. Assuming that contributions of channels 1c and 1d are negligible may cause minor bias by overrating the secondary chemistry. For example,  $\text{CH}$  formation in channel 1a causes minor  $\text{HCN}$  formation by reaction 7,  $\text{NCN} + \text{CH} \rightarrow \text{HCN} + \text{CN}$ . However, as both channels can be safely assumed to be unimportant in the studied temperature range, this is not expected to cause any significant error.

Figure 8.1d shows a sensitivity analysis based on the best-fit  $k_{1b}$  value (and  $k_{17} = 0$ , see below). Similar to the  $^3\text{NCN}$  profile, reaction 1 appears four times in the sensitivity plot for  $\text{HCN}$  as well, with positive  $\sigma(\text{HCN})$  values for channel 1b and negative  $\sigma(\text{HCN})$  values for channel 1a. Such a high contrast in  $\sigma(\text{HCN})$  between channels 1b and 1a is highly desirable, since the main goal was the determination of the  $^3\text{NCN} + \text{H}$  branching fraction  $\phi_{1b}$ . Note that higher sensitivities are observed for  $^3\text{NCN}$ , revealing that  $^1\text{NCN}$  relaxation is fast enough to allow for a reliable determination of the triplet rate constant. However, the  $^1\text{NCN}$  contribution is quite pronounced at short reaction times, making clear that the approximate treatment of  $^1\text{NCN}$  chemistry by simply duplicating the rate constants for both spin states may in fact result in some uncertainty for the overall determined triplet branching fraction. This important point will be discussed further below. In addition to the branching of reaction 1, which clearly dominates the observed  $\text{HCN}$  formation, a few other reactions are relevant as well. Next to the effective H atom yield from the branching of the ethyl iodide decomposition, reaction 13,  $\text{CN} + \text{H}_2 \rightarrow \text{HCN} + \text{H}$ , turns out to be important as an additional source of  $\text{HCN}$ . Under the conditions of this shock tube experiment,  $\text{CN}$  is mostly formed by reaction 6,  $\text{NCN} + \text{C}$ , and molecular hydrogen by reaction 12,  $\text{C}_2\text{H}_4 + \text{H}$ .

Since  $\sigma(\text{HCN})$  for the reaction  $^3\text{NCN} + \text{H}$  is most favorable at reaction times  $t < 100 \mu\text{s}$ , in

a first assessment, the HCN profiles were analyzed by focusing on the initial rise of the HCN concentration-time profile. For the HCN signal shown in Fig. 8.1b, the best-fit value for  $k_{1b}$  determined with the original mechanism (see Section C in the Supplementary material, excluding reaction 17) is shown as a dash-dotted curve. Until about 50  $\mu\text{s}$ , the simulation matches the experimental profile well, but it deviates at later reaction times and does not reproduce the slow long-term formation of HCN at  $t > 100 \mu\text{s}$ . As an increase in  $k_{1b}$  (while keeping  $k_1$  constant) causes too fast initial slopes, we attribute the long-term increase to secondary HCN formation. Most obvious alternative HCN formation pathways that may become important at later reaction times involve transient species such as CN. However, with simulated CN concentration profiles reaching their maxima between 50 and 150  $\mu\text{s}$  and quickly decaying thereafter, reactions like  $\text{CN} + \text{H}_2$  can not explain the long-term HCN trend. We therefore consider the reaction of residual BrCN with hydrogen atoms to be the most likely source of HCN at longer reaction times. High-temperature rate constants of reaction 17,  $\text{BrCN} + \text{H} \rightarrow \text{HCN} + \text{Br}$ , are unknown and therefore, in a second assessment of the data,  $k_{1b}$  and  $k_{17}$  have been adjusted independently to fit the initial increase and long-term trend of the HCN profile, respectively. The resulting fit is shown as a dashed curve in Fig. 8.1b. A direct comparison of the dash-dotted curve ( $k_{17} = 0$ ) and the dashed curve (with  $k_{17}$ ) reveals that the target reaction 1b is responsible for most of the observed HCN. Moreover, simulations with  $k_{1b}$  multiplied or divided by the factor 1.5 (dotted curves) clearly show that a reliable determination of  $k_{1b}$  and thereby  $\phi_{1b}$  was possible.

The individually fitted rate constants  $k_{17}$  yielded consistent values for all experiments (see Fig. B.2 in Section H of the Supplementary Material) that can be expressed by  $k_{17}/(\text{cm}^3 \text{ mol}^{-1} \text{ s}^{-1}) = 9 \times 10^{12} \exp(-22 \text{ kJ mol}^{-1}/RT)$ , with the activation energy fixed to a value taken from the low-temperature chemiluminescence study of Arunan et al. [25]. We tentatively estimated the uncertainty factor of  $k_{17}$  to be around 1.5 based on the minimum and maximum values of the rate constant for  $\text{BrCN} + \text{H}$  that would still be consistent with the HCN concentration within the noise level of the experiments. However, the given expression for  $k_{17}$  should be viewed with caution, since it was only derived indirectly and merely represents our best effort to explain the late HCN formation in the kinetic profiles.

## Rate Constants

Figure 8.2a shows an Arrhenius plot for the reaction  $^3\text{NCN} + \text{H}$ . The  $k_1$  and  $k_{1b}$  values from this study are plotted as solid symbols and are compared with selected literature data from the papers already mentioned in the introduction [6–10]. The upper and lower shaded areas in Fig. 8.2a represent the estimated uncertainty ranges for  $k_1$  from Faßheber et al. [8] and for  $k_{1b}$  as derived in this work.

Regarding the total rate constant  $k_1$ , the experimental values by Faßheber et al. [8] and the results from high-level theory by Klippenstein et al. [7] agree within a factor of 2, but the temperature dependence is significantly different. While the results for  $k_1$  from Klippenstein et al. (long dash-dotted curve) predict a rate constant minimum at around 1930 K, the expression derived by Faßheber et al. reaches its minimal value already around 1120 K. Here, the negative temperature



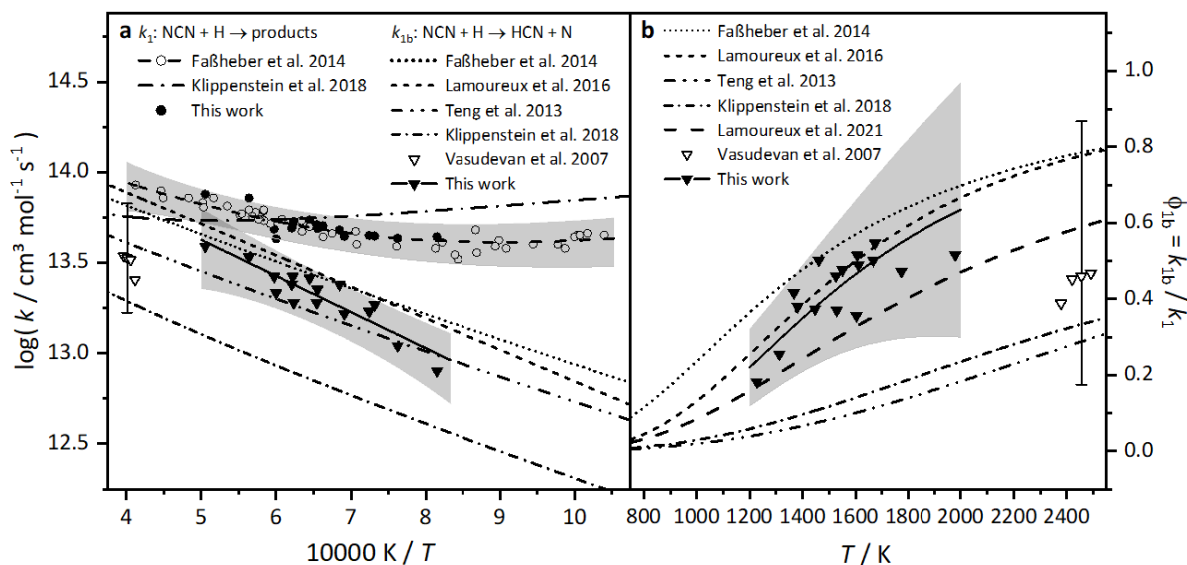


**Figure 8.2:** (a) Arrhenius plot for  $k_1$  and  $k_{1b}$  data ( $^3\text{NCN}$  reactions) derived in this work (solid symbols) in comparison with literature data from Refs. [6–10]. The upper and lower shaded areas indicate the uncertainties of  $k_1$  (adopted from [8]) and  $k_{1b}$  (see text). (b) Temperature dependence of the branching fraction  $\phi_{1b}$  determined in this study (solid symbols), its estimated uncertainty range as shaded area (see text), and  $\phi_{1b}$  values from the literature (1 bar). The solid curve represents  $\phi_{1b}$  calculated with the Arrhenius expressions for  $k_1$  from Faßheber et al. [8] and  $k_{1b}$  from this work. For a colored version of this graph, see Section J of Supplementary Material.

dependence at low temperatures is in line with the association-isomerization channel 1a, whereas the increase of the rate constant toward higher temperatures is a result of the activation-controlled channel 1b. Consequently, the earlier onset of the rate constant increase has been ascribed to channel 1b by Faßheber et al., resulting in a much lower experimental prompt-NO switch temperature  $T_S$  than predicted by theory. As can be seen in Fig. 8.2a, the total rate constant values of this study (solid circles) are in quantitative agreement with their earlier results (open circles). The measurements of Faßheber et al. were conducted under more favorable experimental conditions, i.e., lower concentrations of  $\text{NCN}_3$  to suppress secondary chemistry and higher  $\text{C}_2\text{H}_5\text{I}/\text{NCN}_3$  ratios to ensure pseudo-first order conditions. We therefore take the excellent agreement of the new data of this study as a confirmation of the Faßheber et al. rate constant expression and – as the earlier study also covered a wider range of temperatures and pressures – we adopt their  $k_1$  rate constant expression for further analysis of the branching fraction.

The experimental values for  $k_{1b}$  are shown as solid triangle symbols and the corresponding Arrhenius fit as a solid line,  $k_{1b}/(\text{cm}^3 \text{ mol}^{-1} \text{ s}^{-1}) = 4.2 \times 10^{14} \exp(-38.2 \text{ kJ mol}^{-1}/RT)$ . Over the temperature range studied in this work, the values for  $k_{1b}$  agree with the rate constant expressions of Faßheber et al. [8] (dotted curve, thermochemical/kinetic analysis of their  $k_1$  data), Lamoureux et al. [9] (dashed line, flame modeling), and Teng et al. [6] (dash-double-dotted curve, quantum-chemical kinetic study) within a factor of about 1.5. The work of Klippenstein et al. [7] (dash-dotted curve, quantum-chemical kinetic study) suggests lower  $k_{1b}$  values by a factor of  $\sim 3$ . Notably, the activation energy of our Arrhenius fit is about 5 kJ/mol higher than the  $\sim 33$  kJ/mol



predicted by the theoretical studies. However, within the uncertainty of the experiments, our rate constant data are also consistent with this lower value. Finally, Fig. 8.2a also contains the shock tube results from Vasudevan et al. [10] as open triangle symbols. These values lie outside of the investigated temperature range, but are also largely compatible with the present study.

### Branching fraction

Figure 8.2b illustrates the corresponding temperature-dependent branching fraction  $\phi_{1b}$ . The data from the sixteen individual shock tube experiments,  $\phi_{1b} = k_{1b}^{\text{exp}}/k_1^{\text{exp}}$ , are shown as solid triangles along with  $\phi_{1b}$  values calculated with  $k_{1b}$  from this work and  $k_1$  from Faßheber et al. [8] (solid curve). The results indicate a clear increase of the branching fraction with increasing temperature and are consistent with a prompt-NO switch temperature of  $T_S = 1670$  K. The resulting branching fractions from the aforementioned literature data are shown as well, using the same line styles as in Fig. 8.2a. Again, our derived branching fractions are in good agreement with the earlier experimental data and the flame modeling results, but are not consistent with the much lower predicted theoretical HCN yields. The reason for this striking discrepancy remains unclear, however, it may be related to difficulties in treating the electronic structure of the transition state from  ${}^3\text{NCN} + {}^2\text{H}$  to  ${}^4\text{N}(\text{CH})\text{N}$  that suffers from spin-contamination and symmetry-breaking problems [7] or a yet unidentified role of intersystem crossing pathways between the doublet and quartet surfaces.

In Fig. 8.2b, we also included the branching fraction derived from the shock tube data of Vasudevan et al. [10] (open triangles,  $\phi_{1b} = 0.46_{-0.29}^{+0.41}$ , see Section A of the Supplementary Material) as well as a consensus expression (long-dashed curve) from the recent review of Lamoureux et al. [3]. This consensus expression with  $T_S = 2080$  K represents a best-fit obtained by minimizing the deviations of flame simulation results from several validation targets (NCN, HCN, and NO species profiles in a rich low-pressure premixed methane/air flame; total rate constant  $k_1$ ). Both the experimental data of Vasudevan et al. as well as the consensus expression of Lamoureux et al. are compatible with our  $\phi_{1b}$  data.

### Uncertainties

Relying on the accuracy of two rate constants, the determination of branching fractions is prone to errors. Therefore, we have performed a rigorous error assessment to derive meaningful uncertainty ranges for both  $k_{1b}$  and  $\phi_{1b}$ . Table 8.2 lists all considered quantities, their assumed relative errors either taken from the respective literature [13, 18, 20] or estimated, and the resulting relative uncertainties  $\Delta k_{1b}/k_{1b}$  for three representative temperatures.

The uncertainty of the absorption cross section  $\sigma_{\text{HCN}}$  has been determined from uncertainties of the associated pressure-broadening parameters [13]. As discussed in more detail in Ref. 8, uncertainties in the branching fraction  $\phi_{8a} = k_{8a}/k_8$  directly feed into the uncertainties of the total rate constant for  $\text{NCN} + \text{H}$  due to the effect of  $\phi_{8a}$  on the H atom yield. In contrast, uncertainties in the total rate constant  $k_8$  have a negligible effect on  $k_1$ , since  $\text{C}_2\text{H}_5\text{I}$  decomposes within less than 1  $\mu\text{s}$ . Error margins for  $k_{1b}$  were determined by varying each quantity within its assumed

uncertainty range and by adjusting  $k_{1b}$  to reproduce the best-fit HCN profile as closely as possible. The total error was then obtained by assuming partial error compensation. Error margins for  $\phi_{1b}$  were calculated based on  $\Delta k_1/k_1$  and  $\Delta k_{1b}/k_{1b}$ , except that some contributions to  $\Delta k_{1b}/k_{1b}$  were not considered (marked by asterisks in Tab. 8.2) because they were either already accounted for in  $\Delta k_1/k_1$  [8] or influence both  $k_{1b}$  and  $k_1$  in the same direction and therefore approximately cancel out for  $\phi_{1b}$ . Special attention was given to a possible contribution to HCN resulting from the singlet reaction  $^1\text{NCN} + \text{H}$ . As mentioned above,  $^1\text{NCN}$  may play a significant role at short reaction times. Assuming higher rate constants for  $^1\text{NCN} + \text{H}$  impacts both the HCN and  $^3\text{NCN}$  profiles. In particular, it lowers the yield of  $^3\text{NCN}$  and hence causes a misfit of the  $^3\text{NCN}$  peak mole fraction, which needs to be counteracted by assuming higher initial  $\text{NCN}_3$  concentrations for the simulation. Overall, the obtained  $\phi_{1b}$  decreases with increasing  $k_1(^1\text{NCN})$ . However, increasing  $k_1(^1\text{NCN})$  by more than a factor of 2 would require an unreasonable adjustment of the initial  $\text{NCN}_3$  concentration to a value higher than the concentration set by the mass flow controllers prior to the experiment. Lowering  $k_1(^1\text{NCN})$  has about the opposite effect, but decreasing it by more than a factor of 2 has an insignificant effect because the sensitivity of the  $^1\text{NCN}$  reaction on the profiles vanishes. Thus, we estimate an uncertainty factor of 2 for the  $^1\text{NCN}$  reaction to cover the full range of reasonable situations. The resulting total relative error margins  $\Delta k_{1b}/k_{1b}$  and  $\Delta\phi_{1b}/\phi_{1b}$  are (37–49)% and (42–53)% (shaded areas in Fig. 8.2), respectively, with increasing uncertainty toward the upper and lower temperature limits of the experiment.

Finally, in order to test the validity of the manual iterative fitting procedure outlined above, a global fit analysis of the data has been performed as well. Details are outlined in Section I of the Supplementary Material. In agreement with the outcome of the manual fitting procedure within error limits, on average only 0.07 lower branching fractions have been obtained, corresponding

**Table 8.2:** Error estimation for  $k_{1b}$  and  $\phi_{1b}$ .  $\sigma_{\text{HCN}}$  refers to the absorption cross section of HCN. Here, the term ‘scatter’ refers to the standard error of all 16  $k_{1b}$  values relative to the Arrhenius fit.

Error con-tribution	Uncertainty	$\Delta k_{1b}/k_{1b}$ / %		
		1200 K	1600 K	2000 K
$\sigma_{\text{HCN}}$ [13]		11	10	27
scatter	1.04	4	4	4
$p$	1.03	3	3	3
$T$	1.03	12	3	6
$k_1(^1\text{NCN})$	2	15	32	33
$k_7$	1.5	30	4	3
$\phi_{8a}$ [18]	1.07	*4	*2	*5
$k_{10}$	1.5	*11	*2	*1
$k_{13}$ [20]	1.2	5	6	10
$k_{17}$	1.5	3	6	16
$x(\text{NCN}_3)$	1.1	10	10	10
$x(\text{C}_2\text{H}_5\text{I})$	1.05	*2	*2	*2
$\Delta k_{1b}/k_{1b}$ / % (total)		41	37	49
$\Delta k_1/k_1$ / % [8]		24	20	21
$\Delta\phi_{1b}/\phi_{1b}$ / %		46	42	53

\* Not considered for the relative error of the branching fraction of channel 1b (see text).

to an increase of the prompt-NO switch temperature to  $T_S = 1830$  K. Actually, the automatic fit procedure attributes a higher fraction of the experimentally observed HCN yield to the post hoc introduced lump reaction  $\text{BrCN} + \text{H} \rightarrow \text{HCN} + \text{Br}$  to account for the observed HCN increase on longer reaction times. Therefore, future measurements are desirable to narrow down the uncertainties arising from this side reaction.

## 8.4 Conclusions

For the first time, direct branching fraction measurements for  $^3\text{NCN} + \text{H}$  were conducted by simultaneous detection of HCN and  $^3\text{NCN}$  behind shock waves. The prompt-NO switch temperature of  $T_S = 1670$  K derived in this work is in agreement with flame modeling results of Lamoureux et al. ( $T_S = 1630$  K – 2080 K) [3, 9] and consistent with earlier experimental results of Faßheber et al. (1440 K) [8]. The detected HCN profiles clearly indicate that HCN is already formed to a significant extent by the prompt-NO switch reaction  $^3\text{NCN} + \text{H}$  at typical flame temperatures, contrary to predictions based on recent high-level theoretical results.

## Acknowledgments and Funding

The authors acknowledge the financial support of the German Science Foundation (DFG) through project FR1529/7-1. We thank Johannes Rückelt and Thomas Slawig, Institute of Informatics at Kiel University, for collaborating on the development of a CHEMKIN-II based global fit analysis program in the framework of the Cluster of Excellence FUTURE OCEAN at Kiel University (EXC-80); details on this fitting program, including a performance analysis, will be published elsewhere.

## References

- [1] P. Glarborg, J. A. Miller, B. Ruscic, S. J. Klippenstein, Modeling nitrogen chemistry in combustion, *Prog. Energy Combust. Sci.* **2018**, *67*, 31–68, DOI [10.1016/j.pecs.2018.01.002](https://doi.org/10.1016/j.pecs.2018.01.002).
- [2] L. Moskaleva, M. Lin, The spin-conserved reaction  $\text{CH} + \text{N}_2 \rightarrow \text{H} + \text{NCN}$ : A major pathway to prompt NO studied by quantum/statistical theory calculations and kinetic modeling of rate constant, *Proc. Combust. Inst.* **2000**, *28*, 2393–2401, DOI [10.1016/S0082-0784\(00\)80652-9](https://doi.org/10.1016/S0082-0784(00)80652-9).
- [3] N. Lamoureux, P. Desgroux, M. Olzmann, G. Friedrichs, The story of NCN as a key species in prompt-NO formation, *Prog. Energy Combust. Sci.* **2021**, *87*, 100940/1–34, DOI [10.1016/j.pecs.2021.100940](https://doi.org/10.1016/j.pecs.2021.100940).
- [4] N. Faßheber, L. Bornhorst, S. Hesse, Y. Sakai, G. Friedrichs, The Reaction  $\text{NCN} + \text{H}_2$ : Quantum Chemical Calculations, Role of  $^1\text{NCN}$  Chemistry, and  $^3\text{NCN}$  Absorption Cross Section, *J. Phys. Chem. A* **2020**, *124*, 4632–4645, DOI [10.1021/acs.jpca.0c02631](https://doi.org/10.1021/acs.jpca.0c02631).
- [5] N. Lamoureux, P. Desgroux, A. E. Bakali, J. Pauwels, Experimental and numerical study of the role of NCN in prompt-NO formation in low-pressure  $\text{CH}_4\text{-O}_2\text{-N}_2$  and  $\text{C}_2\text{H}_2\text{-O}_2\text{-N}_2$  flames, *Combust. Flame* **2010**, *157*, 1929–1941, DOI [10.1016/j.combustflame.2010.03.013](https://doi.org/10.1016/j.combustflame.2010.03.013).
- [6] W.-S. Teng, L. V. Moskaleva, H.-L. Chen, M. C. Lin, Ab Initio Chemical Kinetics for  $\text{H} + \text{NCN}$ : Prediction of NCN Heat of Formation and Reaction Product Branching via Doublet and Quartet Surfaces, *J. Phys. Chem. A* **2013**, *117*, 5775–5784, DOI [10.1021/jp402903t](https://doi.org/10.1021/jp402903t).
- [7] S. J. Klippenstein, M. Pfeifle, A. W. Jasper, P. Glarborg, Theory and modeling of relevance to prompt-NO formation at high pressure, *Combust. Flame* **2018**, *195*, 3–17, DOI [10.1016/j.combustflame.2018.04.029](https://doi.org/10.1016/j.combustflame.2018.04.029).

- [8] N. Faßheber, J. Dammeier, G. Friedrichs, Direct measurements of the total rate constant of the reaction  $\text{NCN} + \text{H}$  and implications for the product branching ratio and the enthalpy of formation of  $\text{NCN}$ , *Phys. Chem. Chem. Phys.* **2014**, *16*, 11647–11657, DOI [10.1039/c4cp01107d](https://doi.org/10.1039/c4cp01107d).
- [9] N. Lamoureux, H. E. Merhubi, L. Pillier, S. de Persis, P. Desgroux, Modeling of  $\text{NO}$  formation in low pressure premixed flames, *Combust. Flame* **2016**, *163*, 557–575, DOI [10.1016/j.combustflame.2015.11.007](https://doi.org/10.1016/j.combustflame.2015.11.007).
- [10] V. Vasudevan, R. K. Hanson, C. T. Bowman, D. M. Golden, D. F. Davidson, Shock Tube Study of the Reaction of  $\text{CH}$  with  $\text{N}_2$ : Overall Rate and Branching Ratio, *J. Phys. Chem. A* **2007**, *111*, 11818–11830, DOI [10.1021/jp075638c](https://doi.org/10.1021/jp075638c).
- [11] J. Dammeier, N. Faßheber, G. Friedrichs, Direct measurements of the high temperature rate constants of the reactions  $\text{NCN} + \text{O}$ ,  $\text{NCN} + \text{NCN}$ , and  $\text{NCN} + \text{M}$ , *Phys. Chem. Chem. Phys.* **2012**, *14*, 1030–1037, DOI [10.1039/c1cp22123j](https://doi.org/10.1039/c1cp22123j).
- [12] M. Stuhr, N. Faßheber, G. Friedrichs, Single-tone mid-infrared frequency modulation spectroscopy for sensitive detection of transient species, *Opt. Express* **2019**, *27*, 26499–26512, DOI [10.1364/oe.27.026499](https://doi.org/10.1364/oe.27.026499).
- [13] M. Stuhr, S. Hesse, G. Friedrichs, Quantitative and Sensitive Mid-Infrared Frequency Modulation Detection of  $\text{HCN}$  behind Shock Waves, *Fuels* **2021**, *2*, 437–447, DOI [10.3390/fuels2040025](https://doi.org/10.3390/fuels2040025).
- [14] M. Colberg, G. Friedrichs, Room temperature and shock tube study of the reaction  $\text{HCO} + \text{O}_2$  using the photolysis of glyoxal as an efficient  $\text{HCO}$  source, *J. Phys. Chem. A* **2006**, *110*, 160–170, DOI [10.1021/jp055168r](https://doi.org/10.1021/jp055168r).
- [15] I. Gordon et al., The HITRAN2016 molecular spectroscopic database, *J. Quant. Spectrosc. Radiat. Transfer* **2017**, *203*, 3–69, DOI [10.1016/j.jqsrt.2017.06.038](https://doi.org/10.1016/j.jqsrt.2017.06.038).
- [16] D. E. Milligan, M. E. Jacox, A. M. Bass, Matrix Isolation Study of the Photolysis of Cyanogen Azide. The Infrared and Ultraviolet Spectra of the Free Radical  $\text{NCN}$ , *J. Chem. Phys.* **1965**, *43*, 3149–3160, DOI [10.1063/1.1697289](https://doi.org/10.1063/1.1697289).
- [17] J. Dammeier, B. Oden, G. Friedrichs, A consistent model for the thermal decomposition of  $\text{NCN}_3$  and the singlet-triplet relaxation of  $\text{NCN}$ , *Int. J. Chem. Kinet.* **2012**, *45*, 30–40, DOI [10.1002/kin.20739](https://doi.org/10.1002/kin.20739).
- [18] T. Varga, I. G. Zsély, T. Turányi, T. Bentz, M. Olzmann, Kinetic Analysis of Ethyl Iodide Pyrolysis Based on Shock Tube Measurements, *Int. J. Chem. Kinet.* **2013**, *46*, 295–304, DOI [10.1002/kin.20829](https://doi.org/10.1002/kin.20829).
- [19] D. L. Baulch et al., Evaluated Kinetic Data for Combustion Modelling, *J. Phys. Chem. Ref. Data* **1992**, *21*, 411–734, DOI [10.1063/1.555908](https://doi.org/10.1063/1.555908).
- [20] S. T. Wooldridge, R. K. Hanson, C. T. Bowman, A shock tube study of reactions of  $\text{CN}$  with  $\text{HCN}$ ,  $\text{OH}$ , and  $\text{H}_2$  using  $\text{CN}$  and  $\text{OH}$  laser absorption, *Int. J. Chem. Kinet.* **1996**, *28*, 245–258, DOI [10.1002/\(SICI\)1097-4601\(1996\)28:4<245::AID-KIN2>3.0.CO;2-V](https://doi.org/10.1002/(SICI)1097-4601(1996)28:4<245::AID-KIN2>3.0.CO;2-V).
- [21] W. Tsang, J. T. Herron, Chemical Kinetic Data Base for Propellant Combustion I. Reactions Involving  $\text{NO}$ ,  $\text{NO}_2$ ,  $\text{HNO}$ ,  $\text{HNO}_2$ ,  $\text{HCN}$  and  $\text{N}_2\text{O}$ , *J. Phys. Chem. Ref. Data* **1991**, *20*, 609–663, DOI [10.1063/1.555890](https://doi.org/10.1063/1.555890).
- [22] W. Tsang, Chemical Kinetic Data Base for Propellant Combustion. II. Reactions Involving  $\text{CN}$ ,  $\text{NCO}$ , and  $\text{HNCO}$ , *J. Phys. Chem. Ref. Data* **1992**, *21*, 753–791, DOI [10.1063/1.555914](https://doi.org/10.1063/1.555914).
- [23] P. Han, K. Su, Y. Liu, Y. Wang, X. Wang, Q. Zeng, L. Cheng, L. Zhang, Reaction rate of propene pyrolysis, *J. Comput. Chem.* **2011**, *32*, 2745–2755, DOI [10.1002/jcc.21854](https://doi.org/10.1002/jcc.21854).
- [24] N. Faßheber, G. Friedrichs, Shock Tube Measurements of the Rate Constant of the Reaction  $\text{NCN} + \text{O}_2$ , *Int. J. Chem. Kinet.* **2015**, *47*, 586–595, DOI [10.1002/kin.20932](https://doi.org/10.1002/kin.20932).
- [25] E. Arunan, G. Manke, D. Setser, Infrared chemiluminescence studies of  $\text{H} + \text{BrCN}$  and  $\text{H}$  abstraction by  $\text{CN}$  reactions. Importance of the  $\text{HNC}$  channel, *Chem. Phys. Lett.* **1993**, *207*, 81–87, DOI [10.1016/0009-2614\(93\)85015-g](https://doi.org/10.1016/0009-2614(93)85015-g).

# CHAPTER 9

---

## Summary and Outlook

---

A new single-tone MIR-FM spectrometer has been set up, characterized, and practically employed for gas-phase reaction kinetic applications. As demonstrated in the publications embedded in this work, ST-FMS in the MIR region has proven itself as a reliable diagnostic tool for quantitative and sensitive species detection in reaction kinetic studies, even at short timescales and under harsh experimental conditions. The main accomplishments of the present thesis are summarized below.

**Setup and Characterization of the ST-MIR-FM spectrometer:** For the first time, single-tone application of MIR-FM spectroscopy with external EOM-based frequency modulation was realized and used in pulsed laser photolysis experiments. Spectral measurements of  $\text{CH}_4$  and fixed-frequency kinetic traces of  $\text{HCl}$  and  $\text{OH}$  radicals served to verify the detection capabilities of the ST-MIR-FM spectrometer. The detection sensitivity of the ST-MIR-FM setup was evaluated by means of an Allan analysis using pure FM signal noise.

Three main upgrades were applied to the initial detection system described in the first publication. The newest iteration of the spectrometer includes a resonant EOM in double-pass configuration, a high-bandwidth MIR photodetector with four-stage thermoelectric cooling, and a fast all-digital lock-in amplifier. With comparatively high modulation depth of  $M = 0.97$  at modulation frequency  $\nu_m = 489.0$  MHz, the attenuation contrast between adjacent frequency sidebands, as quantified by the FM factor  $\Delta f$ , is sufficiently high for sensitive species detection even at elevated pressures. Assuming  $\Delta f = 0.6$ , which represents a realistic value for both low-pressure flash photolysis and high-pressure shock tube experiments, the ST-MIR-FM detection system reaches minimum detectable absorption levels of  $A_{\min} = 2.9 \times 10^{-4}$  and  $A_{\min} = 3.8 \times 10^{-5}$  at time resolutions of  $t = 1 \mu\text{s}$  and  $t = 100 \mu\text{s}$ , respectively. These numbers compare well with conventional dual-beam MIR laser-absorption techniques, which are limited to  $A_{\min} \approx 2 \times 10^{-3}$  at around  $t = 1 \mu\text{s}$ .

Currently, RAM noise in the kHz range limits the sensitivity gain of the FM setup on longer timescales. This represents only a minor concern for shock tube-based studies, which usually aim for measuring concentration-time profiles over reaction times less than 1 ms. So far, due to small active areas of available high-bandwidth MIR photodetectors, only relatively low detection beam power  $P_0$  can be used. Consequently, detection sensitivity is still limited by thermal noise, which is a common issue in MIR-based applications of absorption spectroscopy. Shot-noise limited detection, which has been achieved in the visible spectral range in previous studies, is currently not within reach of ST-FMS in the MIR, at least not until MIR photodetectors with higher saturation

limits become available.

**Detection of HCl in low-pressure reactors:** UV photolysis of oxalyl chloride,  $(\text{ClCO})_2$ , was studied in a measurement campaign performed at the vacuum-UV beamline of the Swiss Light Source (SLS) at photolysis wavelengths of 213 nm, 266 nm, and 355 nm. Low-pressure kinetic profiles of  $\text{Cl}_2$  recorded with time-of-flight mass spectrometry served to determine the photolysis quantum yield of direct  $\text{Cl}_2$  formation, which has only recently been proposed as a significant photodecomposition channel. In order to complement the SLS measurements, the newest iteration of the ST-MIR-FM spectrometer was employed for HCl detection in  $(\text{ClCO})_2$  photolysis experiments at Kiel University.  $(\text{ClCO})_2/\text{C}_2\text{H}_6/\text{Ar}$  gas mixtures were subjected to UV photolysis at 266 nm and 355 nm in a low-pressure slow-flow cell. The main photolysis product ClCO undergoes thermal decomposition into CO and Cl atoms, the latter of which were efficiently captured by the reaction with  $\text{C}_2\text{H}_6$  to form HCl. In this way, concentration-time profiles of HCl were recorded with detection limits on the sub-ppm level at  $\mu\text{s}$  time resolution. Kinetic analysis of the HCl profiles provided the rate constant of the thermal ClCO decomposition reaction,  $\text{ClCO} + \text{M} \rightarrow \text{Cl} + \text{CO} + \text{M}$ . The derived rate constant value of  $k = (1.08 \pm 0.10) \times 10^{10} \text{ cm}^3 \text{ mol}^{-1} \text{ s}^{-1}$  at  $T = 295 \text{ K}$  in argon buffer gas is consistent with earlier indirect experimental results. In addition, time-resolved TOF-MS detection of molecular  $\text{Cl}_2$  confirmed that it is a direct product of  $(\text{ClCO})_2$  photofragmentation. With quantum yields of  $(5.0 \pm 1.6)\%$  at 213 nm,  $(10.0 \pm 3.3)\%$  at 266 nm, and  $(5.4 \pm 2.0)\%$  at 355 nm, direct  $\text{Cl}_2$  formation has to be accounted for when using  $(\text{ClCO})_2$  photolysis as a Cl atom source. The results of this study suggest that the previously accepted picture of  $(\text{ClCO})_2$  photolysis is incomplete. Both Cl atoms and  $\text{Cl}_2$  molecules are most likely formed by subsequent decomposition of the vibrationally excited intermediate phosgene,  $\text{Cl}_2\text{CO}$ , a species largely ignored in earlier photodissociation studies.

**Detection of HCN behind shock waves:** In most combustion environments, HCN is one of the primary nitrogen-containing hydrocarbons and the most abundant cyanide component. Yet suitable HCN detection schemes for combustion-related applications are sparse, especially for in-situ real-time measurements. Under harsh conditions behind shock waves, which cause mechanical vibrations in the optical system and pressure-induced birefringence in the shock tube windows, the main forte of FMS becomes evident, since its differential nature makes it largely immune to intensity-related signal disturbances.

A key aspect of this thesis was the first ST-MIR-FM detection of HCN behind shock waves on the ppm level, which enables the direct study of elementary reactions with HCN as reactant or product. To this end, HCN detection was realized on the P(26) rovibrational transition in the fundamental C-H stretch vibration band ( $\nu_1$ ) at  $3228.049 \text{ cm}^{-1}$ . Post-shock FM spectra of HCN were reconstructed from FM signals recorded in individual shock tube experiments. Simulated FM spectra were fitted to the experimental data by adjusting Gaussian and Lorentzian widths of the underlying absorption lineshape in order to extract the pressure-broadening parameters of the P(26) absorption line for argon. Together with literature linestrengths, these parameters form the basis of quantitative absorption-based detection of HCN at high temperatures and pressures. The current version of the ST-MIR-FM spectrometer reaches HCN detection limits of 22 ppm at

$t = 1 \mu\text{s}$  and 2.9 ppm at  $t = 100 \mu\text{s}$  for typical post-shock wave conditions of  $T = 1700 \text{ K}$  and  $p = 1.2 \text{ bar}$ . To the best of the author’s knowledge, the system described in this work represents the first MIR-FM-based scheme for quantitative detection of HCN behind shock waves.

**High-temperature reaction kinetics involving HCN:** The upgraded ST-MIR-FM spectrometer was employed for high-temperature detection of HCN in two reaction kinetic studies. Firstly, the oxidation of HCN by O atoms was investigated behind incident and reflected shock waves, where thermal decomposition of  $\text{N}_2\text{O}$  served as O atom source. Rate constants of the reaction  $\text{HCN} + \text{O}$  were determined in the temperature range  $1400 \text{ K} < T < 2000 \text{ K}$ , resulting in the Arrhenius expression  $k/(\text{cm}^3 \text{ mol}^{-1} \text{ s}^{-1}) = 1.88 \times 10^{14} \exp(-64.5 \text{ kJ mol}^{-1}/RT)$  (+28%, -37%). These measurements complement existing rate constant data on  $\text{HCN} + \text{O}$ , which were obtained by detection of involved species other than HCN, and close the gap between low-temperature discharge-flow reactor measurements ( $T < 900 \text{ K}$ ) and previous shock tube measurements ( $T > 1800 \text{ K}$ ). This study represents the first reaction kinetic application of quantitative HCN detection by FMS behind shock waves.

Secondly, high-temperature HCN detection by means of ST-MIR-FMS was employed to study the prompt-NO switch reaction  $\text{NCN} + \text{H}$ . The NCN radical is one of the key intermediates in the prompt-NO pathway of  $\text{NO}_x$  formation. Under typical conditions of hydrocarbon/air flames, the lifetime of the NCN radical is largely controlled by its reaction with H atoms. In a simplified view, the reaction  $\text{NCN} + \text{H}$  yields either  $\text{CH} + \text{N}_2$  or  $\text{HCN} + \text{N}$ , thereby proceeding either in forward or reverse direction of  $\text{NO}_x$  formation, respectively. Therefore, the branching of  $\text{NCN} + \text{H}$  into the two opposing directions critically determines the fate of the NCN radical. However, there is a great discrepancy between branching fraction values inferred indirectly from measurements and theoretical rate constant predictions.

To address this issue, a series of shock tube experiments with simultaneous detection of the reactant NCN and the product HCN by dual-beam UV spectroscopy and ST-MIR-FMS, respectively, were performed. In this way, values for the total rate constant and the rate constant of the HCN-yielding channel were determined in parallel measurements. This resulted in branching fraction values for the HCN-yielding channel of  $0.22 (\pm 46\%) < \phi < 0.63 (\pm 53\%)$  within the temperature range  $1200 \text{ K} < T < 2000 \text{ K}$ , corresponding to a prompt-NO switch temperature of  $T_S = 1670 \text{ K}$  ( $\phi = 0.5$ ). Within experimental uncertainties, the corresponding branching fraction values for the reaction  $\text{NCN} + \text{H}$  are consistent with indirectly inferred experimental values and recent recommendations from a review study on high-temperature NCN chemistry. The experiments described here represent the first branching fraction measurement of the prompt-NO switch reaction  $\text{NCN} + \text{H}$  and therefore provide valuable insight into prompt-NO formation. Very recently, preliminary branching fraction data were reported in a dissertation (Felix Poschen, KIT). Although effected by large scatter, the determined branching fraction values for the HCN-yielding channel from KIT confirm the results discussed here. The experimental values reported in the present work stand in stark contrast with recent theoretical predictions, which suggest branching fractions of about  $0.06 < \phi < 0.23$  within  $1200 \text{ K} < T < 2000 \text{ K}$  and prompt-NO switch temperatures of  $T_S > 3200 \text{ K}$ . This striking discrepancy is still unresolved and should be addressed



in future experimental and theoretical studies.

There are several possible applications of and potential improvements to the MIR-FM spectrometer. The most promising avenues for future work, which build on the accomplishments described in the present thesis, are outlined below.

**Further applications of high-temperature HCN detection:** Although HCN chemistry in conventional hydrocarbon/air combustion is relatively well-studied, ST-MIR-FM detection of HCN holds potential for related research topics, such as combustion of  $\text{NH}_3$ /hydrocarbon fuel blends and biomass gasification. Also, HCN detection in shock tube studies can still be used to address unresolved questions in combustion research. For example, some channels of the reaction  $\text{HCN} + \text{OH}$ , which is the main HCN removal path besides  $\text{HCN} + \text{O}$ , remain understudied. Depending on the exact experimental circumstances, ST-MIR-FMS may provide additional insight in this context, either in conjunction with other detection schemes or on its own.

**ST-MIR-FM detection of other species:** In the simplest case, already existing MIR-laser absorption schemes for species detection could be enhanced by frequency modulation to improve sensitivity and robustness of detection. For example, MIR detection of  $\text{NH}_3$ ,  $\text{H}_2\text{O}$ , and  $\text{N}_2\text{O}$  has been employed in shock tube studies on  $\text{NH}_3$ /air combustion. Without any further improvements to the ST-MIR-FM detection system, a sensitivity gain of a factor of at least 5 is realistic, as demonstrated by the  $A_{\min}$  values mentioned above. On these grounds, ST-MIR-FM detection of  $\text{NH}_3$  at ambient and post-shock wave conditions is currently being pursued in our research group. It is worth noting, however, that FM detection becomes less attractive towards higher detection wavelengths due to lower efficiency of electro-optic phase modulation and still limited availability of suitable detectors. Switching to FM-based detection should therefore be carefully considered, taking into account the specific constraints and requirements of the application in question.

Moreover, the scope of ST-MIR-FMS should be expanded to include species that are currently detected in the NIR spectral region by targeting overtone and combination bands, which have much lower linestrengths compared to fundamental transitions in the MIR. By switching to MIR detection, assuming similar detection and/or modulation parameters, one can reasonably expect a sensitivity improvement of at least one order of magnitude. As an example, MIR-FM-based detection of the  $\text{HO}_2$  radical, which is an important species in hydrocarbon autoignition and oxidative processes in the atmosphere, represents an interesting target for future research.

Another potential application of ST-MIR-FMS is the detection of hydrogen isocyanide, HNC, which can be formed in high-temperature combustion environments via HCN-HNC isomerization. Since HNC is generally assumed to be much more reactive than HCN with regards to oxidation by  $\text{O}_2$  and OH radicals, HCN-HNC isomerization opens additional pathways of HCN removal. Thus, ST-MIR-FM detection of HNC should be considered to verify recent theoretical rate constant predictions, especially since high-temperature detection of its isomer HCN has already established in the present thesis. Of course, this would require preceding work on the underlying HNC spectroscopy to ensure reliable quantitative detection.

**Instrumental improvements and modifications:** As far as changes to the detection system are concerned, future work should mainly focus on further increasing the detection sensitivity of the spectrometer. For measurements on ms timescales, RAM reduction by counteracting etaloning and EOM-laser polarization mismatch is the most promising approach. In the simplest case, an additional DC voltage could be applied to the EOM in order to correct spurious birefringence of the modulator crystal.

Below time resolutions of  $t < 100 \mu\text{s}$ , detection sensitivity is limited by thermal noise, which can be overcome by increasing the optical power of the detection laser beam  $P_0$ . However, higher saturation limits are currently not feasible without compromising detector bandwidths. For low-pressure applications, which target comparatively narrow absorption lines, ST-FM detection at lower modulation frequencies is an option worth considering. This should ease the stringent detection bandwidth requirements and thereby allow for the use of photodetector variants with larger active areas, i.e., higher acceptable detection beam power  $P_0$ . Since  $A_{\text{min}}$  is currently limited by intensity-independent thermal noise, any increase in  $P_0$  would most likely yield immediate benefits to the detection sensitivity. However, this reasoning does not apply to species detection behind shock waves, where high modulation frequencies are required to ensure sufficient attenuation contrast between adjacent frequency components in the modulated detection light. Moving from single-tone to two-tone MIR-FM detection, which has much lower bandwidth requirements, could help alleviate the issue of low optical power  $P_0$ . Two-tone FM detection does not suffer from loss of attenuation contrast, i.e., low FM factors  $\Delta f$ , in the same way that the single-tone variant does, since carrier attenuation makes strong contributions to two-tone FM signals. Thus, as long as the modulation depths at the two modulation frequencies are sufficiently high, two-tone MIR-FMS could potentially provide a sensitivity gain by allowing for species detection with lower-bandwidth photodetectors at higher  $P_0$  values. However, the prospect of switching to two-tone detection ultimately depends on a number of factors, including the exact relationship between active area and bandwidth of the photodetector, spectral lineshape, and different contributions to FM signal noise. It should also be noted that optical saturation of probed molecular transitions may become an issue at very high detection laser intensities.

In conclusion, the ST-MIR-FM spectrometer established in the present thesis provides a new diagnostic angle for in-situ detection of gaseous chemical species. Even within the current instrumental limitations, the method enables sensitive and quantitative species detection on short timescales, as demonstrated by successful ST-MIR-FM applications in low-pressure and post-shock kinetic experiments. Continued development of FM spectroscopy in the MIR region is desirable, even though the most substantial limitations of this technique can only be lifted with technological advancements in the field of MIR phase modulators and photodetectors.



## A Supplementary Material for Publication II

- A. Experimental conditions for measurements on ClCO decomposition (Tab. [A.1](#))
- B. Experimental conditions for measurements on direct Cl<sub>2</sub> formation (Tab. [A.2](#))
- C. Example profile for deriving the photolysis fraction (Fig. [A.1](#))
- D. Plot of  $r = k_3[M]/k_2$  vs.  $[M]$  (Fig. [A.2](#))
- E. Photoelectron images for Cl<sub>2</sub> (Fig. [A.3](#))
- F. Calculated energies on the PES for (ClCO)<sub>2</sub> photodissociation (Tab. [A.3](#))
- G. Calculated enthalpies of formation for key species (Tab. [A.4](#))
- H. Transition-state structures (Fig. [A.4](#) and Tab. [A.5](#))

## A. Experimental conditions for measurements on ClCO decomposition

**Table A.1:** Experimental conditions for measurements on ClCO decomposition by MIR-FM detection of HCl ( $T = 295$  K).

$\lambda$ / nm	$p$ / mbar	$x(\text{ClCO})_2$ / %	$x(\text{C}_2\text{H}_6)$ / %	$k'_4$ / $10^3 \text{ s}^{-1}$	$r = k_3[\text{M}]/k_2$
266	12.4	1.02	0.517	5.9	1.1
266	23.2	1.02	0.515	10.8	1.3
266	27.4	1.02	0.513	12.3	1.2
266	35.3	1.02	0.513	15.9	1.3
266	44.9	1.02	0.513	20.3	1.3
355	10.4	1.02	0.518	4.0	3.6
355	15.1	1.02	0.515	6.4	5.2
355	20.3	1.02	0.517	8.7	7.4
355	25.3	1.02	0.514	10.8	8.7
355	30.8	1.02	0.513	13.9	10.6
355	40.3	1.02	0.513	17.3	13.4
355	52.6	1.02	0.513	22.7	18.1

## B. Experimental conditions for measurements on direct $\text{Cl}_2$ formation

**Table A.2:** Experimental conditions for measurements on direct  $\text{Cl}_2$  formation by TOF-MS detection of  $\text{Cl}_2$  ( $T = 295$  K).  $(\text{ClCO})_2$  photolysis fractions are denoted as  $[(\text{ClCO})_2]_{\text{ph}}/[(\text{ClCO})_2]$ .

$\lambda$ / nm	$p$ / mbar	$x((\text{ClCO})_2)$ / $10^{-4}$	$[(\text{ClCO})_2]_{\text{ph}}/[(\text{ClCO})_2]$ / %	$\phi(\text{Cl}_2)/\%$
213	2.18	59.8	1.53	5.8
213	2.20	33.9	1.64	4.8
213	2.17	15.3	1.67	5.1
213	4.53	30.3	1.93	5.0
213	9.10	15.0	1.53	4.4
213	9.00	7.5	1.88	4.4
213	8.90	3.7	2.04	4.7
266	2.19	119.7	0.86	10.1
266	2.19	59.5	0.94	9.6
266	4.49	29.8	0.98	9.8
266	8.96	14.9	0.93	10.0
266	9.15	7.5	0.99	9.3
355	2.20	180.0	0.41	5.1
355	9.01	45.0	0.49	5.7
355	9.00	15.0	0.60	6.2

### C. Example profile for deriving the photolysis fraction

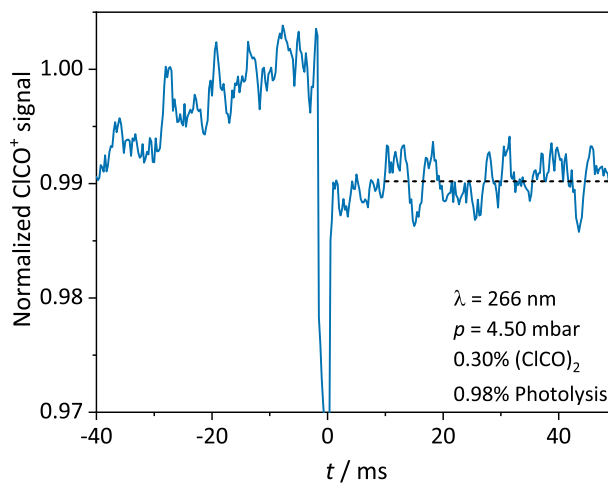


**Figure A.1:** Exemplary  $\text{ClCO}^+$  mass signal ( $m/z$  63, 65) for deriving the photolysis fraction of  $(\text{ClCO})_2$ .

### D. Plot of $r = k_3[\text{M}]/k_2$ vs. $[\text{M}]$

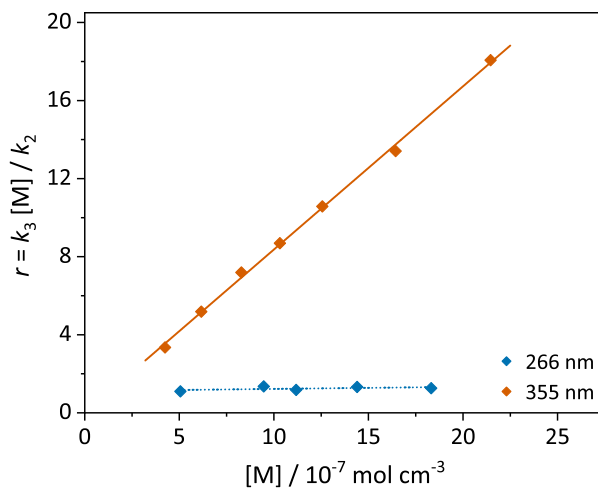


**Figure A.2:** Rate constant ratio  $r = k_3[\text{M}]/k_2$  as function of  $[\text{M}]$  for  $(\text{ClCO})_2$  photolysis at 266 nm and 355 nm.

## E. Photoelectron images for $\text{Cl}_2$

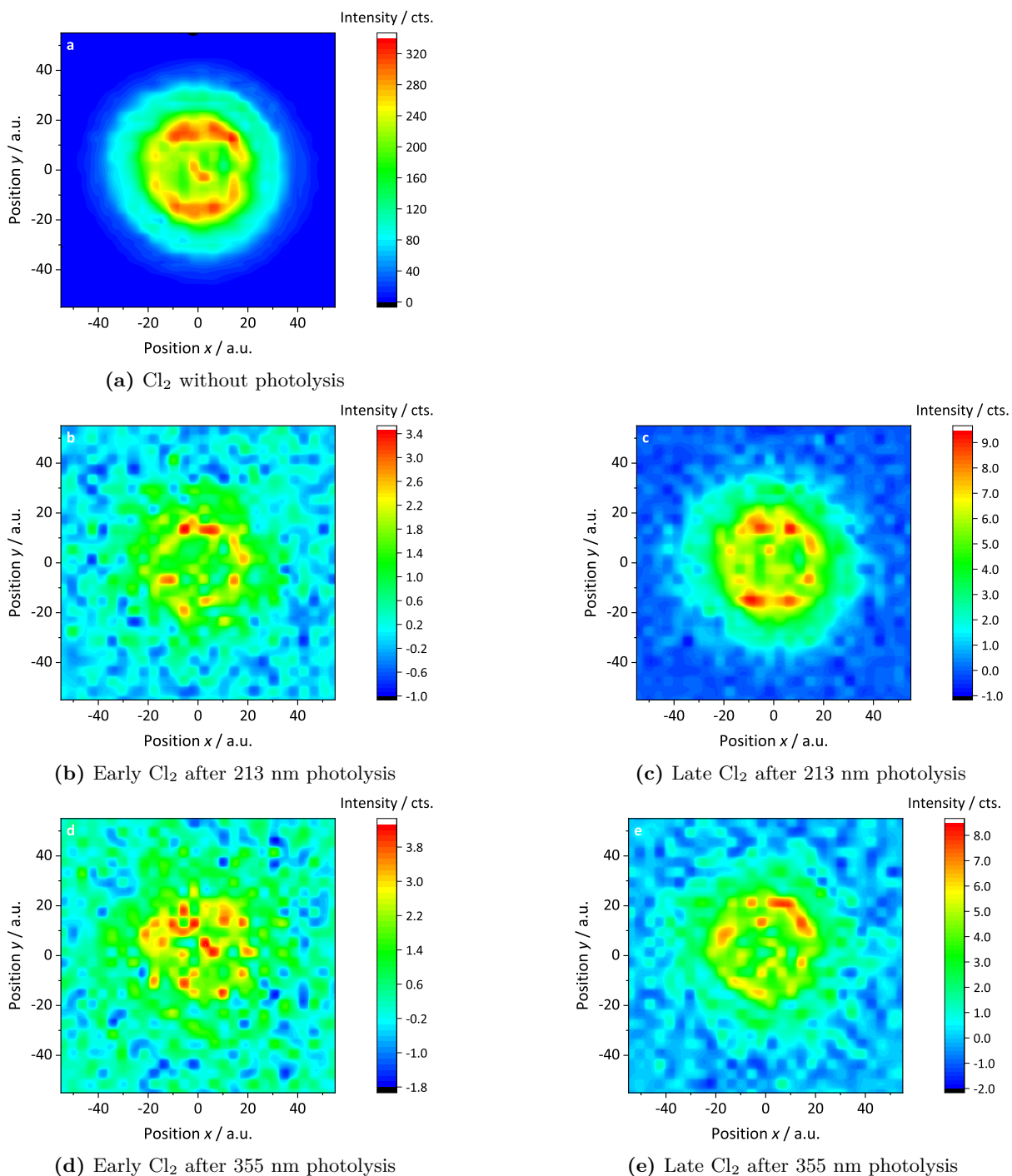


**Figure A.3:** Background-corrected photoelectron images for  $\text{Cl}_2$  ( $m/z$  70) measured at 11.7 eV and with 4-point smoothing in both dimensions. (a) Image for  $\text{Cl}_2$  calibration gas with  $(200 \pm 4)$  ppm  $\text{Cl}_2$  in  $\text{N}_2$  without photolysis. (b-e) Early (2 ms to 22 ms) and late (42 ms to 62 ms) images for  $\text{Cl}_2$  after  $(\text{ClCO})_2$  photolysis at 213 nm ( $p = 9.10$  mbar, 0.15%  $(\text{ClCO})_2$ ) and 355 nm ( $p = 2.20$  mbar, 1.80%  $(\text{ClCO})_2$ ). Note that the color scale varies from image to image. Within uncertainty limits, all five plots show very similar distributions.



## F. Calculated energies on the ground-state PES for (ClCO)<sub>2</sub> photodissociation

**Table A.3:** Energies of reactants, intermediates, transition states, and products on the ground-state PES for (ClCO)<sub>2</sub> photodissociation calculated by the G4 method. Corresponding values from calculations on the CCSD(T)/cc-pVTZ level of theory with B3LYP/cc-pVTZ-optimized geometries are shown for comparison.

Species	$\Delta E$ / kJ mol <sup>-1</sup>	
	G4	CCSD(T)
(ClCO) <sub>2</sub>	0.0	0.0
2 ClCO	280.5	273.3
Cl + CO + ClCO	306.3	286.7
2 Cl + 2 CO	332.0	300.1
TS1	302.5	314.3
ClC(O)COCl	286.8	296.5
ClC(O)CO + Cl	324.5	316.1
TS2	348.3	—
TS3	401.5	388.3
Cl <sub>2</sub> + 2 CO	95.2	85.5
TS4	161.6	164.1
Cl <sub>2</sub> CO + CO	-9.5	-12.6
TS5	339.5	345.3

## G. Calculated enthalpies of formation for key species

**Table A.4:** Enthalpies of formation  $\Delta_f H_{298\text{ K}}$  for the key species of (ClCO)<sub>2</sub> photodissociation calculated by the atomization method with G4 energy and harmonic oscillation approximation. Measured  $\Delta_f H_{298\text{ K}}$  values of <sup>3</sup>C, <sup>3</sup>O, and <sup>2</sup>Cl atoms for the atomization procedure were taken from Chase (NIST-JANAF Thermochemical Tables, 4th Edition, *J. Phys. Chem. Ref. Data, Monograph 9*, 1998). Literature values for  $\Delta_f H_{298\text{ K}}$  from Pedley, Naylor, and Kirby <sup>a</sup> (Thermochemical Data of Organic Compounds, 2nd Edition, 1986) as well as the ATcT database <sup>b</sup> (Ruscic and Bross, <https://atct.anl.gov/>, version 1.122r) are shown for comparison.

Species	$\Delta_f H_{298\text{ K}}$ / kJ mol <sup>-1</sup>	
	G4	Literature
(ClCO) <sub>2</sub>	-328.4	-335.8 <sup>a</sup>
ClCO	-21.7	-20.5 <sup>b</sup>
Cl <sub>2</sub> CO	-220.7	-219.1 <sup>b</sup>
Cl	—	121.3 <sup>b</sup>
CO	-113.7	-110.5 <sup>b</sup>
Cl <sub>2</sub>	2.6	0.0

## H. Transition-state structures

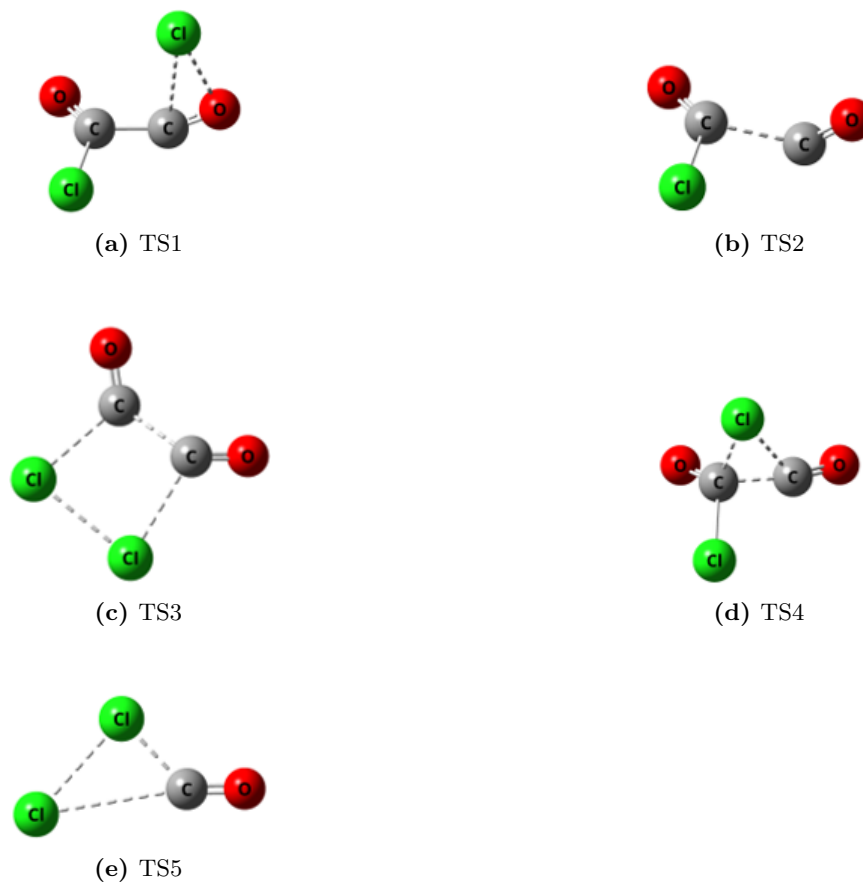


**Figure A.4:** Images of optimized G4 structures for the transitions states TS1–5.

**Table A.5:** Cartesian coordinates of optimized G4 structures for the transitions states TS1–5. Distances are given in Å.

TS1				TS2			
C	-0.926508	0.483762	0.338589	C	0.205450	0.613045	-0.062022
C	0.050795	1.040932	-0.630423	C	-1.592915	-0.106165	0.491709
Cl	-1.738117	-0.877589	-0.391610	Cl	1.382496	-0.755858	-0.003692
Cl	2.086032	-0.676257	0.359667	O	0.438287	1.753083	-0.045601
O	-1.172469	1.016470	1.367572	O	-2.335494	-0.527046	-0.268820
O	1.089934	1.141931	-1.080818				
TS3				TS4			
C	1.059372	-0.935564	0.316568	C	-0.917540	-0.960423	-0.173937
C	1.059478	0.935170	-0.316412	C	0.226944	-0.071498	0.544141
Cl	-1.224970	-1.230678	-0.114585	Cl	1.697178	-0.333091	-0.496601
Cl	-1.224317	1.231127	0.114588	Cl	-0.712099	1.521058	-0.254354
O	1.807545	-1.754052	0.044240	O	-1.825684	-1.585937	-0.416089
O	1.808053	1.753393	-0.044365	O	0.250339	-0.164553	1.734216
TS5							
C	1.236735	-0.565355	0.000002				
O	2.363885	-0.071498	0.000002				
Cl	0.236527	1.049423	-0.000006				
Cl	-1.785438	-0.483835	0.000005				



## B Supplementary Material for Publication V

- A. Branching fraction  $\phi_{1b}$  from Vasudevan et al. data
- B. Thermochemistry of potential  $\text{NCN} + \text{I}$  side reaction (including Tab. [B.1](#))
- C. Reaction mechanism (ASCII file)
- D. Thermodynamic data, NASA polynomials (ASCII file)
- E. Experimental conditions (Tab. [B.2](#))
- F. Additional example profiles for  $\text{HCN}$  and  $^3\text{NCN}$  (Fig. [B.1](#))
- G. Experimental and simulated  $\text{HCN}$  and  $^3\text{NCN}$  profiles (ASCII file)
- H. Arrhenius plot for  $\text{BrCN} + \text{H}$  (Fig. [B.2](#))
- I. Global fit analysis (including Fig. [B.3](#))
- J. Colored version of Fig. [8.2](#) (Fig. [B.4](#))

### A. Branching fraction $\phi_{1b}$ from Vasudevan et al. data

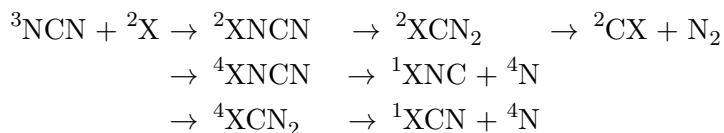
Vasudevan et al. (Ref. 10 of the main text) reported rate constant data for the reaction channel  $\text{NCN} + \text{H} \rightarrow \text{HCN} + \text{N}$ ,  $k_{1b}$ , and for the prompt-NO initiation reaction  $\text{CH} + \text{N}_2 \rightarrow \text{NCN} + \text{H}$  (assuming that NCN is the sole product of the reaction),  $k_{-1a}$ . Therefore, a value for the branching fraction  $\phi_{1b}$  can be obtained by calculating  $k_{1a}$  from thermochemical equilibrium using the recent consensus value of the enthalpy of formation of the  $^3\text{NCN}$  radical ( $\Delta_f H_{298\text{K}}^\circ = (451 \pm 1) \text{ kJ/mol}$ , Ref. 3 of the main text). At a temperature of  $T = 2450 \text{ K}$  one obtains  $\phi_{1b} = 0.46$ .

For an uncertainty estimate, the reported errors in Ref. 10 of the main text for  $k_{-1a}$  (32%, interpolated from the values stated in the abstract) and  $k_{1b}$  (factor of 2) need to be combined with the uncertainty of the enthalpy of formation of  $^3\text{NCN}$  (resulting in 5% uncertainty for the calculated  $k_{1a}$  value). No additional errors were assumed for the other thermodynamic data (all taken from Ref. 3 of the main text). The resulting total uncertainty  $\Delta\phi_{1b}$ , assuming no error compensation, is  $+0.41$  and  $-0.29$  in positive and negative direction, respectively.

The final value,  $\phi_{1b} = 0.46_{-0.29}^{+0.41}$ , has been reported in the Introduction of the main text and is included in Fig. 8.2b as open triangles with error bars.

### B. Thermochemistry of potential $\text{NCN} + \text{I}$ side reaction

Using thermal ethyl iodide decomposition as a source of H atoms goes along with the formation of I atoms at comparable concentration levels. Although it is known that, in general, iodine atom reactivity is much lower than that of H atoms – mainly due to energetic reasons – the reaction  $\text{NCN} + \text{I}$  holds the potential to interfere with the rate constant determination of the total rate constant of reaction 1 ( $\text{NCN} + \text{H}$ ) from the measured NCN decay profiles. If so, neglecting the extra NCN loss would result in systematically too high rate constant values  $k_1$  and hence systematically too low branching fractions for the reaction channel 1b yielding  $\text{HCN} + \text{N}$  as products. In order to assess the need to include this potentially important side reaction, quantum-chemical calculations have been performed to evaluate the thermochemistry of feasible reaction products. Here, it was assumed that the  $\text{NCN} + \text{I}$  reaction takes place on a potential energy surface similar to the one of the  $\text{NCN} + \text{H}$  reaction. The most important reaction channels, including possible recombination products that may become important at high pressure/low temperature conditions, are as follows:



Here, X represents either an H or I atom. Note that the reaction can proceed both on the doublet potential energy surface, yielding  $^2\text{CH}/^2\text{CI} + \text{N}_2$  or the thermodynamically favored recombination product  $^2\text{HNCN}/^2\text{INCN}$ , and on the quartet surface, yielding either  $^1\text{HNC}/^1\text{INC} + ^4\text{N}$  or  $^1\text{HCN}/^1\text{ICN} + ^4\text{N}$ . As outlined in the main text and described in more detail in Ref. 1, at typical combustion conditions the H atom reaction yields  $^2\text{CH} + \text{N}_2$  and  $^1\text{HCN} + ^4\text{N}$  as the two main prompt-NO switch reaction products.

For this Supplemental Material, quantum chemical calculations have been performed using the Gaussian16 program suite [2] on the M062X DFT level of theory using the Karlsruhe def2-TZVP valence triple-zeta polarization basis set that allows for the treatment of iodine-containing reactions. To check the reliability of the energy calculations, the predicted reaction enthalpies were compared with literature values taken from the most recent ATcT thermodynamic database [3]. Reaction enthalpies  $\Delta_r H^\circ(298\text{ K})$  of the following simple bond fission reactions are reproduced within 10 kJ/mol on average:  $\text{I}_2 \rightarrow 2\text{ I}$  (142 kJ/mol; ATcT 151 kJ/mol),  $\text{N}_2 \rightarrow 2\text{ N}$  (929 kJ/mol; ATcT 945 kJ/mol),  $\text{HI} \rightarrow \text{H} + \text{I}$  (286 kJ/mol; ATcT 298 kJ/mol),  $\text{HCN} \rightarrow \text{H} + \text{CN}$  (533 kJ/mol; ATcT 529 kJ/mol), and  $\text{ICN} \rightarrow \text{I} + \text{CN}$  (333 kJ/mol; ATcT 325 kJ/mol). A comparison of the predicted reaction enthalpies in the  ${}^2\text{X} + {}^3\text{NCN}$  reaction system is shown in Tab. B.1.

**Table B.1:** Standard reaction enthalpies  $\Delta_r H^\circ(298\text{ K})$  calculated with Gaussian16 in kJ/mol for the  ${}^2\text{X} + {}^3\text{NCN}$  reaction system ( $\text{X} = \text{H}, \text{I}$ ).  $\Delta(\text{I-H})$  represents the reaction enthalpy difference for the iodine reaction system ( $\text{X} = \text{I}$ ) compared to the respective hydrogen counterpart ( $\text{X} = \text{H}$ ).

Product	$\Delta_{\text{r}}H^\circ(298\text{ K})$				$\Delta(\text{I-H})$
	X = H		X = I		
	This work	ATcT [3]	This work	ATcT [3]	
<b><math>^2\text{XNCN}</math></b>	-342	-349	-108	–	234
$^2\text{XCN}_2$	-177	–	9	–	186
<b><math>^2\text{CX} + \text{N}_2</math></b>	-59	-73	21	–	80
$^4\text{XCN}_2$	-96	–	-5	–	91
<b><math>^1\text{XCN} + ^4\text{N}</math></b>	-57	-68	143	136	200
$^4\text{XNCN}$	-15	–	-11	–	4
<b><math>^1\text{XNC} + ^4\text{N}</math></b>	-4	-5	254	256	258

Main reaction channels of the  ${}^3\text{NCN} + {}^2\text{X}$  system are printed in bold type. Next to the two key channels  ${}^2\text{CH} + \text{N}_2$  and  ${}^1\text{HCN} + {}^4\text{N}$ , the channel  ${}^1\text{HNC} + {}^4\text{N}$  becomes more important at temperatures higher than studied in this work and the formation of the recombination product  ${}^2\text{HNCN}$  is competitive at low temperatures and very high pressures (also not important for this study) [4]. Overall, the predicted relative energies for the  ${}^3\text{NCN} + {}^2\text{H}$  reaction compare well with the available ATcT values and the potential energy surface outlined in Fig. 1 of Ref. 1, hence giving confidence to the  ${}^3\text{NCN} + {}^2\text{I}$  data as well. Although a full kinetic treatment of the reaction system would need to consider all involved transition states and should be based on a RRKM/master equation type modeling of the multi-well association-rearrangement-dissociation reaction, first conclusions can be drawn from the reaction enthalpies of the different reaction channels alone. On the one hand, compared to the H atom reaction, the reaction enthalpies for all three low-pressure product channels (i.e.,  ${}^2\text{CX} + \text{N}_2$ ,  ${}^1\text{XCN} + {}^4\text{N}$ ,  ${}^1\text{XNC} + {}^4\text{N}$ ) become endothermic – going along with expected much lower rate constant values for the iodine reaction. On the other hand, with  ${}^2\text{CI} + \text{N}_2$  becoming endothermic, the recombination of the intermediate  ${}^2\text{INCN}$  may become feasible. However, the bond dissociation enthalpy of this species is predicted to be only 108 kJ/mol (compared to 342 kJ/mol for  ${}^2\text{HNCN}$ ). For such a weak bond, the thermodynamic equilibrium will



be shifted completely to the side of the dissociation product. Consequently, this species is not stable under high-temperature reaction conditions. Note that this bond is even much weaker than the C-I bond of ethyl iodide (about 233 kJ/mol [5]), which undergoes practically instantaneous dissociation on the time scale of our experiments.

In conclusion, although the maximum H and I atom concentration levels are comparable in our experiments, the reaction  $\text{NCN} + \text{I}$  cannot compete with the fast  $\text{NCN} + \text{H}$  reaction. Feasible reaction channels are either endothermic or the recombination products are too weakly bound to play a significant role at high temperatures. Therefore, the reaction  $\text{NCN} + \text{I}$  can be safely neglected for the analysis of the observed NCN decay profiles.

- [1] N. Lamoureux, P. Desgroux, M. Olzmann, and G. Friedrichs; The story of NCN as a key species in prompt-NO formation, *Prog. Energy Combust. Sci.* 87 (2021) 100940/1–34.
- [2] M. J. Frisch, G. W. Trucks, H. B. Schlegel, G. E. Scuseria, M. A. Robb, J. R. Cheeseman, G. Scalmani, V. Barone, G. A. Petersson, et al.; Gaussian 16, Revision C.01, Gaussian, Inc., Wallingford CT, 2016.
- [3] B. Ruscic and D. H. Bross; Active Thermochemical Tables (ATcT) values based on ver. 1.122r of the Thermochemical Network (2021); available at <https://ATcT.anl.gov> (last access: March 17, 2022)
- [4] S. J. Klippenstein, M. Pfeifle, A. W. Jasper, and P. Glarborg; Theory and modeling of relevance to prompt-NO formation at high pressure, *Combust. Flame* 195 (2018) 3–17.
- [5] T. Bentz, M. Szőri, B. Viskolcz, and M. Olzmann; Pyrolysis of Ethyl Iodide as Hydrogen Atom Source: Kinetics and Mechanism in the Temperature Range 950–1200 K, *Z. Phys. Chem.* 225 (2011) 1117–1128.

### C. Reaction mechanism

The reaction mechanism applied in this work was compiled using the GDFkin3.0 as a base mechanism (see Ref. 9 of the main text). Only reactions from GDFkin3.0 with sensitivity coefficients  $|\sigma(^3\text{NCN}, \text{HCN})| > 1 \times 10^{-4}$  within the studied temperature range were included in the reduced mechanism. Rate constant parameters for the remaining reactions were adopted from recent literature and the mechanism was supplemented with additional reactions to account for  $\text{NCN}_3/\text{NCN}$ ,  $\text{C}_2\text{H}_5\text{I}$ , and  $\text{BrCN}$  chemistry. See also separate ASCII file.

```
!Target reaction: NCN + H
3NCN + H = CH + N2          1.64E13      0.00   -1633.0 !(k_1 - k_1b)
1NCN + H => CH + N2          1.64E13      0.00   -1633.0 !(k_1 - k_1b)
3NCN + H = HCN + N           4.20E14      0.00    9130.0 !This work
1NCN + H => HCN + N           4.20E14      0.00    9130.0 !This work
!Other important reactions
BRCN + H = HCN + BR          9.00E12      0.00    5200.0 !This work
!NCN3 decomposition and 1NCN relaxation
NCN3 => 1NCN + N2            4.90E09      0.00   16969.0 ![1]
1NCN + M => 3NCN + M          6.45E11      0.00    6975.0 ![28]
!Ethyl iodide decomposition and related reactions
C2H5I = C2H5 + I              3.39E13      0.00   48631.0 ![2]
```

---

C2H5I = HI + C2H4	4.68E13	0.00	53988.0 ! [2]
C2H5 + M = C2H4 + H + M	1.00E18	0.00	33385.0 ! [2]
C2H5I + H => C2H5 + HI	1.00E15	0.00	5153.0 ! [2]
C2H5I + I => C2H5 + I2	3.98E13	0.00	16700.0 ! [3]
C2H5 + I2 => C2H5I + I	1.00E13	0.00	0.0 ! [3]
!NCN decomposition and NCN/CN/C2N2 reactions			
3NCN + M = C + N2 + M	8.90E14	0.00	62140.0 ! [4]
3NCN = N + CN	2.95E30	-5.29	117100.0 ! [5]
1NCN + 3NCN => 2CN + N2	1.10E13	0.00	2807.0 ! [28]
1NCN + 1NCN => 2CN + N2	1.10E13	0.00	2807.0 ! [28]
3NCN + N = N2 + CN	1.00E13	0.00	0.0 ! [6]
1NCN + N => N2 + CN	1.00E13	0.00	0.0 ! [6]
3NCN + C = 2CN	5.32E14	0.00	4770.0 ! [28]
1NCN + C => 2CN	5.32E14	0.00	4770.0 ! [28]
3NCN + CN = C2N2 + N	2.08E13	0.00	7333.0 ! [28]
1NCN + CN => C2N2 + N	2.08E13	0.00	7333.0 ! [28]
CN + M = C + N + M	2.53E14	0.00	141090.0 ! [7]
CN + N = C + N2	1.04E15	-0.50	0.0 ! [8]
CN + C = C2 + N	3.00E14	0.00	36000.0 ! [9]
C2N2 + M = 2CN + M	7.39E17	0.00	113066.0 ! [28]
C2 + M = C + C + M	1.50E16	0.00	142400.0 ! [10]
!NCN/CN/N/CxNyHz reactions with			
!hydrocarbons/hydrogen and HCN reactions			
3NCN + H2 = HNCN + H	3.22E05	2.46	23901.0 ! [11]
1NCN + H2 = HNCN + H	7.94E08	1.69	16133.0 ! [11]
1NCN + H2 = NH2 + CN	1.24E11	1.07	23016.0 ! [11]
3NCN + CH => HCN + CN	3.21E13	0.00	-860.0 ! [6]
1NCN + CH => HCN + CN	3.21E13	0.00	-860.0 ! [6]
3NCN + CH2 => H2CN + CN	7.99E13	0.00	4630.0 ! [6]
1NCN + CH2 => H2CN + CN	7.99E13	0.00	4630.0 ! [6]
3NCN + CH2 => HCN + HNC	7.99E13	0.00	4630.0 ! [6]
1NCN + CH2 => HCN + HNC	7.99E13	0.00	4630.0 ! [6]
3NCN + CH3 = CH2NH + CN	4.34E13	0.00	-1175.0 ! [12]
1NCN + CH3 => CH2NH + CN	4.34E13	0.00	-1175.0 ! [12]
CN + H2 => HCN + H	2.95E05	2.45	2238.0 ! [13]
HCN + H => CN + H2	3.73E14	0.00	24854.0 ! [7]
CN + HCN = C2N2 + H	1.51E07	1.71	1530.0 ! [14]
CN + HNC = C2N2 + H	1.00E13	0.00	0.0 ! [15]
NH + H = N + H2	3.00E13	0.00	0.0 ! [15]
CH + N = CN + H	9.55E13	0.00	0.0 ! [16]
CH2 + N = HCN + H	5.00E13	0.00	0.0 ! [8]
C2H4 + N = HCN + CH3	1.60E10	0.00	700.0 ! [17]
C2H3 + N = HCN + CH2	2.00E13	0.00	0.0 ! [8]
H2CN + N = N2 + CH2	6.00E13	0.00	397.0 ! [18]
H2CN => HCN + H	5.05E30	-6.29	31215.9 ! [18]

```

!0.395 atm rate.
!   PLOG / 0.1           1.30E29   -6.03   29894.0/
!   PLOG / 1.0           6.00E31   -6.46   32110.0/
!   PLOG / 10.0          3.50E29   -5.46   32547.0/
HCN + M = H + CN + M      3.37E35   -5.13  133075.0 ![7]
HCN + H => H2CN           3.31E13    0.00   4849.0 ![7]
HCN + M = HNC + M        1.60E26   -3.23  49581.0 ![18]
HNC + H = HCN + H        7.80E13    0.00   3600.0 ![15]
CH2NH + H = H2CN + H2    2.40E08    1.50   7323.0 ![18]
CH2NH + H = HCNH + H2    3.0E008    1.50   6131.0 ![18]
!Iodine reactions
I + H2 => HI + H          2.72E14    0.00  33922.0 ![19]
I + HI = I2 + H           8.01E14    0.00  37130.0 ![20]
I2 + M = I + I + M        9.80E13    0.00  30400.0 ![21]
I2 + H2 => HI + HI        1.94E14    0.00  40976.4 ![22]
HI + HI => H2 + I2        2.50E13    0.00  43758.5 ![22]
HI + H => H2 + I          6.61E13    0.00   976.0 ![2]
HI + C2H5 => C2H5I + H    5.00E13    0.00  17900.0 ![3]
!NCN + I => PRODUCTS      0.00E00    0.00    0.0 !see Section B
!Hydrocarbon/hydrogen reactions
H + H + M = H2 + M        4.96E15   -1.21   612.0 ![23]
CH + H = C + H2           3.70E14    0.01  5337.0 ![24]
CH2 + H = CH + H2         6.02E12    0.00  1789.0 ![25]
C2H2 + H = C2H + H2       6.02E13    0.00  27821.0 ![25]
C2H2 + H (+M) = C2H3 (+M) 8.43E12    0.00  2583.0 ![25]
    LOW/                  1.20E18    0.00  1471.0/
C2H4 + H = C2H3 + H2      5.42E14    0.00  14904.0 ![25]
C2H5 + H2 = C2H6 + H      3.80E00    3.60   845.0 ![26]
C2H4 + M = C2H2 + H2 + M  3.50E16    0.00  71539.0 ![25]
C2H4 + M = C2H3 + H + M   2.59E17    0.00  96578.0 ![25]
!Bromine chemistry
BRCN + M = BR + CN + M    1.06E14    0.00  76600.0 ![27]
BR + BRCN = BR2 + CN      2.00E14    0.00  23000.0 ![27]
CN + BRCN = C2N2 + BR     4.00E11    0.00    0.0 ![27]
2BRCN = BR2 + C2N2        5.00E14    0.00  65000.0 ![27]
BR2 + M = BR + BR + M     2.14E11    0.50  31300.0 ![27]

```

- [1] Dammeier et al., Int. J. Chem. Kinet., 2012, 45, 30-40.
- [2] Varga et al., Int. J. Chem. Kinet., 2014, 46, 295–304.
- [3] Westbrook, Proc. Combust. Inst., 1982, 19, 127–141.
- [4] Dammeier et al., Phys. Chem. Chem. Phys., 2012, 14, 1030–1037.
- [5] Busch, PhD thesis, Karlsruher Institut für Technologie, 2010.
- [6] Moskaleva and Lin, Proc. Combust. Inst., 2000, 28, 2393–2401.
- [7] Tsang and Herron, J. Phys. Chem. Ref. Data, 1991, 20, 609–663.

- 
- [8] Miller and Bowman, *Prog. Energy Combust. Sci.*, 1989, 15, 287–338.
- [9] Slack, *J. Chem. Phys.*, 1976, 64, 228–236.
- [10] Kruse and Roth, *J. Phys. Chem. A*, 1997, 101, 2138–2146.
- [11] Faßheber et al., *J. Phys. Chem. A*, 2020, 124, 4632–4645.
- [12] Hesse et al., 37th international Symposium on Combustion, 2P006, 2018.
- [13] Wooldrigde et al., *Int. J. Chem. Kinet.*, 1996, 28, 245–258.
- [14] Tsang, *J. Phys. Chem. Ref. Data*, 1992, 21, 753–791.
- [15] Dagaut et al., *Prog. Energy Combust. Sci.*, 2008, 34, 1–46.
- [16] Brownsword et al., *J. Chem. Soc. Faraday Trans.*, 1996, 92, 727–727.
- [17] Paraskevopoulos and Winkler, *J. Phys. Chem.*, 1967, 71, 947–951.
- [18] Dean and Bozelli, *Combustion Chemistry of Nitrogen*, In: *Gas-Phase Combustion Chemistry*, Springer New York, 2000.
- [19] Michael et al., *Chem. Phys. Lett.*, 2000, 319, 99–106.
- [20] Garrett and Truhlar, *J. Am. Chem. Soc.*, 1979, 101, 5207–5217.
- [21] Troe and Wagner, *Z. Phys. Chem.*, 1967, 55, 326–328.
- [22] Baulch et al., *J. Phys. Chem. Ref. Data*, 1981, 10, 1–721.
- [23] Varga et al., *Int. J. Chem. Kinet.*, 2016, 48, 407–422.
- [24] Han et al., *J. Comput. Chem.*, 2011, 32, 2745–2755.
- [25] Baulch et al., *J. Phys. Chem. Ref. Data*, 1992, 21, 411–429.
- [26] Tsang and Hampson, *J. Phys. Chem. Ref. Data*, 1986, 15, 1087–1279.
- [27] Tabayashi et al., *J. Phys. Chem.*, 1975, 79, 204–209.
- [28] Hesse et al., Shock tube study on the reaction  $\text{NCN} + \text{NCN}$  with  $^3\text{NCN}$  and CN detection, preliminary data from unpublished work.

#### D. Thermodynamic data, NASA polynomials (ASCII file)

NASA polynomials for the species included in the mechanism are provided in a separate ASCII file.

## E. Experimental conditions

**Table B.2:** Experimental conditions and results for the rate constants  $k_1$  and  $k_{1b}$  as well as the corresponding branching fractions  $\phi_{1b}$ .  $x(\text{NCN}_3)$  refers to the pre-shock  $\text{NCN}_3$  mole fraction accounting for adsorption losses (see main text).

$T / \text{K}$	$\rho \times 10^{-6} / \text{mol cm}^{-3}$	$x(\text{NCN}_3) / \text{ppm}$	$x(\text{C}_2\text{H}_5\text{I}) / \text{ppm}$	$x(\text{BrCN}) / \text{ppm}$	$x(\text{N}_2) / \text{ppm}$	$k_1 \times 10^{-13} / \text{cm}^3 \text{mol}^{-1} \text{s}^{-1}$	$k_{1b} \times 10^{-13} / \text{cm}^3 \text{mol}^{-1} \text{s}^{-1}$	$\phi_{1b}$
1227	3.80	42	357	17	20	4.4	0.8	0.19
1312	4.92	66	622	35	64	4.3	1.1	0.26
1367	4.96	44	328	18	33	4.4	1.9	0.43
1381	3.95	39	357	17	29	4.5	1.7	0.38
1447	3.58	47	445	17	25	4.4	1.7	0.39
1461	4.25	40	328	18	33	4.8	2.4	0.50
1526	3.74	49	534	16	20	4.9	2.3	0.47
1529	3.62	39	445	17	25	5.1	1.9	0.37
1551	3.78	39	264	17	31	5.5	2.6	0.47
1604	3.18	48	445	17	26	5.3	1.9	0.36
1607	3.51	98	802	33	48	5.1	2.7	0.53
1611	3.67	99	713	33	40	4.9	2.4	0.49
1667	3.01	95	802	33	56	4.3	2.2	0.51
1674	3.28	98	802	33	49	4.9	2.7	0.55
1774	3.04	47	225	17	27	7.2	3.4	0.47
1979	5.35	48	328	18	33	7.6	3.9	0.51

## F. Additional example profiles for HCN and $^3\text{NCN}$

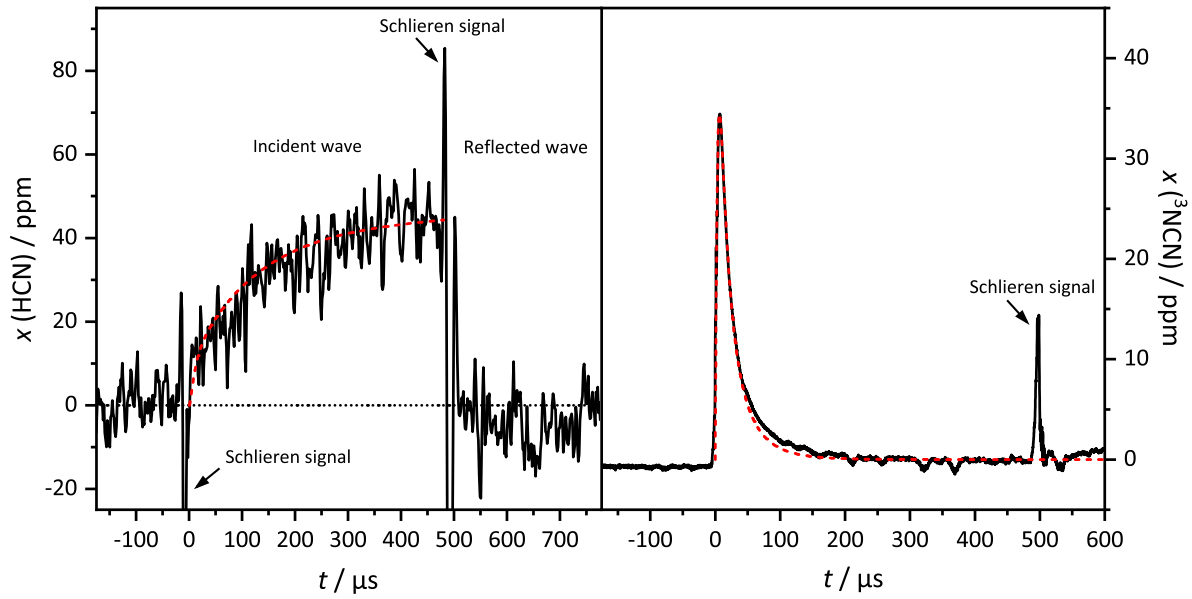


**Figure B.1:** Example kinetic profiles of HCN (a) and  $^3\text{NCN}$  (b) at 1312 K and 537 mbar with 66 ppm  $\text{NCN}_3$ , 622 ppm  $\text{C}_2\text{H}_5\text{I}$ , 35 ppm  $\text{BrCN}$ , and 64 ppm  $\text{N}_2$ . The small dips in the  $^3\text{NCN}$  signal were caused by instabilities of the external SHG resonator of the UV laser source, the Schlieren signal around 500  $\mu\text{s}$  indicates the arrival of the reflected shock wave.

## G. Experimental and simulated HCN and $^3\text{NCN}$ profiles (ASCII file)

All experimental profiles of  $^3\text{NCN}$  and HCN alongside their simulated counterparts are available in a separate ASCII file. In this file, the profiles are only identified by temperature, while pressures and concentrations can be found in Tab. B.2 in Section E. Due to technical issues during the experiments, two  $^3\text{NCN}$  profiles were not recorded (1367 K, 1607 K). For the purpose deriving the branching fractions  $\phi_{1b}$  for these experiments,  $k_1$  values from two  $^3\text{NCN}$  profiles measured at similar temperatures (1381 K, 1611 K) were adopted.

## H. Arrhenius plot for $\text{BrCN} + \text{H}$

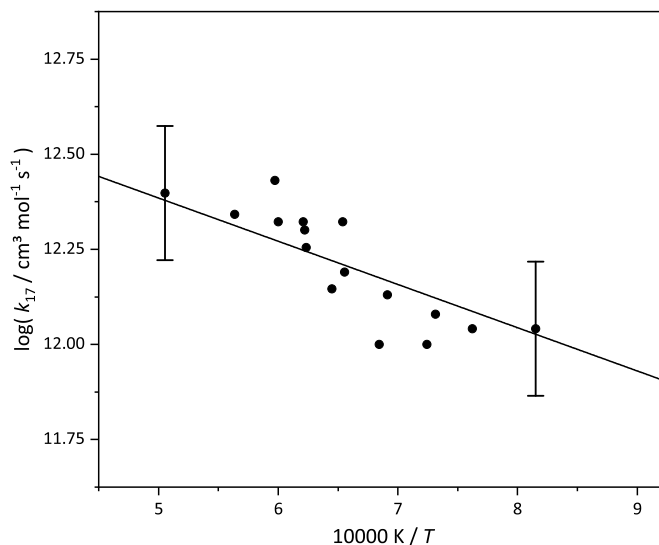


**Figure B.2:** Arrhenius plot for reaction  $\text{BrCN} + \text{H}$  (reaction 17 in the main text) as derived indirectly from the late HCN formation with the activation energy set to the value from Arunan et al. (Ref. 25 of the main text).

## I. Global fit analysis

A global fit program [1] using the the FORTRAN Feasible Sequential Quadratic Programming (FFSQP) subroutine [2] is currently under development in our research group. It was used to verify the manual iterative fit procedure as described in the main text. The global multi-parameter fit routine relies on the CHEMKIN-II package to perform numerical simulations of concentration-time profiles and takes experimental profiles with the corresponding experimental conditions, a reaction mechanism, and thermodynamic data of the involved species as main input. Centering on the rate constant expressions reported in Section C, upper and lower bounds for the adjustable Arrhenius parameters need to be specified. For each run of the program, the values of the Arrhenius parameters for the selected reactions are placed randomly within the parameters space and the program optimizes the rate parameters of the selected reactions by minimizing the misfit function (i.e., by minimizing the sum of the deviations of all experimental profiles from their simulated counterparts.)

5000 runs of the global fit routine were performed to derive optimized rate constant values for

channels 1a and 1b of reaction  $\text{NCN} + \text{H}$  and for reaction  $\text{BrCN} + \text{H}$ . Each set of the obtained rate constants reflects a local minimum on the hypersurface of the misfit function. All profiles of  $^3\text{NCN}$  and  $\text{HCN}$  recorded in this work were used for the global fit. Weights were assigned to the individual kinetic profiles based on the square root of their signal-to-noise ratios. For reaction  $\text{NCN} + \text{H}$ , the pre-exponential factors  $A$  for channel 1a and 1b were allowed to vary within a factor of 2, whereas the respective activation energies  $E_a$  were altered within a factor of 1.2.  $A$  of reaction 17 was allowed to vary within a factor of 2.5, while  $E_a$  of reaction 17 was fixed to the value given by Arunan et al. (Ref. 25 of the main text). Rate constant parameters for  $^1\text{NCN}$  and  $^3\text{NCN}$  were assumed to be equal. From the 5000 individual runs, the ten runs with the smallest misfit values were identified. Here,  $k_{1b}$  is on average 28% lower than the values obtained from the manual analysis, while  $k_1 = k_{1a} + k_{1b}$  is only around 10% lower. This clearly shows that  $k_1$  can be reliably extracted from the experimental  $^3\text{NCN}$  profiles. However,  $k_{17}$  from the automatic fit turned out to be larger by a factor of about 2. Evidently, the global fit suggests that a slightly higher amount of  $\text{HCN}$  is formed by reaction  $\text{BrCN} + \text{H}$  rather than by reaction  $\text{NCN} + \text{H}$ .

Figure B.3 shows the global fit results in terms of the branching fraction, with  $\phi_{1b}$  of the best run drawn as the dashed black curve and  $\phi_{1b}$  of the ten best runs as solid grey curves. The branching fraction values from the best fit are on average 0.07 lower than the branching fractions derived from the manual analysis, corresponding to a relative change of 10–34%, depending on temperature. The lower  $\phi_{1b}$  values are easily explained by the reduced  $\text{HCN}$  atom yield due to the lower  $k_{1b}$  values of the global fit compared to the manual analysis. However, within the specified uncertainty range (grey shaded area), the results of the global fit routine are fully compatible within the manually derived  $\phi_{1b}$  values. The prompt-NO switch temperature  $T_S$  ( $\phi_{1b} = 0.5$ ) of the best global fit result is 1830 K, still consistent with  $T_S = 1670$  K from the manual procedure and  $T_S = 2080$  K as derived by Lamoureux et al. in the 2021 review on  $\text{NCN}$  chemistry (Ref. 3 of the main text).

Although an automatic fit seems to be a more objective way of deriving rate constant data at first sight, it is still based on uncertain assumptions (e.g., using a post hoc lump reaction  $\text{BrCN} + \text{H} \rightarrow \text{HCN} + \text{Br}$  to account for the observed  $\text{HCN}$  increase on longer reaction times). Moreover, signal anomalies such as baseline instabilities arising from shock tube-induced acoustic noise components are difficult to handle for automatic fit routines. Such problems have to be accounted for by lower weighting or masking of data points in the kinetic profiles. We therefore take the overall good agreement of the global analysis with the outcome of the manual iterative fit procedure as a further verification of our reported results.

- [1] J. Rückelt, T. Slawig, S. Hesse, M. Stuhr, M. Thiele, G. Friedrichs. A Chemkin-based Fit Program for Global Analysis of Multi-Species Kinetic Measurements. Program under development, to be published elsewhere.
- [2] J. L. Zhou, A. Tits, C. T. Lawrence (1998). FFSQP version 3.7b: A fortran code for solving optimization problems, Tech. Report SRC-TR-92-107r5, University of Maryland, College Park, MD 20742, USA.

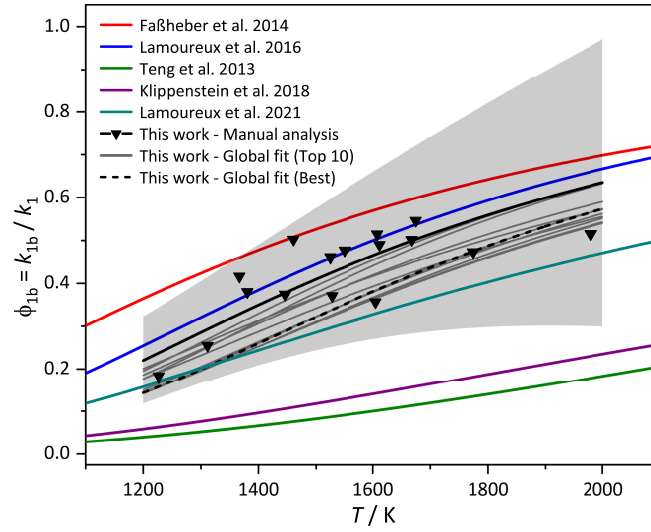


**Figure B.3:** Branching fraction plot for  $\phi_{1b}$  comparing the results of the manual analysis (solid black curve and black triangles, see main text), the results of the global fit procedure (grey and dashed black curves), and literature values (colored curves).

## J. Colored version of Fig. 8.2

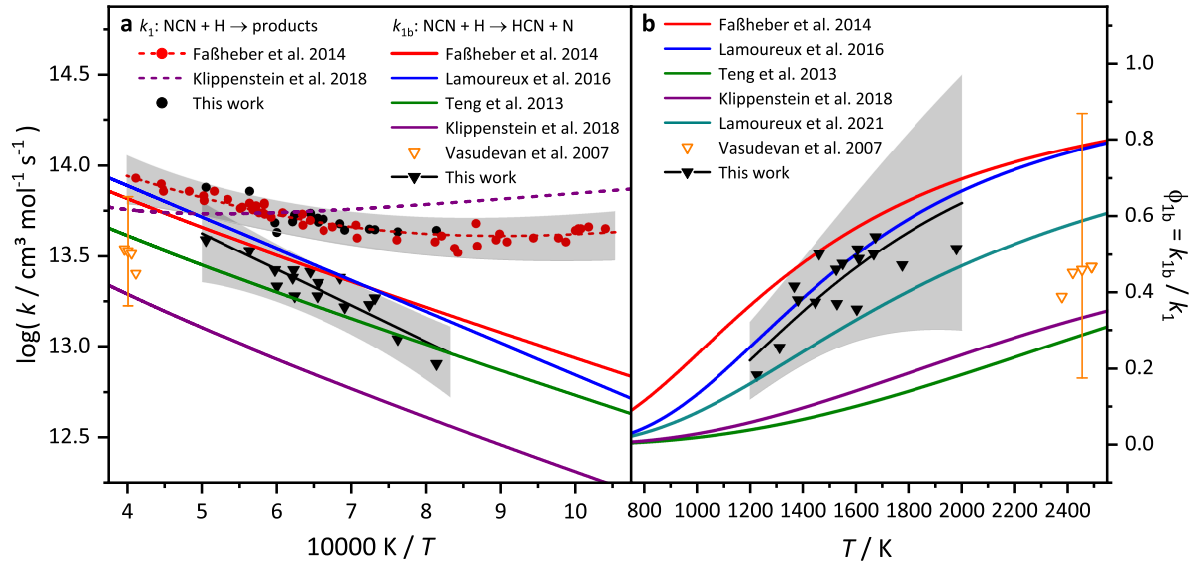


**Figure B.4:** Arrhenius plot for  $k_1$  (a) and branching fraction plot for  $\phi_{1b}$  (b) in color (see Fig. 2).





## Scientific Contributions

Work related to the present thesis is marked with an asterisk (\*).

### Full Papers

- **M. Stuhr**, N. Faßheber, and G. Friedrichs, Single-Tone Mid-Infrared Frequency Modulation Spectroscopy for Sensitive Detection of Transient Species, *Opt. Express* **2019**, 27, 26499–26512, DOI [10.1364/oe.27.026499](https://doi.org/10.1364/oe.27.026499) (Editors' Pick). \*
- I. Sadiék, A. Hjältén, F. S. Vieira, C. Lu, **M. Stuhr**, A. Foltynowicz, Line Positions and Intensities of the  $\nu_4$  Band of Methyl Iodide Using Mid-Infrared Optical Frequency Comb Fourier Transform Spectroscopy, *J. Quant. Spectrosc. Radiat. Transfer* **2020**, 255, 107263/1–8, DOI [10.1016/j.jqsrt.2020.107263](https://doi.org/10.1016/j.jqsrt.2020.107263).
- **M. Stuhr**, S. Hesse, and G. Friedrichs, Quantitative and Sensitive Mid-Infrared Frequency Modulation Detection of HCN behind Shock Waves, *Fuels* **2021**, 2, 437–447, DOI [10.3390/fuels2040025](https://doi.org/10.3390/fuels2040025). \*
- **M. Stuhr** and G. Friedrichs, Mid-Infrared Frequency Modulation Detection of HCN and Its Reaction with O Atoms behind Shock Waves, *J. Phys. Chem. A* **2022**, 126, 50, 9485–9496, DOI [10.1021/acs.jpca.2c06817](https://doi.org/10.1021/acs.jpca.2c06817). \*
- **M. Stuhr**, S. Hesse, and G. Friedrichs, Branching Fraction Measurement of the Prompt-NO Switch Reaction  $\text{NCN} + \text{H}$ , *Proc. Combust. Inst.* **2023**, 39, 147–156, DOI [10.1016/j.proci.2022.07.146](https://doi.org/10.1016/j.proci.2022.07.146). \*
- **M. Stuhr**, S. Hesse, N. Faßheber, M. Wohler, M. Pal, Y. Sakai, P. Hemberger, and G. Friedrichs, UV Photolysis of Oxalyl Chloride: ClCO Radical Decomposition and Direct  $\text{Cl}_2$  Formation Pathways, *submitted to Int. J. Chem. Kinet.*. \*

### Conference Papers

- I. Sadiék, A. Hjältén, **M. Stuhr**, G. Friedrichs, and A. Foltynowicz, Towards a Transferable Standard for Nitrous Oxide Isotopomer Ratio, Conference on Lasers and Electro-Optics (CLEO), *OSA Technical Digest* **2020**, DOI [10.1364/CLEO\\_SI.2020.STu4N.4](https://doi.org/10.1364/CLEO_SI.2020.STu4N.4).
- I. Sadiék, A. Hjältén, **M. Stuhr**, C. Lu, F. S. Vieira, and A. Foltynowicz, Mid-Infrared Comb-Based Fourier Transform Spectroscopy of Halogenated Volatile Organic Compounds, Conference on Lasers and Electro-Optics (CLEO), *OSA Technical Digest* **2020**, DOI [10.1364/CLEO\\_SI.2020.SM1M.8](https://doi.org/10.1364/CLEO_SI.2020.SM1M.8).
- A. Hjältén, M. Germann, I. Sadiék, C. Lu, F. S. Vieira, K. Krzempek, A. Hudzikowski, A. Głuszek, D. Tomaszewska, **M. Stuhr**, G. Soboń, and A. Foltynowicz, Fourier Transform Spectroscopy Using Difference Frequency Generation Comb Sources at  $3.3\ \mu\text{m}$  and  $7.8\ \mu\text{m}$ , *OSA Technical Digest 2021*, DOI [10.1364/AIS.2021.JTu4D.3](https://doi.org/10.1364/AIS.2021.JTu4D.3).
- M. Pal, **M. Stuhr**, N. Faßheber, A. Petersen, F. Greiner, and G. Friedrichs, Mid-IR frequency modulation spectroscopy for sensing  $\text{C}_2\text{H}_2$  in a dusty plasma, Optical Sensors and Sensing Congress *Technical Digest Series*, **2022**, DOI [10.1364/LACSEA.2022.LM4B.4](https://doi.org/10.1364/LACSEA.2022.LM4B.4).

## Other Contributions to Conferences

- **M. Stuhr** and G. Friedrichs, Mid-Infrared Frequency Modulation Spectroscopy for Reaction Kinetics Applications, *Annual Meeting of the German Bunsen Society of Physical Chemistry*, Hanover, Germany, May 2018 (**Hot Topic Talk**). \*
- **M. Stuhr**, S. Hesse, and G. Friedrichs, Quantitative and Sensitive Mid-Infrared Frequency Modulation Detection of HCN behind Shock Waves, *10th European Combustion Meeting*, Napoli, Italy, April 2021 (Online, Poster). \*
- A. Hjältén, I. Sadiq, C. Lu, F. S. Vieira, **M. Stuhr**, M. Germann, and A. Foltynowicz, High-Resolution Measurements of Halogenated Volatile Organic Compounds Using Frequency Comb Fourier Transform Spectroscopy, *European Quantum Electronics Conference 2021*, Munich, Germany, June 2021 (Online, Talk).
- **M. Stuhr**, S. Hesse, and G. Friedrichs, Branching Fraction Measurement of the Prompt-NO Switch Reaction  $\text{NCN} + \text{H}$ , *39th International Symposium on Combustion*, Vancouver, Canada, July 2022 (Talk). \*
- M. Pal, **M. Stuhr**, N. Faßheber, A. Petersen, F. Greiner, G. Friedrichs, Quantitative detection of  $\text{C}_2\text{H}_2$  in a dusty plasma environment using sensitive mid-IR frequency modulation spectroscopy, *SAMOP21: DPG Meeting*, Germany, September 2021 (Online, Poster).
- S. Hesse, **M. Stuhr**, and G. Friedrichs, Multiple Detection Schemes for Investigating High-Temperature Radical Cross Reactions of NCN behind Shock Waves, *36th International Symposium on Free Radicals*, Stockholm, Sweden, April 2022 (Poster). \*
- M. Pal, **M. Stuhr**, and G. Friedrichs, Quantitative and calibration-free mid-IR two-tone frequency modulation spectroscopy (TTFMS), *Annual Meeting of the German Bunsen Society of Physical Chemistry*, Berlin, Germany, June 2023 (Talk).
- **M. Stuhr**, S. Hesse, N. Faßheber, M. Wohler, M. Pal, Y. Sakai, P. Hemberger, and G. Friedrichs, UV Photolysis of Oxalyl Chloride: Decomposition of the ClCO Radical and Quantum Yield of Molecular  $\text{Cl}_2$  Elimination, *12th International Conference on Chemical Kinetics*, Hefei, China, June 2023 (**Poster Award**). \*

# Curriculum Vitae

## Personal Information

Name	Michael Stuhr
Date of birth	August 27, 1991
Place of birth	Bad Oldesloe, Schleswig-Holstein, Germany
Citizenship	German
Contact	michael-stuhr@hotmail.de / stuhr@phc.uni-kiel.de
Identifiers	<a href="#">ORCID</a> : 0000-0002-4536-6060 <a href="#">ResearchGate</a> : Michael-Stuhr-2 <a href="#">LinkedIn</a> : michael-stuhr-489042241

## Academic Education

10/2011 - 09/2014	B.Sc. Chemistry, Kiel University  Title of B.Sc. thesis: 'Setup and Characterization of a High-Resolution NIR-Diode Laser Absorption Spectrometer' (in German)
10/2014 - 05/2017	M.Sc. Chemistry, Kiel University  Title of M.Sc. thesis: 'Setup of a Mid-IR-cw-OPO Absorption Spectrometer for Highly Sensitive Detection of Gas-Phase Species' (in German)
June 21st, 2017	Master certificate

## Doctorate

05/2017 - present	PhD student at the Institute of Physical Chemistry, Research Group Friedrichs, Kiel University
-------------------	--



## Acknowledgments

I would like to express my gratitude to the many people who have helped me along the way – my family, friends, past and present colleagues, collaborators, members of the institute, and many others.

Each of them, in their own way, has played a role in the completion of this dissertation. I am deeply grateful to them for providing general advice, scientific feedback, administrative/technical assistance, and personal support, or for putting up with my work-related tirades.

Special thanks are due to my thesis advisor Prof. Dr. Gernot Friedrichs, whose continuous support and professional guidance have shaped me as a scientist and as a person since I was still a bachelor student.



## Declaration

I hereby declare that the present dissertation is my own work and effort, prepared under the guidance of my thesis supervisor Prof. Dr. Gernot Friedrichs. When other sources or tools were used, they have been acknowledged.

This work represents my first dissertation and it has not been previously submitted in whole or in part to any other university or institution for any other dissertation attempts. No academic degree that I have received has ever been revoked.

Parts of this thesis have already been published or submitted as research articles (Publications I–V, Chapters [4–8](#)).

The present dissertation complies with the Rules of Good Scientific Practice as proposed by the German Research Foundation (DFG).

April 19, 2024, Kiel

A handwritten signature in black ink, appearing to read 'M. Stuhr', with a stylized, cursive script.

Michael Stuhr



